INHIBITION-RELATED FUNCTIONS IN THE HUMAN SUBCORTEX

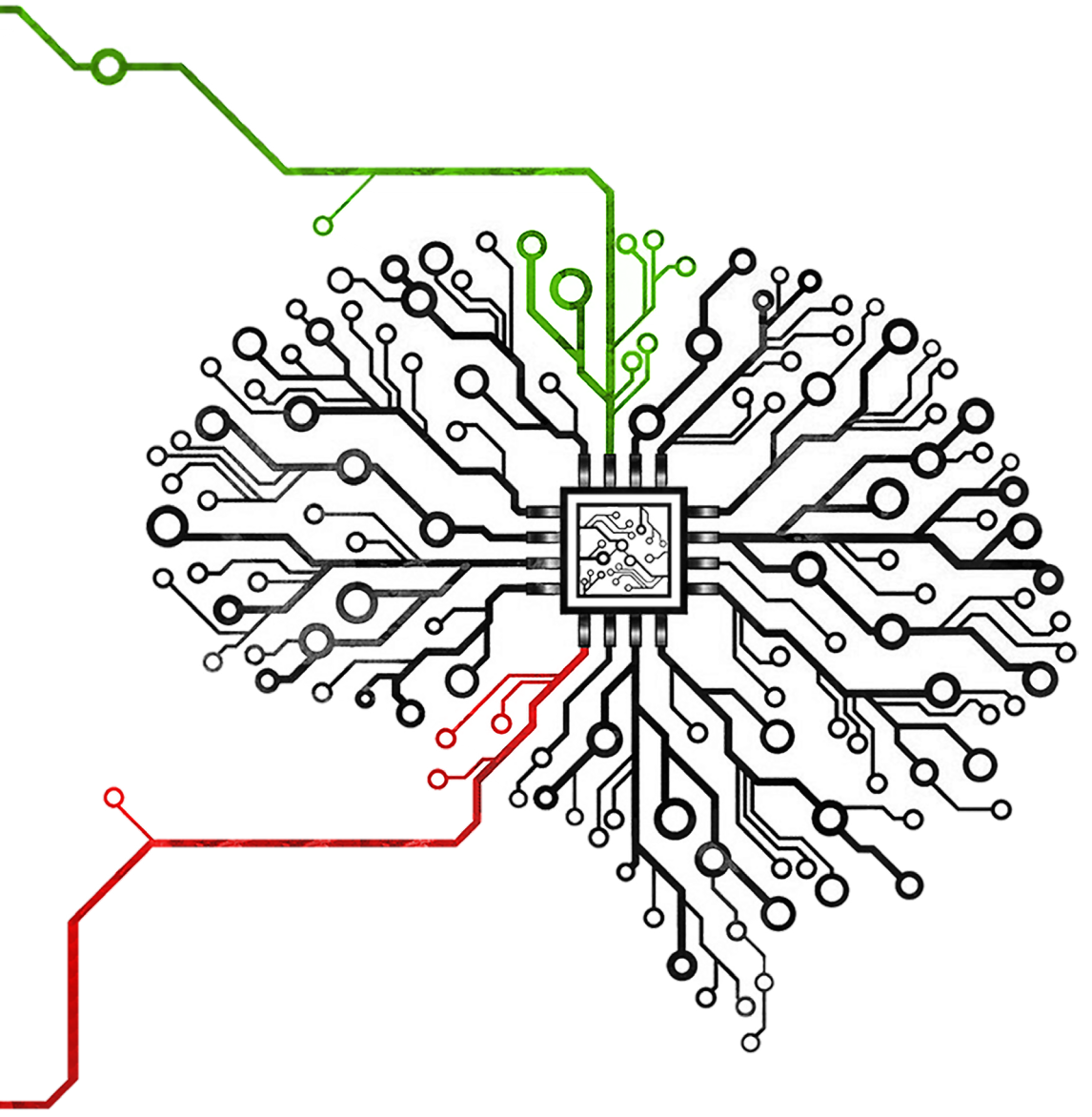

SCOTT J.S. ISHERWOOD

Inhibition-related functions in the human subcortex

Scott J.S. Isherwood

ISBN 978-94-6473-268-9

Inhibition-related functions in the human subcortex

ACADEMISCH PROEFSCHRIFT

ter verkrijging van de graad van doctor

aan de Universiteit van Amsterdam

op gezag van de Rector Magnificus

prof. dr. ir. P.P.C.C. Verbeek

ten overstaan van een door het College voor Promoties ingestelde commissie,

in het openbaar te verdedigen in de Agnietenkapel

op maandag 16 Oktober 2023, te 14.00 uur

door Scott Jie Shen Isherwood

geboren te Chertsey

Promotiecommissie

Promotor:	prof. dr. B. U. Forstmann	Universiteit van Amsterdam
Copromotor:	dr. P. L. E. A. Bazin	Universiteit van Amsterdam
Overige leden:	prof. dr. A. J. Heathcote	Universiteit van Amsterdam
	dr. D. Matzke	Universiteit van Amsterdam
	dr. W. P. M. van den Wildenburg	Universiteit van Amsterdam
	dr. A. Sebastian	University Medical Center of the Johannes Gutenberg-University Mainz
	dr. H. S. Scholte	Universiteit van Amsterdam

Faculteit der Maatschappij- en Gedragswetenschappen

The research for this doctoral thesis received financial assistance from the Netherlands Organisation for Scientific Research (NWO) under project number 016.Vici.185.052.

"Any action born of noise produces more noise, more confusion"
- Jiddu Krishnamurti

Contents

Chapter 1

Introduction

The field of cognitive neuroscience has come a long way since the advent of magnetic resonance imaging (MRI) in the 70s. Since this pinnacle point, there has been a boom of structural and functional findings of the human brain across the field. The brain has long been split into three distinct parts: the cerebral cortex, the subcortex, and the cerebellum. The subcortex, which simply translates to 'beneath the cortex', accounts for around 25% of the entire brain. Since Korbinian Brodmann's renowned cytoarchitectural breakdown of the cerebral cortex at the start of the 20th century, our maps of the brain have been in constant evolution. In 1998 the Federative Committee on Anatomical Terminology produced the Terminologia Anatomica, the holy bible of anatomy, describing the 455 structures within each hemisphere of the human subcortex (Federative Committee on Anatomical Terminology, 1998). Of these 455 structures, only around 7-8% of them are represented in MRI atlases. The cortex on the other hand has received the lion's share of attention throughout the history of cognitive neuroscience. This outer region of the brain has been mapped vigorously and continuously, and most recently defined to be made up of approximately 180 different regions (Glasser et al., 2016). So-called 'corticocentric' views have long dominated the field. The subcortex is therefore rightly considered as *terra incognita* (Alkemade et al., 2013). The question is: why has there been such an underrepresentation of a large portion of the brain?

Over the course of my research, it has become apparent that there are two likely reasons for this underrepresentation. The first, is that it was long believed that the subcortex is just not that important. As our understanding of the human brain grew, it became more and more evident that it is the cerebral cortex that separates us from the rest of the animal kingdom. This caused our search for the anatomy and functions of the cortex to overshadow the deep brain. On the surface this makes sense, other species of mammal have a cortex that seems inferior to ours, while the subcortex appears to be relatively consistent in size and shape. This view resulted in the idea that the subcortex does not drive any aspects of higher-level cognition, and that our enormous cerebral cortex is what truly underpins our

distinctly human aspects of behaviour and cognition (Bystron et al., 2008). But, is this so? Is the subcortex merely a sluggish artifact of our primitive ancestry, passed down as a tag along to our superior and uniquely human cerebral cortex? Interestingly, when digging deeper researchers found that subcortical differences in gene regulation between humans and other primates actually outweighs that of the cortex (McCoy et al., 2017; Vermunt et al., 2016). There is also now an abundance of evidence supporting the role of the subcortex in many aspects of human cognition and that proper functioning of subcortical nuclei is required for an array of adaptive and core day-to-day human behaviours such as learning, action selection and memory (Aron and Poldrack, 2006; Fortin et al., 2002; Frank, 2006; Glimcher, 2004; Obeso et al., 2008; Sutton, Barto, et al., 1998). The subcortex is not only highly interconnected within itself, including the brainstem, but also with the cortex and cerebellum, with both extensive reciprocal and non-reciprocal circuits (Alexander et al., 1986; Middleton and Strick, 1994). These more recent findings mean the subcortex is only just beginning to be appreciated in the human neurosciences.

The second reason for this underrepresentation is a practical one: the subcortex is hard to get to. Both invasive and non-invasive techniques of studying neuroanatomy are inherently easier when studying the outer regions of the brain. Subcortical structures are located deep within the brain, and their small size, biophysical properties and close spatial proximity to other nuclei make it challenging to obtain high-resolution images (Miletić et al., 2022). For methods such as MRI and electroencephalography (EEG), the distance of the middle of the brain from the measuring equipment outside of the skull makes acquiring a reasonable signal difficult. Only recently has precise observation of the subcortex *in vivo* become possible with these methods. Recent advances in neuroimaging and neurophysiological techniques are beginning to shed light on the importance of the subcortex, and it is likely that future research will increasingly focus on this often-overlooked part of the brain.

More holistic approaches to brain mapping are difficult, advanced methodologies and equipment are needed to visualize the subcortex and cerebellum. Even here, this thesis focuses on imaging the subcortex, and unfortunately mostly disregards the cerebellum due to these difficulties. On the bright side, imaging methods that can observe the subcortex are usually also able to image the cortex with the same rigor. Throughout this thesis I bring together techniques that provide knowledge closer to the level of the whole brain. While I will emphasize the role of the subcortex, it is important to state that the value of the cortex and

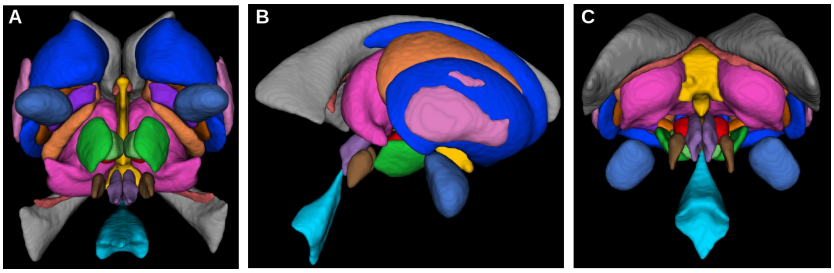

Figure 1.1: MASSP structures (adapted from Bazin et al., 2020). The 17 subcortical structures currently included in the parcellation algorithm in axial (A), sagittal (B), and coronal (C) views.

cerebellum in human cognition and behaviour is by no means underestimated. Recent breakthroughs in neuroimaging and image processing have allowed the development of superior atlases of the subcortex. The multi-contrast anatomical subcortical structures parcellation (MASSP) atlas is one of the most updated maps of the deep brain, supporting the ability to automatically parcellate grey matter nuclei in the subcortex at an unprecedented scale and accuracy (see Fig 1.1; Bazin et al., 2020). Now that it is possible to visualize these structures from *in vivo* scans, we can more precisely analyze their roles in human behaviour.

The present introduction follows the themes of the chapters in this thesis. Now that I have described the importance and underrepresentation of the subcortex, we will move on to its structure and its roles in health and disease. I will mostly discuss a subset of regions within the subcortex called the basal ganglia, a bundle of structures involved in a wide range of motor, cognitive and limbic functions. As given away by the title of this book, I will then focus more specifically on the role of the subcortex in inhibition-related functions, namely response inhibition and interference resolution.

The subcortex in health and disease

The subcortex is comprised of hundreds of structures, though the regions making up the basal ganglia have received the most attention over the years. This group of nuclei are involved in a wide range of functions, including response inhibition, interference resolution and motor movement (see Fig 1.2). The nuclei making up the basal ganglia include the dorsal striatum (caudate nucleus and putamen), ventral striatum (nucleus accumbens and olfactory tubercle), subthalamic nucleus (STN), substantia nigra (SN) and the globus pallidus (GP). One way in which the basal ganglia interact with the cortex is through a series of *direct*, *indirect*, and *hyperdirect* pathways. These pathways are essential for regulating the flow of

information between the cortex and the basal ganglia and for coordinating the execution of movements. The *direct* pathway, which is mediated by neurons in the striatum that express dopamine D1 receptors, facilitates movement by funneling information from the cortex to the globus pallidus interna (GPi) and substantia nigra pars reticulata (SNr), reducing their activity which in turn, disinhibits the thalamus. This pathway promotes the initiation and execution of movement by exciting motor cortex regions that are responsible for motor output. The *indirect* pathway, which is mediated by neurons in the striatum that express dopamine D2 receptors, is thought to inhibit movement by disinhibiting the globus pallidus externa (GPe), which in turn inhibits the thalamus. The *indirect* pathway serves as a brake on movement, preventing unwanted or inappropriate actions. The *hyperdirect* pathway, which connects the cerebral cortex directly to the STN, is suggested to provide rapid and direct inhibition of movement by bypassing the *indirect* pathway and triggering GPi/SNr activation. Overall, these pathways work together to maintain a normal state of voluntary movement.

One of the first recorded associations between the basal ganglia and an abnormal state of voluntary movement came in 1912 (Wilson, 1912). The specific type of abnormal movement described, dyskinesias, was attributed to lesions in the basal ganglia. The neurologist who made this connection, Samuel Alexander Kinnier Wilson, aptly named the disease that caused this Wilson's disease. Since then, the abnormal movements associated with Wilson's disease have been more closely tied to the putamen and GP (Lorincz, 2010; Yousaf et al., 2009). Additionally, many studies have shown that dysfunction in the cortico-basal-ganglia pathways can lead to motor and cognitive deficits, including impairments in response inhibition (Caballol et al., 2007; Chang and Guenther, 2020; Chudasama and Robbins, 2006; Salmon and Filoteo, 2007). For example, degeneration of or damage to the basal ganglia can result in hyperactivity in the *indirect* pathway. This is one of the main mechanisms thought to underly some of the observable symptoms of Parkinson's disease (PD). PD is a progressive and chronic neurodegenerative disease, characterized by the degeneration of dopamine-producing neurons in the SN. This degeneration can lead to disruptions in the balance between the *direct* and *indirect* pathways, resulting in motor impairments such as rigidity, tremors, and bradykinesia (Burke and O'Malley, 2013; Tinaz et al., 2011). One observable side effect of PD is an impairment in response inhibition (Gauggel et al., 2004; Ye et al., 2015). The STN has long been implicated as an important node underlying successful response inhibition. One effective symptomatic therapy for PD has leveraged this by targeting the STN using deep brain stimulation (DBS). DBS

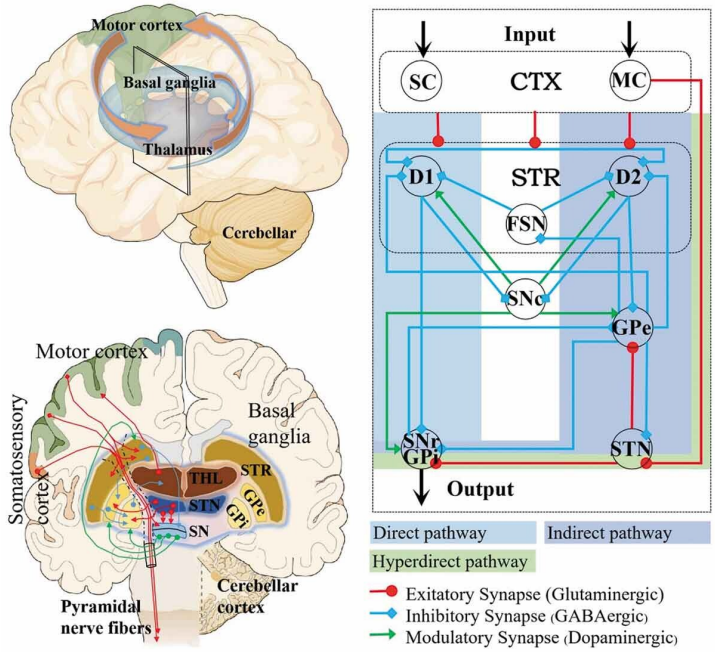

(a) The cortico-BG-thalamocortical global loop.

(b) BG topology connection diagram.

Figure 1.2: The cortico-basal-ganglia model (adapted from Song et al., 2023). a) Anatomical depiction of the connections between the cortex and subcortex. The loop connects parts of the cortex, such as the somatosensory and motor cortex, to nodes within the basal ganglia, such as the STN and SN, and the thalamus. b) Diagram indicating the connections between different nodes of the *direct*, *indirect*, and *hyperdirect* pathways. CTX, cortex; GPi/e, globus pallidus interna/externa; MC, motor cortex; SC, somatosensory cortex; SN, substantia nigra; SNc, SN pars compacta; SNr, SN pars reticulata; STN, subthalamic nucleus; STR, striatum; THL, thalamus.

has also shown promise in another basal ganglia disease: obsessive compulsive disorder (OCD). OCD is a chronic psychiatric disease in which a person presents with uncontrollable thoughts or behaviours that they feel the urge to repeat over and over again. The manifestations of PD and OCD are very different, but their symptoms can both be improved by similar treatments: DBS of the STN. The chapters of this thesis will cover the topic of STN function in further detail, for now it is only important to note that its exact functions have been difficult to pin down, but it is evidently involved in a multitude of motor, cognitive and limbic functions.

Many other neurological and psychiatric disorders have been associated with both abnormalities in the basal ganglia and in inhibition-related functions. Schizophrenia, a psychiatric disorder, has been linked to volume differences in the thalamus, GP and the striatum, which may contribute to symptoms such as delusions, hallucinations, and cognitive deficits (Kapur, 2003; Okada et al., 2016; Van Erp et al., 2016). Attention deficit hyperactivity disorder (ADHD), in which persons present with difficulties in controlling attention and impulses, has also been associated with volumetric differences in regions of the basal ganglia (Qiu et al., 2009). Both of these disorders are affected with underlying deficiencies in inhibition-related functions (Matzke et al., 2017; Nigg, 2001). Finally, dystonia, a movement disorder, is characterized by sustained and intermittent muscle contractions that can cause muscle spasms, abnormal or painful contractions and tremors (Albanese et al., 2013). These motor abnormalities are thought to be a result of the overactivation of the *direct* pathway, though the exact pathophysiology is unknown. As someone with dystonia, the roles of the nuclei within these pathways have been of particular interest to me. What has become clear, is that there is a delicate homeostasis of excitation and inhibition within the basal ganglia that is tightly controlled (Hallett, 1998; Hallett, 2006). Understanding the role of specific subcortical nuclei is therefore imperative to develop effective treatments against these diseases. To be able to understand their roles, I employed specific tasks aimed at stimulating different aspects of inhibition. In the section below I will describe these inhibition-related processes in more depth and how we examine them experimentally.

Inhibition-related functions

Inhibition-related functions can be deconstructed into three main categories (Nigg, 2000): (1) prepotent response inhibition, (2) resistance to distractor interference,

and (3) resistance to proactive interference. While on the surface these constructs display a conceptual overlap, structural equation modelling later suggested that the latter was not suited to this umbrella of inhibition-related functions (Friedman and Miyake, 2004). I therefore limit the scope of this work to the two formers. It should be noted that the nomenclature of these constructs is inconsistent across the field of psychology. Prepotent response inhibition also goes by the terms motor inhibition, global inhibition, or behavioural inhibition. Here we will refer to it as response inhibition. Resistance to distractor interference also has a long list of synonyms, including conflict resolution, selective inhibition, cognitive inhibition, and interference resolution. Here we will use the latter. Response inhibition refers to the ability to inhibit prepotent or automatic responses in favour of a more appropriate one. Interference resolution is the ability to suppress distracting information that is irrelevant to the task at hand. These processes have been associated with multiple behavioural traits in humans such as impulsivity (Jauregi et al., 2018), sensation seeking (Andrew et al., 2015), and agreeableness (Jensen-Campbell et al., 2002). While inhibition-related functions are only a small subset of functions that the brain carries out, I believe that understanding how they are implemented is of huge importance to developing treatments for related disorders. Deficiencies in one or both of these processes is postulated to underly many manifestations of Parkinson's disease, obsessive compulsive disorder, schizophrenia, and dystonia.

There are a wide range of psychiatric and neurological subcortical diseases that exhibit altered capacities in inhibition-related functions. On the implementation level, the cortico-basal-ganglia loop is thought to be crucial for the proper functioning of these processes. Inhibition was for a long time looked at as a unitary construct, but their taxonomy as related but separable mechanisms was later formalized (Friedman and Miyake, 2004; Nigg, 2000). These mechanisms, response inhibition and interference resolution, as well as other aspects of cognitive control, enable individuals to engage in adaptive behavior in everyday life. As previously mentioned, response inhibition refers to the ability to inhibit ongoing actions. Imagine you are reaching for a hot pan, when an internal realization or external cue triggers the stopping process, allowing you to inhibit this already initiated action. Such a mechanism is commonly assessed using the stop signal task (SST). The SST is a two-alternative choice reaction time task, where inhibition is assessed by the ability to forego an ongoing action (Logan and Cowan, 1984; Verbruggen et al., 2019). There are two trials types in the SST, *go* trials, where individuals are instructed to respond to a *go* stimulus as quickly as possible, and *stop* trials, where individuals are instructed to withhold their response if they see a *stop* stimulus

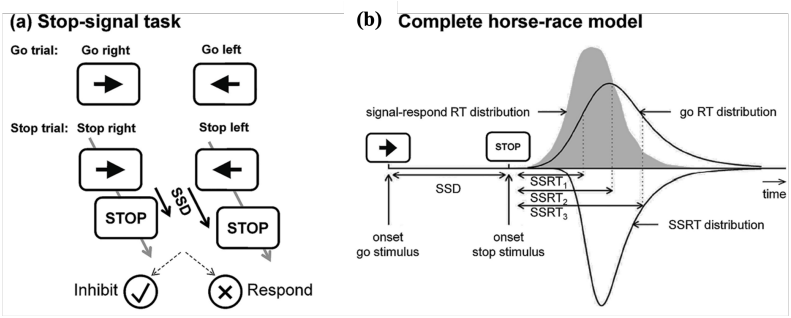

Figure 1.3: The stop signal task and the associated horse-race model (adapted from Sebastian et al., 2018). a) The experimental design of the stop signal task. On a go trial, participants only see a go stimulus and are required to respond. On a stop trial, a stop stimulus is presented after the go stimulus and participants are required to withhold their response. b) The complete horse-race model treats go RT and stop-signal reaction time (SSRT) as independent random variables representing the finishing times of the go and stop processes, respectively.

(see Fig 1.3). The *stop* stimulus is only ever shown after the *go* stimulus. *Go* trials dominate the task, usually at a 3:1 ratio. This primes individuals to expect *go* trials, and find *stop* trials more salient, an important aspect of the task. One method of formalizing behaviour during decision making tasks such as the SST, is cognitive modelling (see Fig 1.3). Behaviour during this task specifically can be conceptualized as a race between two competing but independent processes: a *go* process that is triggered upon presentation of the *go* stimulus, and a *stop* process that is triggered by the presentation of a subsequent *stop* stimulus. If the *go* process finishes first, the response is implemented; if the *stop* process finishes first, the response is inhibited (Logan and Cowan, 1984). This is called the horse-race model. Due to the nature of the task, generally only around 12.5% of all trials are successful stop trials. This is not a large issue for behavioural studies as you can simply increase the number of trials with minimal consequence, but for imaging studies this can cause considerable problems. Importantly, inhibition success is tracked and modified by adapting the time between presentation of the *go* stimulus and *stop* stimulus, known as the stop signal delay (SSD). This 'staircase' procedure keeps participants inhibition success at around 50%. The race model allows us to estimate the stop signal reaction time (SSRT), a measure of the latency of the unobservable stopping response. Most methods of SSRT estimation produce only a summary measure, and do not integrate the spread of the RT distribution. I believe that methods that use the reaction time data from the SST more thoroughly and produce a distribution of SSRTs provide greater insight into behaviour in this task (Matzke et al., 2017; Matzke et al., 2013).

Our second inhibition subtype, interference resolution, describes the ability to suppress irrelevant or distracting information. Such an ability is important in daily life, as it allows us to focus on task-related sources of information and filter out unimportant internal or external stimuli. For example, it has been shown that bilingual individuals possess better conflict monitoring abilities than those with only a single language, most likely due to the practice in inhibiting competing words in different languages (Abutalebi et al., 2012; Hernández et al., 2010). Several tasks are commonly used to assess interference resolution including the Simon, Flanker and multi-source interference tasks (MSIT; Bush et al., 2003; Eriksen and Eriksen, 1974; Simon, 1969). In this thesis, I focus on the latter, the MSIT, which combines aspects of both the Simon and the Flanker effect. The MSIT involves identification of the number that is the odd one out in series of three numbers, where the other two numbers are the same (see Fig 1.4). The paradigm is therefore a three-alternative choice task, where participants are required to respond with the identity of the unique number. As these numbers are mixed, a Simon effect arises, whereby the position of the number in the sequence interferes with the processing of its identity. Moreover, due to the two non-unique numbers acting as distractors, a Flanker effect arises. The Flanker effect causes interference due to the distractor numbers biasing the responder towards the wrong numerical response. These effects gives rise to a mechanism of selective inhibition, forcing participants to inhibit a response biased by one, or both of these interference effects. There have been no previous efforts to model the behaviour in the MSIT. Here I apply a model-based cognitive neuroscience approach to these subtypes of inhibition by applying a novel method of cognitive modelling to the MSIT. I combine ultra-high field MRI (UHF MRI) with these advanced modelling techniques to shed light on the mechanisms underlying inhibition-related functions. The main advantage of model-based methods is the ability to ascribe specific processes to specific regions of the brain. The two tasks described above have been used extensively in both healthy individuals and clinical populations to study the neural and cognitive mechanisms underlying these types of inhibition. These subtypes of inhibition have been studied relatively independently, here I attempt to formalize their similarities and differences.

Imaging the subcortex

It should be clear now that the subcortex is important for normal functioning of inhibition behaviours, as well as daily life in general. One main method I use to further our knowledge of the subcortex, both structurally and functionally, is

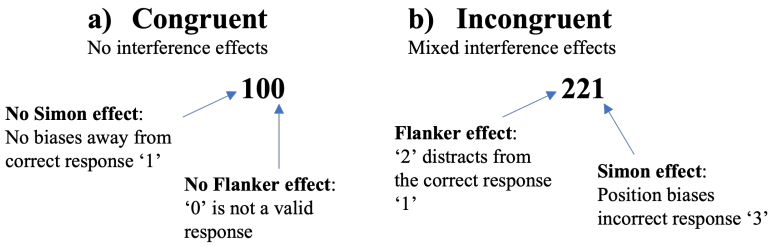

Figure 1.4: Examples of stimuli in the MSIT. In both examples, '100' and '221', the correct response is '1'. a) One of three possible stimuli in the congruent condition showing that there are no interference effects. b) One of 12 possible stimuli in the incongruent condition showing how the Flanker and Simon effects arise.

MRI. A key advantage of MRI is that it allows us to image in the human brain *in vivo*. There are three different levels of scale at which one can attempt to map the anatomy of the different regions of the brain: the macroscopic, mesoscopic and the microscopic scales (Forstmann et al., 2017). MRI scanning can span both the macroscopic (on the scale of centimeters) and mesoscopic (on the scale of millimeters) levels, though cannot yet in most cases with appropriate signal, image at the microscopic level (on the scale of micrometers). With UHF MRI the scale and accuracy at which we can image both the cortex and subcortex is becoming ever more improved. The benefit of UHF MRI compared with lower field strength MRI is evident (Cho et al., 2008; Isaacs et al., 2020; Kerl et al., 2012). As field strength increases, the signal-to-noise (SNR) increases linearly with it (Edelstein et al., 1986). This is important, especially for the subcortex, as the SNR decreases substantially in deeper parts of the brain due to the distance of the regions from the head coils. In addition to an increase in SNR, the contrast-to-noise ratio (CNR) also increases with field strength due to the larger difference in relaxation times between grey and white matter (van der Zwaag et al., 2016). The gain in signal can be used as a tradeoff with other MR parameters, such as spatial resolution or acquisition time. This propensity for increased spatial resolution is especially helpful for the subcortex, due to the size and spatial proximity of many of its nuclei. The basal ganglia, for example, contains nuclei that are notoriously densely packed and, as with the STN, have volumes as little as 80 mm^3 (Alkemade et al., 2020a). With structural imaging, where the average spatial resolution is approximately 1 mm^3, it is possible to acquire enough voxels within these structures to know where they are. In functional imaging, where the standard spatial resolution is approximately 27mm^3, it would only be possible to acquire around 3-4 voxels within the STN. Moreover, this has not yet taken into account partial voluming effects, meaning the

signal within each voxels is likely a mixture of multiple structures, a 'subcortical cocktail' if you will (De Hollander et al., 2015).

The field of functional MRI is almost exclusively based on the qualitative assessment of neural activity, namely, the blood-oxygen level dependent (BOLD) response. The basic assumption of BOLD imaging is that when regions of the brain are recruited to perform a function, they will require an increased blood flow of oxygenated blood, to match the neuronal energy demand. This is known as neurovascular coupling. As the neural activity will also increase oxygen consumption in the area, the observed BOLD response is a mixture of both processes; increased presence of oxygenated blood (increasing signal) and increased oxygen consumption (decreasing signal). As one could expect, the BOLD response is therefore also heavily dependent on the vascular properties and organization of a particular region. The interpretation of the BOLD response relies on the assumed linearity between the hemodynamic response function (HRF) and neural activity. This method, although the standard in the field, is by no means perfect, as will become apparent throughout the work in this thesis and the discussion that follows. Although multiple studies have at least partially confirmed the linearity of the relationship between the HRF and neural activity (Liu et al., 2010; Logothetis et al., 2001), these findings have almost exclusively focused on the cortex (Kim and Ress, 2017; Taylor et al., 2018). As will become incessantly apparent throughout this thesis, the subcortex is underrepresented. Few studies have attempted to characterize the effect of vasculature on the HRF in the deep brain, though differences between the cortex and subcortex have been found (Duvernoy, 1999; Lewis et al., 2018; Tatu et al., 1998; Wall et al., 2009). Subcortical BOLD responses appear to peak earlier than those observed in the cortex and the post-stimulus undershoot normally associated with the canonical HRF is not always seen (Kim et al., 2022). Physiological noise is also more of an issue in the subcortex due to its proximity to large vessels (Singh et al., 2018). The cardiac system produces artefacts due to changes in blood flow and physical pulsation of vessels (Dagli et al., 1999; Krüger and Glover, 2001), while the respiratory system produces artefacts due to arterial pressure changes and effects on B0 (Raj et al., 2001; Wise et al., 2004). Due to all of this, accurately imaging the subcortex requires numerous technical considerations.

To overcome at least some of these limitations, I have developed and implemented protocols tailored to the subcortex and used advanced processing steps to aid in reducing aspects like physiological noise (e.g., RETROICOR; Glover et al., 2000). Additional promising technical steps have allowed us to improve the signal we acquire, or at least lower the scanning time required. For example, partial

Fourier imaging allows us to directly measure only a subset of k-space, while maintaining the ability to reconstruct the entire image. While in theory only 50% of k-space data needs to be collected, in practice functional imaging requires around 75%. Another method that I use to cut down the acquisition time is multiband. Multiband allows us to excite multiple slices of a volume at once, giving the opportunity to increase spatial or temporal resolution. Parallel imaging techniques such as GeneRalized Autocalibrating Partial Parallel Acquisition (GRAPPA) can similarly aid in cutting down the acquisition time. Of course, these all come with their own set of drawbacks, usually in the form of a signal-to-noise penalty. A careful balance between these parameters has given us the ability to image the subcortex in unprecedented detail.

Based on all of this, it is obvious that imaging the subcortex is a difficult feat. It is therefore not surprising that controversies have arisen around MRI findings of subcortical structures. The cortico-basal-ganglia model described in Fig 1.2 is based on countless research into the anatomy of action selection and inhibition. Recent advances in UHF methods have however, brought these models into dispute (Hollander et al., 2017; Isherwood et al., 2023a; Miletić et al., 2020). Researchers investigating human behaviour are often limited to either mathematical models describing behavioural data or statistical models describing activity patterns in the brain. These endeavors focus on different levels of analysis (Marr, 1982), but are rarely combined. In terms of these levels of analysis, one can describe a problem in the algorithmic sense, where we focus on the process behind the computation (using mathematical models). On the implementation side, we focus on where the computation takes place in the brain (by analyzing brain patterns). To make the most of both the behavioural and neural data, I attempt to associate the algorithmic and implementational levels. Such associations can provide way to mechanistically interpret our findings, something that standard analysis methods in functional imaging or behavioural analysis cannot do.

Outline thesis

The aim of this thesis is to elucidate the underlying mechanisms that govern response inhibition and interference resolution within the human subcortex. To achieve this objective, I used an interdisciplinary approach that integrated methods of meta-analyses, structural and functional UHF MRI, and cognitive modelling techniques. Specifically, I used model-based methods to attempt to garner new perspectives on how these subtypes of inhibition are implemented in the brain,

and to what extent they overlap on a behavioural and computational scale. A core aim is that the outcomes of this research can be leveraged to advance our understanding of subcortical functioning, and that the techniques I developed can serve as a valuable resource for the research community in the years to come. I will now provide a short overview of each chapter of the thesis.

Chapter 2 marks the beginning of our endeavor to uncover the intricacies of accurately imaging the human brain. We started by creating an up-to-date catalogue of MRI databases that focus on the neurotypical population. We wanted to extract quantitative measures of image quality across different databases, to create an accurate outlook of the state of the MR field. The chapter evidences the benefits of UHF MRI in brain imaging, particularly to the subcortex, and discusses the tradeoffs between parameters such as acquisition time, spatial resolution and SNR. The chapter also highlights the huge gains that open-access data sharing can provide to the field and the choices that researchers face when balancing data quantity and quality.

In **chapter 3**, we extend our structural investigation into the deep brain, focusing on age-related changes across the adult lifespan and the composition of 17 subcortical structures. The chapter defines these regions in terms of approximate iron and myelin contents and their morphometry. We acquire novel insights into the heterogeneity of these complex regions including locational changes, which have large consequences for general use atlases of the human subcortex. The chapter emphasizes the need to accurately map subcortical structures for both structural and functional inference and outlines the vast array of information we can gain from tailored MR sequences.

In **chapter 4**, we delve into the existing literature that examines response inhibition and interference resolution. This allowed us to gain a comprehensive understanding of the knowledge gaps within the field, providing a valuable foundation for our own research. While the previous chapters focused on our structural understanding of subcortex, we here change perspective and investigate their functional counterpart. To do this, we employed an activation likelihood estimation methodology to aggregate previous functional studies of inhibition-related functions, focusing on studies that adhere to a strict set of criteria. Our results indicate a relatively unharmonious functional map of inhibition across the research field, citing large differences in regions between different meta-analyses as well as between various subtypes of inhibition. Although we answered questions relating to inter-individual similarities and differences between response inhibition and interference resolution, many questions remained unanswered.

To complement the inter-individual results of our meta-analysis, **chapter 5** outlines our intra-individual investigation into response inhibition and interference resolution. Using the information from our previous chapters, we designed, streamlined, and optimized a functional study that provided us with state of the art structural, functional and behavioural data in both response inhibition and interference resolution tasks. Our methodology allowed us to compare the subtypes of inhibition, while minimizing individual differences using intra-individual comparisons. We found that not only do response inhibition and interference resolution tasks have relatively little behavioural overlap, but that their implementation in the brain is also rooted in distinct networks. By advancing our analysis with a model-based technique, we also show differences in computational aspects of the two inhibition-related functions.

Our exploration of response inhibition culminates in **chapter 6**, where the outcomes of our functional and behavioral investigations are merged, and four additional SST datasets are reprocessed and reanalyzed to shed light on the inconsistencies present within the field. We take advantage of open-access data to combine data points from multiple datasets without the need to incorporate only summary measures. We found that, in contrast to historical models of response inhibition, successful inhibition does not appear to rely on the canonical cortico-basal-ganglia pathways. We instead found that failures of response inhibition drive the activation of multiple subcortical nodes previously theorized to underpin successful inhibition. These findings, mixed with other literature on the topic, suggest that there is much more investigation needed into the networks that underly successful response inhibition in the human subcortex.

Finally, **chapter 7** provides a comprehensive summary of the key findings presented in this thesis and elucidates their implications for future research. I follow this with a contextual discussion of these findings, presented in relation to recent publications.

Chapter 2

Quantity and quality: Normative open-access neuroimaging databases

This chapter is published as:
S. J. S. Isherwood, P.-L. Bazin, A. Alkemade, and B. U. Forstmann (2021a). Quantity and quality: Normative open-access neuroimaging databases. *PLOS ONE* 16.3, pp. 1–30. DOI: 10.1371/journal.pone.0248341.

Abstract

The focus of this article is to compare twenty normative and open-access neuroimaging databases based on quantitative measures of image quality, namely, signal-to-noise (SNR) and contrast-to-noise ratios (CNR). We further the analysis through discussing to what extent these databases can be used for the visualization of deeper regions of the brain, such as the subcortex, as well as provide an overview of the types of inferences that can be drawn. A quantitative comparison of contrasts including T1-weighted (T1w) and T2-weighted (T2w) images are summarized, providing evidence for the benefit of ultra-high field MRI. Our analysis suggests a decline in SNR in the caudate nuclei with increasing age, in T1w, T2w, qT1 and qT2* contrasts, potentially indicative of complex structural age-dependent changes. A similar decline was found in the corpus callosum of the T1w, qT1 and qT2* contrasts, though this relationship is not as extensive as within the caudate nuclei. These declines were accompanied by a declining CNR over age in all image contrasts. A positive correlation was found between scan time and the estimated SNR as well as a negative correlation between scan time and spatial resolution. Image quality as well as the number and types of contrasts acquired by these databases are important factors to take into account when selecting structural data for reuse. This article highlights the opportunities and pitfalls associated with sampling existing databases, and provides a quantitative backing for their usage.

2.1 Introduction

The purpose of this article is to summarize and compare some of the most prominent existing normative open-access structural magnetic resonance imaging (MRI) databases from a variety of research institutions, including our own Amsterdam ultra-high field adult lifespan (AHEAD) database (Alkemade et al., 2020a). The need for and benefit of open-access imaging databases has been emphasized in a number of recent reviews (Eickhoff et al., 2016; Madan, 2017; Milham et al., 2018). The community-wide movement towards open-access data sharing in the last decade is expected to massively advance the neuroimaging field and share the wealth of available data between researchers and institutions. Some of these benefits are obvious, such as the financial advantage of data sharing and the reuse of data between institutions. The re-analysis of acquired MR images also serves to aid reproducible research and provide multi-party levels of quality control. On top of this, the ability of new processing pipeline tools and analyses methods benefit greatly from the larger sum of data that the software can be trained on. It is important to acknowledge that large-scale data-sharing comes with its own disadvantages. Analyses based on post-hoc hypotheses and 'data-mining' can lead to spurious false positive findings (Poldrack and Gorgolewski, 2014). Due to the sheer number of possible analyses in larger databases this problem grows increasingly likely. Data acquired within a specific framework and collected with a specific purpose may affect the extent to which this data can be used for separate analyses (Verheij et al., 2018). The questions investigated by the numerous neuroimaging databases described in this paper are diverse, with some attempting to bridge the gap between genetic influences and brain structure and others looking at the impact of the environment on the development of the human brain (Holmes et al., 2015; Nooner et al., 2012; Van Essen et al., 2013). To this end, there are already a multitude of findings and publications arising from the data made accessible through these databases (Betzel et al., 2014; Chan et al., 2018; De Hollander et al., 2015; DuPre and Spreng, 2017; Geerligs et al., 2015; Glasser et al., 2016; Gratton et al., 2018; Holmes et al., 2012; Huntenburg et al., 2017; Mikhael et al., 2018; Pagliaccio et al., 2015; Wang et al., 2015; West et al., 2019). To our knowledge, a systematic comparison of these data, in terms of image quality, has not yet been published. This information is invaluable for the users of such databases to determine what conclusions they can reliably draw from the wealth of information provided. Through this analysis, we aim to aid in the accurate and valid use of the vast imaging data researchers have at their fingertips.

Additionally, though many of these databases contain functional (f)MRI data (both resting state and task-specific), we will focus instead on brain anatomy and the inferences that can be made from structural imaging techniques. For comparisons, we will use quantitative measures of image quality, namely the signal-to-noise ratios (SNRs) and contrast-to-noise ratios (CNRs) associated with the MR images provided by each database. In short, the SNR infers the propensity of an MR image to delineate brain structures and detect pathology (Michaely et al., 2007). By providing these estimates for each database, we are giving a quantitative measure of two dimensions; image quality (SNR) and contrast (CNR). An increase in these quantitative measures improve the qualitative ability of e.g., manual or automatic parcellation. The CNR gives a valuable inference on the ability to spatially resolve detail in an image. Therefore, using different databases with varying CNRs may result in different outcomes depending on the reason they are being used (e.g., segmentation, volumetric measurements, delineation of cortical folding). SNR inherently provides an estimate of the noise level in a structure or image and higher image quality is both quantitively and qualitatively useful. Of course, the SNR is often used as a trade-off parameter to gain improvements in another aspect of the imaging method such as resolution, scan time, field of view (FOV) and indirectly, sample size. For example, a database with a low CNR and a large sample size may not be pragmatic to use for the parcellation of subcortical nuclei but would provide accurate volumetric whole brain estimates of a population. Conversely, a database with a high CNR and small sample size may not be able to provide reliable information at a population level but may deliver an insight into the substructure of a single region. Thus, larger databases with vast and multimodal data of each individual have already provided population-level information on cortical arrangement as well as the impact of genetics and the environment on the human brain (Bischof and Park, 2015; Blesa et al., 2016; Cheng et al., 2020; Glasser et al., 2016; Lyu et al., 2020; Strike et al., 2019) which would not be possible in smaller databases.

There are currently at least 71 whole-body 7T MRI scanners worldwide (Forstmann et al., 2017). Given the number of articles now specifically comparing 3T and 7T imaging of neurological disease, it is evident that higher field strengths are beneficial to answer questions in both the cognitive and clinical neurosciences (De Graaf et al., 2013; Moon et al., 2016; Noebauer-Huhmann et al., 2015; Springer et al., 2016; Tallantyre et al., 2009). The signal-to-noise ratio (SNR) increases in an almost linear fashion with field strength (Collins and Smith, 2001; Vaughan et al., 2001) giving the potential for both greater spatial resolution and a higher

CNR. Some of the databases described here have taken advantage of this, but the cost of use of these higher field strengths and their limited availability make it challenging for many large-scale studies or institutions without access. Thus, the trade-off between the quantity and quality of acquired MR data arises.

The gains from ultra-high field MRI (UHF MRI) are especially important when investigating deeper regions of the brain (e.g., subcortex). UHF MRI can provide reduced partial volume effects due to increased spatial resolution, allowing for the visualization of finer anatomical detail (Federau and Gallichan, 2016; Lüsebrink et al., 2013). Historically, the lack of signal and contrast within the deep brain is the reason for the only recent development of subcortical maps in vivo (Johansen-Berg, 2013; Keuken and Forstmann, 2015). UHF MRI and its accompanying increase in SNR and contrast capacity will aid in the understanding of the structure of these deeper structures. Around 93% of the grey matter nuclei within the subcortex, making up almost a quarter of the total human brain volume, are currently not represented in standard MRI atlases (Alkemade et al., 2013; Evans et al., 2012). Some subcortical structures can be delineated through the use of these atlases, such as parts of the striatum, but most are too small to be manually or automatically parcellated (Levitt et al., 2013). Iron-rich structures including regions constituting the basal ganglia are difficult to delineate on standard T1w scans (Priovoulos et al., 2018; Visser et al., 2016), but specialised sequences can take advantage of the larger T2* contrast differences at higher field strengths (Cho et al., 2011). For example, the abundance of iron in the substantia nigra (SN) and subthalamic nucleus (STN) make it an ideal target for T2* and SWI contrasts which can take advantage of these differences (Alkemade et al., 2017; Kerl et al., 2012; Schäfer et al., 2012; Shroff et al., 2009). The delineation of these structures is made even harder by the limited SNR, due to the larger distance from the head coils (Hollander et al., 2017).

Methods to improve image quality in MRI are not only limited to increasing the field strength of the scanner. The gradient strength, radiofrequency coils and use of optimized sequences also have a marked effect on acquisition efficiency. One such example is the Connectom scanner, of which there are currently only three in the world, which benefits from gradient strengths 3-8 times that found in standard 3T scanners. As with field strength, this factor facilitates both an increase in spatial resolution and a reduction scan time. Though previous studies have indicated the advantage of non-standard sequences (e.g., T2*, QSM, SWI), owing to their capacity to increase the number of observable structures and to observe smaller brain regions (e.g., fibre tracks, nuclei) in deeper areas of the brain (Deistung et al., 2013; Kerl et al., 2012). The vast majority of databases

focus on more standard T1w and T2w images, which are essential for volumetric calculations and distinguishing between grey and white matter regions but do not have the ability to quantify or delineate smaller and adjacently located nuclei (Keuken et al., 2014; Trutti et al., 2019).

2.2 Methods

The purpose of this article was not to present and analyse an exhaustive list of all currently available open-access neuroimaging databases, but to provide quantitative measures and accessing instructions for some of the most notable ones that meet our criteria. Most of the databases were identified using a structural MRI database list kindly provided from a cited paper which can be accessed here: `https://github.com/cMadan/openMorph` (Madan, 2017). Two of the databases were identified as they were associated with the authors of this article (Alkemade et al., 2020a; Forstmann et al., 2014) and a further two databases were identified from the literature (Haxby et al., 2011; Tardif et al., 2016). All data was freely accessed in November 2018 and downloaded using the accessing instructions in Table A.1.

The selection criteria of the databases presented in this article were based on three characteristics. Firstly, the databases had to be normative, that is, made up of individuals that were reported as healthy at the time of scanning with no clinical presentation of neurological, psychiatric, neurodegenerative or peripheral disease. Secondly, the databases had to be a collection of curated images, uni- or multi-modal, that were acquired to be of similar composition (based on sequences and/or sites) to that of other images in the database. The reason for this criterion is that we assess five subjects randomly from each database and therefore must be sure that their quality reflects that of the rest of the database accurately. Thirdly, these databases are open-access to the extent that they are accessible to the worldwide scientific community completely free of charge and without access barriers. Such access barriers include, for example, memberships, a specific institutional position (e.g., professorship) or the requirement of some type of institutional infrastructure (e.g., Federalwide Assurance).

The quality of the images acquired through the use of MRI are characterized by three main components: the acquired spatial resolution, the signal-to-noise ratio (SNR) and the contrast-to-noise ratio (CNR). These three aspects are in turn governed by the specific acquisition parameters used when obtaining the MR images. In the analysis presented here, the SNR was calculated by measuring the mean signal at the most posterior part of the corpus callosum (CC) and dividing it

by its standard deviation. We also calculated the SNR of a grey matter region, namely the caudate nuclei (CN). To provide a measurement of CNR for each image, we computed the ratio of the difference in signal to the difference in noise of the CC and left and right caudate nuclei (LCN and RCN, respectively). These regions were chosen as we opted to compare the signal between a white matter area (CC) and a grey matter area (CN) of deeply situated brain regions. The SNR was calculated in both the left and right CN as a quality control step, under the assumption that these would yield similar SNR estimates. To test this, we used the programming language R and the 'BayesFactor' package to compute both frequentist and Bayesian t tests, respectively (Morey and Rouder, 2015; Team R. Core., 2019). The latter allows us to provide evidence for the null hypothesis (that there is no difference in signal between the left and right caudate nucleus). In order to have a singular SNR measure for both CN, we used the summation of the signal from 27 voxels from both regions and divided it by the standard deviation of the overall 54 voxels. This results in an SNR that is different than simply taking the mean of both SNR measurements for each CN. Equation 2.1 shows the calculation for which CNR values were computed. μ_{CC} indicates the mean signal of the CC, μ_{CN} indicates the mean signal of both CN. σ_{CC} specifies the standard deviation of the CC and σ_{CN} specifies the standard deviation of both CN.

$$CNR = \frac{\mu_{CC} - \mu_{CN}}{\sqrt{{\sigma_{CC}}^2 + {\sigma_{CN}}^2}} \tag{2.1}$$

As many of the databases described here do not report SNR estimates, we decided to download a sample of the available data from each database and compute these indices to be able to make accurate comparisons between them. Importantly, even when SNR estimations were calculated by the databases, we performed a re-estimation to ensure that all SNRs presented here were estimated using the same protocol. The SNRs can be estimated using different structures and therefore derive values that are not always comparable between different procedures. To do this, five subjects from each database were selected at random and their available images downloaded. The SNRs and CNRs were calculated for each available contrast within each database. Databases that include large age ranges were split into age groups of young (18 – 28), middle-aged (34 – 53) or elderly (63 – 86). For these databases, five participants were taken from each age

group so that we could compare SNR and CNR estimations across age-ranges. Although the proportion of each database used for the analysis may differ, they are statistically comparable as the same number of participants were selected randomly from the sample of each database.

For comparisons between databases the analysis focuses on the SNR of the CC (SNR_{CC}), for simplicity, unless otherwise stated. Sequences incorporating multiple echo times (e.g., MP2RAGEME) technically provide multiple contrasts in one sequence and were therefore all included in the estimates. For example, a sequence with four TEs (e.g., MP2RAGEME) would give four contrasts per participant. We chose five subjects to ensure feasibility of the manual measures while accounting for potential variations in quality within a database. The CC and CN may not be the optimal structures for SNR comparisons for all of the contrasts for each database, but using these structures allows comparability over the entire analysis. To calculate the SNR of the CC, LCN and RCN, one expert rater manually delineated the regions using the MIPAV imaging software (Medical Image Processing, Analysis and Visualization; McAuliffe et al., 2001). Once the centre of the regions of interest were accurately delineated, a 3 x 3 x 3 cube of voxels was taken around one midpoint voxel to calculate the SNR using the mean and standard deviation of 27 contiguous voxels in the structure (Fig 2.1). A second method to calculate the SNR of these structures was also explored. Instead of taking 27 contiguous voxels, we took the voxel volumes of each image into account and measured the signal of 27 voxels from the same volumetric space. This involves simply normalizing the size of the cube of voxels measured by the images with the largest voxel size, so to measure from approximately the same area of each structure. The results were in line with what is reported here, and therefore we only report the measurements acquired from the first method.

To analyze the relationship between scan time and spatial resolution and scan time and SNR_{CC}, two linear regression models were setup. Both models used scan time as a predictor variable and either spatial resolution or SNR_{CC} as the independent variable. This would allow us to observe a linear relationship between either of the two parameters. To correct for multiple comparisons, a Bonferroni adjustment was employed to maintain a 95% confidence in the analysis, giving a new significance threshold of 0.025.

We also present comparisons between slab images (small FOV) and whole brain images from databases that offer both, in order to demonstrate differences in SNR and CNR at higher resolutions. Both frequentist and Bayesian t tests were employed in R to compare these. To compare age differences across multiple contrasts,

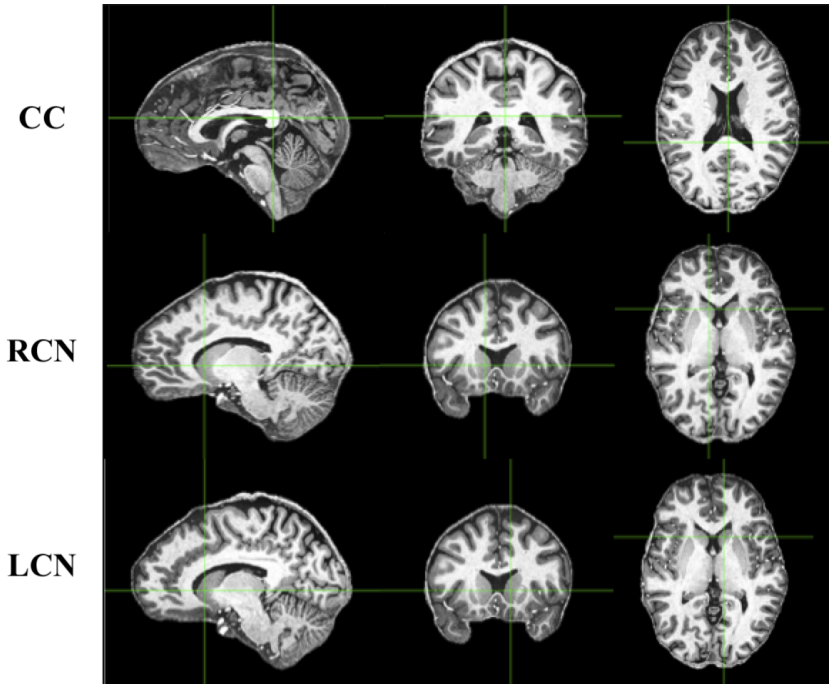

Figure 2.1: Sagittal (left), axial (middle), and coronal (right) views indicating the structures from which SNR measurements were taken. These T1w images were taken from one subject in the MPI-CBS database. CC, corpus callosum; RCN, right caudate nucleus; LCN, left caudate nucleus.

linear mixed effect models from the 'lme4' R package were used (Bates et al., 2014). Model 1 (null model) included the respective databases as a random intercept without adding any effect of age on SNR/CNR. Model 2 (full model) included both the database as a random intercept and age as a fixed effect. The likelihood estimations of each model were then compared by a likelihood ratio test though the use of an Analysis of Variance (ANOVA). A Bayesian linear modelling technique was also used, where the resultant Bayes factors were compared between model 1 and model 2. We opted to include the SNR and CNR data from all of the databases, even those without large age ranges, so to use as much of the wealth of information as possible for our statistical tests. This results in a larger centre of mass on the younger age group than the middle-aged and elderly groups, and although this does not result in an increase in power, it provides a more accurate estimate of the effect of age on SNR and CNR. For the model comparisons, age was used as a continuous predictor and therefore categorical ages were not used within the statistical analysis, these were only used for visualization.

To address the issue of reliability when taking a small subpopulation from large samples, we re-ran some of the SNR and CNR analysis with a different sample from the databases. 5 or 15 (if they included large age-ranges) additional samples were taken from each database that allowed it (dependent on the original sample size) and SNR measurements were calculated again from their T1w images for comparison against the original sample. Of the 20 databases included in this article, 17 had a sample size large enough for us to take additional measurements. SNR measurements were taken from the left caudate nucleus, right caudate nucleus and corpus callosum of 164 separate T1w images.

2.3 Results

Based on our search, 41 databases were initially identified. After the first screening, 5 were excluded on the basis of access requirements. Of the remaining 36 databases, 20 were included in this article for description and comparison (see Fig 2.2 for Preferred Reporting Items for Systematic Reviews and Meta-Analyses; PRISMA flow diagram). Below we discuss these 20 databases that follow the three criteria including 250 (Lüsebrink et al., 2017), a completed Germany-based database which highlights its potential use for building an in vivo MR brain atlas due to its ultrahigh resolution whole brain images of one subject; Age-ility (Karayanidis et al., 2016), a completed Australia-based database investigating the relationship between cognitive control and adaptive/maladaptive behaviours across the adult lifespan; the AHEAD database (Alkemade et al., 2020a), an ongoing Netherlands-based database aiming to acquire high-resolution images of the human subcortex and map so-called terra incognita; the Atlasing of the Basal Ganglia (ATAG) project (Forstmann et al., 2014), a completed Netherlands/Germany-based database whose aim was to acquire high-resolution data to observe anatomical differences over the adult lifespan; the Brain Genomics Superstruct Project (GSP; Holmes et al., 2015), a completed US-based database looking to solidify and find links between brain function, behaviour and genetic variation; the Cambridge Centre for Aging and Neuroscience (Cam-Can; Shafto et al., 2014; Taylor et al., 2017), an ongoing UK-based database aiming to characterize age-related changes in cognition and brain structure and function, and to uncover the neurocognitive mechanisms that support healthy aging; the Dallas Lifespan Brain Study (DLBS; `http://fcon_1000.projects.nitrc.org/indi/retro/dlbs.html`), an ongoing US-based database designed to accelerate our understanding of both the preservation and decline of cognitive functioning across the adult lifespan; the Human

Connectome Project Young Adult (HCP-YA; Milchenko and Marcus, 2013; Van Essen et al., 2013; Xu et al., 2012), an ongoing US-based database aiming to generate a complete and accurate description of the connections amongst grey matter locations in the human brain at the millimeter scale. Information eXtraction from Images (IXI; `http://www.brain-development.org`), a completed UK-based database from three London Hospitals aimed to aid in decision support in healthcare and the analysis of images obtained in drug discovery; Kirby 21 (Landman et al., 2011), a completed US-based database aiming to assess the scan-rescan reproducibility of a 60 minute scanning session, wanting to establish a baseline for developing multi-parametric imaging protocols; Maastricht (Gulban et al., 2018), a completed Netherlands-based database with the aim of facilitating the development of segmentation algorithms on the challenging nature of 7T MR data; Multiple Acquisitions for Standardization of Structural Imaging Validation and Evaluation (MASSIVE; (Froeling et al., 2017)), a completed Netherlands-based single-subject dataset aiming to serve as a representative testbed for diffusion-MRI correction strategies, image processing techniques and microstructural modelling approaches; the Midnight Scan Club (MSC; Gordon et al., 2017), a completed US-based database of scientific volunteers wanting to increase our understanding of brain function on the individual level, as opposed to just the central tendencies of populations; the Max Planck Institute – Human Brain and Cognitive Sciences repository (MPI-CBS; Tardif et al., 2016), a completed Germany-based database wanting to stimulate the development of imaging processing tools for high resolution and quantitative imaging, that have been mainly designed for lower quality images; Max Planck Institute – Leipzig Mind Brain Body (MPI-LMBB; Mendes et al., 2017), another completed Germany-based databases which aimed to explore individuals variance across cognitive and emotional phenotypes in relation to the brain; Nathan Kline Institute – Rockland Sample (NKI-RS; Nooner et al., 2012), an ongoing US-based database aiming to provide normative trajectories of brain development so to facilitate the identity of pathological markers; Pediatric Template of Brain Perfusion (PTBP; Avants et al., 2015), a completed US-based database focusing on increasing our understanding of adolescent brain development with multi-model MR imaging and its relationship with both environmental and cognitive measures; RAIDERS (Haxby et al., 2011), a completed US-based database focusing on functional imaging during segments of full-length feature film "Raiders of the Lost Ark"; the Southwest University Adult Lifespan Dataset (SALD; Wei et al., 2018), a completed China-based database aiming to observe how the normative brain changes structurally and functionally over the adult lifespan;

and StudyForrest (Hanke et al., 2014; Sengupta et al., 2016), an ongoing German-based database aiming to provide data in a more complex setting, as opposed to the simplified experimental designs normally used, to therefore provide a more ecologically valid insight into brain function.

Table 2.1 presents an overview of these databases including information on field strength, sequences and the number of participants. Example T1-weighted (T1w) images taken from each database are presented in Fig 2.3. Further information, including the website address and accessing instructions of each database can be found in Table A.1. Detailed descriptions of the individual databases can be found on their website address or descriptor papers.

We would like to acknowledge the importance of other neuroimaging databases that do not meet our selection criteria, such as the Open Access Series of Imaging Studies (OASIS; Marcus et al., 2010; Marcus et al., 2007, 1000 Functional Connectome Project (FCP; Mennes et al., 2013), Alzheimer's Disease Neuroimaging Initiative (ADNI; Mueller et al., 2005; Weiner et al., 2015), Autism Brain Imaging Data Exchange (ABIDE; Di Martino et al., 2014), Brain Images of Normal Subjects (BRAINS; Job et al., 2017), Australian Imaging Biomarkers and Lifestyle Study of Aging (AIBL; Ellis et al., 2009), Pediatric Imaging, Neurocognition, and Genetics (PING; Jernigan et al., 2016), Adolescent Brain Cognitive Development (ABCD) study (Casey et al., 2018), Attention Deficit Hyperactivity Disorder (ADHD) 200 (Bellec et al., 2017), Child Mind Institute Healthy Brain Network (CMI-HBN; Alexander et al., 2017), Center for Biomedical Research Excellence (COBRE; `http://fcon_1000.projects.nitrc.org/indi/retro/cobre.html`), Consortium for Reliability and Reproducibility (CoRR; Zuo et al., 2014), Function Biomedical Informatics Research Network (fBIRN; Keator et al., 2016), Minimal Interval Resonance Imaging in Alzheimer's Disease (MIRIAD; Malone et al., 2013), National Alzheimer's Coordinating Center (NACC; Morris et al., 2006), National Consortium on Alcohol and Neurodevelopment in Adolescence (NCANDA; Brown et al., 2015), Philadelphia Neurodevelopmental Cohort (PNC; Satterthwaite et al., 2014), Mindboggle-101 (Klein and Tourville, 2012), SchizConnect (Wang et al., 2016), OpenNeuro (Poldrack et al., 2013) and the UK Biobank (Sudlow et al., 2015). These databases, such as the ABCD database, and the PING database are also of great interest, but they are not openly available to researchers outside of NIH institutions, and thus do not meet our criteria for inclusion in this study (see Table A.2 for an overview of the inclusion criterion these databases did not meet). Additionally, we would like to recognize that many clinical databases also contain images of healthy individuals. The reuse of databases consisting of only healthy

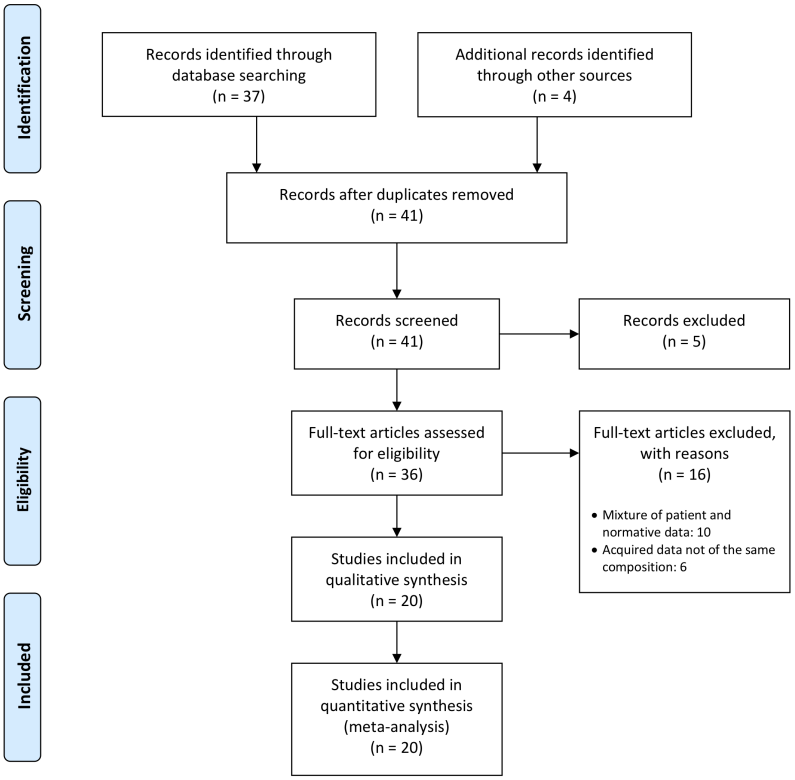

Figure 2.2: PRISMA flow diagram.

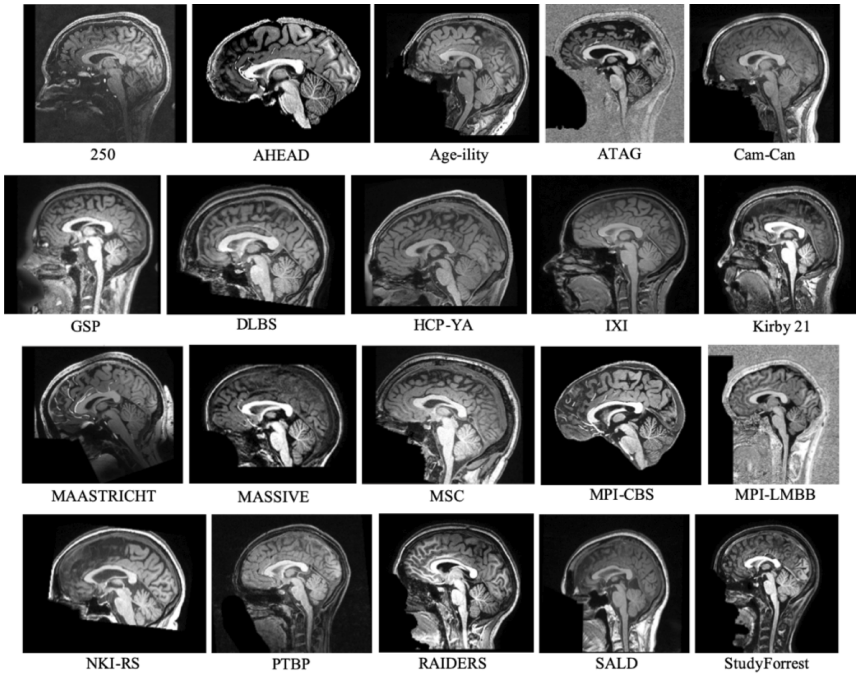

Figure 2.3: Mid-sagittal T1w images from each neuroimaging database. One participant was selected at random from each of the databases to serve as an example of the image quality expected.

individuals is more convenient, creating an even lower threshold for the reuse of data. We would like to emphasize that the exclusion of normative data from clinical databases, databases containing non-harmonious data or databases that have institutional and/or positional requirements is in no way a comment on their data quality or usefulness.

Table 2.1: N, number of participants; TR, repetition time; TE, Echo time; TI, inversion time; MPRAGE, magnetization prepared rapid gradient echo; MP2RAGE, magnetization prepared 2 rapid acquisition gradient echoes; ME, multiple echo; FLASH, fast low angle shot; SPACE, sampling perfection with application of optimized contrasts using different flip angle evolutions; FLAIR, fluid attenuation inversion recovery; IR, inversion recovery; TSE, turbo spin echo; TFE, turbo field echo; sb, slab; – indicates unknown or not applicable information.

Database	N	Field stre-ngth (T)	Structural sequence	Contrast	TR (ms)	TE (ms)	TI (ms)	Scan time (min:sec)	Voxel size (mm)
250	1	7	MPRAGE	T1w	3580	2.41	1210	53:00	0.25 x 0.25 x 0.25
AHEAD	106	7			6.2TR1, 31TR2	3			
			MP2RAGEME	T1w, T2*w, PDw, QSM	6778TR	3, 11.5, 19, 28.5	670, 3675.4	19:53 x 2	0.64 x 0.64 x 0.7
			MP2RAGEME-sb	T1w, T2*w, PDw	8TR1, 32TR2	4.6	670, 3738	-	0.5 x 0.5 x 0.5
					8330TR	4.6, 12.6, 20.6, 28.6			
AGE-ILITY	131	3	MPRAGE	T1w	2200	3.5	-	6:45	1 x 1 x 1
ATAG	53	7	ME-3D-FLASH	T2*w	41	11.22, 20.39, 29.57	900, 2750	17:18	0.5 x 0.5 x 0.5
			MP2RAGE	T1w	5000	2.45	900, 2750	10:57	0.7 x 0.7 x 0.7
			MP2RAGE-sb	T1w	5000	3.71		9:07	0.6 x 0.6 x 0.6
GSP	1570	3	MEMPRAGE	T1w	2200	1.5, 3.4, 5.2, 7.0	1100	2:12	1.2 x 1.2 x 1.2
CAM-CAN	280	3	MPRAGE	T1w	2250	2.99	900	4:32	1 x 1 x 1
			SPACE	T2w	2800	408	-	4:30	1 x 1 x 1
DLBS	315	3	MPRAGE	T1w	8135	3.7	1100	3:57	1 x 1 x 1
HCP-YA	1206	3	3D MPRAGE	T1w	2400	2.14	1000	7:40	0.7 x 0.7 x 0.7
			3D SPACE	T2w	3200	565	-	8:24	0.7 x 0.7 x 0.7
IXI	619	3	-	T1w	9.6	4.6	-	-	0.94 x 0.94 x 1.2
			-	T2w	5725.79	100	-	-	0.9 x 0.9 x 1.2
			-	PDw	-	-	-	-	0.9 x 0.9 x 1.2
KIRBY 21	21	3	MPRAGE	T1w	6.7	3.1	842	5:56	1 x 1 x 1.2
			FLAIR	T2w	8000	330	2400	8:48	1.1 x 1.1 x 1.1
MAASTRICHT	5	7	MPRAGE	T1w	3100	2.42	1500	13:30	0.7 x 0.7 x 0.7
			MPRAGE	PDw	1380	2.42	-	5:53	0.7 x 0.7 x 0.7
			MPRAGE	T2*w	4910	16	-	21:20	0.7 x 0.7 x 0.7
MASSIVE	1	3	3D-IR-TSE	FLAIR	4800	300	1650	3:45	1 x 1 x 1
			3D-TFE	T1w	8000	1.25	-	3:45	1 x 1 x 1
			3D-TSE	T2w	2500	213	-	2:45	1 x 1 x 1
MSC	10	3	-	T1w	2400	3.7	1000	-	0.8 x 0.8 x 0.8
			-	T2w	3200	497	-	-	0.8 x 0.8 x 0.8
MPI-CBS	28	7	MP2RAGE	T1w	5000	2450	900, 2750	28:02	0.5 x 0.5 x 0.5
			ME-FLASH	T2*w	44	9.18, 17.33, 25.49, 33.65	-	26.12	0.5 x 0.5 x 0.5
MPI-LMBB	321	3	3D-MP2RAGE	T1w	5000	2.92	700, 2500	8:22	1 x 1 x 1
			FLAIR	-	-	-	-	-	0.49 x 0.49 x 1
NKI-RS	1000	3	MPRAGE	T1w	1900	2.52	900	4:18	1 x 1 x 1
PTBP	120	3	MPRAGE	T1w	2170	4.33	1100	8:08	1 x 1 x 1
RAIDERS	11	3	MPRAGE	T1w	9850	4530	-	-	0.938 x 0.938 x 1
SALD	494	3	MPRAGE	T1w	1900	2.52	900	4:26	1 x 1 x 1
STUDYFORREST	20	3	3D-TFE	T1w	2500	5.7	900	12:49	0.67 x 0.67 x 0.7
			3D-TSE	T2w	2500	230	-	7:40	0.67 x 0.67 x 0.7
			3D Presto FFE	SWI	19	26	-	7:13	0.43 x 0.43 x 0.35

Because of the large age-ranges, fifteen participants were used for the following subset of databases (AHEAD, ATAG, CAMCAN, DLBS, IXI, MPI-LMBB, NKI-RS, SALD). Ten databases therefore present a mean SNR value of five participants, eight databases present a mean SNR value of fifteen participants and two databases (MASSIVE and 250) were comprised of only one subject. For this case, five scanning sessions were taken, and the mean SNR calculated. 670 images were analysed in total for the main analysis, and a further 164 to test the reliability of the initial sample.

Described below are the results of the SNR and CNR analysis. To comply with the Health Insurance Portability and Accountability Act (HIPAA, `https://www.hhs.gov/hipaa/index.html`) and the European equivalent General Data Protection Regulation (GDPR, `https://eugdpr.org/`), it is agreed upon by the scientific community that high resolution MRI images give the means for identifiability and facial reconstruction and must therefore be subject to precautionary measures to ensure privacy (Bischoff-Grethe et al., 2007). Therefore, the images provided here by the cited databases are coupled with a defacing mask to protect against identifiability, with the exception of the IXI and MSC databases. Other than this essential step, all included databases offer unprocessed images or both unprocessed and pre-processed images, with the exception of the MPI-CBS database. When available, all calculations regarding SNR and CNR used the unprocessed MR images.

Due to the inherent trade-off between SNR and spatial resolution, we opted to normalize the SNR and CNR by dividing the original ratio values by the voxel dimensions of the acquired images. This gives a more accurate depiction of the image quality of each database. Therefore, unless otherwise specified, or in the case of quantitative images, we show normalized SNR values, not raw SNR values. A graphical comparison of the raw SNR and the normalized SNR for the T1w images of each database is shown in Fig A.1.

2.3.1 Comparing T1w images

As all the databases presented here contained a T1w image for each participant, these were used as the main sample to be compared. A frequentist and Bayesian paired t-test were used to compare the values of the two caudate nuclei within each database, concluding that there were indeed no significant differences between the calculated SNR, as there is substantial evidence for the null hypothesis ($p = 0.630$, $t = 0.492$, $DF = 14$, $BF = 0.292$; Jeffreys, 1935). The SNR of each nuclei, averaged by database, are visualized in Fig 2.4.

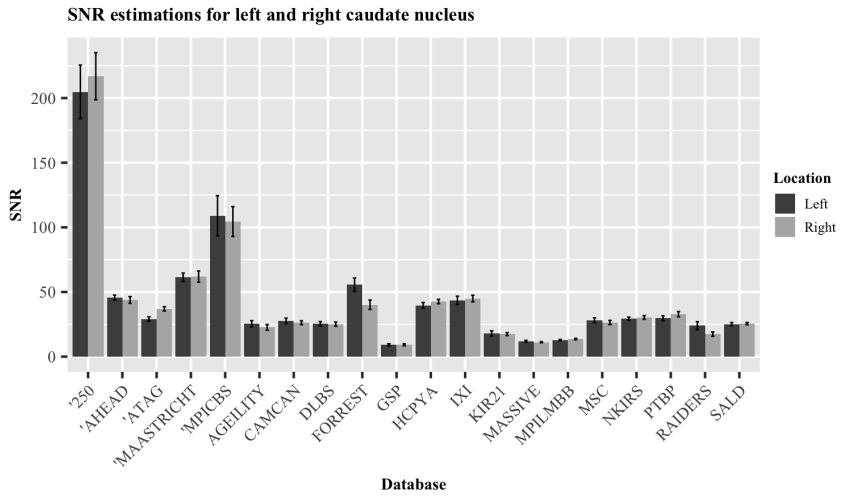

Figure 2.4: SNR estimations for the left and right caudate nucleus. Data averaged over the individuals of each database. Error bars indicate standard error of the mean.

Fig 2.5 visualizes the relationship between sample size and SNR. This indirect tradeoff between the two is perhaps anticipated, simply due to the costs associated with both an increased number of participants and superior acquisition methods (e.g., higher field strengths and increased scan time). Of course, both sides of the spectrum are accompanied with their own advantages and disadvantages. Larger sample sizes can reduce the susceptibility to spurious findings and deliver greater statistical power, but may have to sacrifice some features of the imaging data (e.g., voxel resolution, SNR or number of modalities). For example, databases with large sample sizes and large voxel sizes may not be suitable for studying morphometric changes that occur in small subcortical nuclei but can provide accurate estimations of cortical thickness with a high statistical power.

Fig 2.6 displays the normalized SNR_{CC} and CNR values of the T1w images from each database. The results are present as ascending from bottom to top, based on their SNR estimation, ranging from 15.8 (GSP) to 292.3 (250 database). Their numerical values are presented in Table 2.2.

To investigate the similarity of the first sample of measurements to the second sample, a Bayesian ANOVA was used to provide evidence for or against the null hypothesis (that these samples were taken from the same distribution). The Bayes Factors (BF) resulting from this analysis for each structure are as follows: corpus callosum SNR BF = 0.139, caudate nuclei SNR BF = 0.129, and the CNR BF = 0.224. Based on Jeffreys, 1935 this provides substantial evidence for the null hypothesis,

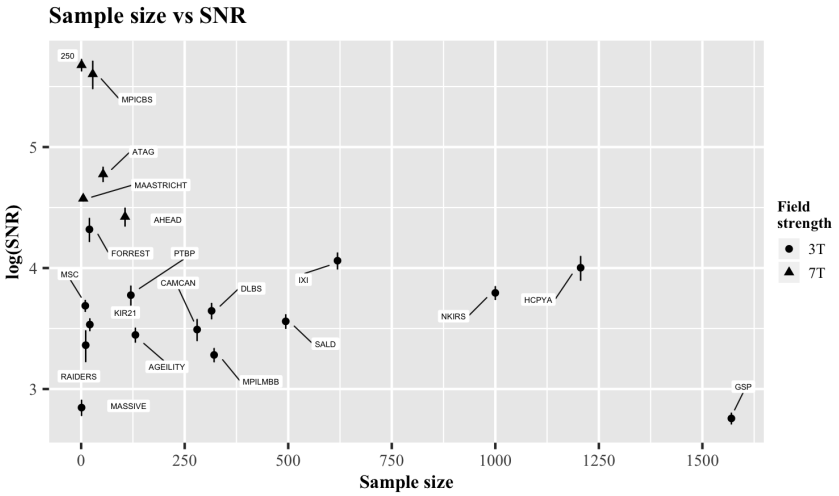

Figure 2.5: The relationship between sample size and SNR_{CC}. Error bars indicate standard error of the mean. Both the SNR values and the standard errors are presented on the log scale. Circular symbols indicate 3T data, triangular symbols indicate 7T data.

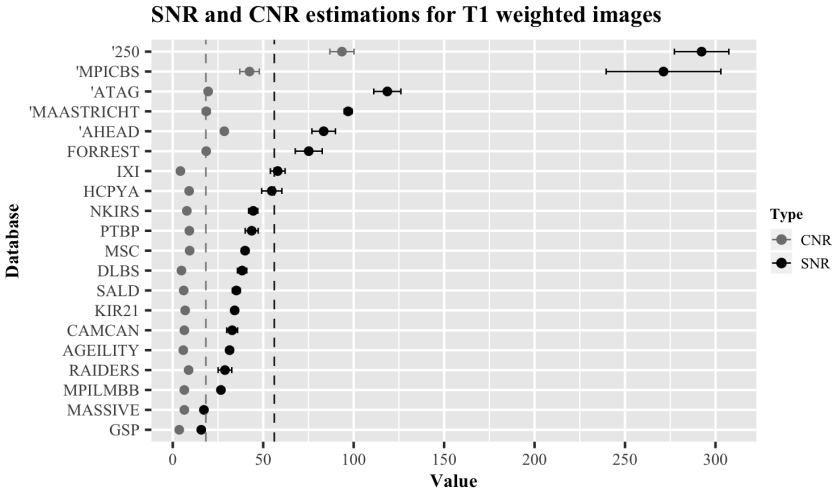

Figure 2.6: Overview of ratios for databases containing a T1w image. SNR_{CC} values are shown in black, CNR values in grey. Each value has been normalized by the voxel dimensions specific to the image it describes. Error bars indicate standard error of the mean. Databases marked with an apostrophe (') indicate 7T data. The dotted vertical lines indicate the mean of the SNR_{CC} (black) and CNR (grey).

Table 2.2: Summary table describing the SNR_{CC}, SNR_{CN} and CNR of the T1w images of each database. Each ratio value is shown as the mean of all the subjects ± the standard error of the mean. n indicates the number of subjects used for the calculations.

Database	Sequence	Contrast	SNR_{CC}	SNR_{CN}	CNR	N
250	MPRAGE	T1w	292.3 ± 15.0	198.3 ± 14.6	93.5 ± 6.7	1
AHEAD	MP2RAGEME	T1w	83.4 ± 6.5	39.5 ± 1.3	28.5 ± 1.3	15
Age-ility	MPRAGE	T1w	31.4 ± 2.0	20.4 ± 2.0	5.8 ± 0.9	5
ATAG	MP2RAGE	T1w	118.6 ± 7.5	29.6 ± 1.4	19.6 ± 0.7	15
Cam-Can	MPRAGE	T1w	32.8 ± 3.0	24.1 ± 1.2	6.1 ± 0.5	15
GSP	MEMPRAGE	T1w	15.8 ± 0.8	8.8 ± 0.7	3.6 ± 0.2	5
DLBS	MPRAGE	T1w	38.3 ± 4.2	19.4 ± 2.7	4.8 ± 0.7	15
HCP-YA	MPRAGE	T1w	54.7 ± 5.6	40.4 ± 1.8	9.1 ± 1.3	5
IXI	-	T1w	58.0 ± 4.1	33.7 ± 1.8	4.2 ± 0.4	15
Kirby 21	MPRAGE	T1w	34.2 ± 1.8	16.7 ± 1.1	6.9 ± 0.6	5
MAASTRICHT	MPRAGE	T1w	96.9 ± 2.2	36.6 ± 3.3	18.5 ± 2.1	5
MASSIVE	3DTFE	T1w	17.2 ± 1.2	10.6 ± 0.3	6.4 ± 0.3	1
MSC	-	T1w	40.0 ± 2.0	26.6 ± 1.3	9.3 ± 0.2	5
MPI-CBS	MP2RAGE	T1w	271.3 ± 31.8	93.1 ± 15.9	42.4 ± 5.4	5
MPI-LMBB	MP2RAGE	T1w	26.6 ± 1.6	12.7 ± 0.3	6.4 ± 0.3	15
NKI-RS	MPRAGE	T1w	44.5 ± 2.5	28.1 ± 1.0	7.8 ± 0.4	15
PTBP	MPRAGE	T1w	43.6 ± 3.6	28.2 ± 1.8	9.2 ± 0.7	5
RAIDERS	MPRAGE	T1w	28.9 ± 3.8	16.9 ± 1.6	8.8 ± 0.9	5
SALD	MPRAGE	T1w	35.1 ± 2.1	23.9 ± 0.8	6.0 ± 0.2	15
StudyForrest	3DTFE	T1w	75.2 ± 7.5	43.5 ± 4.1	18.5 ± 1.1	5

that both samples from each database come from the same distribution. This shows that our sample-based method is reproducible across samples of the databases. Although it would ideally be best to manually segment the CC and CN in each subject, the simplified approach we take here provides a good trade-off between accuracy and manageability given the large of amount of manual delineation that had to be done in the original (665) and the second (164) sample.

2.3.2 Comparing T2w images

Fig 2.7 presents an overview of the estimated SNR_{CC} and CNR of the six databases containing T2w images. The results are ordered as ascending from bottom to top, based on the SNR_{CC} estimation, ranging from 11.8 (Cam-Can) to 51.6 (StudyForrest). Their numerical values can be found in Table 2.3.

2.3.3 Relationships with scan time

We then turned to analyze the relationships between scan time and SNR_{CC} as well as scan time and the acquired spatial resolution. Fig 2.8A shows the relationship between scan time and the normalized SNR for both 3T and 7T scanners separately. It can be seen that there is a significant positive correlation within the 3T data,

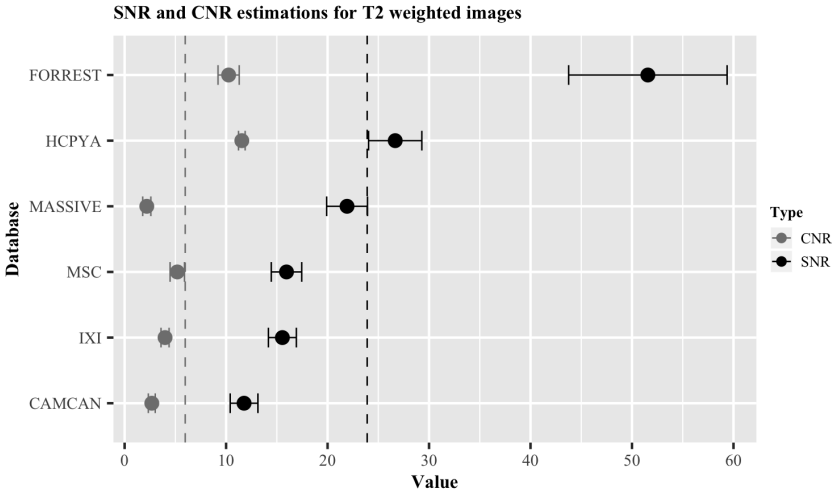

Figure 2.7: Overview of the ratios for databases containing a T2w image. SNR_{CC} values are shown in black, CNR values in grey. Error bars indicate standard error of the mean. The dotted vertical lines indicate the mean of the SNR_{CC} (black) and CNR (grey).

Table 2.3: Summary table describing the SNR_{CC}, SNR_{CN} and CNR of the T2w images of each database. Each ratio value is shown as the mean of all the subjects ± the standard error of the mean. n indicates the number of subjects used for the calculations.

Database	**Sequence**	**Contrast**	**SNR_{CC}**	**SNR_{CN}**	**CNR**	**N**
Cam-Can	SPACE	T2w	11.8 ± 1.4	14.3 ± 0.7	2.7 ± 0.2	15
HCP-YA	SPACE	T2w	26.7 ± 2.6	37.7 ± 3	11.5 ± 0.3	5
IXI	-	T2w	15.5 ± 1.4	17.7 ± 1	4.0 ± 0.2	15
MASSIVE	3DTSE	T2w	21.9 ± 2.0	13.8 ± 1.8	2.2 ± 0.4	1
MSC	-	T2w	16.0 ± 1.5	23 ± 2.3	5.2 ± 0.7	5
Forrest	3DTSE	T2w	51.6 ± 7.8	66.0 ± 3.0	10.2 ± 1.0	5

Table 2.4: Normalized SNR_{CC}, SNR_{CN} and CNR values for the databases that presented slabs as well as whole brain data. 15 subjects were used for all contrast types in these databases. Standard errors of the mean are given for normalized SNR_{CC} and CNR values. qT1, quantitative T1 map; T1w, T1 weighted; PDw, proton density weighted; qT2*, quantitative T2* map; WB, whole brain; SB, slab.

Database	Sequence	Contrast	Type	SNR_{CC}	SNR_{CN}	CNR
AHEAD	MP2RAGEME	qT1	WB	84.4 ± 8.3	68.4 ± 4.8	20.9 ± 2.1
AHEAD	MP2RAGEME	qT1	SB	123.3 ± 5.8	115.0 ± 6.4	34.7 ± 1.3
AHEAD	MP2RAGEME	T1w	WB	83.4 ± 6.1	39.5 ± 1.5	28.5 ± 1.3
AHEAD	MP2RAGEME	T1w	SB	157.1 ± 7.5	103.1 ± 5.9	37.4 ± 1.3
AHEAD	MP2RAGEME	PDw	WB	97.5 ± 6.2	29.5 ± 2.4	1.5 ± 0.5
AHEAD	MP2RAGEME	PDw	SB	147.8 ± 8.2	79.5 ± 6.4	8.3 ± 2.5
AHEAD	MP2RAGEME	qT2*	WB	37.0 ± 2.1	22.1 ± 2.2	3.0 ± 0.4
AHEAD	MP2RAGEME	qT2*	SB	63.8 ± 2.7	49.8 ± 4.4	6.4 ± 1.9
ATAG	MP2RAGE	qT1	WB	69.0 ± 2.7	51.8 ± 2.4	18.0 ± 0.6
ATAG	MP2RAGE	qT1	SB	110 ± 5.2	90.7 ± 3.9	22.6 ± 1.2
ATAG	MP2RAGE	T1w	WB	118.6 ± 6.5	29.6 ± 1.4	19.6 ± 0.7
ATAG	MP2RAGE	T1w	SB	146.2 ± 9.1	47.9 ± 2.1	23.3 ± 1.3

and the 7T data displays the same trend but does not show significance. This relationship is expected, since longer scan times are associated with better image quality. In addition to scan time predicting image quality in terms of SNR_{CC}, a negative relationship between scan time and the acquired voxel volume was found (Fig 2.8B). Longer scan times in the presented databases are therefore indicative of better T1w images both in terms of SNR and spatial resolution.

2.3.4 Quantitative T1 and FOV

Four databases provide quantitative T1 maps (qT1) in addition to T1w images. Two of these databases also provide both whole-brain images as well as slabs with higher resolution and a smaller FOV. A comparison of the normalized SNR_{CC} associated with the qT1 and T1w images of the same databases are shown in Fig 2.9.

Table 2.4 displays the SNR_{CC} and CNR associated with the whole-brain and slab images of the same contrasts acquired by these two databases (ATAG and AHEAD). A frequentist and Bayesian paired t-test indicates that the slab images have a significantly larger SNR_{CC} than the whole brain images, demonstrating the benefits of high resolution ($p = 0.0017$, $t = 6.06$, $DF = 5$, $BF = 25.81$). Though, this does not appear to translate to a higher CNR ($p = 0.074$, $t = 2.3$, $DF = 5$, $BF = 1.57$).

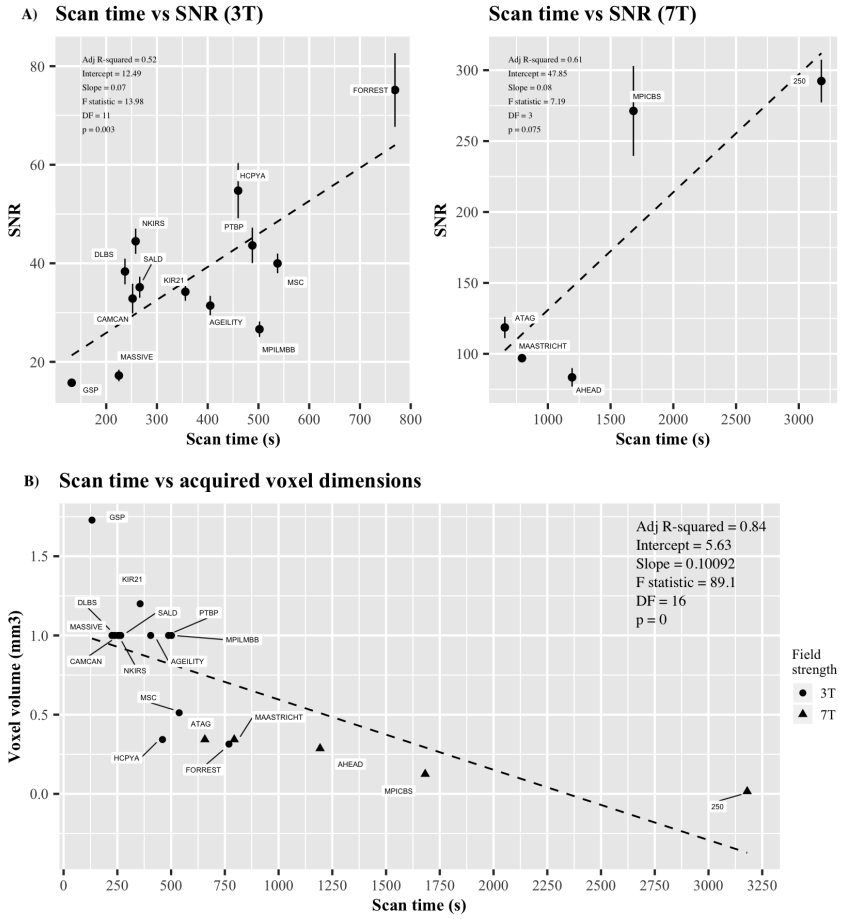

Figure 2.8: The relationship between the SNR_{CC} and voxel dimensions of T1w images with scanning time in 18 databases. A) Graphical representation of SNR_{CC} and scan time. Error bars indicate standard error of the mean. B) Graphical representation of voxel dimensions and scan time. Both legends contain information relating to the adjusted R-squared value, intercept, slope, F statistic, degrees of freedom and p-value. Circular symbols indicate 3T data, triangular symbols indicate 7T data.

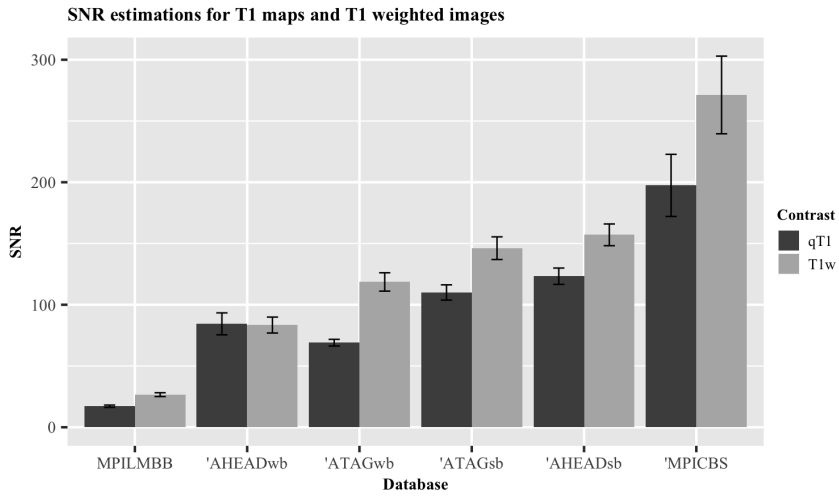

Figure 2.9: Graphical representation of difference in normalized SNR_{CC} values for quantitative T1 maps and T1-weighted images. Databases marked with an apostrophe (') indicate 7T data. qT1, quantitative T1 map; T1w, T1-weighted; wb, whole-brain; sb, slab. Error bars indicate standard error of the mean.

2.3.5 Age-related differences

Figs 2.10 and 2.11 display the differences in the SNR and CNR across the age groups of young (age: 18 – 28), middle-aged (age: 34 – 53) and elderly subjects (age: 63 - 86) in both T1w and T2w images. 165 T1w images and 50 T2w images were used for model comparison. For the SNR_{CC} on the T1w images, the full model comprising age as a predictor was a significantly better fit than the null model (p = 0.011). This relationship was also found for the T1w CNR results (p = 0.00037). In addition to age-related differences in the SNR of white matter areas (SNR_{CC}) and the CNR of T1w images, we also tested the relationship between age and the SNR of a grey matter region (SNR_{CN}). A significant effect of age was found, indicating a loss of signal in the CN over age (p = 0.0062). We then turned to analyze the effect of age on the MR signal of T2w images. Again, we were interested in age differences in the SNR_{CC} the SNR_{CN} and the contrast difference between the grey and white matter regions (CNR). Similarly to the T1w images, an age-related decline in SNR_{CN} and CNR was observed in the T2w images (p = 0.0019, p = 0.000022, respectively) even though the model comparison indicated that the age-related differences in SNR_{CC} were non-significant in the T2w images (p = 0.24).

To gain a greater insight into the relationship between age and the acquired signal from these white and grey matter structures, we used a Bayesian linear modelling technique. The resulting BFs from this method indicated a less conclusive relationship than its frequentist counterpart in some respects. In terms of an age-related reduction in signal within the T1w images, moderate evidence was found for this hypothesis in the CN (BF = 5.52), followed by further moderate evidence within the CC (BF = 4.29), and very strong evidence for this hypothesis was found for the CNR (BF = 61.90). Turning to the T2w images, no evidence in either direction was found for an age-related reduction in signal from the CC (BF = 1.89), strong evidence was found for this hypothesis in the CN (BF = 14.51), and across the age groups, the CNR appeared to show extreme evidence for a relationship (BF = 504.22). Taken together, these results suggest the presence of an age-related deterioration in signal in the caudate nuclei, inferred by both the T1w and T2w images.

As a further assessment of age-related differences, we also compared the SNR and CNR values across qT1 and qT2* images. We again compared linear mixed effect models including age as a fixed effect and the database as a random intercept to a null model without an effect of age. One database, MPILMBB, provides age ranges of five years for each of their participants as opposed to a single age value, presumably for privacy purposes. In order to derive reliable estimates when comparing these mixed effect models, we randomly sampled ages for participants in this database from a uniform distribution of the age range reported. We then iterated over this a total of 1000 times and calculated results from the frequentist and Bayesian model comparisons for each sampled age, below we report the mean results for these iterations. Similarly to the T1w and T2w comparisons, both qT1 and qT2* maps showed a significant change in CNR across the adult lifespan (p = 0.00032, BF = 73.25; p = 0.035, BF = 1.12). The SNR_{CN} significantly declined in both the qT1 and qT2* images (p = 0.0015, BF = 19.68; p = 0.00019, BF = 247.99, respectively). A similar decline was found for the SNR_{CC} in the qT2* images (p = 0.00063, BF = 34.83). Although, only a negligible decline in signal was found for the CC in the qT1 images (p = 0.020, BF = 2.49).

2.4 Discussion

We present the first quantitative comparison exploring the image quality offered by twenty open-access databases of structural MRI freely available to researchers world-wide. To this end, SNRs were calculated from both the corpus callosum and caudate nuclei. From these calculations, CNRs were derived, which in this case

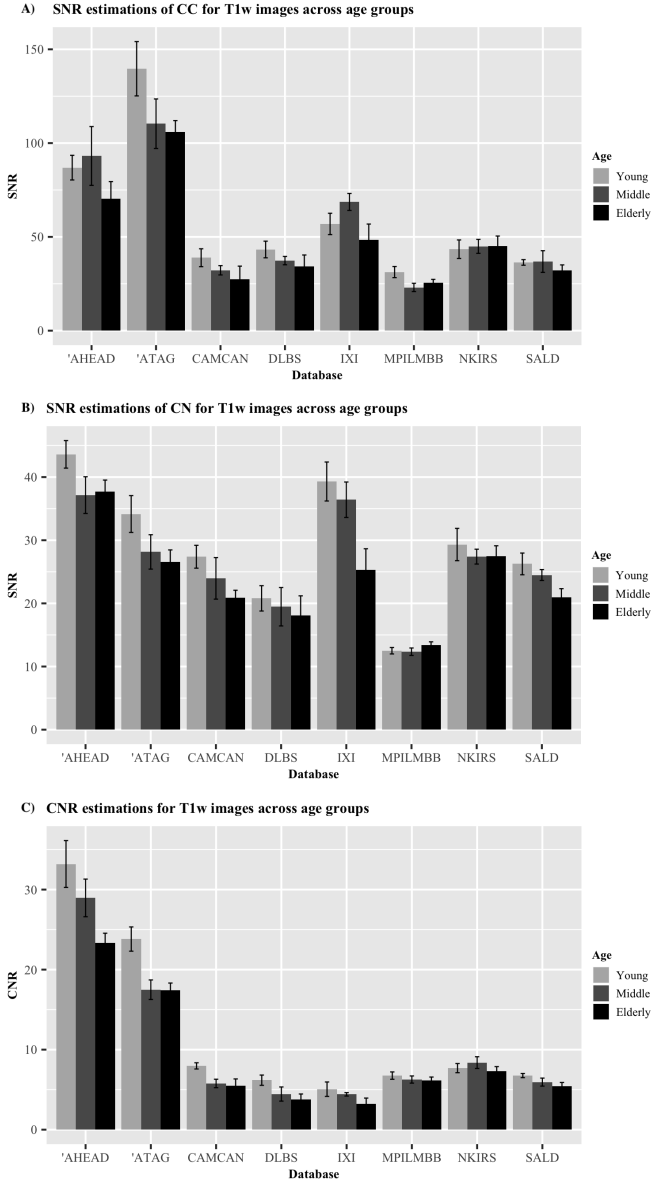

Figure 2.10: Comparison of ratios for T1w images across age groups. A) SNR_{CC}. B) SNR_{CN}. C) CNR. Error bars indicate standard error of the mean. Each bar singular represents five participants. Databases marked with an apostrophe (') indicate 7T data.

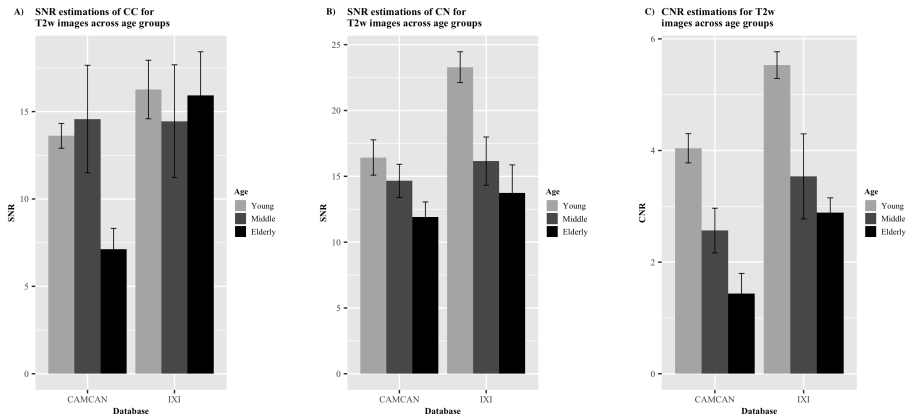

Figure 2.11: Comparison of ratios for T2w images across age groups. A) SNR_{CC}. B) SNR_{CN}. C) CNR. Error bars indicate standard error of the mean. Each bar singular represents five participants.

can indicate the extent to which these images can distinguish between grey and white matter. An additional analysis assessed differences in T1w and T2w SNR values across the adult lifespan, taking advantage of larger imaging databases with accompanying demographic information and large age ranges. Due to the wealth of data provided by these databases, clear relationships between the scan time and both acquired voxel dimensions and acquired SNRs could also be found, indicating the efficiency of specific scanning protocols. As only a subset of the databases offered multiple contrasts, direct inter-database comparisons between all contrast types could not be provided. Within this subset, intra-database comparisons between contrasts are possible. SNR and CNR estimations for the contrasts offered by each database are displayed in the Table A.3.

The results of the SNR and CNR calculations show a clear benefit of using UHF MRI, with the five 7T databases (250, AHEAD, ATAG, MAASTRICHT and MPI-CBS) obtaining the largest values in the CC. Moreover, the MPI-CBS and 250 databases showed much higher image quality compared to the other databases. It should be noted, however, that the images offered from the MPI-CBS database include image post-processing pipelines that are not applied in any of the other databases. Such processing pipelines can increase image quality substantially, and are another benefit of openly accessible imaging data and protocols. Through the availability of this data, exciting new data pipelines and tools can be developed and shared. In Table A.3, you can find the SNR_{CC}, SNR_{CN} and CNRs for all the images analyzed for each database. Note that this includes two databases (HCPYA

and 250), which provide both processed and unprocessed images. A clear benefit of post-acquisition processing pipelines can be seen when comparing these ratios within-database. The processed T1w images provided by the 250 database increase the SNR_{CC} from 292.3 ± 15.0 to 570.4 ± 123.5, a similar increase can be seen in the SNR_{CN}, increasing from 198.3 ± 14.6 to 368.0 ± 53.5, though this did not benefit the CNR (93.5 ± 6.7 and 93.7 ± 14.6 for the unprocessed and processed images, respectively). Within the HCPYA database, increases in the SNRs and CNRs of both the T1w and T2w images are also apparent. Taken together, this suggests that optimizing post-acquisition processing methods can provide additional increases in image quality that are not trivial.

While the analysis presented here quantifies an important aspect of the databases, they are not the only factor to take into account when selecting imaging data for further research purposes. At an overview, our results indicate a strong advocation for the MPI-CBS and 250 databases, owing to their SNR and CNR far above the rest. However, there are also other factors to consider, for example, sample size, age-range and the number of contrasts included are just some of a long list of criteria many research questions need to consider. As such, the small sample size, limited age-range and limited contrasts make the MPI-CBS and 250 databases less attractive for many lines of research.

Although the relationships of SNR and voxel dimensions with scan time presented here are obvious and reflect basic MRI physics, it is nonetheless interesting to see the efficiency of separate MRI protocols. These relationships are particularly informing when aspects of image quality largely deviate from linearity. Optimized MR sequences or contrasts that allow for high spatial resolution or high SNRs with short scan times offer preferable performance. These comparisons also indicate further favourability for 7T imaging, with most of the resultant 7T database images residing on the efficient side of the linear trends displayed with scan time.

We present here age-related differences across four MRI contrasts; T1w, T2w, qT1, and qT2*. Our SNR_{CN} analyses suggest a consistent age-related decline in all image types. Age-related changes in relaxation values in the human brain have been long-known (Bottomley et al., 1984). There is also evidence that T2* values reflect iron concentration in neural tissues (Brooks et al., 1989). During healthy aging, iron-deposition appears to increase in some brain structures (e.g., parts of the basal ganglia) (Aquino et al., 2009; Haacke et al., 2005; Hallgren and Sourander, 1958; Morris et al., 1992). The decline of qT2* measures in the CN therefore likely reflects this increase in iron deposition. The lowering in effective T2 found here is also in line with previous work (Keuken et al., 2017; Siemonsen et al., 2008).

Volume loss in this region is another known process observed in the healthy aging brain (Di et al., 2014; Raz et al., 2003), which would be accompanied by a declining proton density, lowering the signal derived from T1 recovery and T2 relaxation. Taken together, these declines in signal would suggest an age-related structural change of the caudate nuclei. A more complicated picture is painted for the SNR_{CC} measurements. A SNR decline in the CC was found in T1w, qT1 and qT2* images, though this decline is not as apparent as in the CN. Post mortem histological analyses of white matter regions have shown that the myelination of nerve fibres decreases with age (Marner and Pakkenberg, 2003). This process of demyelination is associated with an increase in SNR in qT1 and T1w images (Keuken et al., 2017), in opposition to what was found here. It should be noted, however, that there appears to be an increase in image noise in the elderly population (measured as the standard deviation of the 27 voxels measured per image). This increase in noise was not accompanied by a decrease in mean signal of the region, and therefore likely drives the small decline in SNR found. For the other relationships, this increase in noise as a function of age is also apparent. However, since this increase is also accompanied by a decrease in mean signal, it most likely reflects an underlying structural change. We note that age-related structural changes are heterogeneous across different regions of the brain. The processes underlying these changes are similarly heterogeneous and a combination of a multitude of factors, including changes in the small vessels supplying the regions, regional brain atrophy, loss of myelination and impaired white matter (Bullitt et al., 2010; Marner and Pakkenberg, 2003; Pagani et al., 2008; Resnick et al., 2003). These changes, in addition to increased subject motion during scanning could all impact the increase level of noise found in the elderly population. It has been suggested that head motion increases as a function of age (Savalia et al., 2017), although some findings have suggested a more non-linear relationship between the two (Pardoe et al., 2016). Even subtle forms of motion artefacts have been shown to affect interpretability of imaging analysis results (e.g., cortical thickness estimates; (Fjell et al., 2009)). Image noise introduced through head motion also lowers SNR estimates and degrades image quality (Havsteen et al., 2017). This highlights the need for motion correction in structural MRI. Due to our limited snapshot of the data available, we can only show results that hint at these intricate relationships.

For the CNR measurements, there consistently appears to be an age-related decline across the adult lifespan, as indicated by the analysis of all four contrasts. Such CNR differences are also found when comparing adult and infant brains (Mewes et al., 2006). This decrease in CNR over the adult lifespan is a by-product

of the physical changes to the contrasted regions (CC and CN). The observed decrease in SNR in these two regions leads to this decrease in CNR. The analyses of age-related differences presented here illustrates just one of the many interesting ways these open-access databases can be used for in the future.

It should be stressed that there are a variety of methods to calculate both the SNR and CNR of structural MR images, note that most of these methods are not applicable to all situations. For SNR estimation, there are two other prominent methods used in the field. The first involves measuring the SNR of the region of interest (ROI) within the brain and dividing it by the SNR of the background of the image outside of the brain. The second involves measuring only the mean signal of the ROI inside the brain and dividing it by the standard deviation of a region outside of the brain. A commonality in both of these methods is that they assume that measuring an area outside of the brain captures only the noise induced by the MR scanner itself. One reason we opted for the method used here is that due to inhomogeneities in the magnetic field of each scanner and differences in the spatial distribution of noise (Pruessmann et al., 1999; Sodickson and Manning, 1997), the area of the background image chosen for the measurement of noise could differ significantly between sites and sequences. Of course, our method does not remove the problem of bias, but as this bias is the same across all of the images measured here, we believe the comparison is fair. Regardless of the method used for the measurement of the SNR, the most important requirement for an objective comparison is that the method used is consistent across all data. To signify that this method was indeed reliable within the databases, we ran the validation study on the separate T1w images. The reproducibility of the estimates that we took indicate that the methods holds as a consistent measurement of SNR.

As spatial resolution increases, sensitivity to both voluntary or involuntary motion and physiological noise will also increase, and therefore continue to be a ceiling on image quality at all field strengths. Methods to overcome such movement artefacts include both retrospective and prospective motion correction (Haacke and Patrick, 1986; Lee et al., 1996). Both approaches have displayed their ability to increase image quality at 3T and 7T, providing a way around subject motion at high resolution (Federau and Gallichan, 2016; Gallichan et al., 2016; Stucht et al., 2015; Zaitsev et al., 2017). Removing this confound completely while scanning healthy individuals is infeasible, but post mortem MRI can benefit from the lack of movement artefacts, allowing for scan times inconceivable in live subjects. These scan times can facilitate the visualization of a much larger number of smaller brain structures (Oguz et al., 2013). For the purpose of creating probabilistic atlases of

the human brain, such a technique when used in concurrence with histological methods can provide greater detail than in vivo MRI alone (Forstmann et al., 2017).

We acknowledge that for many of the databases discussed here, we have only analyzed a snapshot of the data and have not taken advantage of all of the data we have access to. This limitation was necessary to keep our analysis level feasible, as the range in sizes of these databases make using all participants problematic. For the future, we would hope that a standardized SNR protocol will become a feature that all new databases will use and present with their data. Ideally, this would include manually segmented masks of the same anatomical areas, from unprocessed imaged in their native spaces. We also hope that open-access databases continue to become the norm across the scientific field.

2.5 Conclusion

The current study provides a quantitative comparison between some of the most fruitful open-access neuroimaging databases available, which can aid researchers in selecting which databases to use. The results presented here give an indication of the large variation in image quality provided by these databases. The estimations (SNR and CNR), as well as the number of contracts provided by each database (as these give visual information to specific tissue types), can aid in the selection process. The benefit of large-scale imaging databases for creating general maps of cortical organization and providing both phenotypic and genetic comparisons across populations is clear. However, large-scale databases often come at the cost of lower image resolution due to the financial implications of using large sample sizes, ultra-high field MRI and extensive scan times. In particular for the human subcortex, image resolution is critical and standard structural 3T MRI data does not provide the required resolution and SNR for small nuclei. The higher quality of 7T databases provides a clear advantage, but high cost and limited access are still preventing the collection of larger cohorts. Each database presented here has assisted an important neuroscientific movement towards open-access imaging data. With the number of subjects ranging from one to over 1500 and the number of sessions from one to 18, the objectives and characteristics of these databases are diverse. We hope that our current efforts will help researchers to choose the appropriate database for their research question and highlight their usefulness to the scientific field in the study of normative human brain structure.

Chapter 3

Charting human subcortical morphometry across the adult lifespan with *in vivo* 7 T MRI

This chapter is published as:
S. Miletić, P.-L. Bazin, S. J. S. Isherwood, M. C. Keuken, A. Alkemade, and B. U. Forstmann (2022). Charting human subcortical maturation across the adult lifespan with in vivo 7 T MRI. *NeuroImage* 249.July 2021, p. 118872. DOI: 10.1016/j.neuroimage.2022.118872.

Abstract

The human subcortex comprises hundreds of unique structures. Subcortical functioning is crucial for behavior, and disrupted function is observed in common neurodegenerative diseases. Despite their importance, human subcortical structures continue to be difficult to study *in vivo*. Here we provide a detailed account of 17 prominent subcortical structures and ventricles, describing their approximate iron and myelin contents, morphometry, and their age-related changes across the normal adult lifespan. The results provide compelling insights into the heterogeneity and intricate age-related alterations of these structures. They also show that the locations of many structures shift across the lifespan, which is of direct relevance for the use of standard magnetic resonance imaging atlases. The results further our understanding of subcortical morphometry and neuroimaging properties, and of normal aging processes which ultimately can improve our understanding of neurodegeneration.

3.1 Introduction

The human subcortex comprises hundreds of unique structures (Alkemade et al., 2013; Forstmann et al., 2017) which receive interest from a broad range of neuroscientific disciplines (e.g. Lozano et al., 2019; Raznahan et al., 2014; Shepherd, 2013; Tian et al., 2020). Subcortical functioning is crucial for normal behavior and physiology including decision making (Ding and Gold, 2013), reward processing (O'Doherty et al., 2004; Schultz et al., 1997), and motor behavior (Mink, 1996). Disruption of subcortical structures is observed in common neurodegenerative diseases including Parkinson's (Hirsch et al., 1988) and Alzheimer's disease (Ehrenberg et al., 2017; German et al., 1987). Subcortical structures are also of interest as (potential) deep brain stimulation (DBS) targets in Parkinson's disease (Fasano and Lozano, 2015; Limousin et al., 1995) and other disorders such as major depression and epilepsy (Lozano et al., 2019).

Research into the subcortex depends on the imaging of individual subcortical structures. However, visualizing subcortical structures using *in vivo* methods such as magnetic resonance imaging (MRI) is challenging due to their close spatial proximity, biophysical properties, and morphometry (Keuken et al., 2018). As a consequence, our understanding of the subcortex remains limited, and lags behind our understanding of the cortex. Quantitative ultra-high field 7 Tesla MRI provides a method to overcome the challenges associated with visualizing subcortical structures (Bazin et al., 2020; Keuken et al., 2018), which we use here to provide a cross-sectional account of the subcortex across the adult lifespan.

The biophysical properties that determine the appearance of brain structures on MR images include the iron and myelin contents, which influence the main sources of contrast in MRI: the longitudinal and effective transverse relaxation rates, and the local susceptibility to magnetic fields. Furthermore, iron and myelin are highly biologically relevant: Myelin plays an important role in plasticity and development (e.g. Fields, 2015; Hill et al., 2018; Turner, 2019), and iron is crucial for normal tissue functioning (e.g. Zecca et al., 2004). Iron deposition (Daugherty and Raz, 2013; Hallgren and Sourander, 1958; Raz and Rodrigue, 2006; Ward et al., 2014; Zecca et al., 2004) and decreased myelination (Raz and Rodrigue, 2006; Shen et al., 2008) are part of normal aging processes, but excessive iron accumulation and myelin degradation are prominent in diseases including Parkinson's and Alzheimer's disease (e.g. Mancini et al., 2020; Zecca et al., 2004). A description of normal age-related changes in iron and myelin content can therefore provide a frame of reference to contrast pathological iron accumulation and myelin degradation, and

to refine methods for the early detection of pathological alterations using MRI measures as biomarkers.

An additional factor determining the appearance of the human subcortex is the small size of the individual structures. Prominent subcortical structures such as the subthalamic nucleus are as small as a few millimeters thick, limiting the number of voxels they encompass on MR images commonly used in research and in the clinic. Moreover, voxels at the border of structures likely include tissue from adjacent structures (partial voluming), which can lead to biases especially when voxel sizes are large relative to the structure (Mulder et al., 2019). Structure size should therefore be taken into account when imaging the subcortex. An important additional consideration here is the development of atrophy with increasing age, which is reflected in reduced volume of gray matter structures (Cherubini et al., 2009; Courchesne et al., 2000; Herting et al., 2018; Lemaitre et al., 2012; Raz, 2004; Raz and Rodrigue, 2006; Walhovd et al., 2005) and which results in more cerebrospinal fluid (CSF) and larger ventricles (Good et al., 2001; Greenberg et al., 2008; Stafford et al., 1988; Walhovd et al., 2005). In addition to volume changes, atrophy can result in a shift in the location of structures (Keuken et al., 2017; Keuken et al., 2013; Kitajima et al., 2008).

These factors combined hamper visualization of the subcortex when using conventional MRI techniques. Furthermore, the age-related alterations in these factors alter the appearance of the subcortex with increasing age. In this study, we provide a detailed account of 17 subcortical structures and ventricles using data from 105 healthy participants across the adult lifespan obtained with *in vivo* methods tailored for studying the human subcortex (Alkemade et al., 2020a). For practical reasons, and without intending to make any claims on how a subcortical structure should be defined, we define subcortical as any anatomical structure located inferior to the corpus callosum.

Compared to previous studies, which often focus on a select set of regions and/or MRI or morphometry measures at a time, we simultaneously study a wider range of structures and measures. These include structures and measures that have not been studied before in the context of aging. The structures under investigation include gray matter regions, white matter tracts, and the ventricles. The inclusion of a variety of structures allows us to study across-region similarities and differences in aging effects. Similarly, the large set of quantitative MRI (qMRI) contrasts and morphometry measures allows us to explore aging as a multidimensional process. As such, we provide a wide picture of subcortical aging across metrics and regions.

Furthermore, we improve upon previous methods by using qMRI acquired at 7 Tesla (T) with 0.7 mm isotropic resolution, and employ the MASSP method (Bazin et al., 2020) to obtain automated delineations with an accuracy that approximates the gold standard of manual delineations (Alkemade et al., 2021; Bazin et al., 2020). Tullo et al. (2019) have shown that the choice of delineation method can influence which age-related change models provide best fits to empirical data, illustrating the importance of high-quality delineations in aging studies. Additional methodological improvements include the development of a subcortical thickness estimation method, which provides a thickness estimate analogous to cortical thickness metrics; as well as the development of iron and myelin approximation methods. Combined, these methods allow us to interpret our results in terms of the hypothesized biological processes that occur during aging: myelin degradation, iron accumulation, and atrophy (changes in size, shape, and location).

3.2 Methods

3.2.1 Participants

We used the Amsterdam ultra-high field adult lifespan database (AHEAD; Alkemade et al., 2020a), which consists of multimodal MRI data from 105 healthy participants. Inclusion criteria were age 18–80 years and self-reported health at the time of inclusion. Exclusion criteria were any factors that could potentially interfere with MRI scanning, including MRI incompatibility (e.g., pacemakers), pregnancy, and self-reported claustrophobia. At least six males and females were included in each age decade to ensure full coverage of the adult lifespan. All participants gave written informed consent prior to the onset of data collection. The local ethics board approved the study.

3.2.2 MRI scanning

Images were acquired at the Spinoza Centre for Neuroimaging in Amsterdam, the Netherlands, using a Philips Achieva 7 T MRI scanner with a 32-channel phased-array coil. Routine quality checks of the quantitative maps appearance were performed previously (Alkemade et al., 2020a) and all subjects from the database were included for analysis. T1-weighted, $T2^*$ contrasts were obtained using a MP2RAGEME (multi-echo magnetization-prepared rapid gradient echo) sequence (Caan et al., 2019). The MP2RAGEME is an extension of the MP2RAGE sequence (Marques et al., 2010) and consists of two rapid gradient echo ($GRE_{1,2}$) images that are acquired in the sagittal plane after a 180 degrees inversion pulse

and excitation pulses with inversion times $TI_{1,2}$ = [670 ms, 3675.4 ms]. A multi-echo readout was added to the second inversion at four echo times (TE_1= 3 ms, $TE_{2,1\text{-}4}$ = 3, 11.5, 19, 28.5 ms). Other scan parameters include flip angles $FA_{1,2}$ = [4, 4] degrees; $TR_{GRE1,2}$ = [6.2 ms, 31 ms]; bandwidth = 404.9 MHz; $TR_{MP2RAGE}$ = 6778 ms; acceleration factor SENSE PA = 2; FOV = 205 $\times$ 205 $\times$ 164 mm; acquired voxel size = 0.7 $\times$ 0.7 $\times$ 0.7 mm; acquisition matrix was 292 x 290; reconstructed voxel size = 0.64 $\times$ 0.64 $\times$ 0.7 mm; turbo factor (TFE) = 150 resulting in 176 shots; Total acquisition time = 19.53 min. No B1 field correction was performed; instead, the B1 field was optimized for subcortex during data acquisition.

3.2.3 Quantitative MRI modeling and parcellation

The MP2RAGEME consists of two interleaved MPRAGEs with different inversions and four echoes in the second inversion. Based on these images, we estimated quantitative MR parameters of R1, $R2^*$ and QSM as follows. First, we took advantage of the redundancy in the MP2RAGEME sequence to perform a PCA-based denoising with LCPCA (Bazin et al., 2019). R1 maps were then computed using the standard look-up table approach of Marques et al. (2010) to recover T1 values from the measured signals. $R2^*$-maps were computed by least-squares fitting of the exponential signal decay over the four echoes of the second inversion. QSM images were obtained from the phase maps of the second, third, and fourth echoes of the second inversion with TGV-QSM (Langkammer et al., 2015). Skull stripping, required for QSM, was performed on the second inversion, first echo magnitude image (Bazin et al., 2014).

The anatomical regions of interest were defined with the MASSP automated algorithm (Bazin et al., 2020) on the basis of the R1, $R2^*$ and QSM image maps. The algorithm combines location, shape, and quantitative MRI priors to define 17 subcortical anatomical regions and ventricles, listed in Table 3.2. Separate masks for left and right hemisphere were obtained except for 3V, 4V, and *fx*.

For this study, the MASSP algorithm was trained on renormalized versions of the quantitative contrasts using a fuzzy C-means clustering of intensities, and linearly interpolating between cluster centroids (Pham and Bazin, 2009). The renormalized contrasts were thus less sensitive to the intensity variations induced by aging. Additionally, the registration to the MASSP atlas was performed in two successive steps, producing more accurate alignment of the anatomical priors with each subject. This second step was particularly important to compensate for the large variability of ventricular size and shape in the study cohort. The algorithm itself was unchanged, and we re-validated the accuracy of the method against

manual delineations as in (Bazin et al., 2020). Improvements were noticeable for more variable structures such as the ventricles, fornix, and claustrum, as well as some of the more challenging smaller structures, see Figure B.1.

3.2.4 Iron and myelin approximation

Iron and myelin are main determinants of MR image contrast (Stüber et al., 2014). Several lines of research indicate that the concentrations of iron and myelin are approximately linearly related to qMRI metrics R1, $R2^*$ and QSM (Hametner et al., 2018; Mangeat et al., 2015; Marques et al., 2017; Metere and Möller, 2018; Rooney et al., 2007; Stüber et al., 2014). Whereas many studies make inferences on iron and myelin contents based on a single MRI modality (e.g., Daugherty and Raz, 2013; Khattar et al., 2021), we use the multimodal quantitative nature of our data to estimate the relation between multiple modalities and iron and myelin. Assuming a linear relationship between iron and myelin on the one hand, and qMRI on the other, linear models can be fit and used to predict iron and myelin contents based on qMRI values (Metere and Möller, 2018):

$$\begin{aligned} Iron &= Intercept + w_{i,qsm} * QSM + w_{i,R2^*} * R2^* + w_{i,R1} * R1 \\ Myelin &= Intercept + w_{m,qsm} * QSM + w_{m,R2^*} * R2^* + w_{m,R1} * R1 \end{aligned} \tag{3.1}$$

Estimating the parameters w of these models requires population-average estimates of iron and myelin content for a variety of regions of interest that cover the range of R1, $R2^*$, and QSM values observed across the brain. Following the approach by Metere and Möller (2018), we obtained these values from the literature (Hallgren and Sourander, 1958; Metere and Möller, 2018; Randall, 1938), and supplemented those values using observations in *post mortem* tissue (detailed below). For iron estimates, Hallgren and Sourander (1958) provided quantifications across a number of subcortical and cortical regions, which, combined with the corresponding qMRI values obtained using our own MRI data, allowed for stable estimators of the weights in Equation 3.1. An iron concentration of 0.061 in the ventricles was assumed (following Metere and Möller, 2018, who based this value on LeVine et al., 1998).

As a reference for myelin concentrations, we used work by Randall (1938), which provides lipid concentrations for the corona radiata, frontal and parietal white matter, brain stem, thalamus, caudate, and frontal and parietal gray matter. Following Metere and Möller (2018), we assumed that these lipid concentrations

reflect myelin concentrations. Unfortunately, the reported regions do not include iron-rich nuclei, which limits the range of (especially) $R2^*$ and QSM values with known corresponding lipid concentrations. Using a limited number of regions of interest to estimate the myelin model could limit the generalizability of the estimated parameters to structures with lower $R2^*$ and/or QSM values, which would bias myelin estimates in iron-rich structures like some basal ganglia nodes (e.g., based on using only Randall's (1938) lipid concentrations, Metere and Möller (2018) obtained *negative* myelin concentrations in various basal ganglia structures).

To supplement the literature-based myelin concentrations, we approximated the myelin contents of other regions of interest using a *post mortem* specimen. Specifically, we used specimen #7 from Alkemade et al. (2020b), which was a 75 year old female, non-demented control. At the time the current experiments were performed, this was the only specimen fully processed. Here, we made the following assumptions:

1. The optic density of tissue in our silver stains is approximately linearly related to the concentration of myelin in that tissue in our regions of interest (see Figure 3.1). Here, we confirmed that silver stains were not saturated even in the white matter regions;

2. The myelin concentrations in the *post mortem* specimen do not show gross abnormalities. We found no indications that our *post mortem* specimen showed major abnormalities in myelin properties. We confirmed that the donor had no clinical record of neurodegenerative disease, a diagnosis that was confirmed *post mortem* by a board-certified neuropathologist;

3. The myelin concentrations in white matter reported by Randall (1938) are in the same range of the myelin concentration in the internal capsule. Similarly, the myelin concentrations in parietal cortex are in the same range of the concentrations in insular cortex.

Seven 200 μm coronal sections of a single specimen were stained according to the method described by Bielschowsky (for details, see Alkemade et al., 2020b). Sections included the caudate nucleus, thalamus, internal capsule, and insular cortex, in which we estimated the median intensity of the lightness of the stain (the optic density). Randall (1938) reports quantified lipid concentrations of the caudate nucleus and thalamus, which can be directly compared to the stain intensities, as well as of parietal gray and white matter. The caudate nucleus, thalamus, and parietal gray and white matter (as reported by Randall (1938)) were not visible in

the same histological section, and we therefore used insular cortex as a reference region for gray matter, and the internal capsule as a reference region for white matter. For each section separately, we then created a linear calibration curve, which allowed us to determine lipid concentrations based on the stain intensity (Figure 3.1) for putamen, globus pallidus, subthalamic nucleus, red nucleus, and substantia nigra.

For the region of which population-averaged iron and myelin contents were known, we estimated the qMRI values using the MRI data. Median qMRI values were calculated using the MASSP masks for subcortical regions, and a MGDM and CRUISE parcellation was used to obtain individual masks for brain stem, cerebellum, and cortex (Bazin et al., 2014). We included only participants of 30 years and older to match the ages of the specimens on which the iron and myelin estimates are based. For brain regions for which we had estimated the myelin content using our *post mortem* specimen, we only included AHEAD subjects of 70 years and older (17 participants total) to approximately match ages of the MRI data and the specimen. Tables B.1 and B.2 list the iron and myelin concentrations, respectively, and their corresponding qMRI values, that were used to estimate the parameters in Equations 3.1.

To test whether all qMRI metrics were required as predictors to accurately predict iron and myelin content, we fitted linear models with all eight possible combinations of R1, R2*, and QSM. Models were fitted using ordinary least squares (OLS). For each model, we estimated the Akaike information criterion (AIC; Akaike, 1973) to identify the model that is expected to have the highest predictive performance, and used the model with lowest AIC values (AIC and BIC values agreed on the winning model). We used the AIC here instead of the BIC as the AIC is expected to select models with the highest cross-validated predictive performance, whereas the BIC is expected to select the data-generating model (Wagenmakers and Farrell, 2004). The model comparisons, including the parameterized winning models, can be found in Table 3.1.

Comparisons of the explained variance (R^2) of the individual models show that, when relying on single qMRI metrics, R2* explained most variance in iron (91.6%), followed by QSM (81.1%). Combining R2* and QSM increased the explained variance to 94.6%, which implies R2* and QSM largely (but not only) explain the same variance in iron. Nonetheless, the increase in variance explained acquired by adding QSM to the R2* model was sufficient to warrant the additional model complexity, as evidenced by the lower AIC and BIC values.

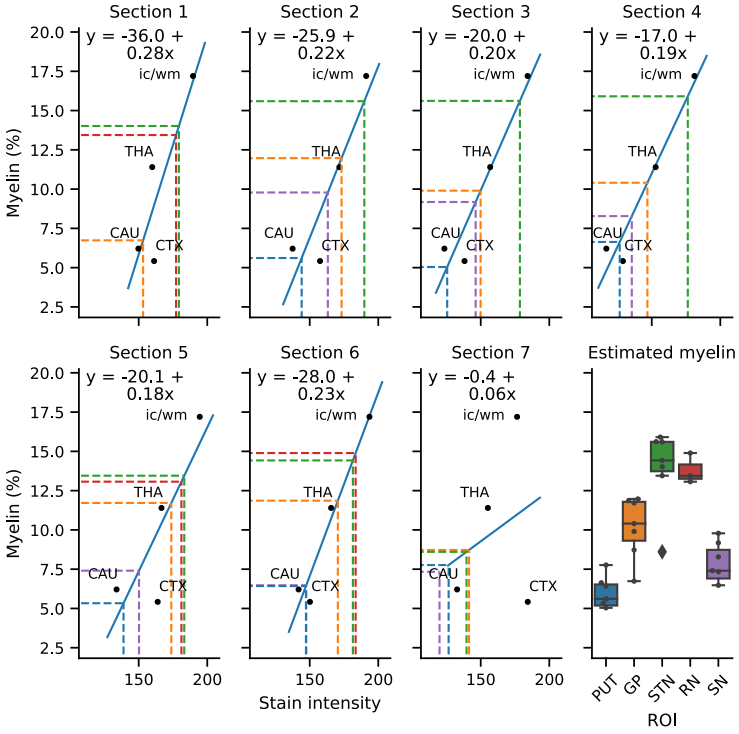

Figure 3.1: Procedure of estimating myelin contents using a *post mortem* specimen. In each section (seven in total), the stain intensities corresponding to CAU, THA, insular cortex (CTX) and the internal capsule (ic/wm) were estimated. For each section individually, a calibration curve was estimated to map stain intensity to myelin values (solid blue lines and equations). Within the range of interest, the relation between stain intensity and myelin content could be approximated with a linear trend. Then, within each section separately, the intensity values for putamen (PUT), GP, STN, RN, and SN were estimated (colored dashed lines; note that not all sections contained all structures), and the corresponding myelin values were calculated. Per region, the median estimate (across sections) was used as a final estimate. Boxplots in the right panel show across-section variability in estimated myelin contents and suggest agreement across sections. The center line in each box marks the median, box limits are the across-section interquartile range, and whiskers are at 1.5 times the interquartile range below and above the box limits. ROI = Region of interest.

Table 3.1: Model comparisons for the iron (top) and myelin (bottom) approximation models. Bold face indicates the winning models, which have the lowest AIC and BIC values.

	Parameterized model	R^2	AIC	BIC
Iron	y = 8.27718	0.0	117.2952	118.1285
	y = -6.83576 + 0.33962×R2*	0.9161	77.1614	78.8278
	y = -11.25376 + 29.28218×R1	0.4811	108.1415	109.8079
	y = -3.45436 -9.2427×R1 + 0.40217×R2*	0.933	75.3461	77.8458
	y = 4.68168 + 274.40993×QSM	0.8107	90.9972	92.6637
	y = -3.82834 + 0.2431×R2* + 98.27947×QSM	**0.9461**	**71.6371**	**74.1368**
	y = -2.59147 + 11.83574×R1 + 227.0019×QSM	0.8651	87.2357	89.7354
	y = -2.41386 -5.22683×R1 + 0.29445×R2* + 82.01402×QSM	0.9507	72.1302	75.463
Myelin	y = 9.34013	0.0	78.8674	79.4324
	y = 4.41227 + 0.09621×R2*	0.2178	77.6741	78.804
	y = -6.25936 + 21.5651×R1	0.7746	61.4997	62.6296
	y = -7.98965 + 31.87483×R1 -0.11182×R2*	**0.8918**	**53.963**	**55.6579**
	y = 8.80294 + 25.38923×QSM	0.0211	80.5908	81.7207
	y = -0.24058 + 0.25117×R2* -155.23593×QSM	0.4399	75.3327	77.0276
	y = -7.7523 + 25.33129×R1 -58.19931×QSM	0.8616	57.1586	58.8535
	y = -7.97876 + 32.10295×R1 -0.11662×R2* + 3.32451×QSM	0.8918	55.9549	58.2147

As expected, R1 explained most variance in myelin (77.4%), while R2* explained only limited variance in myelin (21.78%, only marginally better than an intercept-only model). However, the combination of R1 and R2* explained 89.2% of variance, suggesting R1 and R2* do not largely explain the same variance in myelin, but each explain unique proportions. AIC and BIC values preferred the model that included both R1 and R2* as predictors.

Figure 3.2 visualizes quality of fit of the winning models. Note that the model weights cannot directly be compared to the weights from Stüber et al. (2014), which were obtained using formalin fixated *post mortem* tissue. Formalin fixation can change qMRI values (Birkl et al., 2016; Langkammer et al., 2012; Schmierer et al., 2008; Shepherd et al., 2009; Tovi and Ericsson, 1992). A second complicating factor is that qMRI values can vary between MRI sites (Mancini et al., 2020), suggesting the need to re-estimate model weights when using qMRI obtained at a different site.

Using these simplified biophysical models, we calculated whole-brain iron and myelin maps, and obtained participant-specific myelin and iron values for all structures using the MASSP masks. Iron and myelin maps of a representative participant are shown in Figure 3.3. To confirm our models are able to reproduce the between-region variability in iron and myelin that has been reported in the literature, we compared the myelin and iron predictions to the concentrations in the literature (Figure 3.4). We also compared the myelin predictions to the myelin

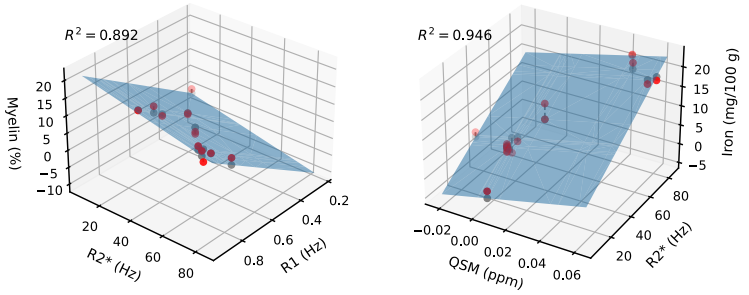

Figure 3.2: Quality of fit of the myelin (left) and iron (right) model. The planes are given by the winning models in Table 3.1. Red dots illustrate data points, gray dots are the model predictions for these data points.

concentrations estimated based on the *post mortem* tissue. These comparisons suggest reasonable correspondence between literature-derived and qMRI-derived iron and myelin concentrations for most regions, but not all. Regions with relatively large discrepancies include the brainstem, which might arise due to the fact that the iron literature reported concentrations in the medulla oblongata, whereas the qMRI data delineation included the entire brainstem. Similarly, the iron literature provided separate estimates for the putamen and caudate, whereas the qMRI delineations included the striatum as a single region, and as such the qMRI-derived iron concentrations cannot recover any differences between the putamen and caudate. Finally, the qMRI-derived myelin estimates are higher than the *post mortem* estimates, which might be related to neuromelanin, as this results in a lower intensity in the *post mortem* tissue, potentially resulting in a negative bias in the corresponding myelin estimate.

It is important to emphasize that the iron and myelin estimates we report are based on simplifying assumptions with regard to the linearity of the relation between qMRI and iron/myelin, and on the iron/myelin concentrations on which the biophysical models are fitted (detailed above). As such, the iron and myelin estimates should be not be interpreted as absolute measurements, but rather as approximations that serve to guide the interpretations of qMRI values in terms of the most likely underlying biological contributors to those values.

3.2.5 Thickness estimation

We calculated local structure thickness based on a medial skeleton representation: for each structure, we estimated the skeleton as the ridge equidistant to the structure boundaries. Thickness was defined as twice the distance between the skeleton

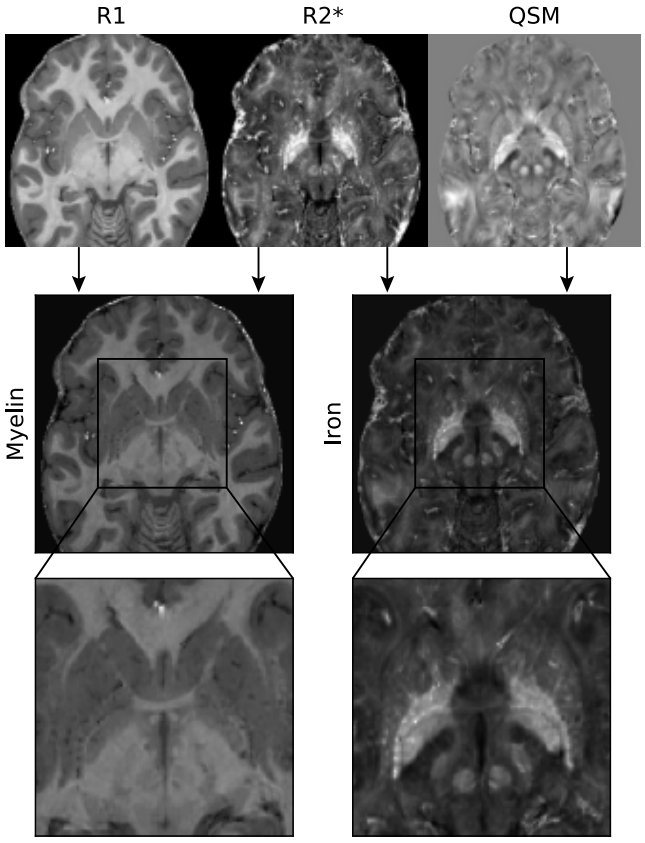

Figure 3.3: Example of myelin (left) and iron map (right) of a representative participant. The top row shows the R1, R2*, and QSM maps, which were linearly combined into myelin and iron maps (middle and bottom row) using the winning models detailed in Table 3.1. Note the hyperintense appearance of iron rich structures such as the rounded shape of the red nucleus.

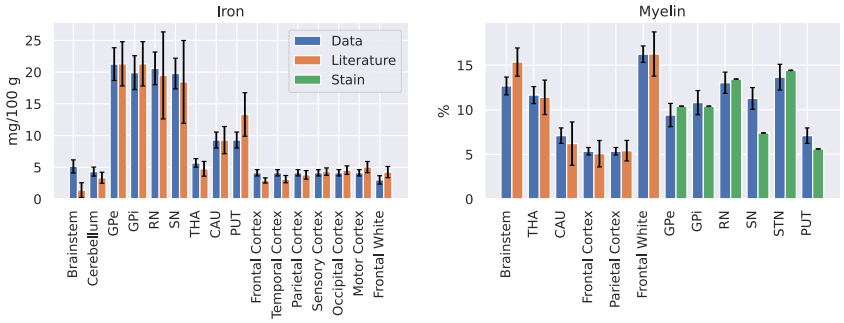

Figure 3.4: Comparison between qMRI-derived iron (left) and myelin (right) values in our data and values reported in the literature. For myelin, we also compare the qMRI-derived estimates to the estimates in the *post mortem* tissue. Error bars indicate standard deviations. No error bars are present for the bars representing *post mortem* tissue, as these come from a single brain.

and the closest boundary, using the method described in Bazin et al. (2020). In other words, local thickness measures at every location inside the structure the distance between the two closest boundaries of that structure, extending the concept of cortical thickness to more complex shapes. Contrary to volume, thickness can be determined at the position of each voxel within a structure, thus providing local information. A similar thickness measure was also used in Ho et al. (2020) to detect subtle shape differences.

3.2.6 Center of mass

For all structures, we calculated the center of masses in Cartesian x, y, and z coordinates per participant after an affine transformation to group space by aligning each subject to the MNI template with ANTs (Avants et al., 2008) using mutual information. The affine transformation was necessary to define a common space in which to compare structure location between subjects. It was preferred over a rigid or a non-linear transformation in order to correct for inter-individual differences in intracranial volume and neurocranium shape, while retaining inter-individual variability in anatomy relative to the neurocranium.

3.2.7 Age-related change modeling

We describe the age-related changes in iron concentration, myelin content, volume, and thickness, as well as in the center of mass in x, y and z coordinates. For iron, myelin and thickness, we report both a median reflecting the central tendency and interquartile range reflecting structure homogeneity. For thickness, the interquartile range reflects the within-structure variability of thickness, quantifying the regularity of the shape. We also analyzed the R1, $R2^*$, and QSM values, which can be found in the online app (`https://subcortex.eu/app`).

Exploratory modeling of the between-hemisphere differences per structure suggested no between-hemisphere difference in aging patterns for most structures. Therefore, we subsequently assumed that the age-related changes in each structure were the same in both hemispheres, to reduce the total number of models fitted. We collapsed across hemispheres by taking the mean value across both hemispheres per structure and participant.

Prior to fitting the aging models, we excluded outliers based on their Mahalanobis distance (cut-off 10.827, corresponding to $p < 0.001$, 0.69% of all data points). Per ROI and dependent variable, we then fit the following set of 24 potential models, with all possible combinations of the following predictors: A linear influence of age, a quadratic influence of age, sex, an interaction between age

and sex, and an interaction between a quadratic influence of age and sex. We excluded models with both interaction terms, as this would imply implausibly large between-sex differences in aging patterns.

Models were fit with OLS as implemented in statsmodels (Seabold and Perktold, 2010) for the Python programming language. Models were compared with the Bayesian Information Criterion (BIC; Schwarz, 1978), which quantifies the quality of fit penalized for model complexity. Lower BIC values indicate more parsimonious trade-offs between quality of fit and model complexity and are preferred. Based on the winning model, we removed influential data points using Cook's distance (cut-off 0.2, 0.18% of all data points; we used a more conservative cut-off than $4/n$, which is sometimes recommended [Rawlings et al., 1998]). We then refitted all models on the data excluding the influential data points, and performed a new model comparison.

Using the winning age-related change models, we quantified the total age-related change. Figure 5 illustrates the procedure to estimate this value, which involves taking the first derivative of the winning model (which quantifies the mean amount of change on every year), then taking the absolute (which quantifies the amount of change, irrespective of the direction of change), and then integrating over the age range of 19 to 75 years old. By integrating over the absolute derivative, age-related decreases and increases in a metric do not cancel out, but both count as 'change' and sum up across the range of the adult lifespan. To retain the mean direction of change in the metric, we took the negative of the total age-related change when the model's predicted value at 75 was lower than at 19.

The age range under consideration was limited to 75 because our data contains only one data point older than 75. Extrapolation of fitted regression models to beyond the range of the original data can lead to biases (e.g., Hahn, 1977), and since our data only contains one data point older than 75, we deemed it more conservative to restrict our inferences to the maximum of 75 years old. For winning models that included sex (or interactions between age and sex) as a predictor, the total age-related changes were calculated for both sexes separately and then averaged. Finally, we divided the total age-related change by the model's predicted value at 19 years old, in order to quantify the total age-related change relative to a baseline value.

3.2.8 Confidence intervals and standard errors

Confidence intervals in Figure 3.6 were obtained using a bootstrapping procedure with 10,000 iterations. We iteratively sampled 105 random observations with

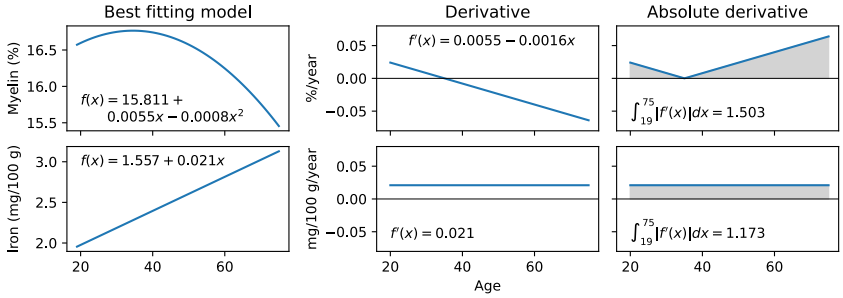

Figure 3.5: Procedure of estimating total amount of change across the adult lifespan. The left column shows two example models: One inverted U-shape (median myelin change in the internal capsule), and one linear increase (median iron change in the amygdala). Formally, change across ages is given by the first derivative (middle column). To collapse over the direction of change (increase or decrease), we took the absolute of the derivative (right column). The sum of this absolute derivative (illustrated by the gray area under the curve) represents the total amount of change in a region. As a final step (not illustrated), the sum of the absolute derivative is divided by the model prediction at 19 years old, which represents the total amount of change relative to the baseline value.

replacement from the data, based on which we estimated the median, and took the 2.5th and 97.5th percentile of the 10,000 medians as the 95% confidence interval. The standard errors in Figure B.4 were obtained using a similar bootstrapping procedure, in which winning model specifications were iteratively fit on 10,000 random samples (drawn with replacement) from the data. Per iteration, the total age-related change metrics were estimated. The standard deviation of the total age-related change metrics across iterations was used as an estimator of the standard error. For winning models that do not include age as a predictor variable, the standard error is 0 since the total age-related change metric is 0 in each iteration.

3.3 Results

One hundred and five healthy volunteers were scanned using an ultra-high field 7 Tesla MRI scanner as part of the openly available Amsterdam ultra-high field adult lifespan database project (AHEAD; Alkemade et al., 2020a). A quantitative, multi-modal MP2RAGE-ME sequence (Caan et al., 2019) with 0.7 mm isotropic resolution was used to simultaneously estimate R1, R2* and quantified susceptibility mapping (QSM) values in a single scanning sequence. For each participant, 17 subcortical structures and ventricles (see Table 3.2) were delineated using the Multi-contrast Anatomical Subcortical Structures Parcellation method (MASSP; Bazin et al., 2020).

Table 3.2: Regions of interest. Midline structures were parcellated as a single structure, all other structures (indicated by bold-faced letters) were parcellated separately per hemisphere. Abbreviations in italics indicate white matter structures.

AMG: Amygdala	**SN**: Substantia nigra
CL: Claustrum	**STN**: Subthalamic nucleus
fx: Fornix	**STR**: Striatum
GPe: Globus Pallidus Externa	**THA**: Thalamus
GPi: Globus Pallidus Interna	**VTA**: Ventral Tegmental Area
ic: Internal Capsule	**LV**: Lateral ventricle
PAG: Periaqueductal gray	3V: Third ventricle
PPN: Pedunculopontine nucleus	4V: Fourth ventricle
RN: Red nucleus	

We analyzed each structure by first estimating the iron and myelin concentrations, using simplified biophysical models that translate the measured R1, $R2^*$, and QSM values into the most likely corresponding iron and myelin concentrations (see Methods). Note that these concentrations are approximations and do not reflect measured myelin and iron concentrations (see Limitations section). We obtained both the (within-structure) median of iron and myelin distributions, and the interquartile range (IQR) which reflects image noise and tissue (in)homogeneity. Second, we analyzed the structure morphometry by estimating volume and thickness. Thickness is defined as twice the distance between the boundary and the internal skeleton of the structure. As a local measure (contrary to volume), it is defined for every voxel in a structure, and it depends on the structure's shape. Also for thickness, we determined both the median and IQR, the latter reflecting the regularity of the structure's shape: Regularly shaped structures (e.g., the red nucleus) have a similar thickness at each voxel's location, resulting in lower between-voxel IQRs compared to complex shaped structures (e.g., the striatum). Third, we determined the location (center of mass in 3 Cartesian coordinates) of each structure. Center of mass was determined after applying an affine transformation to a group template, to account for inter-individual differences in intracranial volume and shape, while retaining inter-individual variability in distances relative to the neurocranium.

The distributions of iron, myelin, and volumes revealed a large between-structure heterogeneity in the human subcortex (Figure 3.6). The globus pallidus externa and interna, red nucleus, substantia nigra, and subthalamic nucleus displayed the highest iron concentrations (both median and IQR), corroborating

earlier reports (Haacke et al., 2005; Hallgren and Sourander, 1958; Ramos et al., 2014). In line with expectations, low iron concentrations in combination with high myelin concentrations were observed in the white matter structures under study: the internal capsule and the fornix. The estimated myelin concentrations of the subthalamic nucleus, red nucleus, and ventral tegmental area were relatively high, which causes the limited visibility of these structures on T1-weighted images (Keuken et al., 2018). For comparison, the estimated myelin concentrations of the striatum and amygdala were substantially lower, resulting in intensities comparable to cortical gray matter on T1-weighted images.

The within-structure IQR of iron scaled with the median estimates. This was the case across participants in all individual structures except for the left claustrum and left periaqueductal gray (lowest significant Pearson's correlation coefficient = 0.206 in the right claustrum; highest correlation coefficient = 0.876 in left striatum; all significant after correction for the false discovery rate at $q < 0.05$), as well as for the median and IQR of iron across structures ($r = 0.827$, $t(26) = 7.35$, $p < 0.001$).

Across subjects, the IQR of myelin decreased with increasing median myelin concentrations for all regions except the left pedunculopontine nucleus, right substantia nigra, left amygdala, both claustrums, right internal capsule, and fornix (significant correlation coefficients varied between -0.2183 for the left VTA and -0.58 for the right periaqueductal gray; all significant after correction for the false discovery rate at $q < 0.05$). Across regions, however, no correlation was observed between the median and IQR of myelin. The fornix had a particularly high IQR of myelin. This could potentially have been caused by partial voluming with the lateral ventricles, decreasing the myelin estimates at voxels near the boundary of the fornix.

3.3.1 Maturation effects

We next studied the age-related alterations in iron, myelin, and morphometry across the adult lifespan. We fit a set of 24 regression model specifications (with, as predictor variables, linear and/or quadratic effects of age, plus sex and potential interactions between sex and age) for all structures and measures individually. As we had no *a priori* hypothesis on lateralization, we collapsed across hemispheres to reduce the total number of fitted models. The model specification that showed the most parsimonious trade-off between quality of fit and model complexity (as quantified using the Bayesian information criterion; Schwarz, 1978) was considered the winning model and used for further analyses. To help navigate the winning models of each structure and measure (including R1, $R2^*$, and QSM values), we devel-

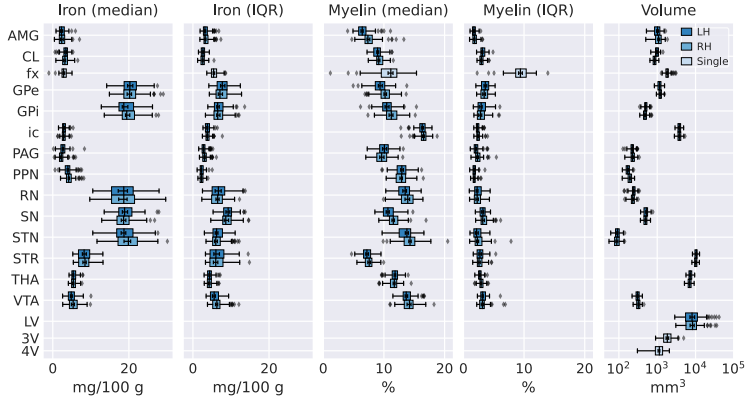

Figure 3.6: Across-participant distributions of within-structure median and IQR of iron and myelin, and volumes per structure. The center line in each box marks the median, box limits are the across-participant IQR, and whiskers are at 1.5 times the IQR below and above the box limits. Error bars drawn inside boxes indicate 95% confidence intervals around the median, obtained by bootstrapping with 10,000 iterations. Colors indicate hemisphere (LH = left hemisphere, RH = right hemisphere, Single = structures that are continuous across the hemispheres), mg/100 g = mg iron per 100 g fresh tissue, mm = millimeter.

oped an online interactive app, which is accessible at `https://subcortex.eu/app` (see also Figure B.3). Next to in the online app, all winning models (including the parameterization) can also be found in Figures B.5—B.11.

We observed (median) iron accumulation in all structures except for the claustrum, globus pallidus interna, and periaqueductal gray, which instead showed stable iron concentrations (Figure 3.7). With the exception of the globus pallidus interna, the iron-rich basal ganglia appeared to accumulate most iron during aging in absolute terms. The IQRs increased with age for all structures, revealing a global decrease in structure homogeneity. Since this decrease in homogeneity was also present in the structures where no median iron increase was observed, it likely partially reflects an increase in image noise. However, the increases in IQR were higher in the structures that accumulate most iron (correlation between median and IQR iron increases across structure $r = 0.598$, $t(12) = 2.584$, $p = 0.024$, two-sided), suggesting that the (median) iron accumulation for these structures was not homogeneously distributed within the structure. This decrease in homogeneity was particularly strong in striatum and the red nucleus.

In line with expectations, we observed a general myelin degradation (see Figure 3.8), except for in the amygdala, claustrum, and substantia nigra, where no alterations in myelin concentrations were detected. The largest (absolute) reduction of myelin was present in the fornix; the other white matter structure, internal capsule,

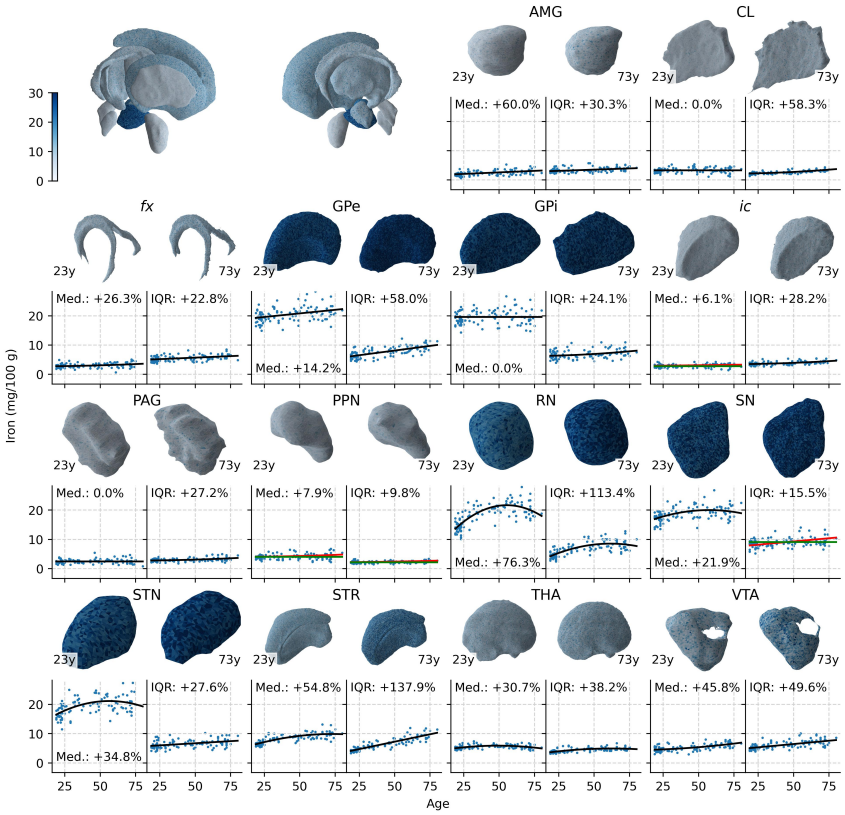

Figure 3.7: Age-related changes in iron content. The meshes are based on the young (18–30 years old, mean 23; left) and elderly (70–80 years old, mean 73; right) participants after a non-linear transformation to MNI2009b space. Mesh colors illustrate the model predictions for the median and IQR of iron distributions at 23 (left) and 73 (right) years old, corresponding to the mean ages of the participant groups on which the meshes were based. Colors in the top-left meshes of all structures indicate model predictions at 23 years old. In case the winning model did not include sex as a predictor variable, the model predictions are shown in black lines; otherwise, green and orange lines are used for the predictions for women and men, respectively. The total amount of change in median (Med.) and IQR are shown in each scatterplot. The ventricles are assumed to have no iron and are excluded from this graph.

showed a smaller decrease in myelin. The globus pallidus interna, periaqueductal gray, pedunculopontine nucleus, substantia nigra, and ventral tegmental area showed slightly higher median myelin concentrations in females than in males. Like in the case of iron, the increases in IQR of myelin reflected a trend of decreasing structure homogeneity across structures. Since these IQR increases were present for structures that did not show any change in median myelin content, they likely partially reflect increases in image noise.

Next, we analyzed the effects of atrophy (Figure 3.9). The lateral and third ventricle showed a substantial volume increase with age, which can at least partially be explained by the filling of the intracranial space created by atrophied brain tissue. Contrary to expectations, the volume of the fourth ventricle decreased rather than increased. Inspection of the mesh of the fourth ventricle in the elderly suggests this may be caused by shrinkage of the superior part. Volume decreases were also found in the striatum, thalamus, amygdala, ventral tegmental area, periaqueductal gray, pedunculopontine nucleus, and red nucleus, likely reflecting atrophy. The internal capsule, fornix and globus pallidus interna showed a small increase in volume with age, suggesting white matter swelling, which could be caused by neuroinflammatory processes.

Atrophy of specific subparts of a structure, as a result of increased vulnerability to atrophy in that part, could result in shape changes (Ho et al., 2020; Raznahan et al., 2014). Shape changes can be detected by analyzing changes the median and IQR of thickness, which depend on the structure's shape. Specifically, when changes in the median thickness and volume point in the same direction (as is the case in, e.g., the lateral ventricles, striatum), this suggests overall thickening or thinning of a structure. Instead, increases in median thickness combined with decreases in volume can indicate atrophy in a thinner part of the structure, as this would decrease the amount of voxels with relatively low thickness, increasing the median thickness. This specific effect appeared to be present in the ventral tegmental area, pedunculopontine nucleus and periaqueductal gray. Furthermore, increases in IQR indicate decreases in structure regularity, which was observed in the globus pallidus interna, substantia nigra, periaqueductal gray, pedunculopontine nucleus, and red nucleus.

A third potential effect of atrophy is a change in the location of individual structures relative to the neurocranium (Keuken et al., 2017; Keuken et al., 2013; Kitajima et al., 2008): As the brain atrophies, the resulting physical space is filled with CSF, leading to location shifts of other brain structures. For the majority of brain structures under investigation, we observed location shifts in the lateral

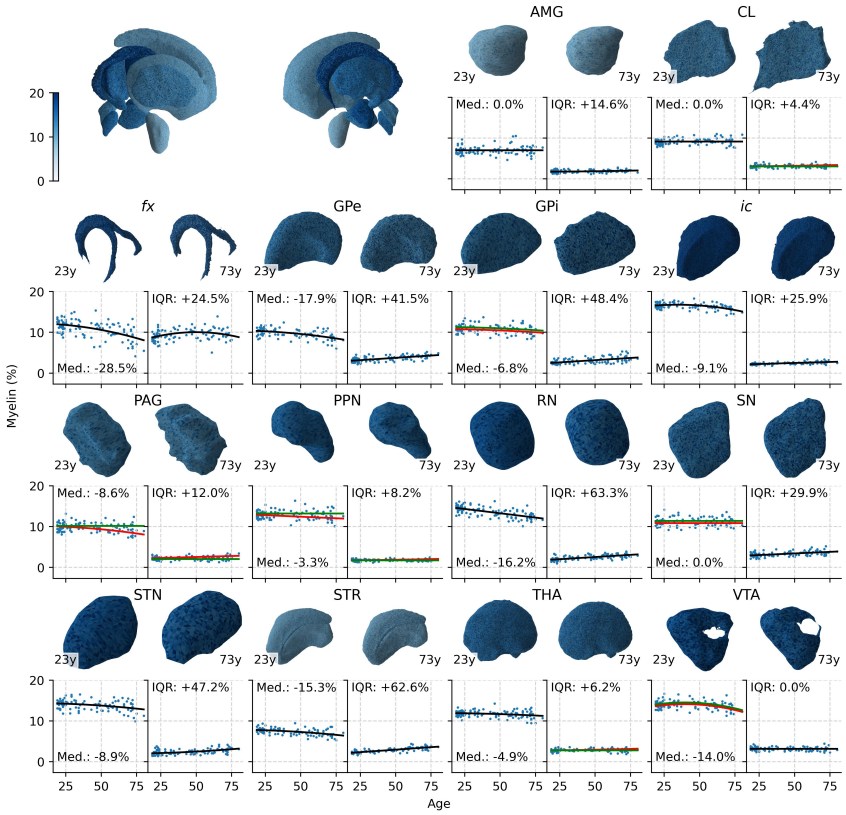

Figure 3.8: Age-related changes in myelin content. The meshes are based on the young (18–30 years old, mean 23; left) and elderly (70–80 years old, mean 73; right) participants after a non-linear transformation to MNI2009b space. Mesh colors illustrate the model predictions for the median and IQR of myelin distributions at 23 (left) and 73 (right) years old, corresponding to the mean ages of the participant groups on which the meshes were based. Colors in the top-left meshes of all structures indicate model predictions at 23 years old. In case the winning model did not include sex as a predictor variable, the model predictions are shown in black lines; otherwise, green and orange lines are used for the predictions for women and men, respectively. The total amount of change in median (Med.) and IQR are shown in each scatterplot. The ventricles are assumed to have no myelin and are excluded from this graph.

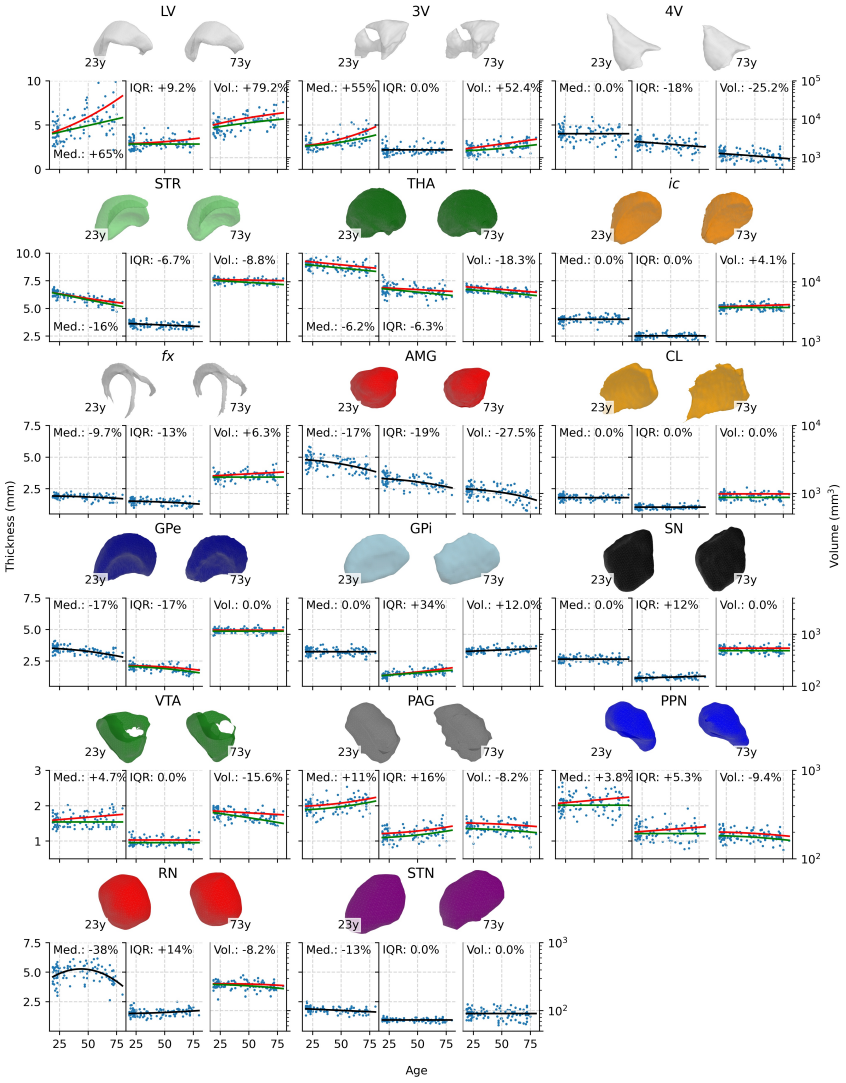

Figure 3.9: Age-related changes in structure morphometry. The meshes are based on the young (18–30 years old, mean 23; left) and elderly (70–80 years old, mean 73; right) participants after a non-linear transformation to MNI2009b space. The lines in each scatterplot visualize the winning model predictions. In case the winning model did not include sex as a predictor variable, the model predictions are shown in black lines; otherwise, green and orange lines are used for the predictions for women and men, respectively. The total amount of change in median (Med.) and IQR of thickness and volume (Vol.) are shown in each scatterplot.

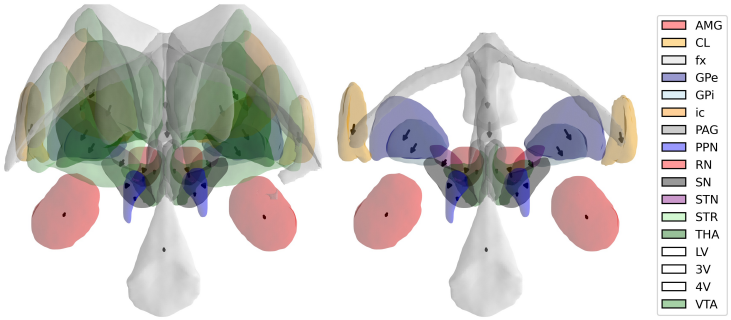

Figure 3.10: Age-related changes in structure location, posterior view. Meshes were based on the young (18–30 years old) participants after non-linearly transforming to MNI2009b space. Arrows depict the model predictions for the location shift, starting at the center of mass of each structure in MNI2009b space, and pointing to the predicted center of mass of the structure at 75 years old. The left graph shows all 17 subcortical structures and ventricles under investigation, the right graph excludes the lateral ventricles, internal capsule, and thalamus, to improve the visibility of the smaller structures.

and inferior direction (Figure 3.10). The center of mass of the lateral and third ventricles and the claustrum also shifted in the posterior direction; the fornix and striatum shifted in anterior direction.

Combined, we observed age-related changes in all measures: iron, myelin, volume, thickness, and location. These effects were in line with the expected effects of iron accumulation, myelin degradation, and atrophy, but there appeared to be strong between-region variability in the degree to which regions change with age, which we focus on in the next section.

3.3.2 Between-structure variability in maturation

Because the winning models of age-related change trajectories included either linear or quadratic influences of age, the parameter estimates of the different models cannot be directly compared. To provide a quantity that summarizes the amount of age-related change (irrespective of the underlying model specification), we calculated the sum of the absolute yearly changes between 19 and 75 years old, relative to the model's predicted value at 19 years old to take into account baseline differences (see Figure 3.5).

For each structure, we then plotted the total age-related change per metric as a radar chart in Figure 3.11, which defines a 'fingerprint' of aging per structure. Formal comparison of these fingerprints by means of a correlation matrix would require more than 7 metrics to achieve sufficient statistical power and assess

significance. Here, we are restricted to qualitative comparisons. These fingerprints suggest strong interregion variability in aging patterns, also within groups of structures that could be grouped on anatomical grounds such as the basal ganglia. However, similarities can be found between various individual structures. For example, the red nucleus and striatum both show strong increases in the IQR of iron and myelin, combined with increases in median iron and decreases in median myelin. Additionally, the aging patterns in the thalamus and ventral tegmental area suggest similarities, with median and IQR iron increases of comparable sizes, and relative stability on the other metrics. Median and IQR increases in iron combined with IQR increases in myelin were found in the substantia nigra and subthalamic nucleus, with the other measures remaining relatively stable. Finally, some structures including the periaqueductal gray, pedunculopontine nucleus, and internal capsule appear to remain relatively stable across all metrics.

3.4 Discussion

Interest in the human subcortex is rapidly growing in cognitive and clinical neuroscience due to the relevance of subcortical regions as (potential) targets for DBS and their role in cognition. Here, we studied 17 subcortical structures and ventricles in terms of their iron and myelin contents, their sizes, as well as the intricate age-related alterations. Our results highlight the heterogeneity in the subcortex, presenting the strong variability in iron, myelin, and morphometry that exists between structures. Furthermore, our results indicate global effects of iron accumulation, myelin degradation, and atrophy in the subcortex across the normal adult lifespan, and strong variability in the extent to which the different structures are affected by each type of age-related change.

To better navigate the rich landscape of subcortical aging, we also share our results in an online app (Figure B.3, `https://subcortex.eu/app`) that can be used to create interactive and intuitive 3D visualizations of the human subcortex across the lifespan and across modalities. It allows for inspection and reuse of the underlying models and data of each individual structure. The app was designed in a flexible way, so that it can be augmented with more structures and contrasts to expand it to a comprehensive chart of the human subcortex. The underlying data can readily be downloaded for further analyses.

Understanding the aging processes in the subcortex is paramount in research and in clinical practice. While iron accumulation and myelin degradation are part of normal aging processes, increased accumulation and myelin degradation are part of multiple neurodegenerative disorders including Parkinson's and Hunting-

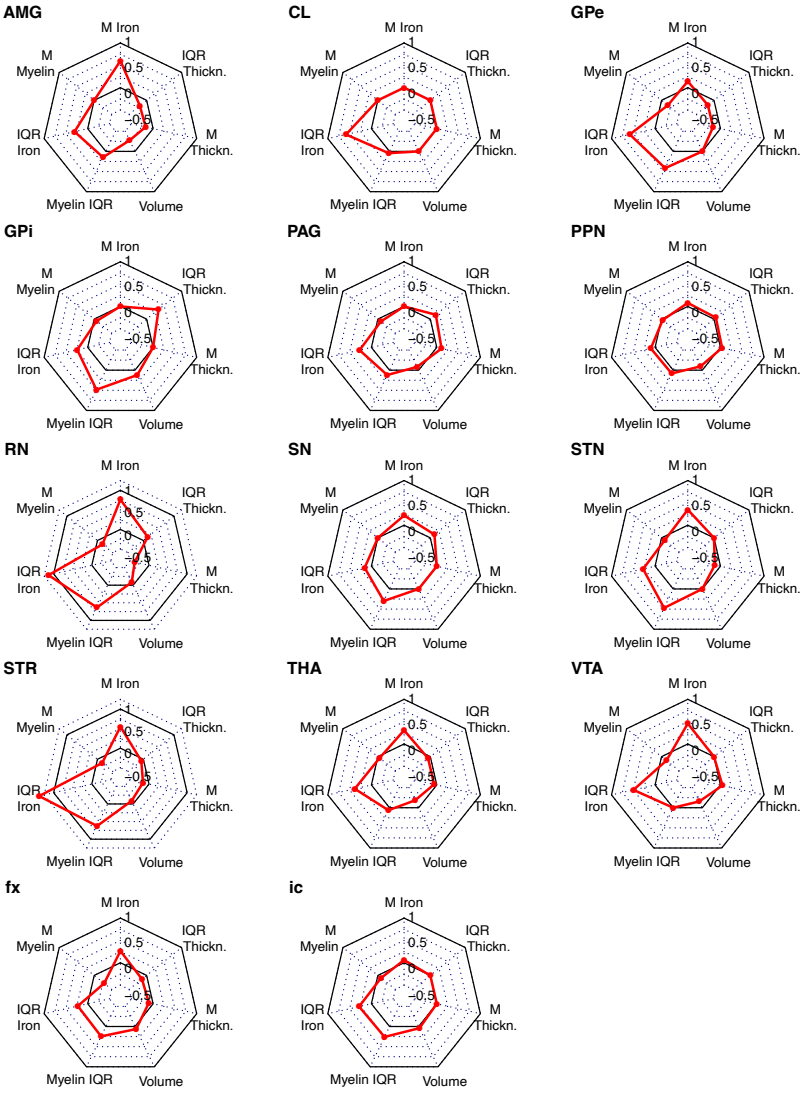

Figure 3.11: Radar charts quantifying the total amount of age-related change (relative to the baseline value at 19 years old) along the seven metrics (radial axes), for each region separately. Each axis runs from -0.5 to 1, which correspond to total amounts of change equal to 50% in negative direction and 100% in positive direction, respectively. The axes for the red nucleus and striatum run to 1.25 to accommodate the large amounts of change in the IQR of iron in these regions. Solid lines indicate 0 (no change) and 1. Red dots indicate the measured amount of change.

ton's disease (Andersen et al., 2014; Collingwood and Davidson, 2014; Ward et al., 2014; Zecca et al., 2004). An accurate description of the distributions of iron and myelin across the lifespan in health provides a frame of reference against which pathological iron accumulation and myelin degradation can be contrasted, and can prove useful in the development of biomarkers for disease (Guan et al., 2017; Mancini et al., 2020; Martin et al., 2008; Schenck and Zimmerman, 2004; Zecca et al., 2004).

Iron and myelin are also the two main determinants of MRI contrast. Many subcortical structures, such as the subthalamic nucleus, cannot readily be distinguished on conventional T1-weighted MRI images due to a lack of contrast with nearby regions. Because of the limited visibility of subcortical structures on conventional MR images, a common practice is to use atlases to locate individual structures (Devlin and Poldrack, 2007; Evans et al., 2012). Stereotactic atlases based on *post mortem* tissue are often used for planning DBS surgery, and probabilistic MRI atlases are conventionally used in cognitive neuroscientific research. Subcortical MRI atlases are growing in numbers (Keuken et al., 2014; Lau et al., 2020; Pauli et al., 2018; Trutti et al., 2021; Ye et al., 2021) due to improvements in MRI resolution and contrasts. However, MRI atlases are typically developed using anatomical images obtained from young participants, which can cause biases when such atlases are subsequently used to infer anatomical information in older participants or patient populations (Evans et al., 2012; Keuken et al., 2013; Samanez-Larkin and D'Esposito, 2008). In cognitive neuroscience research, it is common to apply spatial normalization procedures to a group space to account for individual differences in anatomy, but consistent deviations from the group template are likely to introduce normalization errors (Samanez-Larkin and D'Esposito, 2008). These biases can result from iron accumulation and myelin degradation (which change the contrast of images) and from atrophy (which change the size and the location of structures). Our results can help understand the biases that could occur when conventional MRI atlases, based on young participants, are used to analyze data from older participants, and call for the development of age-specific MRI atlases of the subcortex to remedy these biases.

The between-region variation in iron contents has important consequences for blood oxygenation level dependent (BOLD) functional MRI. Because iron decreases $T2^*$ relaxation times, on which contrast-to-noise ratios (CNR) of BOLD-fMRI sequences depend, BOLD CNR varies substantially between regions. For instance, within young participants, the CNR in the red nucleus is expected to be 74% lower than in the amygdala, when using an echo time of 42 ms at 7 T

(corresponding to the $T2^*$ of the amygdala in young participants), solely due to the differences in $T2^*$ (see supplement for details). Age-related alterations in iron contents can have similar effects. For instance, the CNR in the red nucleus at 50 years old is 32% lower than at 19 years old when using an echo time of 18 ms at 7 T (corresponding to the $T2^*$ of the red nucleus at 19 years old). Thus, iron deposition can confound fMRI studies into age-related changes of BOLD responses.

However, substantial gains in CNR can be achieved by optimizing the echo time to meet the specific requirements of studying a structure of interest (see also Hollander et al., 2017; Miletić et al., 2020). For instance, when targeting the red nucleus, decreasing the echo time to 18 ms (corresponding to the $T2^*$ of the red nucleus at 19 years old) is expected to lead to a 62% higher CNR compared to an echo time of 42 ms (which would be optimal to target the amygdala). Similarly, the echo time can be adjusted to partially mitigate the effects of age-related changes in $T2^*$: By decreasing the echo time from 18 ms to 13 ms (corresponding to the $T2^*$ of the red nucleus at 50 years old), a modest 6% increase in CNR can be expected. Using our online app as a resource for participant-specific predictions of R1, $R2^*$, and QSM values, we envision the use of MRI protocols tailored to the structure of interest and the participant's age and sex.

3.4.1 Comparison with previous aging studies

The majority of previous subcortical aging studies focused on volume metrics. Direct comparison with other studies is hindered by differences in anatomical region definitions (e.g., striatum versus putamen and caudate, entire pallidum versus internal and external segments), delineation methods, modeling approaches (parametric versus non-parametric), and differences in age ranges (see also Coupé et al., 2017; Walhovd et al., 2016), although our results fall in line with previous reports.

The thalamus and striatum are studied most often and have consistently been reported to decrease in volume across the adult lifespan. Studies differ, however, in the shape of the reported trajectories: Some suggest quadratic or cubic volume decreases in both thalamus (Coupé et al., 2017; Dima et al., 2021; Potvin et al., 2016; Tullo et al., 2019; Wang et al., 2019) and striatum (Coupé et al., 2017; Potvin et al., 2016; Tullo et al., 2019), others show linearity or suggest approximate linearity (Fjell et al., 2013; Sullivan et al., 2004; Walhovd et al., 2011; Wang et al., 2019). In concordance with the latter reports, our data suggest linear volume decreases, although we cannot rule out that small non-linear trends are present that we could not detect with our sample size.

Other subcortical structures previously studied include the globus pallidus, for which linear and quadratic volume decreases have been reported (Coupé et al., 2017; Fjell et al., 2013; Goodro et al., 2012; Tullo et al., 2019; Walhovd et al., 2011; Wang et al., 2019), although not consistently: Other studies have reported stable volumes across age (Inano et al., 2013; Jernigan et al., 2001). Our data suggested a stable volume in the external part of the globus pallidus, but we found a volume increase in the internal part (c.f. Keuken et al., 2017, who found volume increases in the external part). In the amygdala, we found quadratic volume decreases. Recent large-sample studies (Coupé et al., 2017; Dima et al., 2021) suggest that the amygdala volume remains stable between approximately 20–70 years old, and then declines. This implies that the maturation pattern strongly depends on the age range studied, which could explain the discrepancies in results from earlier studies that reported stable volumes (Jernigan et al., 2001), and linear (Narvacan et al., 2017; Walhovd et al., 2011; Wang et al., 2019) and quadratic (Goodro et al., 2012; Inano et al., 2013) volume decreases.

Volume increases in the lateral ventricles have been shown to be quadratic previously (Inano et al., 2013; Walhovd et al., 2005; Walhovd et al., 2011; see also Goodro et al., 2012). While our thickness estimates indeed suggest quadratic increases, the volume estimates instead indicate linear increases. Earlier reports on volume changes in the fourth ventricle are not consistent: Some studies have reported volume increases (Walhovd et al., 2005) or stable volumes in the fourth ventricle (Inano et al., 2013; Keuken et al., 2017; Walhovd et al., 2011). Here, we found a volume decrease in the fourth ventricle.

While our method of estimating iron contents has not been used to study aging before, our results can be compared to studies focusing on (q)MRI markers of iron. Daugherty and Raz (2013) provided a meta-analysis of early (q)MRI studies on iron accumulation in the caudate, red nucleus, and substantia nigra, and concluded that iron accumulates in these regions. The underlying studies used R2(*), the field-dependent increase in R2, and phase information based on susceptibility weighted imaging (SWI) as markers for iron. Later studies employing QSM and T2*/R2* are generally consistent with these findings (Acosta-Cabronero et al., 2016; Betts et al., 2016; Callaghan et al., 2014; Keuken et al., 2017; Li et al., 2021; Zhang et al., 2018; but see Khattar et al., 2021, who report no change in these areas). In line with these reports, our results suggest iron accumulation in these regions, specifically in inverted U-shaped trajectories.

Studies on iron accumulation in other subcortical regions have varying and sometimes conflicting conclusions. Daugherty and Raz (2013) also suggested iron

accumulation in the globus pallidus. Our data found linear iron accumulation in the external, but no change in the internal segment. In contrast, Keuken et al. (2017) reported no change in T2* or QSM for the external segment (potentially indicating stable iron concentrations). They did report a T2* increase (which could indicate iron decreases) and stable QSM in the internal segment. Khattar et al. (2021) showed no change the SWI phase in the (entire) globus pallidus, in line with the findings from Li et al. (2021) who studied QSM as an iron marker. Our results suggest linear iron accumulation in the amygdala as well. Based on QSM, Acosta-Cabronero et al. (2016) instead reported stable iron contents in the amygdala (similar to Zhang et al. (2018), although the difference in age ranges under study hinders direct comparison). Finally, we also found inverted U-shaped iron trajectories in the thalamus. Khattar et al. (2021) found decreasing SWI phase in thalamus (suggesting iron increases), but Li et al. (2021) showed decreasing QSM values in the thalamus which instead suggests iron decreases.

Most earlier studies focusing on age-related change in myelin used the ratio of T1w/T2w as a myelin marker, which is controversial (Arshad et al., 2016; Glasser and Van Essen, 2011; Grydeland et al., 2019; Uddin et al., 2018; Uddin et al., 2019). Inverted U-shape trajectories of T1w/T2w have been reported in both cortex (Grydeland et al., 2019), and in the striatum and pallidum (Tullo et al., 2019). Our data instead suggest quadratic but monotonic decreases in myelination in these areas. Other microstructure markers include DTI-derived metrics such as fractional anisotropy and mean diffusivity, which suggested linear declines in microstructure of the thalamus, putamen, and caudate (Cherubini et al., 2009; Wang et al., 2010). Similarly, Callaghan et al. (2014) used magnetization transfer as a microstructure marker in the thalamus and caudate, which also suggested linear declines. Our results for the white matter tracts showed demyelination in fornix and the internal capsule, the pattern of which is qualitatively in line with earlier studies (Lebel et al., 2012; Madden et al., 2012) that analyzed DTI measures in white matter tracts.

More recently, myelin-water fraction (MWF; MacKay et al., 1994) estimation is gaining popularity as a proxy for myelin. Arshad et al. (2016) demonstrated that MWF in the internal capsule shows an inverted U-shaped age-related change trajectory, which shows qualitative similarity to our results in the internal capsule. Finally, Khattar et al. (2021) used MWF to analyze subcortical nuclei, which suggested inverted U-shaped aging trajectories across many subcortical regions, even for those where our results suggested stable myelin contents or monotonically decreasing trends.

3.4.2 Limitations

The present study has several limitations. A first limitation is the estimation of iron and myelin, which was done using simplified biophysical models that translate qMRI contrast values into the most likely underlying iron and myelin concentrations. The basic assumption underlying these models is that qMRI values are linearly related to iron and myelin concentrations. This is supported by previous studies (Mangeat et al., 2015; Marques et al., 2017; Metere and Möller, 2018; Rooney et al., 2007; Stüber et al., 2014).

Stüber et al. (2014) fit the parameters of their linear models using the iron, myelin concentrations and qMRI values in a single *post mortem* specimen, across many voxels. Metere and Möller (2018) generalized this approach by fitting the linear models on population-average myelin, iron concentrations and qMRI values, across many regions. The literature on the population-average iron and myelin concentrations, however, is sparse, especially in the case of myelin. This sparsity required us to estimate myelin contents of several subcortical regions using a *post mortem* specimen, which in turn required additional simplifying assumptions. The lack of a well-established, quantified 'ground truth' of myelin concentrations across the human brain is a limitation not only for the accuracy of the estimated calibration curve, but also prevents us from validating our results directly against it.

Our myelin estimates can be validated indirectly by qualitative comparison with observations from earlier reports that rely on other methods. While there is currently no exact qMRI marker of myelin, the aforementioned MWF estimation (MacKay et al., 1994) has been shown to be a relatively accurate method (Mancini et al., 2020). Khattar et al. (2021) reported MWF estimates in subcortical regions, and consistent with our results, their data suggest that myelin concentrations in subcortical gray matter regions may exceed myelin concentrations of cortical gray matter. Similarly, comparison with histology suggests that optical densities of myelin stains in deep gray matter regions such as the thalamus and globus pallidus are higher than cortical gray matter (e.g., Hametner et al., 2018).

Despite their limitations, our estimates of iron and myelin —compared to qMRI values— offers a distinct advantage in terms of interpretation. Multiple previous studies (reviewed above) into age-related changes aim to infer changes in iron concentrations by relying on a single (q)MRI metric such R2* or QSM, but R2* (Li et al., 2009) and QSM (e.g., Hametner et al., 2018; Liu et al., 2015) have been shown to also correlate with myelin concentrations (see also Daugherty and Raz, 2015).

Similarly, there currently exists no perfect method to estimate myelin contents in vivo (Mancini et al., 2020), and while R1 covaries with myelin, studies suggest that it also covaries with iron (Ogg and Steen, 1998; Rooney et al., 2007; Stüber et al., 2014; but see Steen et al., 2000). As such, disentangling the contributions of iron and myelin to qMRI contrasts requires simultaneously consideration of multiple qMRI contrasts at once. Future studies that quantify iron and myelin concentrations across the brain, for example using systematic chemical assays or advanced microscopy (e.g. Brammerloh et al., 2021) on post mortem materials, can provide key information to validate and further improve upon our modelsFinally, qMRI measurements are also prone to biases, for instance B1 inhomogeneities in R1 mapping (Haast et al., 2016), which are recalibrated when transforming qMRI values to myelin and iron estimates.

A second limitation is that the number of structures included in these studies is still limited. We intend to expand the number of structures in our future efforts. The hippocampus is of particular interest in the context of aging due to its well-known atrophy associated with cognitive decline and neurodegenerative disease (Bettio et al., 2017). However, given its cortical origin, the hippo-campus has not been prioritized in this research and at present cannot be delineated by the MASSP algorithm. Since gold standard manual delineations have not been performed on the present data, we are currently unable to confirm the reliability of other algorithms for hippocampal delineation on our specific data. We intend to incorporate the hippocampus in MASSP in a future study.

Third, we cannot exclude age-related changes in parcellation accuracy. This is a general problem with aging studies, as parcellation accuracy tends to decrease with age due to decreased contrast between structures, even when structures are delineated manually. We relied on the MASSP algorithm (Bazin et al., 2020) to parcellate the 17 subcortical regions and ventricles in each participant individually. The performance of MASSP, like manual delineations, varies per structure, and depends on structure size and contrast (Alkemade et al., 2021). Compared to manual delineations, the performance of MASSP also tends to decrease with age. Fortunately, the impact of age-related biases in parcellation was shown to be limited for the quantitative MRI measures (Bazin et al., 2020) on which the iron and myelin estimates are based, suggesting that the age-related changes in myelin and iron are unlikely to be caused by age-related differences in parcellation performance. On the other hand, size estimates (volume and to a lesser extent thickness) are more susceptible to the age-related changes in parcellation quality. Here, we used an improved version of MASSP to mitigate these effects and could

observe increased delineation accuracy for ventricles, fornix, claustrum, GPi and VTA (see Figure B.2). However, a replication of the age dependency study of Bazin et al. (2020) using the improved version of MASSP did not show much improvement in the consistency of thickness and volume estimate in smaller structures, where we cannot exclude age-related decreases in parcellation accuracy. While other automated parcellation algorithms incorporate certain structures of interest (such as the hippocampus, see above), we are not aware of any algorithm that can parcellate the same breadth of subcortical regions on qMRI data as MASSP. Future developments of MASSP or other algorithms might improve parcellation accuracy and thereby improve the robustness of models of age-related changes.

Finally, we are limited to descriptions of the age-related changes that result from iron accumulation, myelin degradation, and atrophy. While our results indicate a between-region heterogeneity in the age-related changes, they do not explain why certain regions appear to change more than others with increasing age. Similarly, we did not study the specific relation between qMRI metrics and morphometry (Lorio et al., 2016; Tardif et al., 2017; Weiskopf et al., 2015).

3.4.3 Conclusions

Our results extend previous studies into aging patterns of the subcortex, which focus on a smaller number of typically large subcortical areas, often based on MRI with lower field strengths (Aquino et al., 2009; Cherubini et al., 2009; Daugherty and Raz, 2013; Daugherty and Raz, 2016; Fjell et al., 2013; Greenberg et al., 2008; Herting et al., 2018; Keuken et al., 2017; Khattar et al., 2021; Li et al., 2014; Raz, 2004; Raz et al., 2005; Raz and Rodrigue, 2006; Raznahan et al., 2014; Walhovd et al., 2005; Wang et al., 2019). Experiments using very large numbers of participants detected complex nonlinear age-related changes in some subcortical structures (Coupé et al., 2017; Dima et al., 2021; Fjell et al., 2013). Our study had a more modest sample size, which did not allow to evaluate complex non-linear trends. On the other hand, by leveraging an open database of ultra-high field 7 T quantitative MRI, we could provide a first view on many structures and variables at once, which may be refined as more 7 T quantitative MRI data sets become available. As such, our study provides a richer and more extensible description of subcortical composition, morphometry and aging.

Chapter 4

Cortical and subcortical contributions to interference resolution and inhibition – an fMRI ALE meta-analysis

This chapter is published as:
S. J. S. Isherwood, M. C. Keuken, P.-L. Bazin, and B. U. Forstmann (2021b). Cortical and subcortical contributions to interference resolution and inhibition - An fMRI ALE meta-analysis. *Neuroscience and biobehavioral reviews* 129, pp. 245–260. DOI: 10.1016/J.NEUBIOREV.2021.07.021.

Abstract

Interacting with our environment requires the selection of appropriate responses and the inhibition of others. Such effortful inhibition is achieved by a number of interference resolution and global inhibition processes. This meta-analysis including 57 studies and 73 contrasts revisits the overlap and differences in brain areas supporting interference resolution and global inhibition in cortical and subcortical brain areas. Activation likelihood estimation was used to discern the brain regions subserving each type of cognitive control. Individual contrast analysis revealed a common activation of the bilateral insula and supplementary motor areas. Subtraction analyses demonstrated the voxel-wise differences in recruitment in a number of areas including the precuneus in the interference tasks and the frontal pole and dorsal striatum in the inhibition tasks. Our results display a surprising lack of subcortical involvement within these types of cognitive control, a finding that is likely to reflect a systematic gap in the field of functional neuroimaging.

4.1 Introduction

Cognitive control as a whole describes an array of processes required for optimal and adjustable human behaviour and decision-making (Aron, 2007; Botvinick et al., 2001). Under this umbrella of cognitive control are two associated but inherently distinct mechanisms that aid in supporting the ability of goal-directed behaviour; interference resolution and global inhibition (Nigg, 2000). These concepts have drawn the attention of psychologists since the late 19th century (Bergstrom, 1894), where the terms were initially used interchangeably but due to clinical psychology and neuroscience results it became apparent that these are two related but functionally diverse phenomena (Nee et al., 2007). In general, global inhibition is defined as the global dampening of an already initiated or no longer relevant action (Aron, 2007). Interference resolution is considered a more selective inhibition process, where task-irrelevant stimuli and goal-irrelevant responses must be dampened but relevant responses maintained (Nigg, 2000). In the past, both these types of inhibition processes have been largely studied independently. Global inhibition has commonly been investigated using the Stop-Signal task (Logan and Cowan, 1984) or the Go/No-Go task (Donders, 1969), which overlap in terms of global inhibition but differ with respect to the underlying proactive or reactive mechanism. Interference resolution has been largely studied through the use of the Eriksen-Flanker task (Eriksen and Eriksen, 1974), Stroop task (Stroop, 1935), Simon task (Simon and Rudell, 1967) and multi-source interference task (Bush et al., 2003).

Generally agreed upon theories of the biological architecture underlying these types of cognitive control rest on the involvement of both the cortex and subcortex (Albin et al., 1989; Aron et al., 2016; Nambu et al., 2002; Neumann et al., 2018; Wiecki and Frank, 2013). It has long been hinted that a cortico-striatal loop modulates the capacity of interference resolution (Mink, 1996; Utter and Basso, 2008), and there is evidence that the STN plays a key role in the net-inhibition of inappropriate movements (Beauregard and Lévesque, 2006; Forstmann et al., 2012; Frank, 2006; Keuken and Forstmann, 2015; Wessel et al., 2019). Recent studies have found evidence that the fronto-striatal network supports the ability to selectively inhibit such movements (Schmidt et al., 2018; Schmidt et al., 2020), in line with theories suggesting that the basal ganglia modulate these cortical pathways to some extent (Alexander et al., 1986; Mink, 1996; Utter and Basso, 2008). Another source of evidence for the involvement of subcortical areas in interference resolution and global inhibition comes from intracranial recordings studies. There

is a sizable and growing body of literature showing the involvement of the STN in stopping ongoing action as a result of surprising events as well as mediates post-error slowing in subsequent trials e.g,(Alegre et al., 2013; Bastin et al., 2014; Benis et al., 2014; Brittain et al., 2012; Cavanagh et al., 2014; Fischer et al., 2017; Kelley et al., 2018; Kühn et al., 2004; Ray et al., 2012; Siegert et al., 2014; Wessel et al., 2016a; Wessel et al., 2016b; Zavala et al., 2013; Zavala et al., 2014). Yet, time and time again, these deeper regions are often underrepresented in fMRI studies and as a result the meta-analytical evidence for subcortical involvement in interference resolution is limited e.g., (Chen et al., 2018; Nee et al., 2007). As previous recognized, this appears to be an accidental by-product of imaging techniques and accessibility to more sensitive hardware (Forstmann et al., 2016; Johansen-Berg, 2013; O'Callaghan et al., 2014). Studying the contribution of subcortical nuclei with MRI is inherently more difficult than the cortex simply due their distance to the head coils. Lower field strengths are further disadvantaged due to the lack of penetration and therefore sensitivity here (Collins and Smith, 2001; Vaughan et al., 2001). The picture is further complicated by the need for specific contrasts in order to be able to accurately delineate some of these iron-rich nuclei such as the STN and SN (Kerl et al., 2012; Keuken et al., 2017; Keuken et al., 2018; Shroff et al., 2009). Due to the differences in iron content the subcortex also requires slightly different fMRI acquisition parameters to optimize the BOLD contrast sensitivity e.g., (Hollander et al., 2017; Miletić et al., 2020).

The goal of this meta-analysis is to investigate the overlap and differences in cortical and subcortical contributions to recent fMRI studies of interference resolution and global inhibition. A number of fMRI meta-analysis on the topic of cognitive control have been conducted in the past e.g., (Cieslik et al., 2015; Criaud and Boulinguez, 2013; Gavazzi et al., 2020; Guo et al., 2018; Huang et al., 2020; Hung et al., 2018; Niendam et al., 2012; Rae et al., 2014; Song et al., 2017; Swick et al., 2011; Xu et al., 2016; Zhang et al., 2017). However, as a number of these meta-analysis either included a low number of studies (Eickhoff et al., 2016; Müller et al., 2018), used a software version of gingerALE that was later shown to contain a number of implementation errors (Eickhoff et al., 2017; Garrison et al., 2019), or included studies from the early 90's and early 00's that used 1.5T MRI (Hollander et al., 2017; Krasnow et al., 2003; van der Zwaag et al., 2009). As such it is perhaps not surprising that the meta-analytical evidence for the subcortical involvement is limited.

Here, we set out to compare activation patterns in the tasks used to tap into these two subtypes of cognitive control, with a main focus on subcortical involve-

ment. To that end we employed a fairly strict list of inclusion criteria to facilitate the inclusion of studies for which it was a priori conceivable that they reported subcortical activations with high anatomical precision. Accordingly, we only included studies from the last decade, that employed a high spatial resolution fMRI acquisition protocol on 3T or higher field-strength MRI with little smoothing. To maximize the number of studies given these demanding criteria, we conducted a comprehensive literature search for experiments investigating interference and inhibition tasks and convolved the results using activation likelihood estimation (ALE).

4.2 Materials and Methods

4.2.1 Comprehensive literature search

4.2.1.1 Paradigms included

We included six different paradigms in the meta-analysis that are thought to tap into interference and inhibition mechanisms, namely the Eriksen Flanker, Simon, Stroop, Multi-Source Interference, Go/No-Go and Stop-Signal tasks. The selection of tasks was based on a number of previous meta-analysis focussing on interference and inhibition (Hung et al., 2018; Li et al., 2017; Nee et al., 2007; Song et al., 2017; Swick et al., 2011).

Interference tasks

Eriksen Flanker task: a paradigm in which participants are shown a central target stimulus flanked by a number of adjacent distractors. The participants are instructed to press a button associated with the target stimulus. A trial is congruent if the distractors are identical to the central target stimulus, whereas the trial is incongruent if the distractors differ from the target stimulus.

Simon task: a paradigm in which participants have to respond to a given stimulus with a given button press, irrespective of the location of the stimulus. The trial is congruent if the location of the stimulus is on the same side as the correct response hand, whereas the trial is incongruent if the stimulus is on the contralateral side of the correct response hand.

Stroop task: in the classic Stroop task participants have to read a word while ignoring the font colour. The trial is congruent if the meaning of the word and the font colour are identical, whereas the trial is incongruent if they differ. Since the original paper in 1935 several variants such as the numerical and affective Stroop

task have been developed. We chose not to discard any Stroop variants as we were interested in general inhibition and interference processes.

Multi-source interference task: a paradigm in which different aspects of the Stroop, Eriksen Flanker and Simon tasks are combined. Participants are shown three different items and are instructed to indicate which item differs from the other two by pressing a button. Depending on the relative font size, type of distractor or location of the target relative to the response finger a trial is either congruent or incongruent.

Inhibition tasks

Go/No-Go task: a paradigm in which participants have to respond to a frequent go stimulus while withholding their response to an infrequent no-go stimulus. Due to the frequent nature of the go stimuli, a prepotent response needs to be suppressed during the no-go stimulus.

Stop-Signal task: a paradigm in which participants need to respond to a given stimulus while having to inhibit their response when an infrequent stop signal is subsequently presented.

4.2.1.2 Inclusion criteria

All of the articles found by the query search were read by two raters (SJSI and MCK) and either kept or discarded based on our predetermined inclusion criteria:

1. the study was published in a peer-reviewed English language journal between the 1st of January 2010 and the 4th of May 2020 (date of the query),

2. the study employed fMRI in healthy adults; the results obtained from patients and children (17 years and younger) were excluded. When studies with patients included a healthy control group, the data of these healthy controls were included if the results were reported separately or if the authors provided us with the necessary information upon request,

3. participants engaged in a Eriksen Flanker, go/no-go, multi-source interference, Simon, stop-signal or Stroop task where the following contrasts were reported or provided by the authors on request:

    - Eriksen Flanker: Incongruent $>$ Congruent
    - Go/No-Go: no-go $>$ go
    - Multi-Source interference task: Incongruent $>$ Congruent

- Simon: Incompatible > neutral; Incompatible > Compatible
- Stop-signal task: successful stop > go
- Stroop: Incongruent > neutral; Incongruent > Congruent

For all contrasts, if there was an affective manipulation, we only included the neutral or control trials.

4. the event related fMRI data was acquired at 3 Tesla (T) or above,

5. the fMRI images were acquired whole brain at a resolution of 3mm or lower, where the voxel geometry was isotropic or near-isotropic (e.g. less than 10% deviation along the three edges of the voxel. This means that a voxel size of 2.5x2x5x3.0 is excluded but 2.5x2.5x2.75 is included (Mulder et al., 2019). The voxel size was determined without taking the interslice gap into account.

6. a GLM voxel-based approach was used to statistically analyse the fMRI data while using a maximum Gaussian smoothing kernel of 8mm FWHM. This maximum smoothing kernel is between 2-3 times the maximum size of the voxel and is thought to be a reasonable trade-off between robust statistical group level results and the reduction of anatomical specificity (Mikl et al., 2008; Pajula and Tohka, 2014).

7. the whole-brain activations are reported as 3D coordinates in stereotactic space of Talairach or the Montreal Neurological Institute (MNI),

8. single-subject reports and experiments where the between-group effects relate to handedness, sex and genotype were excluded.

All relevant reviews and meta-analysis that were included in the above search were identified based on their abstract and cross-referenced to identify other potential empirical papers.

4.2.1.3 Search strategy

An exhaustive literature search was conducted using the PyMed and Neurosynth python modules within Python. PyMed is a search tool use for querying the PubMed database. The Neurosynth module queries the Neurosynth fMRI database. The query date for both searches was 4th May 2020. The following keyword terms were used to query the PubMed database using the Entrez query tool from the Bio module in Python: "interference", "interference control", "conflict", "conflict control", "cognitive control", "stroop", "simon", "flanker",

"stop-signal", "stop signal", "stop task", "stop-signal reaction time", "stop signal reaction time", "go/no go", "go no go", "go-no go", "go/nogo", "go/no-go", "go-no-go", "selective inhibition", "global inhibition", "inhibition", "response inhibition", "inhibitory control", "multi source interference task", "msit" and "multi-source interference task". These keywords were coupled with further search terms to limit our results to only fMRI studies: “fmri”, “functional mri” and “functional magnetic resonance imaging”. Due to the co-occurrence search strategy that PubMed uses; we used all combinations of these two search term lists (81 in total) to ensure that we found as many potential articles as possible. For Neurosynth, we queried the database using both their innate feature list and also searching their abstracts using our custom keywords. Since Neurosynth only archives fMRI studies, we only used the first list of terms given above to query the database.

The PubMed query resulted in 26.391 unique abstracts, the Neurosynth query in 1.832 unique abstracts. After removing abstracts that were published before 2010 and abstracts that were found through both database searches, a total of 19.598 unique abstracts were identified. Raters 1 and 2 (SJSI and MCK) read and rated all unique abstracts, with an inter-rater reliability (IRR) score of 0.69, 18.526 articles were excluded based on this. The 410 abstracts that were not agreed upon were rated again by both raters, with an IRR = 0.72, a further 261 abstracts were excluded based on this. During the abstract rating, any review or meta-analysis articles were kept for their references to be cross-referenced with the articles that the raters had decided as being eligible for inclusion. 56 previous reviews or meta-analyses were found, and each rater independently checked 28 each, with 476 unique references found within them (that were not already part of the initial database search). Both raters then read and rated the abstracts of these articles, with an IRR=1.00. Both raters agreed that none of these new abstracts met the inclusion criteria for the study, and therefore were all excluded. This suggests that most, if not all, relevant studies were found in the initial database search. The IRR scores at the three different interrater stages all indicated substantial or higher levels of agreement between the two raters (Landis and Koch, 1977). A factor contributing to the lower IRR at the first stage (IRR = 0.69) was that one of the raters included abstracts using the anti saccade task, whereas the other rater did not. As this task was not part of our predetermined list of inclusion criteria, these abstracts were excluded in the second stage, and contributed to a slightly higher IRR of 0.72.

This process left 755 full-text articles for the raters to assess. Of these, 5 were immediately excluded for being duplicates or written in a non-English language. Each rater took half of the remaining 750 articles each, to evaluate, resulting in 632 exclusions. This left 118 studies to be included in the ALE meta-analysis, based on whether the articles had the required information, or the authors were able to provide the required data necessary for the analysis. After mining the information accessible in the original articles and contacting the authors where required, we included 57 studies and 73 contrasts in the final analysis.

See Figure 4.1 for an overview of the selection and inclusion process and Table 4.1 for a short description of the included studies.

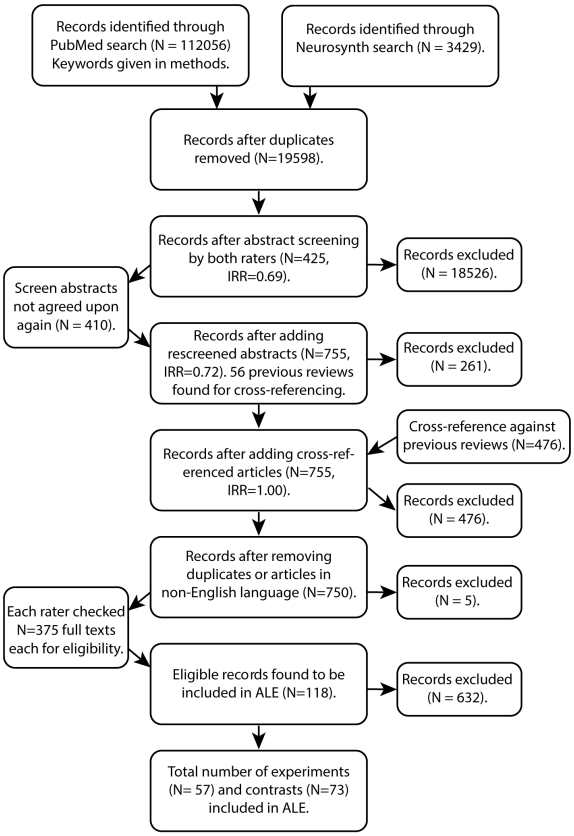

Figure 4.1: The selection procedure for the inclusion of empirical studies. The flow of information illustrates the different steps used in the meta-analysis to identify the relevant empirical studies and is based on the PRISMA flow-diagram (Liberati et al., 2009). In between brackets the number of unique papers (N) and the interrater reliability score (IRR) are shown where relevant.

Table 4.1: A summary of the included studies per domain.

Domain	Task	Authors	Year	Sample size	Gender ratio (f)	Mean Age (SD)	Field strength (T)	FWHM (mm)	Voxel resolution (mm)	Ratio of Salient events
Interference	Flanker	Panagiotaropoulou et al.	2019	30	7	27.8 (7.7)	3	8	3x3x3	50/50
	Flanker	Siemann et al.	2016	19	ns	ns**	3	8	3x3x3	50/50
	Flanker	Voegler et al.	2016	27	9	33.3 (8.2)	3	8	3x3x3	50/50
	Flanker	Won et al.	2019	32	24	66.2 (7.3)	3	4	3x3x3	50/50
	Flanker	Yamamoto et al.	2018	38	15	36.5 (7.1)	3	8	3x3x3	50/50
	MSIT	James et al.	2017	43	26	32 (10)	3	8	3x3x3	50/50
	Simon	Jiang & Egner	2014	29	15	21.3 (ns)	3	8	3x3x3	50/50
	Simon	Kampa et al.	2020	47	30	24.7 (3.1)	3	6	2.5x2.5x2.5	50/50
				99	64	19.2 (0.8)	3	6	2.5x2.5x2.5	50/50
	Simon	Salzer et al.	2018	28	14	24.9 (6.9)	3	5	2.5x2.5x2.5	50/50
	Simon	Sebastian et al.	2013b	49	30	40.0 (17.1)	3	8	3x3x3	50/50
	Simon	Sebastian et al.	2013a	24	15	27.4 (5.6)	3	8	3x3x3	50/50
	Simon	Sebastian et al.	2012	24	13	30.3 (8.1)	3	8	3x3x3	50/50
	Simon	van Eijk et al.	2015	18	18	25.3 (4.5)	3	6	3x3x3	50/50
				25	25	27.0 (5.9)	3	6	3x3x3	50/50
	Stroop	Araneda et al.	2018	16	6	40.9 (12.1)	3	5	2.75x2.75x3	55/45
	Stroop	Basten, Stelzel & Fiebach	2011	46	22	22.3 (2.0)	3	8	3x3x3	50/50
	Stroop	Carmichael et al.	2019	50	37	51.3 (4.4)	3	6	3x3x3	50/50
	Stroop	Chechko et al.	2013	18	13	36 (10.3)	3	8	3x3x3	50/50
	Stroop	Fitzhugh et al.	2019	20	11	23.9 (4.7)	3	6	3x3x3	50/50
	Stroop	Godinez et al.	2016	9	ns	ns**	3	5	3x3x3	50/50
	Stroop	Hinault et al.	2018	22	10	23.8 (4.5)	3	8	3x3x3	50/50
	Stroop	Jiang & Egner	2014	29	15	21.3 (ns)	3	8	3x3x3	50/50
	Stroop	Köhler, Bär & Wagner	2016	45	26	27.5 (7.8)	3	6	2.67x2.67x2.7	50/50
	Stroop	Krebs et al.	2013	20	12	22.5 (4.3)	3	6	3x3x3	33/67

Domain	Task	Authors	Year	Sample size	Gender ratio (f)	Mean Age (SD)	Field strength (T)	FWHM (mm)	Voxel resolution (mm)	Ratio of Salient events
	Stroop	Purmann & Pollmann	2015	18	10	23.7 (3.2)	3	6	3x3x3	50/50
	Stroop	Robertson et al.	2014	16	8	23 (ns)	3	8	2.5x2.5x2.5	50/50
	Stroop	Taylor et al.	2016	16	6	24.2 (4.7)	7	6	2x2x2	25/75
	Stroop	Wagner et al.	2013	34	28	24.1 (6.4)	3	8	2.7x2.7x2.7	50/50
Inhibition	Go/NoGo	Asci et al.	2019	24	16	23.4 (2.8)	3	7	3x3x3	50/50
	Go/NoGo	Brown et al.	2012	20	13	22.5 (2.4)	4.7	8	3x3x3	20/80
	Go/NoGo	Chiu & Egner	2015	24	10	24.4 (4.3)	3	8	3x3x3	50/50
	Go/NoGo	Gonzalez Alam et al.	2018	27	19	20.7 (2.2)	3	5	3x3x3	20/80
	Go/NoGo	Köhler et al.	2018	33	17	26.8 (5.2)	3	4	1.4x1.4x1.4	26/74
	Go/NoGo	Mehren et al.	2019	20	4	29.5 (7.0)	3	8	3x3x3	35/65
	Go/NoGo	Morein-Zamir et al.	2014	21	6	28.6 (7.0)	3	6	3x3x3	13/87
	Go/NoGo	Rodriguez-Nieto et al.	2019	22	0	24.8 (4.8)	3	6	3x3x3	25/75
	Go/NoGo	Rothmayr et al.	2011	12	7	23.7 (ns)	3	8	3x3x3	20/80
	Go/NoGo	Sebastian et al.	2012	24	13	30.3 (8.1)	3	8	3x3x3	29/71
	Go/NoGo	Sebastian et al.	2013b	49	30	40.0 (17.1)	3	8	3x3x3	29/71
	Go/NoGo	Sebastian et al.	2013a	24	15	27.4 (5.6)	3	8	3x3x3	29/71
	Go/NoGo	Rodriguez-Nieto et al.	2019	22	0	24.8 (4.8)	3	6	3x3x3	25/75
				25	25	27.0 (5.9)	3	6	3x3x3	29/71
	Go/NoGo	Yoshida et al.	2013	19	9	22.5 (4.2)	3	8	3x3x3	20/80
	SST	Boehler et al.	2010	15	9	22.9 (ns)	3	8	3x3x3	20/80
	SST	Boehler et al.	2014	16	15	22.8 (ns)	3	8	3x3x3	36/64
	SST	Eijsker et al.	2019	21	17	32.4 (10.0)	3	8	3x3x3	25/75
	SST	Fujimoto et al.	2020	20	10	26.6 (9.2)	3	6	2x2x2	25/75
	SST	Gaillard et al.	2020	38	23	26.6 (7.2)*	3	8	3x3x3	29/71
	SST	Hampshire et al.	2010	14	ns	ns***	3	8	3x3x3	26/74
	SST	Jahfari et al.	2015	23	16	21.6 (1.7)	3	5	3x3x3	30/70
	SST	Kampa et al.	2020	47	30	24.7 (3.1)	3	6	2.5x2.5x2.5	25/75

Domain	Task	Authors	Year	Sample size	Gender ratio (f)	Mean Age (SD)	Field strength (T)	FWHM (mm)	Voxel resolution (mm)	Ratio of Salient events
				99	64	19.2 (0.8)	3	6	2.5x2.5x2.5	25/75
	SST	Lorenz et al.	2015	38	19	47.3 (19.3)	3	7	3x3x3	25/75
	SST	Mohammadi et al.	2015	17	7	53 (ns)	3	5	3x3x3	25/75
	SST	Morein-Zamir et al.	2015	32	14	30.9 (8.1)	3	8	3x3x3	17/83
	SST	Osada et al.	2019	14	7	28.1 (9.9)	3	6	2x2x2	25/75
	SST	Rae et al.	2014	17	5	28 (ns)	3	8	3x3x3	25/75
	SST	Schel et al.	2014	24	13	21.5 (2.4)	3	8	2.75x2.75x2.75	25/75
	SST	Sebastian et al.	2012	24	13	30.3 (8.1)	3	8	3x3x3	25/75
	SST	Sebastian et al.	2016	28	17	26.1 (5.7)	3	8	3x3x3	25/75
	SST	Sebastian et al.	2013b	49	30	40.0 (17.1)	3	8	3x3x3	25/75
	SST	Sebastian et al.	2013a	24	15	27.4 (5.6)	3	8	3x3x3	25/75
	SST	Tabu et al.	2011	13	5	27.5 (5.2)	3	6	3x3x3	25/75
	SST	Tabu et al.	2012	13	2	30.7 (4.1)	3	6	3x3x3	25/75
	SST	van Eijk et al.	2015	18	18	25.3 (4.5)	3	6	3x3x3	25/75
				25	25	27.0 (5.9)	3	6	3x3x3	25/75

4.2.2 Activation likelihood estimation

4.2.2.1 Contrasts

Given the number of studies that we identified, we were able to compute the following main interference and inhibition contrasts (Eickhoff et al., 2016): Incongruent > Congruent (based on 25 studies with 29 experiments, 387 foci and 834 unique subjects) and Stop | NoGo > Go (32 studies with 44 experiments, 945 foci and 865 unique subjects). While there were too few studies per task to warrant a robust comparison between the different tasks, an exploratory comparison was done between the Go/No-Go and Stop-Signal tasks. There were four studies which reported the coordinates in Talairach space and were converted to MNI using the Lancaster transform as implemented in GingerALE (V.3.0.2; (Lancaster et al., 2007)).

4.2.2.2 NiMARE parameters

An activation likelihood estimation (ALE; (Eickhoff et al., 2012; Fonov et al., 2011; Fonov et al., 2009; Turkeltaub et al., 2002; Turkeltaub et al., 2012) meta-analysis was performed using NiMARE (V.0.0.5; (Salo et al., 2020). Modeled activation maps were generated for each experiment by convolving each focus with a Gaussian kernel determined by sample size. For voxels with overlapping kernels, the maximum value was retained. The modeled activation maps were rendered in MNI 152 space (Fonov et al., 2011; Fonov et al., 2009) at 2x2x2mm resolution. A map of ALE values was then computed for the sample as the union of modeled activation values across experiments. Voxel-wise statistical significance was determined based on an analytically derived null distribution using the method described in (Eickhoff et al., 2012), prior to multiple comparisons correction. A cluster-forming threshold of $p < 0.001$ was used to perform cluster-level FWE correction. 10.000 iterations were performed to estimate a null distribution of cluster sizes, in which the locations of coordinates were randomly drawn from a grey matter template and the maximum cluster size was recorded after applying an uncorrected cluster-forming threshold of $p < 0.001$. The negative log-transformed p-value for each cluster in the thresholded map was determined based on the cluster sizes. See Figure 4.2 for a schematic of the ALE method employed for the main contrasts.

Following dataset-specific ALE meta-analyses, a subtraction analysis with 10.000 iterations was performed to compare the two datasets according to the procedure from (Laird et al., 2005). In short, the subtraction analysis entailed that all experiments that contributed to the initial contrast were pooled and randomized over two groups. The ALE values for these two randomly assigned groups were

then calculated, and the difference between these ALE values was recorded per voxel. This process was repeated 10,000 times and resulted in a null distribution for the difference in ALE values. The actual observed difference between the two contrasts was then compared to the null-distribution and resulted in a Z-value map. As there is no established method for multiple comparison corrections for ALE difference maps a conservative threshold of $p < 0.001$ was used to extract the clusters (Eickhoff et al., 2011). Note that contrary to GingerALE the subtraction analysis in NiMARE considers all voxels instead of only evaluating the voxels that were significant in the main contrasts. As such the subtraction analysis looks at the whole brain difference between the two contrasts and can result in clusters that were not found in the main ALE contrasts. The table of clusters was extracted using AtlasReader (V.0.1.2; (Notter et al., 2019)) using the resulting Z-map, a respective threshold of 1.645 or 3.091 for the main and subtraction analysis which corresponds to the one-sided Z-value, with a 95% and 99.9% confidence interval and a minimum cluster size of 64mm3. Since cluster-level inference was used for the main contrasts, the cluster itself has an associated probability and subpeaks are not meaningful (Woo et al., 2014). As such, all voxels that are part of a given cluster are set to the cluster-level Z-value significance and therefore the entire cluster is set to a single cluster-level significant value. The reported cluster coordinates therefore correspond to the centre of mass (COM) and not to the peak Z-value of a given cluster.

4.2.2.3 Anatomical labels

As the clusters can span across a number of distinct cortical and subcortical areas, we chose to report the anatomical labels for which the cluster overlaps instead of simplifying a cluster to a single COM coordinate. Another reason why we did not solely focus on the COM is that the coordinate can be located outside of the body of a cluster due to its irregular shape. The anatomical labels for the resulting clusters were determined using a number of atlases (AAL2, Harvard-Oxford and Julich; (Desikan et al., 2006; Eickhoff et al., 2006; Eickhoff et al., 2007; Eickhoff et al., 2005; Frazier et al., 2005; Goldstein et al., 2007; Makris et al., 2006; Rolls et al., 2015) where the overlap of the cluster with the main anatomical labels are provided.

4.2.3 Open science

A python notebook to query PubMed and Neurosynth is provided on the following link. All syntax used to run the ALE analyses with the corresponding input and output files are also provided in the following link.

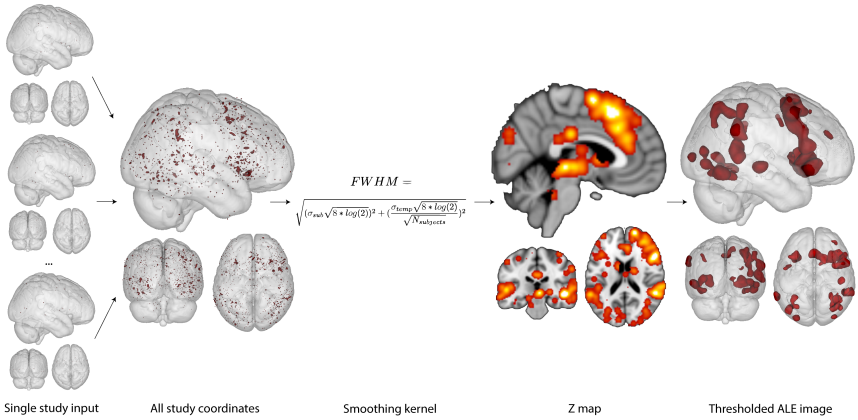

Figure 4.2: Overview of the ALE method. Peak coordinates from each included study are inputted into NiMARE. The spatial uncertainty for each foci from each study is estimated using sample size dependent gaussian kernels, where larger sample sizes have less spatial uncertainty and therefore smaller kernels. The resulting modelled activation maps are combined to create an uncorrected ALE union map. We end with the final thresholded ALE-map, which indicates clusters at which the convergence of foci is above what would be expected at chance-level. The diagram uses data from the main contrast of the inhibition subtype. FWHM: full width at half maximum.

4.3 Results

4.3.1 Main contrast results

Because each significant cluster is generally not solely within one specific brain area, we provide the main anatomical regions that overlap within each cluster. The percentage overlap of each of these structures within the significant clusters can be found in Supplementary Table 4.1 for each of the three atlases used (AAL2, Harvard-Oxford and Julich).

4.3.1.1 Interference resolution

The NiMARE ALE analysis found 9 significant activation clusters within the main contrast (Incongruent > Congruent) for the Flanker, Simon, Stroop and multi-source interference tasks (see Figures 4.3 and 4.4). Significant clusters within this contrast included the bilateral SMA, bilateral insula, left occipital inferior lobule, left anterior intra-parietal sulcus, left IFG, left superior frontal gyrus and left superior parietal lobule (see Table 4.2).

4.3.1.2 Global inhibition

The NiMARE ALE analysis found 14 significant activation clusters within the main contrast (Stop | NoGo > Go) for the go/no-go and stop-signal tasks (see Figures

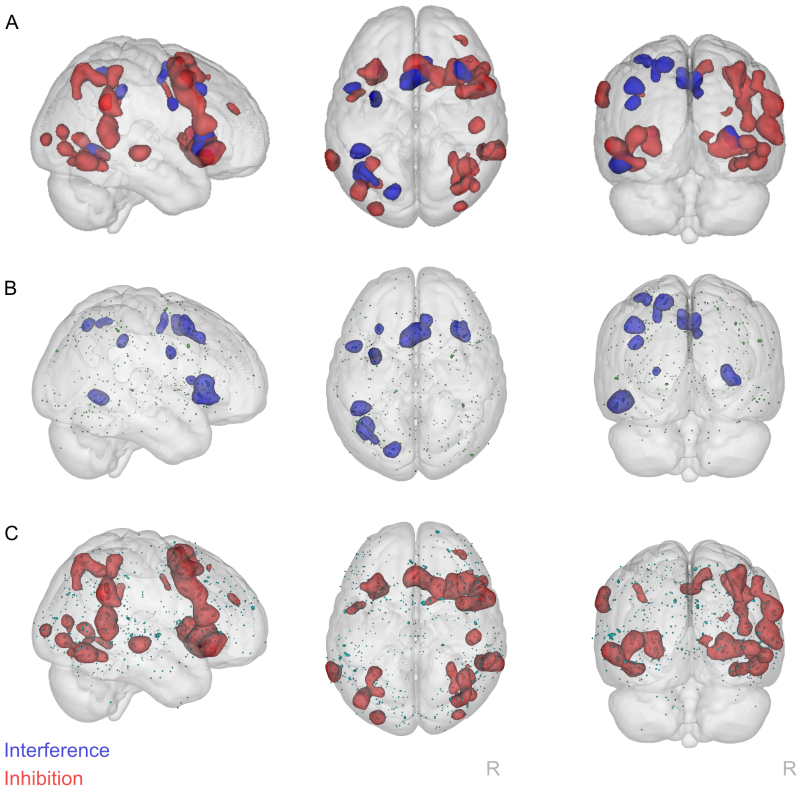

Figure 4.3: A 3D representation of the activation clusters for the interference and inhibition ALE analyses. A) Shows the clusters for both the interference (blue) and the inhibition (red) contrasts. B) Shows the clusters for the interference contrast only and the input coordinates from all interference tasks (green). C) Shows the clusters for the inhibition contrast only and the input coordinates for all inhibition tasks (green). The three columns show the right, superior and posterior view. R: right.

4.3 and 4.4). Significant clusters within this contrast includes the bilateral insula, bilateral inferior parietal lobule, right precentral cortex, right inferior temporal lobule, left fusiform gyrus, bilateral SMA, bilateral visual cortex and right mid cingulate cortex (see Table 4.2).

Table 4.2: Significant activation clusters of the interference and inhibition ALE analysis. BA: Brodmann area. COM: Center of Mass; SMA: supplementary motor area; IFG: inferior frontal gyrus; L: left, R: right. The x, y and z coordinates are in MNI space. Note that the Center of Mass for irregular shapes may lay outside of the actual cluster used to extract the anatomical labels. If the reader is interested in using the clusters for a region of interest analysis, we recommend using the actual 3D shape files provided here.

Contrast	Cluster ID	Volume (mm3)	Cluster Z-value	COM X	COM Y	COM Z	Main anatomical overlap
Interference	1	4144	3,72	2	12	48	L & R SMA
	2	3112	3,72	38	20	0	R Insula, R Frontal operculum cortex
	3	2760	3,72	-44	-64	-12	L Occipital inferior lobule, L Temporal inferior lobule, L V5
	4	1400	3,54	-38	-42	40	L Anterior intra-parietal sulcus (hIP1, hIP2, hIP3)
	5	1200	3,24	-44	4	30	L Precentral cortex (BA6), L IFG pars opercularis (BA44)
	6	1160	3,09	-26	-6	56	L Superior frontal gyrus, L Precentral gyrus (BA6), L Middle frontal gyrus
	7	1160	3,09	-14	-70	52	L Superior parietal lobule (7A, 7P), L Precuneus
	8	1056	2,81	-30	-58	56	L Superior parietal lobule (7A, 7PC)
	9	856	2,36	-30	20	4	L Insula
Inhibition	1	9920	3,72	36	18	-4	R Insula, R Putamen, R Inferior frontal orbital
	2	9256	3,72	50	-48	28	R Inferior parietal lobule (PFm, Pga, PF), Anterior intra-parietal sulcus (hIP3)
	3	8960	3,72	46	8	36	R Precentral cortex (BA6), R IFG pars opercularis (BA44)
	4	5544	3,72	-32	18	-2	L Insula, L IFG pars triangularis (BA45)
	5	4312	3,72	42	-62	-10	R Inferior temporal lobule, R Fusiform gyrus, R V4, R V5
	6	4032	3,72	-40	-70	-8	L Fusiform gyrus, R V4, R V5

Contrast	Cluster ID	Volume (mm3)	Cluster Z-value	COM X	COM Y	COM Z	Main anatomical overlap
	7	3824	3,72	8	14	54	L & R SMA
	8	1704	3,72	-60	-48	34	L Supramarginal gyrus, posterior division, L Inferior parietal lobule (PF, PFm)
	9	1488	3,35	50	-24	-6	R Insula Id1, R Superior temporal gyrus posterior division
	10	1456	3,24	-30	-90	6	L Occipital pole, L Visual cortex (V2, V3V, V4)
	11	1136	2,58	-40	-2	42	L Precentral gyrus (BA6)
	12	1088	2,48	36	-88	2	R visual cortex (V3V, V4)
	13	1000	2,28	34	40	24	R Frontal pole
	14	768	1.65	8	22	34	R Mid cingulate cortex

Note that previous work (Wessel, 2018) has shown that the probability of a salient event and the pace of the trials both influence what cognitive process is actually elicited by a Go/No-Go task. In Supplementary Table C.2, two additional control analyses are reported where the robustness of the inhibition contrast results was tested. When excluding the two Go/No-Go studies with equal probability of a salient event, 14 similar clusters as reported in Table 4.2 were found. When additionally excluding the six Go/No-Go studies that had a maximum trial length longer than 4 seconds, minor differences were found as only 12 similar clusters were found. Whether maximum trial length was the determining factor or whether this difference was due to a reduced number of contrasts contributing to the ALE analysis remains unclear.

4.3.1.2.1 Go/No-Go > Stop-Signal task

An exploratory analysis was done to directly compare the Go/No-Go and Stop-Signal tasks. It should be noted that the number of contributing studies is low for each of the two tasks and should therefore be interpretated with caution. The Go/No-Go minus Stop-Signal subtraction analysis displayed a single significant cluster in the right precentral cortex and the main anatomical overlap is given in Table 4.3.

4.3.1.2.2 Stop-Signal > Go/No-Go task

The Stop-Signal minus Go/No-Go subtraction analysis displayed 5 significant clusters located respectively in the left inferior parietal cortex, right visual cortex, right premotor cortex, left insula and finally the left fusiform cortex. The main anatomical overlap within each cluster can be seen in Table 4.3.

4.3.2 Comparison between interference and inhibition types

High overlap of activation clusters is found between interference and global inhibition, it should be noted that the latter appears to recruit many more regions than the former during the main contrasts for these task types. Recruitment of the bilateral SMA, bilateral Insula, and left IFG is shown for both inhibition types.

4.3.3 Subtraction analysis

Here, we present results firstly for the subtraction analysis of the interference-specific activations minus the inhibition-specific activations, and then the reverse of this, to indicate where these processes differ on a neural level.

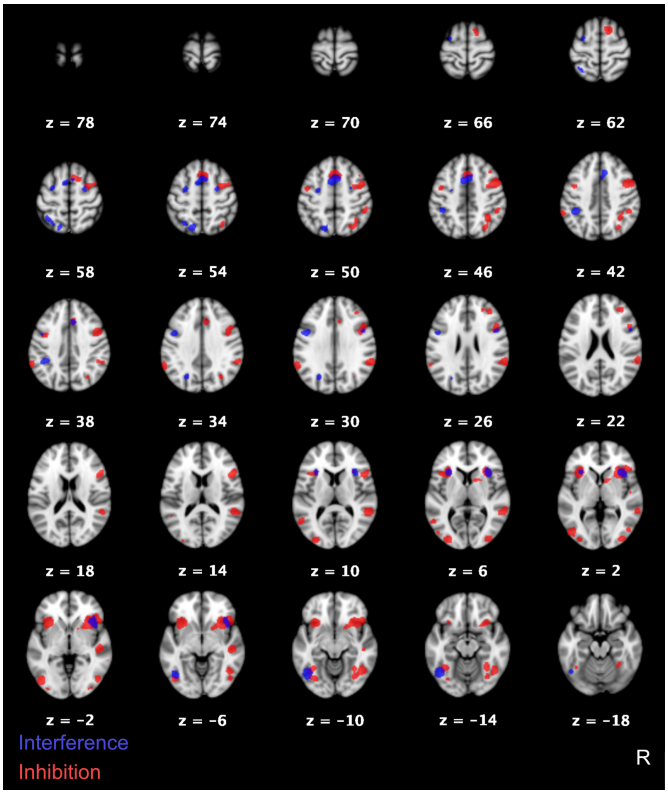

Figure 4.4: The activation clusters for the interference and inhibition ALE analysis in standard MNI space. The blue clusters correspond to the interference contrast, whereas the red clusters correspond to the inhibition contrast. The numbers indicate the Z coordinates in MNI space. R: right.

Table 4.3: Significant activation clusters of the Go/No-Go and Stop-Signal subtraction ALE analysis. SST: Stop-Signal task, COM: Center of Mass L: left, R: right. The x, y and z coordinates are in MNI space. Note that the Center of Mass for irregular shapes may lay outside of the actual cluster used to extract the anatomical labels.

Contrast	Cluster ID	Volume (mm3)	Cluster Z-value	COM X	COM Y	COM Z	Main anatomical overlap
Go/NoGo > SST	1	1376	3.45	26	-16	50	R Premotor cortex (BA6)
SST > Go/NoGo	1	3976	3.50	-56	-36	32	L Inferior parietal lobule (PF)
	2	3064	3.38	22	-74	-14	R Visual cortex (V3)
	3	2920	3.50	4	24	36	R Premotor cortex (BA6)
	4	1960	3.52	-40	12	-6	L Insula
	5	1632	3.25	-26	-56	-2	L Fusiform cortex

Table 4.4: Significant activation clusters of the interference and inhibition subtraction ALE analysis. BA: Brodmann area. COM: Center of Mass; L: left, R: right. The x, y and z coordinates are in MNI space. Note that the Center of Mass for irregular shapes may lay outside of the actual cluster used to extract the anatomical labels.

Contrast	Cluster ID	Volume (mm3)	Cluster Z-value	COM X	COM Y	COM Z	Main anatomical overlap
Interference > Inhibition	1	1976	3.54	-36	-32	36	L Inferior parietal lobule (PFt)
	2	680	3.45	0	-70	52	L Precuneus
	3	590	3.37	-8	-50	38	L & R Precuneus, L mid cingulate cortex
Inhibition > Interference	1	21792	3.59	56	-52	18	R Inferior parietal lobule (Pga, PFm)
	2	12496	3.73	-34	26	-14	L Frontal orbital cortex, L frontal pole
	3	9128	3.59	46	2	44	R Premotor cortex (BA6)
	4	4160	3.50	22	48	22	R Frontal pole
	5	3889	3.53	-58	-54	38	L inferior parietal lobule (PFm, PF)
	6	3504	3.63	26	20	-6	R Putamen, R orbital frontal cortex, R insula, R caudate
	7	744	3.28	-52	-80	12	L Lateral occipital cortex, L visual cortex (V4, V5)
	8	616	3.32	-20	-98	18	L Occipital pole, L visual cortex (V1, V2)

4.3.3.1 Interference > Inhibition

The interference minus inhibition subtraction analysis displayed 3 significant clusters. The main anatomical overlap within each cluster can be seen in Table 4.4. The largest clusters appear to be in the left inferior parietal lobule, bilateral precuneus, and left mid cingulate cortex (see Figure 4.5).

4.3.3.2 Inhibition > Interference

The inhibition minus interference subtraction analysis displayed 8 significant clusters. The main anatomical overlap within each cluster can be seen in Table 4.4. The largest clusters here appear to be in the bilateral inferior parietal lobule, bilateral frontal poles, right premotor cortex, right striatum, and the left early visual cortex (see Figure 4.5).

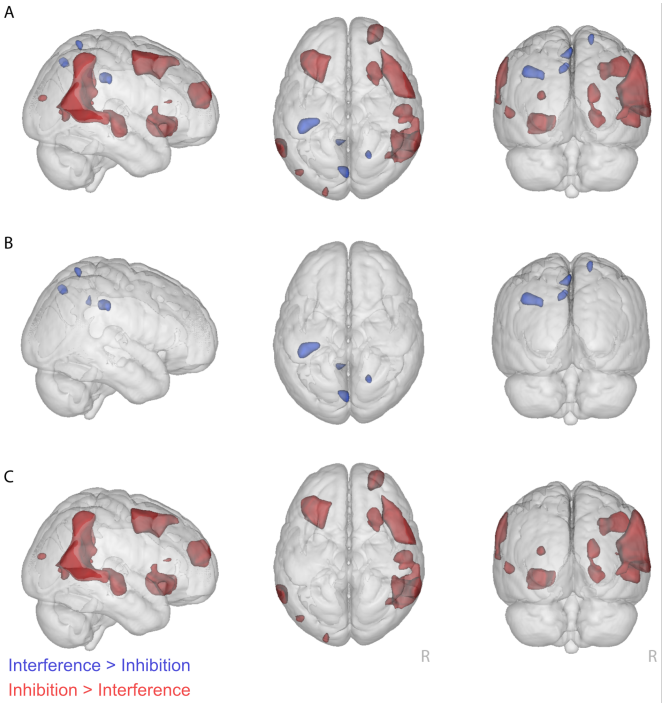

Figure 4.5: A 3D representation of the activation clusters for the subtraction analyses. A) Shows the clusters corresponding to the interference>inhibition subtraction (blue) and the clusters corresponding to the inhibition>interference subtraction (red). B) Shows the clusters for the interference>inhibition subtraction only. C) Shows the clusters for the inhibition>interference subtraction only. The three columns show the right, superior and posterior view. R: right.

4.4 Discussion

4.4.1 Dissociation between interference resolution and global inhibition networks

Using the meta-analytical method of ALE, we sought to shed light on our current understanding of the functional overlap between interference resolution and global inhibition in the cortex and subcortex. The meta-analysis provides an updated view on cognitive control by including only papers published in the last decade. For the interference tasks, the associated regions were the bilateral SMA, bilateral insula, left intraparietal sulcus, left superior parietal lobule, left superior frontal gyrus, left inferior occipital lobule, and the left precentral gyrus. Brain areas activated in the inhibition tasks include the bilateral insula, right IFG, bilateral precentral gyrus, right inferior temporal lobule, left fusiform gyrus, left supramarginal gyrus, bilateral SMA, visual cortex and frontal pole. The main anatomical overlap of the interference and inhibition tasks was found in the bilateral SMA and bilateral insula. Our subtraction analysis indicates that the bilateral precuneus and mid cingulate cortex were implicated as distinct brain areas involved in interference resolution but not global inhibition. The subtraction analysis also revealed a number of regions involved in global inhibition that were not recruited during interference resolution, namely the bilateral inferior parietal lobule, the right premotor cortex and bilateral frontal pole. The differences in neural recruitment between the Go/No-Go and Stop-Signal task seem to follow the results as presented by (Swick et al., 2011) but as stated, the number of contributing studies was low and should not be overinterpreted.

Generally, interference resolution appears to recruit more left-lateralized and global inhibition more right-lateralized regions. Note that this lateralization pattern for interference and inhibition tasks has been reported before (Aron et al., 2004; Vanderhasselt et al., 2009; Zhang et al., 2014), although that is not always the case (Serrien and Sovijärvi-Spapé, 2013). Taken together, the results of the meta-analysis are clear-cut in terms of supporting the need for separating these subtypes of cognitive control. Although there is evidence for some overlap between the networks that subserve these mechanisms, the results here, combined with previous work (Huang et al., 2020; Hung et al., 2018; Tobia et al., 2016), largely suggests that these cognitive processes are rooted in a number of distinct cortical brain areas.

Contrary to previous findings, our results do not show activation of the ACC in either contrast. Although the ACC is commonly implicated in cognitive control

(Hung et al., 2018; Mayer et al., 2012; Nee et al., 2007; Zhang et al., 2017) discrepancies have been shown (Veroude et al., 2013) and lesion studies have indicated that the region is not necessary for functional cognitive control (Di Pellegrino et al., 2007; Fellows and Farah, 2005; Mansouri et al., 2009). This is in contention to early models of ACC function which suggest that the ACC plays a pivotal role in conflict monitoring and action selection (Botvinick et al., 2001; Holroyd and Coles, 2008).

4.4.2 Subcortical involvement in cognitive control

Imaging the subcortex is notoriously difficult using standard fMRI acquisition and analysis protocols (De Hollander et al., 2015; Hollander et al., 2017; Keuken et al., 2018; Miletić et al., 2020; Mulder et al., 2019; Torrisi et al., 2018). To account for these challenges, we only included studies that employed 3 Tesla or higher field strengths with (near) isotropic voxel sizes of 3x3x3mm or smaller. Furthermore, we only included studies that processed the fMRI data with FWHM smoothing kernels that were smaller or equal to 8mm. Due to the whole brain acquisition inclusion criteria, a number of studies had to be excluded that focussed on a number of a-priori defined subcortical regions e.g., (Hollander et al., 2017; Miletić et al., 2020). The stringent MRI parameter inclusion criteria did not, however, result in a large number of studies that used ultra-high field MRI as 55 out of the 57 included studies employed 3T MRI, which might not be ideal for imaging the subcortex (Forstmann et al., 2016; Hollander et al., 2017; Isaacs et al., 2020).

Regardless of the field strength of the 73 contrasts used in the final analysis, 27 (15 within global inhibition, 12 within interference resolution) of them reported a peak coordinate within the subcortex. The average voxel volume of all included studies analysed here was 24.6mm, which would give approximately 3-4 voxels in the STN (82.5 ± 22.5mm), 19-20 voxels in the SN (469.9 ± 88.8mm) and 34-35 in the Globus Pallidus externa (GPe; 860.3 ± 137.7mm; (Alkemade et al., 2020a), whereas optimized UHF fMRI sequence for the subcortex can achieve voxel volumes of 3.38mm with relative ease (Hollander et al., 2017; Miletić et al., 2020).

As is clear from the results, there appears to be an absence of consistent subcortical activation patterns in both the global inhibition and interference tasks. This was surprising given the intracranial recording work and recent coordinate-based fMRI meta-analyses for response inhibition (Hung et al., 2018; Zhang et al., 2017). The only evidence found for the involvement of the subcortex was the putamen (inhibition contrast, cluster 1), but no clear evidence for the thalamus or other basal nuclei, in contrast to previous single studies (Aron, 2007; Duann et al., 2009;

Wimmer et al., 2015; Zandbelt and Vink, 2010) and meta-analyses (Cieslik et al., 2015; Guo et al., 2018; Hung et al., 2018). The putamen has been implicated as a vital element for motor control in the process of global inhibition (Alexander et al., 1986; Zandbelt and Vink, 2010). As such it remains unclear from this meta-analysis which aspects of cognitive control are implemented in the subcortex and how these processes are shared between interference resolution and global inhibition.

It appears that as methodology has progressed in the last decade, little improvement was made toward increasing sensitivity in subcortical areas. This has made sufficient aggregation of subcortical data by standard whole brain meta-analytical methods problematic. As whole-brain acquisition usually entails sacrificing spatial resolution, whole-brain coordinate based meta-analyses may not be optimal for aggregating functional data for small subcortical regions. It should also be noted that cluster-based thresholding inherently biases against small clusters, such as those normally found in the subcortex (Woo et al., 2014). This suggests that ROI- and image-based methods may be superior for inferring subcortical contributions to cognitive mechanisms as investigated here (Colizoli et al., 2020; De Hollander et al., 2015).

As a consequence, when conducting meta-analyses focusing on the human subcortex one may use less conservative criteria (e.g., lower resolution, lower field strengths), leading to more partial voluming and low numbers of voxels in smaller structures or use stricter criteria, which results in lower sensitivity and a lower number of studies. Such a choice can be overcome by moving away from coordinate based meta-analyses and instead using analyses directed by predefined regions of interest.

4.4.3 Limitations of the current study

A general limitation is the anatomical specificity of the results. In a coordinate-based meta-analysis such as in the current study we only incorporate the reported peak coordinates of what is likely a much larger cluster of activation. This limitation can be addressed by conducting an image-based meta-analysis using either the raw data or statistical maps of the included studies. This would, however, require that the data is publicly shared on a data repository such as Neurovault (https://neurovault.org; (Gorgolewski et al., 2015)) or OpenNeuro (https://openneuro.org; (Poldrack et al., 2013)) which can be accompanied by a data descriptor paper ("More Bang for Your Byte," 2014; (Shaklee, 2014)). None of the data analysed here was openly available online on such websites, though most authors do make their data available upon direct request. A specific limitation

of the current meta-analysis are the specific tasks that were included. Based on a number of previous meta-analysis we chose to only include the Go/No-Go and Stop-Signal task for global inhibition. Future work should extend this selection of paradigms to also include tasks such as the anticipated response inhibition task (Slater-Hammel, 1960) and countermanding saccade task (Hanes et al., 1998). Other potential tasks of interest might be the random dot motion paradigm which has been used in the past to investigate stimulus and response conflict processing (e.g., (Wendelken et al., 2009). Note that ideally the number of experiments across the different paradigms which contributed to the contrast is balanced (Müller et al., 2018). Finally, due to the selection of specific tasks, the interference contrast is mostly based on equal probable salient events whereas this is approximately 1:3 for the inhibition contrast. This difference in saliency might explain the involvement of the parietal areas (and potentially the right IFG) in the interference contrast as these have been linked to attentive processing (e.g., (Boehler et al., 2011)).

4.5 Conclusion

We set out to investigate the contribution of recent, high-resolution fMRI in the study of cognitive control through an extensive meta-analysis. This has revealed a gap in the neuroscientific literature pertaining to high resolution neuroimaging of interference and inhibition tasks. In particular, subcortical findings did not result in clusters that survived statistical threshold. The results presented here show large overlaps but also some discrepancies with previous work investigating the brain regions underpinning interference resolution and global inhibition. Cortically, the involvement of the insula and SMA in both mechanisms is not surprising, though the lack of significant activation in the ACC indicates that our understanding of the inhibitory and attentional networks is not yet complete. Future studies focusing on imaging the subcortex are required to shed light on the networks involved in cognitive control at a whole-brain level.

Chapter 5

Investigating intra-individual networks of response inhibition and interference resolution using 7T MRI

This chapter is published as:
S. J. S. Isherwood, P.-L. Bazin, S. Miletić, N. R. Stevenson, A. C. Trutti, D. H. Y. Tse, A. Heathcote, D. Matzke, R. J. Innes, S. Habli, D. R. Sokolowski, A. Alkemade, A. K. Håberg, and B. U. Forstmann (2023a). Investigating Intra-Individual Networks of Response Inhibition and Interference Resolution using 7T MRI. *NeuroImage*, p. 119988.

Abstract

Response inhibition and interference resolution are often considered subcomponents of an overarching inhibition system that utilizes the so-called cortico-basal-ganglia loop. Up until now, most previous functional magnetic resonance imaging (fMRI) literature has compared the two using between-subject designs, pooling data in the form of a meta-analysis or comparing different groups. Here, we investigate the overlap of activation patterns underlying response inhibition and interference resolution on a within-subject level, using ultra-high field MRI. In this model-based study, we furthered the functional analysis with cognitive modelling techniques to provide a more in-depth understanding of behaviour. We applied the stop-signal task and multi-source interference task to measure response inhibition and interference resolution, respectively. Our results lead us to conclude that these constructs are rooted in anatomically distinct brain areas and provide little evidence for spatial overlap. Across the two tasks, common BOLD responses were observed in the inferior frontal gyrus and anterior insula. Interference resolution relied more heavily on subcortical components, specifically nodes of the commonly referred to indirect and hyperdirect pathways, as well as the anterior cingulate cortex, and pre-supplementary motor area. Our data indicated that orbitofrontal cortex activation is specific to response inhibition. Our model-based approach provided evidence for the dissimilarity in behavioural dynamics between the two tasks. The current work exemplifies the importance of reducing inter-individual variance when comparing network patterns and the value of UHF-MRI for high resolution functional mapping.

5.1 Introduction

Response inhibition is defined as the global inhibition of a planned or already initiated response, commonly investigated using the stop-signal task (SST; Aron (2011) and Logan and Cowan (1984)). Interference resolution is a selective inhibition process that functions to suppress prepotent but suboptimal behaviour and is required for tasks such as the multi-source interference task (MSIT; Bush et al. (2003). Although both constructs are placed under the umbrella of inhibition-related functioning, concrete knowledge on their overlap in neural implementation is lacking (Isherwood et al., 2021b; Nee et al., 2007; Schmidt et al., 2020; Swick et al., 2011). Both the SST and MSIT have yielded robust results in functional magnetic resonance imaging (fMRI) studies and lend themselves well to cognitive modelling, although the neural architectures underlying behaviour in the tasks have not been directly compared (Bush and Shin, 2006; Deng et al., 2018; Hollander et al., 2017; Miletić et al., 2020).

Accumulating evidence indicates response inhibition is executed via a complex cortico-basal-ganglia network which is also involved in action planning and initiation (Albin et al., 1989; DeLong, 1990; Jahanshahi et al., 2015; Wessel and Aron, 2017), though some work has revealed inconsistencies in this theory (Hollander et al., 2017; Miletić et al., 2020). Through these intricate subcortical-cortical connections the idea is that the direct pathway plays a pivotal role in the initiation of movement (see Fig. 5.1). It is generally accepted that two separate pathways, the indirect and hyperdirect, work in tandem to pause or inhibit planned or already initiated movement (Diesburg and Wessel, 2021; Schmidt and Berke, 2017). While the role of this network in response inhibition has been widely investigated, its role in interference resolution remains elusive. With the idea that interference resolution is a type of selective inhibition, and response inhibition a more global method of inhibition, we sought to investigate to what extent they share common neural substrates within and outside of these canonical inhibitory pathways.

Previous meta-analyses and original studies indicate that the two types of inhibitory control utilize several distinct brain areas, namely the pre-supplementary motor area (preSMA) and subthalamic nucleus (STN) in response inhibition and the anterior cingulate cortex (ACC), superior parietal lobule (SPL) and striatum in interference resolution (Cieslik et al., 2015; Hung et al., 2018). However, overlapping activation has been found in the anterior insula (aI), preSMA, and inferior frontal gyrus (Cieslik et al., 2015; Hung et al., 2018; Isherwood et al., 2021b). These studies also suggest that response inhibition recruits a more right-lateralized, and

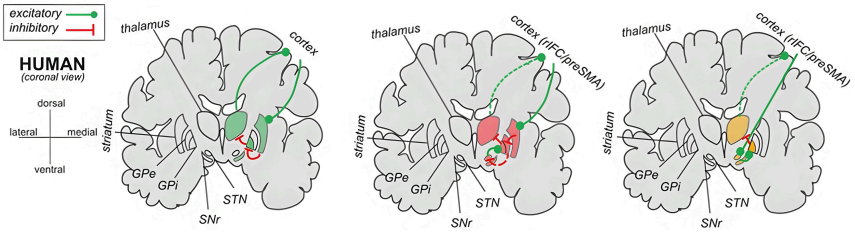

Figure 5.1: The *direct*, *indirect* and *hyperdirect* pathways in humans (adapted from Diesburg and Wessel (2021)). Glutamatergic connections are represented as green lines, GABAergic connections as red and a reduction in signaling as dotted. IFG, inferior frontal gyrus; preSMA, pre-supplementary motor area; GPe, globus pallidus externa; GPi, globus pallidus interna; SNr, substantia nigra pars reticulata; STN, subthalamic nucleus.

interference resolution a more left-lateralized network. Combined, these studies found little evidence of common subcortical involvement across the tasks. It is important to note that almost all meta-analyses are based mostly on 1.5T or 3T data and may lack the signal quality (in terms of signal-to-noise ratios) necessary to uncover activation in deeper parts of the brain. As such, there is an abundance of studies investigating both response inhibition and interference resolution in isolation, but few that have focused on intra-individual overlaps (Sebastian et al., 2013), especially at higher field strengths.

In addition to a lack of within-subject studies, model-based imaging approaches are missing (Maanen et al., 2015; Sebastian et al., 2018). Such an approach allows us to further understand the algorithmic level underlying behaviour as well as the implementation level in the brain (Marr, 1982), giving us the tools to gain mechanistic understanding. For example, if a parameter of a cognitive model correlates with brain activity in a specific region, there is an indication that the region could be involved in the specific process that parameter defines. To gain a deeper understanding of the neural signatures of response inhibition and interference resolution, here we apply both a well-established and a novel method of cognitive modelling to the two tasks (Matzke et al., 2017; Matzke et al., 2013). The stop-signal reaction time (SSRT) is the canonical marker of behavioural stopping ability during the SST and can be estimated using several methods (Logan and Cowan, 1984; Matzke et al., 2018). This marker has been shown to correlate negatively with nodes of the indirect pathway including the rIFG, caudate nucleus, and STN activity (Aron and Poldrack, 2006; Li et al., 2006; Whelan et al., 2012). To the best of our knowledge, there are no model-based fMRI studies of the MSIT. Here, we apply an evidence accumulation model, the racing Wald, to identify whether we can capture behaviour during interference resolution

in terms of changes in drift rate, threshold or non-decision time (Logan et al., 2014; Stevenson et al., 2023).

To accurately compare these two tasks, we employed ultra-high field magnetic resonance imaging (UHF-MRI) to acquire within-subject fMRI data of the SST and MSIT. UHF-MRI allowed us to obtain high resolution and optimized contrasts in deep subcortical areas as well as maintaining sufficient signal in the cortex (Isherwood et al., 2021a; Miletić et al., 2020). The echo time is important for optimal BOLD-sensitivity and should be equal to the T2* of the tissue of interest, for the STN and GPe this is around 14 ms (Posse et al., 1999). We therefore 'tailored' the sequence to the subcortex, by choosing a TE more optimal for it (Miletić et al., 2020). This, of course, results in a suboptimal TE for imaging cortical regions (which is around 30 ms). Due to the increased signal you achieve in the cortex, simply from being closer to the MRI head coils, we chose to focus on increasing sensitivity to subcortical BOLD responses which are widely underrepresented in functional studies.

We fit both whole-brain and region of interest (ROI) based general linear models (GLMs) for each participant of the study and compared their activation patterns. As the precise delineation of smaller subcortical structures is crucial for accurate statistical analysis, we here used the multi-contrast anatomical subcortical structures parcellation (MASSP) algorithm to directly obtain individual masks for each participant (Bazin et al., 2020). To better understand the mechanisms underlying observed behaviour in each task, we utilized separate cognitive modelling techniques. Based on previous literature, we expected to replicate findings of cortical overlap of response inhibition and interference resolution in the aI, preSMA, and IFG. Additionally, by using the high-resolution subcortical masks derived we aimed to explore possible commonalities in basal ganglia structures that constitute canonical inhibitory pathways.

5.2 Materials and Methods

5.2.1 Participants

A total of 37 participants (20 female; mean age 26.3 ± 5.6; age range 19 – 39 years) completed the study, which was approved by the ethical committee at the University of Amsterdam, the Netherlands, and the Regional Committees for Medical and Health Research Ethics, Norway. Written informed consent and MRI screening forms were obtained from all participants. The participants were recruited from

the Norwegian University of Science and Technology and had corrected-to-normal vision and no history of epilepsy or overt clinical neuropsychiatric disease.

5.2.2 Scanning Protocols

Each participant was scanned in a total of four MR sessions as part of a larger project on a Siemens MAGNETOM TERRA (Tesla (T) = 7; gradient strength = 80 mT/m at 200 T/m/s) with a 32-channel head coil. Here, we only describe the sessions that acquired the high resolution anatomical images and the SST and MSIT experimental data. The anatomical session acquired a multi-echo gradient recalled echo scan (GRE; TR = 31.0 ms, TE1 = 2.51 ms, TE2 = 7.22 ms, TE3 = 14.44 ms, TE4 = 23.23 ms, FA= 12°, FOV = 240 × 240 × 168 mm) and an MP2RAGE scan (TR = 4300 ms; TE = 1.99 ms; inversions TI1 = 840 ms, TI2 = 3270 ms; flip angle 1 = 5°, flip angle 2 = 6° Field of View (FOV) = 240 x 240 x 168 mm; bandwidth (BW) = 250 Hz/Px; Marques et al. (2010)). The experimental session consisted of four functional echo-planar imaging runs with subsequent acquisition of 4 EPI volumes with opposite phase encoding direction for susceptibility distortion purposes. The functional data was collected using a single echo 2D-EPI BOLD sequence (TR = 1380 ms; TE = 14 ms; MB = 2; GRAPPA = 3; voxel size = 1.5 mm isotropic; partial Fourier = 6/8; flip angle = 60°; MS mode = interleaved; FOV = 192 x 192 x 128 mm; matrix size = 128 x 128; BW = 1446 Hz/Px; slices = 82; phase encoding direction = A » P; echo spacing = 0.8 ms). Each task had a total of 2 runs, each with a 13:27 min acquisition time, for a total of 4 runs and 53:48 min functional scanning.

5.2.3 Physiological data

Physiological data (heart and breathing rate) were recorded for all participants in order to estimate the effects of physiological noise on the fMRI data. An 18 regressor RETROICOR model was fit (Glover et al., 2000). This included a fourth order phase Fourier expansion of the heart rate signal, second order phase expansion of the respiration signal, and a second order phase Fourier expansion of the interaction between heart rate and respiration (Harvey et al., 2008). Additional regressors were used to model heart rate variability (HRV; Chang et al. (2009), and respiratory volume per time unit (RVT; Birn et al. (2008) and Harrison et al. (2021).The PhysIO toolbox (Kasper et al., 2017) as executed in the TAPAS software (Frässle et al., 2021) was used for physiological regressor estimation.

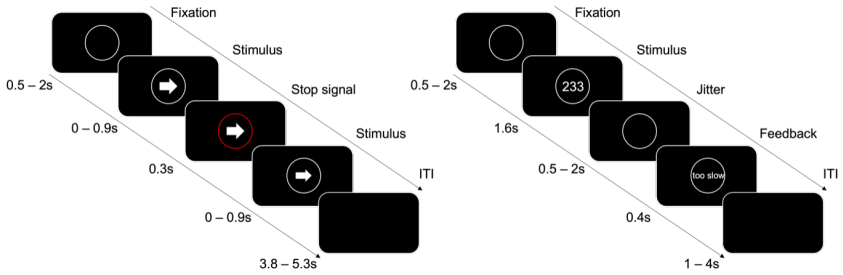

Figure 5.2: Task design of the SST (left) and MSIT (right). Trials in the SST lasted 7 seconds and were either go or stop trials: a) shows an example of a stop trial, where the participant should have attempted to inhibit responding to the right facing arrow. Trials in the MSIT also lasted 7 seconds. b) An example of an incongruent trial, where the correct response is 2 (middle finger on the button box).

5.2.4 Experimental Paradigms

5.2.4.1 Stop Signal Task (SST)

To test response inhibition, we used the SST (Logan and Cowan, 1984; Verbruggen et al., 2019). Participants were presented with a right or left-facing arrow surrounded by a white circle in the middle of the screen. They were instructed to respond to the direction of the arrow as quickly and as accurately as possible, using the index finger on their left or right hand (see Fig. 5.2). 25% of the trials were 'stop' trials, where the circle surrounding the stimulus turned red. The other 75% of the trials are termed 'go' trials, where the circle remains white. When presented with a stop trial, participants were instructed to inhibit their response to the direction of the arrow. On go trials, participants should respond to the arrow as initially instructed. The time delay between the presentation of the arrow stimulus on stop trials and the visual stop signal (the red circle), is defined as the stop signal delay (SSD). The SSD was adjusted to the stopping ability of the participant by means of a staircase procedure, where the SSD is increased 50ms if the participant successfully stopped and decreased by 50ms when the participant failed to stop. The SSD was initially set at 200ms for all participants. For analysis, trials were categorized into go trials (GO; no visual stop signal cue), successful stops (SS; visual cue presented, and response inhibited) and failed stops (FS; visual cue presented but response still initiated).

5.2.4.2 Multi-source Interference Task (MSIT)

To test interference resolution, we used the MSIT (Bush et al., 2003). Participants were presented with three numbers inside a white circle in the middle of the screen

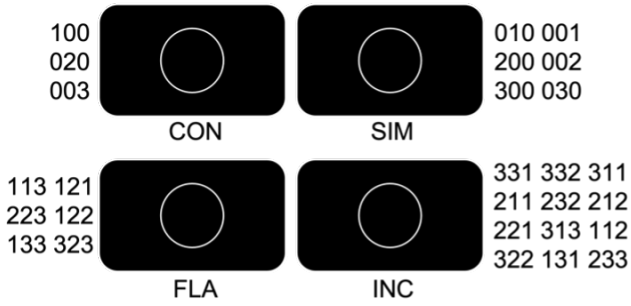

Figure 5.3: Conditions and stimuli presented in the MSIT. Possible stimuli are shown left or right of the conditions. There were three possible stimuli in the CON condition, six possible stimuli in the SIM and FLA conditions, and twelve possible stimuli in the INC condition. Each subject was presented with three selected stimuli from each condition during the experiment. CON, congruent; SIM, Simon; FLA, Flanker; INC, incongruent.

(see Fig. 5.2). Of these three numbers, two were identical and one differed. These numbers could either be a 0, 1, 2 or 3. Participants responded by indicating the identity, but not the position, of the number that was the odd one out as quickly and accurately as possible using the index, middle and ring fingers of their right hand. For example, the correct response to the stimulus '1 3 1' was to press the button corresponding to the number 3. There were four conditions; congruent (CON), Simon (SIM), Flanker (FLA), and incongruent (INC; see Fig. 5.3).

CON trials incurred stimuli such as '1 0 0' or '0 2 0', in which the correct responses were 1 and 2, respectively, and include a congruency between position and identity of the correct response. SIM trials contained stimuli such as '0 0 1' or '2 0 0', where the correct responses were also 1 and 2, respectively. The Simon effect caused an inconsistency between the position and identity of the correct answer, increasing the difficulty of the choice. FLA trials contained stimuli such as '1 2 2' or '3 2 3', in which the correct responses were 1 and 2, respectively. FLA trials also include a congruency between the position and identity of the correct response, but this response was surrounded by goal-irrelevant stimuli which act as distractors, which further increases choice difficulty, known as the Flanker effect. Finally, INC trials contained stimuli such as '3 3 1' or '1 1 2', with correct answers as 1 and 2, respectively. In INC trials, both the Simon and Flanker effects were present. We defined interference effects as a bias towards a possible choice option that is incorrect, the CON condition therefore had no interference effects, as the zeros did not bias participants towards a potential or valid response option. As there were different numbers of possible stimuli in each condition (e.g., three for the CON condition but twelve for the INC condition), each participant

was pseudorandomly assigned three stimuli from each condition as to harmonize any learning effects. After the response window, feedback of either 'in time' (responses less than 600ms), 'too slow' (responses between 600 – 900ms) or 'very slow' (for response more than 900ms) was shown. This feedback was aimed to keep participants responding quickly.

5.2.5 Behavioural Analyses

For both runs of the SST, median reaction times (RTs) on go and stop trials, the mean stop-signal delay (SSD) and proportion of successful stops (SS) were calculated. For each participant, the main measure of response inhibition, the stop-signal reaction time (SSRT) were calculated using modelling techniques described below. For both runs of the MSIT, median RTs and accuracy were calculated for all four conditions. Bayes factors (BFs) were computed using the BayesFactor package (Morey and Rouder, 2015).

5.2.6 Cognitive Modelling

5.2.6.1 SST

The SST was modelled using the Bayesian Estimation of Ex-Gaussian Stop-Signal (BEESTS) reaction time distributions method (Matzke et al., 2017; Matzke et al., 2013). The aim of modelling the SST is to estimate the efficiency of the unobservable stopping response, commonly defined as the stop signal reaction time (SSRT). The model is based on the standard horse-race model (see Fig. 5.4), where the go process, initiated upon presentation of the stimulus, and the stop process, initiated by the presentation of the visual stop signal, independently race against each other. If the go process finishes the race first, the prepared action is executed. If the stop process finishes first, this action is inhibited. This can be further formalized, if the go RT is faster than the SSD + SSRT on a given trial, then the go process wins and a signal-response RT (SRRT) is observed. If the go RT is slower than the SSD + SSRT, then the stop process wins, and the action is inhibited. The RT distribution derived from failed stop trials are estimated as a partially known (censored) go RT distribution. The race model assumes that, on average, these SRRTs are quicker than go RTs. Due to the simplicity of the go choice, incorrect response on go trials were removed from the analysis (0.24% of all go data).

By using a Bayesian parametric approach (BPA), the entire distribution of SSRTs is estimated, as opposed to using the mean or median approach, which provides only a summary measure. The BPA assumes that go RTs and SSRTs follow an ex-gaussian distribution (Matzke and Wagenmakers, 2009; Ratcliff and Murdock,

1976). Such a distribution is defined by three parameters, the mean of the gaussian component (μ), the standard deviation of the gaussian component (σ) and the mean of the exponential component (τ). The BPA model simultaneously estimates the go (μ_{go}, σ_{go}, τ_{go}) and stop (μ_{stop}, σ_{stop}, τ_{stop}) RT distribution parameters. The mean of the ex-gaussian distribution is the sum of the μ and τ parameters, μ_{go} + τ_{go} derives the mean go RT and μ_{stop} + τ_{stop} derives the mean SSRT. Posterior distributions for these go and stop parameters are estimated using Markov chain Monte Carlo sampling (Gilks et al., 2003). Proper convergence of these chains during sampling is diagnosed using the Gelman-Rubin statistic, where values of 1.1 or lower indicate the chains have converged (Gelman and Rubin, 1992). The stop signal data is analyzed hierarchically, therefore assuming that subject-level go and stop signal parameters are drawn from group-level distributions. Both group-level and subject-level parameters are estimated simultaneously, where the group-level distributions define the between-subject variability of the subject-level parameters (Gelman and Hill, 2006). Hierarchical methods allow adjustment or "shrinkage" of extreme or unlikely parameters estimates towards the group mean.

Attentional failures are captured by the model by means of trigger failures (tf), where the stop process is not initiated and go failures (gf), where the go process is not initiated. The overall probability of stopping remains the same, as stopping and trigger failures are, by definition, mutually exclusive. Similarly, go responses are not observed upon the manifestation of a go-failure. The priors used for the population-level parameters of the model were truncated normal distributions, constrained between 0 and 1000ms for the go and stop parameters and normal distributions between -6 and 6 for P(tf) and P(gf) parameters. The priors for the group-level means and group-level standard deviations are weakly informative uniform distributions, as in (Matzke et al., 2017). After model estimation, an inverse probit transformation that simultaneously considers the population-level mean and the population-level standard deviation was applied to the P(tf) and P(gf) parameters to convert them to the probability scale. The described model is therefore comprised of 8 parameters (μ_{go}, σ_{go}, τ_{go}, μ_{stop}, σ_{stop}, τ_{stop}, P(tf), P(gf)).

5.2.6.2 MSIT

There have been few attempts to investigate the MSIT within a model-based framework. Here, we use a process-orientated approach developed by Stevenson et al. (2023) to model participant behaviour during the task. Through cognitive modelling, the aim is to disentangle the individual contribution that both the Simon and Flanker effects have on behaviour, as well as their cumulative effects

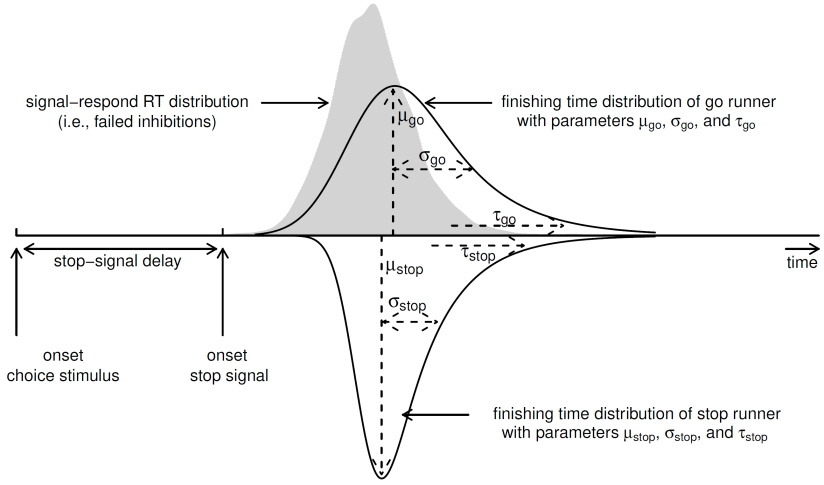

Figure 5.4: Schematic representation of the horse-race model (Heathcote et al., 2019). The horse-race model treats go RTs and SSRTs as independent random variables, defining the finishing times of either the go or the stop process. The signal-response RT (SRRT) distribution (grey) is treated as a censored Go RT distribution. If the go RT on any given trial is longer than SSD + SSRT, the response is successfully inhibited. SRRTs occur when the go RT on the given trial is shorter than SSD + SSRT. Figure available at `tinyurl.com/5hnyzz2w` under CC-BY 2.0 license (`https://creativecommons.org/licenses/by/2.0/`).

when both are present. The evidence accumulation model we used was the racing Wald model (Logan et al., 2014). This model is characterized by three parameters: the rate of evidence accumulation (drift rate), the decision threshold (B) and non-decision time (t0). We assume that evidence accumulates during each trial of the task at some rate until evidence for a certain decision reaches a threshold, upon which a decision is triggered. The model assumes that most of the between-condition effects can be put down to differences in drift rates. Since there are three potential responses, there are three accumulators racing on each trial. As a reminder, there are four conditions in this task, a CON condition (no Simon or Flanker), SIM condition (Simon only), FLA condition (Flanker only) and INC condition (both Simon and Flanker). We hypothesized that the drift rate for each choice is jointly driven by an urgency component and the evidence supporting that choice. The drift rate for any choice is therefore an addition of the urgency component (ν_0), target evidence (ν_{Target}), Simon evidence (ν_{Simon}), and Flanker evidence (ν_{Flank}). Furthermore, we also found that response time and accuracy were influenced by the position of the target, possibly due to left to right reading effects (Stevenson et al., 2023). We therefore modified the drift rate of the accumulator corresponding to the target based on position of the target.

Additionally, the evidence accumulation process is subject to Gaussian noise W, with standard deviation σ, defining within-trial variation in drift rate, was fixed to 1 to satisfy scaling constraints. Consequently, the drift rate in our MSIT model can be described as:

Where, vCorrect is equal to the summation of vTarget and the positional drift rate modifier, which can vary among positions (1, 2 or 3). The positional drift rate modifier ν_{pos3} was fixed to 0, by which the other positional modifiers (ν_{pos1} and ν_{pos2}) were relative. In total our MSIT model comprised 8 estimated parameters (ν_{Flank}, ν_{Simon}, ν_{Target}, ν_{pos1}, ν_{pos2}, ν_0, B, t0). The above-described model was selected after model comparison against competing models as in Stevenson et al. (2023). Uninformed priors were used for all parameters constituting a Gaussian distribution centred on 0 with a standard deviation of 1.

5.2.7 Procedure and exclusions

Prior to the MRI session, all participants completed a practice version of the two tasks to ensure that the task instructions were correctly understood. Each trial of the functional tasks lasted 7 seconds. For the SST, six participants were excluded on the basis of having (1) more than 10 go-omissions (non-responsive during Go trials) across both runs. One of these participants also had (2) a stopping accuracy of less than 35% or more than 65%. No participants were excluded for having (3) a go-accuracy of less than 95%. Two of the already excluded participants had (4) mean signal respond RTs that were longer on average than go RTs (inconsistent with the race model; Logan and Cowan (1984)). For the MSIT, participants were excluded if they performed below chance level (33%) in any of the four conditions. One subject was excluded for using incorrect response buttons. Based on these exclusions the final sample for the analysis was a total of 31 participants for the SST (17 female; mean age 26.7 ± 5.9; age range 19 -39) and 36 participants for the MSIT (19 female; mean age 26.4 ± 5.7; age range 19 - 39).

5.2.8 fMRI preprocessing pipeline

fMRIPrep was used to preprocess all acquired anatomical and functional data (Esteban et al., 2020; Esteban et al., 2018). For each of the 2 BOLD runs found per task per subject, the following preprocessing was performed. First, a reference volume and its skull-stripped version were generated by aligning and averaging 1 single-band references (SBRefs). A B0-nonuniformity map (or fieldmap) was estimated based on two echo-planar imaging (EPI) references with opposing phase-encoding directions, with 3dQwarp (Cox and Hyde (1997); AFNI 20160207). Based

on the estimated susceptibility distortion, a corrected EPI (echo-planar imaging) reference was calculated for a more accurate co-registration with the anatomical reference. The BOLD reference was then co-registered to the T1w reference using bbregister (FreeSurfer) which implements boundary-based registration (Greve and Fischl, 2009). Co-registration was configured with six degrees of freedom. Head-motion parameters with respect to the BOLD reference (transformation matrices, and six corresponding rotation and translation parameters) are estimated before any spatiotemporal filtering using mcflirt (FSL 5.0.9, Jenkinson et al. (2002)). BOLD runs were slice-time corrected using 3dTshift from AFNI 20160207 (Cox and Hyde (1997); RRID:SCR _005927). First, a reference volume and its skull-stripped version were generated using a custom methodology of fMRIPrep. The BOLD time-series (including slice-timing correction when applied) were resampled onto their original, native space by applying a single, composite trans- form to correct for head-motion and susceptibility distortions. These resampled BOLD time-series will be referred to as preprocessed BOLD in original space, or just preprocessed BOLD. Several confounding time-series were calculated based on the preprocessed BOLD: framewise displacement (FD), DVARS (the spatial standard deviation of difference images), and three region-wise global signals. FD was computed using two formulations following Power (absolute sum of relative motions, Power et al. (2014)) and Jenkinson (relative root mean square displacement between affines, Jenkinson et al., 2002). FD and DVARS are calculated for each functional run, both using their implementations in Nipype (following the definitions by Power et al., 2014). The three global signals are extracted within the CSF, the WM, and the whole-brain masks. Additionally, a set of physiological regressors were extracted to allow for component-based noise correction (CompCor, Behzadi et al. (2007)). Principal components are estimated after high-pass filtering the preprocessed BOLD time-series (using a discrete cosine filter with 128 s cut-off) for the two CompCor variants: temporal (tCompCor) and anatomical (aCompCor). tCompCor components are then calculated from the top 2% variable voxels within the brain mask. For aCompCor, three probabilistic masks (CSF, WM and combined CSF + WM) are generated in anatomical space. The implementation differs from that of Behzadi et al. (2007) in that instead of eroding the masks by 2 pixels on BOLD space, the aCompCor masks are subtracted a mask of pixels that likely contain a volume fraction of GM. This mask is obtained by dilating a GM mask extracted from the FreeSurfer's aseg segmentation, and it ensures components are not extracted from voxels containing a minimal fraction of GM. Finally, these masks are resampled into BOLD space and binarized by thresholding at 0.99 (as in

the original implementation). Components are also calculated separately within the WM and CSF masks. For each CompCor decomposition, the k components with the largest singular values are retained, such that the retained components' time series are sufficient to explain 50 percent of variance across the nuisance mask (CSF, WM, combined, or temporal). The remaining components are dropped from consideration. The head-motion estimates calculated in the correction step were also placed within the corresponding confounds file. The confound time series derived from head motion esti- mates and global signals were expanded with the inclusion of temporal derivatives and quadratic terms for each (Satterthwaite et al., 2013). Frames that exceeded a threshold of 0.5 mm FD or 1.5 standardised DVARS were annotated as motion outliers. All resam- plings can be performed with a single interpolation step by composing all the pertinent transformations (i.e. head-motion transform matrices, susceptibility distortion correction when available, and co-registrations to anatomical and output spaces). Gridded (volumetric) resamplings were performed using antsApplyTransforms (ANTs), configured with Lanczos interpolation to minimize the smoothing effects of other kernels (Lanczos, 1964). Non-gridded (surface) resamplings were performed using mri _vol2surf (FreeSurfer). Many internal operations of fMRIPrep use Nilearn 0.6.2 (Abraham et al. (2014), RRID:SCR _001362), mostly within the functional processing workflow.

5.2.9 fMRI analyses

5.2.9.1 General Linear Models (GLMs)

GLM analyses were performed at both a whole-brain voxel-wise and region-specific level. A canonical double gamma hemodynamic response function (HRF) with temporal derivative was used as the basis set for both tasks and both methods of analysis (Glover, 1999). The design matrix consisted of either the three experimental conditions for the SST (GO, FS, SS) or the four for the MSIT (CON, SIM, FLA, INC). Functional data were first spatially smoothed using SUSAN (kernel size full width half maximum = 1.5 mm) and high-pass filtered before GLM analysis (Smith and Brady, 1997). In addition to the task-specific regressors, six motion parameters were also included (three translational and three rotational) as well as DVARS and framewise displacement estimated during preprocessing. 20 physiological regressors obtained from RETROICOR estimations were also included in the design matrix. For two participants on the second runs of the SST physiological data were not collected due to technical reasons, the first 20 aCompCor components were used instead (Behzadi et al., 2007). Therefore, a total of 31 or 32 regressors were used in the model, depending on the task being

analyzed (SST or MSIT, respectively). The SST consists of three possible contrasts: FS - GO, FS - SS and SS - GO. The MSIT consists of six possible contrasts: INC - CON, INC - SIM, INC - FLA, SIM - CON, SIM - FLA and FLA - CON.

Whole-brain analyses were computed using the FILM method from FSL FEAT (Jenkinson et al., 2012; Woolrich et al., 2001), accounting for autocorrelated residuals. Fixed effects analyses were used to combine the resulting run-level GLMs per task. Group-level models were subsequently estimated using FLAME1 and FLAME2 from FSL (Woolrich et al., 2001). Statistical parametric maps (SPMs) were generated to visualize the resulting group-level models. The maps were corrected for the false discovery rate (FDR) using critical value of $q < 0.05$ (Yekutieli and Benjamini, 1999).

Region of interest (ROI) analyses were then performed. Timeseries were extracted from each subcortical region of interest using probabilistic masks provided by MASSP (Bazin et al., 2020), each voxels contribution to the mean signal of the region was therefore weighted by its probability of belonging to the region. Cortical regions parcellations were provided by the Harvard-Oxford cortical atlas (Rizk-Jackson et al., 2011). The timeseries were subsequently converted to percentage signal change by dividing each timepoint by the mean timeseries signal, multiplying by 100 and subtracting 100. These timeseries were extracted from unsmoothed data so to ensure regional specificity. Runs were concatenated within task. We only infer from positive BOLD responses due to the discrepancy around negative BOLD responses (Schridde et al., 2008; Wade, 2002).

5.2.9.2 Comparisons

To investigate the similarities and differences in neural implementation during the two tasks, we performed both a conjunction and subtraction analysis on the GLMs. To do this, we first had to define a contrast for both tasks that best fits the inhibition construct we were measuring. The SS - GO contrast of the SST represents the triggering and successful implementation of the global inhibition pathway, and therefore is the baseline definition of the network behind canonical response inhibition. The INC – CON contrast of the MSIT exemplifies the highest cognitive load of selective inhibition in the task and was therefore used for these analyses. A conjunction map was generated by overlaying the FDR corrected group-level z-maps of the two contrasts and keeping only voxels that survived significance in both instances. For the subtraction analysis, we calculated a voxel-wise comparison of the contrasts by nullifying voxels on the FDR corrected group-level z-map

in the MSIT contrast that also survived thresholding in the SST contrast, and vice versa.

In addition to brain-level comparisons, we also investigated behavioural-level associations. To do this, we correlated the model estimates derived from the independent modelling techniques described above. The mean of the group-level parameter estimates were correlated with one another using Pearson's r and FDR corrected to account for multiple comparisons (Pearson, 1895).

5.3 Results

5.3.1 Cognitive modelling

5.3.1.1 SST

To assess the goodness of fit of the model to the data, we plot averaged simulated posterior predictive data and the raw data averaged over all participants (see Fig. 5.5). The cumulative density functions (CDFs) show the average cumulative probability of observing a correct RT. The sum of each asymptote in each condition equals the probability of making a response. In stop trials, this was around 0.5 due to the frequency of successful stops, where no response is observed. Overall, the model fits the data very well, though it slightly overestimates the RT in STOP conditions. In addition to CDFs referenced above, we also plot the group level inhibition function and median signal-respond RTs (SRRTs). To account for individual differences in participant-specific SSDs, we normalized the inhibition function by averaging equal percentile ranges of SSDs for each participant. As expected, the inhibition function increases with SSD, suggesting that the probability of responding increases as the SSD increases. Additionally, the median SRRTs increased as a function of SSD as expected. The median estimated parameter values and 95% credible intervals for the SST model are as follows; μ_{go} = 0.54 (0.48, 0.59), σ_{go} = 0.08 (0.05, 0.11), τ_{go} = 0.09 (0.07, 0.11), μ stop = 0.21 (0.20, 0.22), σ stop = 0.01 (0.0068, 0.031), τ stop = 0.018 (0.0098, 0.043), P(tf) = 0.0062 (0.0019, 0.021), P(gf) = 0.018 (0.011, 0.029), SSRT = 0.23 (0.21, 0.24).

5.3.1.2 MSIT

To assess goodness of fit of the model and the MSIT data, we compared the average posterior predictive data to the average observed data collected from each participant (see Fig. 5.6). For accuracy estimates, the model fits each condition relatively well, though it slightly underestimates the accuracy in the INC condition. Estimates for the three quantiles of RT data fit very well, though also underestimating RTs in the INC condition and overestimating the spread of RTs

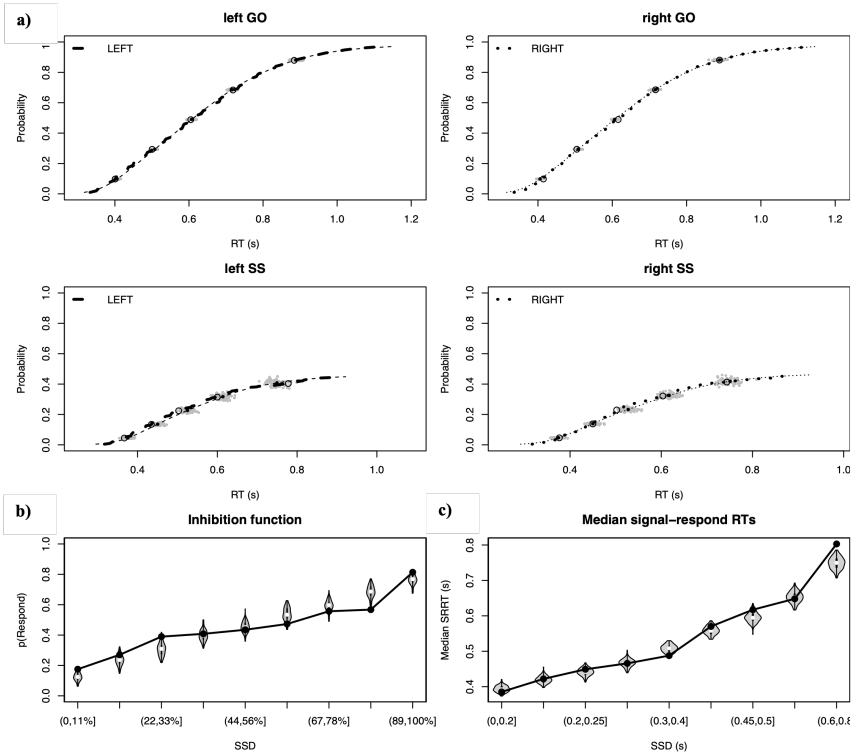

Figure 5.5: Goodness of fit graphs for the SST. **a)** Cumulative distribution functions. The data are shown with thick lines, with open points marking the 10th, 30th, 50th, 70th, and 90th percentiles. Model predictions are shown with thin lines and solid points, with the clusters of grey dots showing the uncertainty in the percentiles from 100 randomly selected samples from the joint posterior. **b)** Average inhibition function across all participants, as a function of nine equal percentile ranges. **c)** Average median signal response RTs across all participants, as a function of nine time intervals over the range of SSDs for each participant. The data are shown with solid points. The uncertainty of the model predictions resulting from 100 randomly selected samples from the joint posterior is shown with violin plots, with the white dots indicating the median of the predictions.

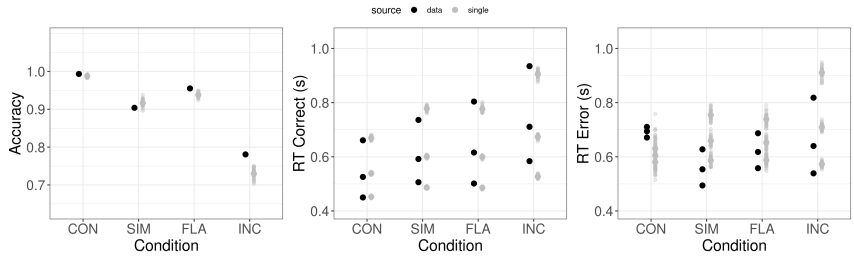

Figure 5.6: Model fit for accuracy, RTs on correct trials and RTs on error trials in the MSIT. The accuracy graph displays group-level accuracy for each of the four conditions. The RT figures display the 10th, 50th and 90th percentiles for the correct (middle) and error (right) trials. Black denotes the acquired data; shaded grey denotes the model predictions. The uncertainties of the model estimates resulting from 100 randomly selected samples from the joint posterior are denoted by the spread of the shaded area.

in the SIM condition. Due to the small number of errors in the task, RT data for incorrect responses had a more variable model fit. The mean parameter values and 95% credible intervals for the MSIT model are as follows; ν_{Flank} = 1.25 (1.06, 1.44), ν_{Simon} = 1.31 (1.09, 1.52), ν_{Target} = 3.32 (3.00, 3.66), ν_{pos1} = 0.46 (0.25, 0.68), ν_{pos2} = 0.068 (-0.09, 0.24), ν_0 = -0.08 (-0.34, 0.19), B = 1.69 (1.57, 1.84), t0 = 0.27 (0.24, 0.29). As shown from the parameter estimates, the ν_{Flank} and ν_{Simon} parameters are of similar values suggesting that both types of interference introduce a similar amount of conflict to resolve. These results indicate that both types of interference biased participants equally.

5.3.2 Comparisons

To identify behavioural associations between the two tasks, we correlated the estimated model parameters within-subject. Fig. 5.7 shows the results of this analysis. There were no significant correlations in parameter estimates between models after multiple comparison correction. This suggests that the parameters we estimated by decomposing the behavioural data in the two tasks are not linearly dependent.

5.3.3 Behavioural analyses

5.3.3.1 SST

The Go RTs for correct responses were within normal range for fMRI studies of response inhibition (Miletić et al., 2020; Verbruggen et al., 2019). Overall, participants had a mean stopping accuracy of 54 ± 1%. Go omissions and Go errors were slightly higher than previous studies (Hollander et al., 2017; Miletić

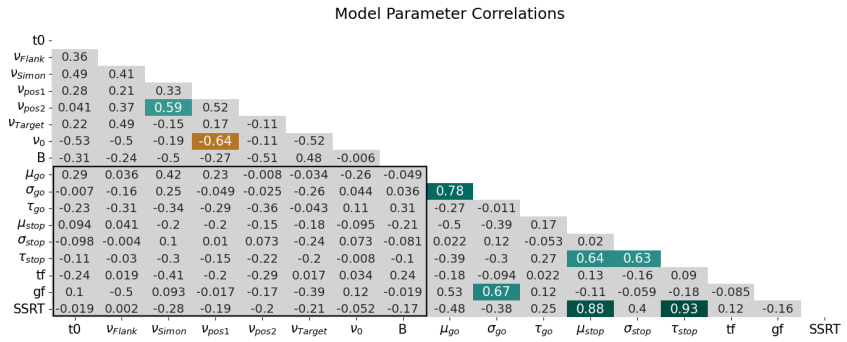

Figure 5.7: Correlation heatmap depicting associations within and between models for the SST and MSIT. Darker colours indicate larger correlations, grey denotes correlations that were non-significant (p > 0.05 FDR corrected). Between-model correlations are shown within a black box.

Table 5.1: Group-level descriptive statistics of the main quantitative aspects of the SST. Standard errors are given.

Median go RT (ms)	Median failed stop RT (ms)	Go omissions (%)	Go errors (%)	Mean SSRT (ms)	Median SSD (ms)	Mean stopping accuracy (%)
626 ± 25	543 ± 22	1.9 ± 0.4	2.2 ± 0.4	251 ± 6	350 ± 30	54 ± 1

et al., 2020). SSRT was calculated using the modelling parameters estimated with BEESTS where SSRT is equal to the addition of μ_{stop} and τ_{stop}. Median Go RT did not correlate with estimates of SSRTs when corrected for trigger failures, in accordance with the independence assumption of the independent race model (Aron and Poldrack, 2006; Logan and Cowan, 1984).

5.3.3.2 MSIT

Table 5.2 illustrates the differences in RTs and accuracy between the four conditions. All RTs and accuracies were significantly different between conditions based on BFs and FDR correct p-values. Based on FDR-corrected p-values and BFs the differences in RT and accuracy between all conditions were highly significant (p < 0.001; BF > 1e3) with the exception of the SIM – FLA comparisons (RT: p = 0.003, BF = 2.1e1; Accuracy: p = 0.006, BF = 9.7).

5.3.4 GLMs: Whole-brain analyses

5.3.4.1 SST

For the FS - GO contrast (see Fig. 5.8) we observed many areas that show significant BOLD responses, in line with previous findings (Hollander et al., 2017; Miletić et al., 2020; Ray Li et al., 2008). Cortically, these regions included the IFG, preSMA,

Table 5.2: Group-level median RTs and mean accuracies for each condition in the MSIT. Standard errors are given.

	Median RT (ms)	**Mean accuracy (%)**
CON	536 ± 10	99.3 ± 0.3
SIM	604 ± 12	90.4 ± 1.7
FLA	630 ± 12	95.5 ± 0.8
INC	702 ± 15	78.1 ± 2.5

ACC, and aI. Subcortically, significant differences between the FS and GO trials were found in the caudate nucleus (CN), putamen (PUT), thalamus (Tha), STN, and SN. For the FS - SS contrast, we observed similar activation patterns as with the former contrast, both cortically and subcortically. For the SS - GO contrast, we found significant cluster differences in four cortical regions; the aI, M1, IFG, and occipital fusiform gyrus, and two subcortical regions; the CN and Tha.

5.3.4.2 MSIT

For our main measure of interference resolution, the INC – CON contrast, we observe marked differences in recruitment of the ACC, insula, Tha, and VTA (see Fig. 5.9). We also observe larger recruitment of the ACC and insula in the FLA - CON contrast, but not for the SIM - CON contrast, suggesting these regions are more engaged when resolving the Flanker effect. The SIM - FLA contrast does not display significant differences in activation patterns in the voxel-wise GLMs and is therefore not included in Fig. 5.9. The contrasts comparing the FLA and SIM conditions to the INC condition display similar differences in the recruitment of the ACC and insula, though to a much lesser extent.

5.3.5 Conjunction analysis

To investigate the overlap between response inhibition and interference resolution on a network-level, we calculated a conjunction map between the SS - GO and INC – CON contrasts of the SST and MSIT, respectively. The conjunction map was calculated using the minimum FDR corrected z-score of each contrasts group-level model (see Fig. 5.10). Notable overlap of activation patterns between the two tasks includes the bilateral aI and rIFG.

5.3.6 Subtraction analysis

To observe regions of the brain recruited specifically for response inhibition or interference resolution, we compared the statistically significant activation of the SS - GO contrast from the SST and the INC - CON contrast from the MSIT. Fig. 5.11

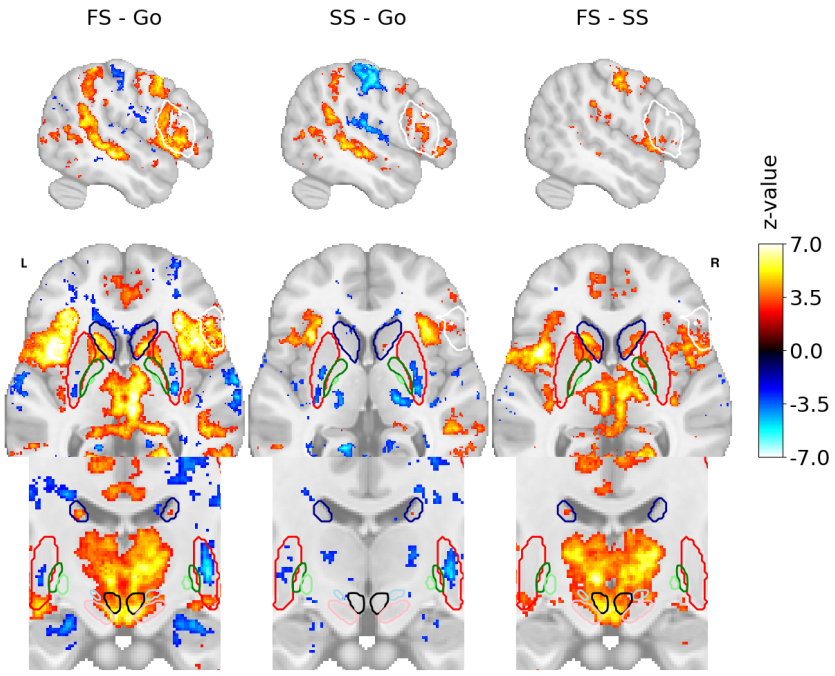

Figure 5.8: Group-level SPMs of the three main contrasts of the SST. Activation colours indicate FDR thresholded (q < 0.05) z-values. Sagittal (top), axial (middle) and a zoomed in coronal (bottom) view are shown. Coloured contour lines indicate regions of interest (CN in dark blue, PUT in red, STN in light blue, GPe in dark green, GPi in light green, VTA in black, rIFG in white, and SN in pink. The background template and coordinates are in MNI2009c (1mm); slices are drawn through x = 51 (top), y = -13 (bottom), and z = 2 (middle).

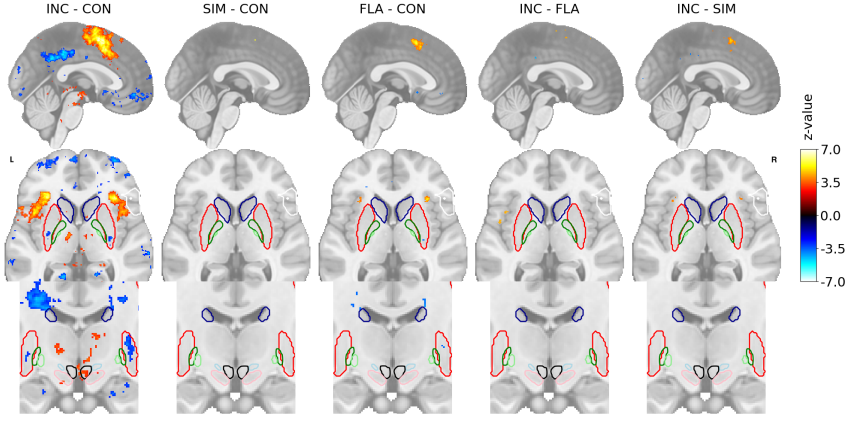

Figure 5.9: Group-level SPMs of five of the six contrasts of the MSIT. Activation colours indicate FDR thresholded (q < 0.05) z-values. Sagittal (top), axial (middle) and a zoomed in coronal (bottom) view are shown. Coloured contour lines indicate regions of interest (CN in dark blue, PUT in red, STN in light blue, GPe in dark green, GPi in light green, VTA in black, rIFG in white, and SN in pink. The background template and coordinates are in MNI2009c (1mm), where x = 0, y = -13, and z = 2.

Figure 5.10: Conjunction analysis between activation from the SS – GO contrast in the SST and INC – CON contrast in the MSIT. Activation colours indicate FDR thresholded (q < 0.05) z-values. The background template and coordinates are in MNI2009c (1mm).

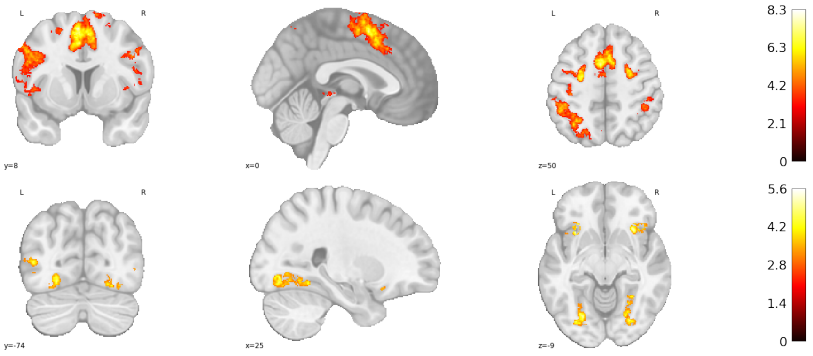

Figure 5.11: Subtraction analyses between activation from the SS – GO contrast in the SST and INC - CON contrast in the MSIT. The MSIT - SST subtraction map is shown on the top, and the SST - MSIT subtraction map on the bottom. Activation colours indicate FDR thresholded (q < 0.05) z-values. The background template and coordinates are in MNI2009c (1mm).

shows significant activation in the INC condition that were not significant in the SS condition (MSIT - SST) and vice versa (SST - MSIT). The MSIT - SST subtraction map indicates a number of significant clusters including the ACC, preSMA, lIFG, anterior supramarginal gyrus (aSG), and Tha. The SST - MSIT subtraction map shows significant activation in the posterior SG (pSG), orbitofrontal cortex, and occipital fusiform gyrus.

5.3.7 GLMs: ROI analyses

5.3.7.1 SST

To statistically quantify the different activation patterns within each trial type and contrast of the SST, we fit a set of GLMs using the canonical HRF to the timeseries extracted from each ROI (see Fig. 5.12). t-values were calculated per run, per ROI for each participant against baseline. In line with previous work (Hollander et al., 2017; Miletić et al., 2020), significant bilateral STN activation was found in FS and GO trials and right STN activation in SS trials (see Supplementary Fig.

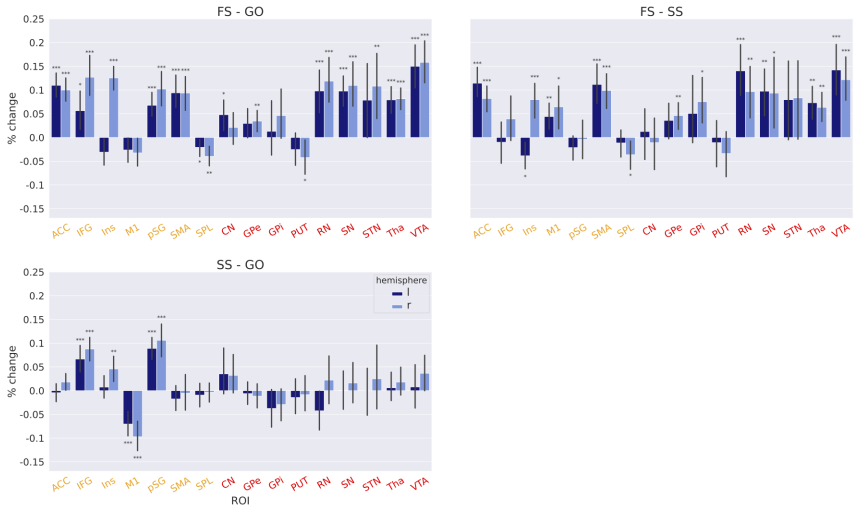

Figure 5.12: ROI analyses for all contrasts in the SST. The y-axis displays percent signal change and the x-axis, ROIs. T-value significance are FDR corrected ($q < 0.05$). Error bars depict the 95% confidence intervals for each region. Left hemisphere is shown in dark blue, and right in light blue. Asterisks denotes significance. FS, failed stops; SS, successful stops; ACC, anterior cingulate cortex; IFG, inferior frontal gyrus; Ins, insula; M1, motor cortex 1; pSG, posterior supramarginal gyrus; SMA, pre-supplementary motor area; SPL, superior parietal lobule; CN; caudate nucleus; GPe, globus pallidus externa; GPi, globus pallidus interna; PUT; putamen; RN, red nucleus; SN, substantia nigra; STN, subthalamic nucleus; Str, striatum; Tha, thalamus; VTA, ventral tegmental area. Orange denotes cortical regions, red, subcortical.

D.1). Other nodes of the direct, indirect, and hyperdirect pathways also showed significant activation in all trial types (rIFG, preSMA, aI, SN, and Tha). Turning to the contrasts of interest, we replicated previous findings that showed that FS trials drive a large portion of activation in the subcortex (Hollander et al., 2017; Miletić et al., 2020). Indeed, the only significant differences in activation found between SS and GO trials in our ROIs were the bilateral IFG, pSG and M1, and right insula. Although SS trials displayed a largely bilateral recruitment of ROIs, the analysis provided evidence of some type of right-lateralized network in the IFG, insula, GPe, GPi, RN, and STN. In the FS – GO contrast, significantly larger activation was found in the ACC, rIFG, r-insula, pSG, preSMA, lCN, rGPe, RN, SN, rSTN, Tha, and VTA. Both cortically and subcortically, similar activation profiles for the FS – GO and FS – SS contrasts were found, with the notable exception of the IFG, pSG, and lCN which showed similar recruitment on both types of stop trials.

5.3.7.2 MSIT

The same ROI analysis was performed for the MSIT (see Fig. 5.13). Compared to baseline, all trial types displayed significant activation in most if not all cortical and

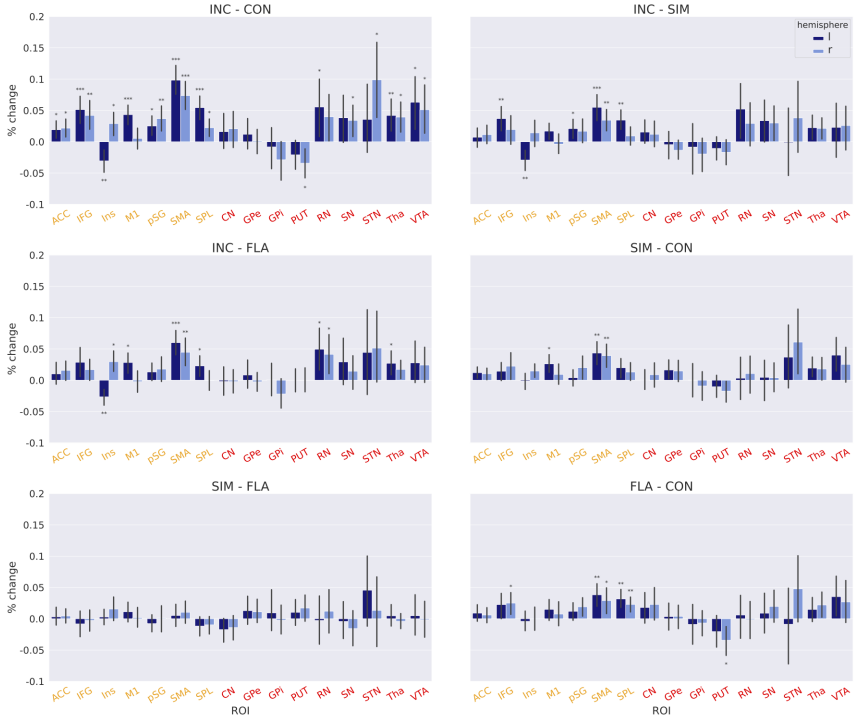

Figure 5.13: ROI analyses for all contrasts in the MSIT. The y-axis displays percent signal change and the x-axis, ROIs. T-value significance are FDR corrected ($q < 0.05$). Error bars depict the 95% confidence intervals for each region. Left hemisphere is shown in dark blue, and right in light blue. Asterisks denotes significance.INC, incongruent; FLA, Flanker; SIM, Simon; CON, congruent; ACC, anterior cingulate cortex; IFG, inferior frontal gyrus; Ins, insula; M1, motor cortex 1; pSG, posterior supramarginal gyrus; SMA, pre-supplementary motor area; SPL, superior parietal lobule; CN, caudate nucleus; GPe, globus pallidus externa; GPi, globus pallidus interna; PUT, putamen; RN, red nucleus; SN, substantia nigra; STN, subthalamic nucleus; Str, striatum; Tha, thalamus; VTA, ventral tegmental area. Orange denotes cortical regions, red, subcortical.

subcortical ROIs (see Supplementary Fig. D.2). Cortically, significant differences in activation between the INC and CON trial types appeared in the ACC, IFG, insula, and preSMA, replicating previous studies of the MSIT (Deng et al., 2018). Subcortically, we found regions that have not been previously observed in this task. Subcortical contribution to the INC - CON contrast included the lRN, rSN, rSTN, Tha, and VTA. All of the INC, SIM and FLA trial types displayed a significant difference in the preSMA from the easiest of the conditions CON, suggesting the cortical region plays an important role in the Simon, Flanker, and joint Simon and Flanker types of interference. For the SIM and FLA conditions, no significant activation differences were found.

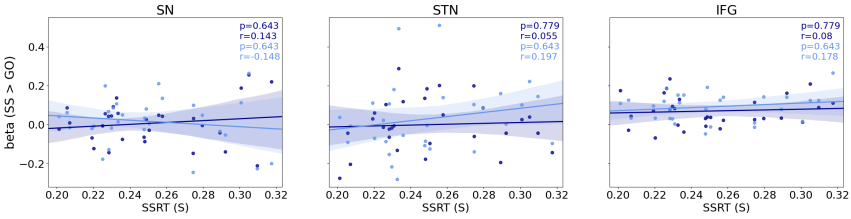

Figure 5.14: Group-level correlations between GLM betas on the SS > Go contrast and SSRTs in the SST. Significance is FDR corrected. r denotes the Pearson correlation, with p the corresponding p-value. Left hemisphere is shown in dark blue. Right hemisphere is shown in light blue.

5.3.8 Model-based analyses

5.3.8.1 SST

To gain insight into which regions code for inhibition, we correlated ROI-based brain activation with our SST model parameters, zooming in on SSRTs (see Fig. 5.14). No significant correlations between ROI activity and model parameters were found. We did not replicate previous findings showing a negative correlation between SSRTs and brain activation in SS > GO trials in the STN and the rIFG (Aron and Poldrack, 2006; Li et al., 2006; Whelan et al., 2012). The same is also true when correlating SSRT with brain activity on SS trial or the FS > SS contrast (see Supplementary Fig. D.3). In order to compare these results to previous literature, we have also correlated brain activity during the SST with SSRTs calculated using the mean method (Logan and Cowan (1984); see Supplementary Fig. D.4) This method calculates SSRT by subtracting the mean SSD from the mean RT of each individual. When correlating SSRT (calculated by the mean method) with the contrast of SS > GO we do not find any significant correlations, in contention to previous work (Aron and Poldrack, 2006; Li et al., 2006). In addition, as the modelling method of SSRT estimation we use here takes significantly more behavioural information into account, and allows the estimation of the entire distribution of SSRTs, we make inferences only based on these SSRTs, not SSRTs calculated using the mean method.

5.3.8.2 MSIT

To observe which regions may code for aspects of interference resolution, we correlated the MSIT model parameters with ROIs that are theorized to be involved in selective inhibition (see Fig. 5.15). For this, we used the difference in drift rate between the incongruent and congruent conditions, which results in $\nu_{Simon} + \nu_{Flank}$ for each participant separately. For our measure of neural activity, we calculated

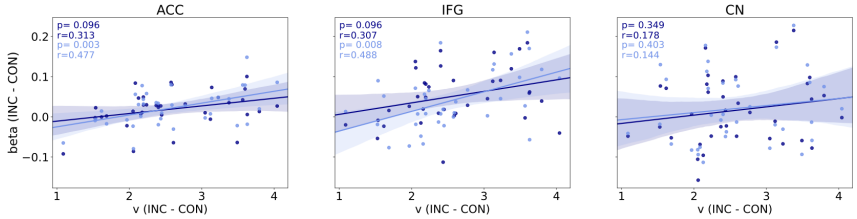

Figure 5.15: Group-level correlations between GLM betas on INC trials and the drift rate of INC trials in the MSIT. Significance is FDR corrected. p denotes the significance level; r denotes the Pearson correlation. Left hemisphere is shown in dark blue. Right hemisphere is shown in light blue.

the difference in activation in each ROI on incongruent and congruent trials. After multiple comparison correction, we found that these cognitive model parameters correlated positively with activation in the right ACC and right IFG. We did not find significant correlations in the left ACC, left IFG, or bilateral CN.

5.4 Discussion

This study aimed to gain insights into the neural and behavioural overlap of response inhibition and interference resolution using a within-subject design. To do so, we tested participants on two tasks, the SST and MSIT, to tap into these subcomponents of inhibition and identify areas of similarities or differences that inter-individual and meta-analytical techniques may miss. Using ultra-high field (UHF) magnetic resonance imaging (MRI), tailored sequences and a high voxel resolution, we were able to obtain robust results, especially in smaller, deeper regions of the brain with a higher SNR than using canonical fMRI at lower fields. Additionally, we used a model-based cognitive neuroscience approach to tap into the latent level of response inhibition and interference control. The results provide evidence of a common network for inhibition-based decision-making as well as the existence of distinctive activation patterns. The whole-brain conjunction map shows that shared activation was found in one central region of the canonical inhibition network, the rIFG, as well as in the aI. Divergent activation regions were found in the main contrast of the MSIT including the ACC, preSMA, lIFG, aSG, and Tha. Inhibition during the SST also involved the recruitment of regions not required for interference resolution, namely the pSG, orbitofrontal cortex (OFC), and occipital fusiform gyrus. The ROI-based analysis is largely in accordance with these whole-brain findings, while suggesting that the posterior division of the supramarginal gyrus may be recruited both in interference resolution and response inhibition.

First, we will discuss the findings of each task separately and compare them to previous task-specific findings before turning to the between-task comparison. For the SST, we replicate recent imaging findings that call into question the idea of the classical inhibitory pathway underlying response inhibition in humans (Hollander et al., 2017; Jahfari et al., 2011; Miletić et al., 2020; Ray Li et al., 2008). Our whole-brain and ROI analyses indicate that neither the STN, nor any other basal ganglia regions displayed heightened activity when comparing SS trials to GO trials, in contrast to much of the literature on response inhibition (Aron and Poldrack, 2006; Aron et al., 2014; Eagle et al., 2008). A large-scale pattern of greater activation in the basal ganglia nuclei when comparing FS trials to GO trials was observed. This suggests that the act of stopping does not drive the recruitment of the canonical indirect or hyperdirect pathway, but that activation in these subcortical regions is driven by a failure to inhibit one's actions. Contrasting FS trials with SS and GO trials displays an almost identical network of heightened activity in the ACC, IFG, insula, preSMA, STN, SN, VTA, Tha, and RN. It is however worth noting that SS and GO trials do recruit these nodes when compared to baseline, but to a much lesser extent than FS trials (see Supplementary Fig. D.1). Significant bilateral IFG activation was observed when comparing both types of stop trials (FS and SS) to GO trials, suggesting the region may play a role in the detection and integration of the salient stop signal, which is a role that has been theorized before and may not be specific to inhibition tasks (Aron et al., 2004; Hampshire et al., 2010; Hampshire et al., 2009; Miller and Cohen, 2001; Shallice et al., 2008; Wessel and Aron, 2013). Although it seems that the BOLD response in this region does not differentiate between successful and failed stopping, electrocorticography has shown increased signaling in successful vs failed stopping (Swann et al., 2009; Wessel and Aron, 2013).

For the MSIT, group-level model estimates of the ν_{Simon} and $\nu_{Flanker}$ parameters are comparable, suggesting that participants are equally biased by the Simon and Flanker effects during the task. In addition, the ROI-based analyses observed no differences in activation between the SIM and FLA conditions at the group-level in any ROI, suggesting that these interference types are rooted in similar brain regions and that they are recruited to a similar degree. Due to the similarity in the two constructs, it may be that a greater number of trials or higher field strength may be required to observe neural differences in their implementation. Contrasting the SIM and FLA conditions with the INC condition display similar responses, with greater activation found in the IFG, preSMA, and SPL for both. For the INC – CON contrast, we observed a marked recruitment of both cortical

and subcortical regions that appear to be required for interference resolution. A recent meta-analysis found activation differences in the ACC, preSMA, IFG, insula and putamen when contrasting these conditions (Deng et al., 2018) Here, we replicate these findings as well as provide evidence that a larger network including the SPL, pSG, GPi/e, STN, SN, RN, Tha, and VTA are also activated during interference resolution. In contrast to other previous findings, we did not see significant activation of the CN during interference resolution (Schmidt et al., 2020).

We performed both conjunction and subtraction analyses of the two tasks to observe common and distinct brain areas involved in response inhibition and interference resolution, respectively. The conjunction analysis indicates an overlap in the rIFG and bilateral aI. We do not observe significant differences in lateralization patterns across the two tasks, in contention to previous meta-analytical findings (Isherwood et al., 2021b). Multiple regions were identified that are recruited during interference resolution and not response inhibition, namely the ACC, preSMA, lIFG, aSG, and Tha. The ACC and preSMA are highly connected and potentially work together to resolve interference in the environment (Nachev et al., 2008). We also found evidence that the OFC and occipital fusiform gyrus play a role in response inhibition but not interference resolution. Many studies have associated the OFC with the ability to inhibit (Adnan Majid et al., 2013; Eagle et al., 2008; Kringelbach and Rolls, 2004). Although the OFC appears to be recruited during response inhibition, the activation does not appear inhibition-specific as it is observed in a wide variety of roles including value-based decision-making (Montague and Berns, 2002; O'Doherty, 2014), prediction error signaling (Schultz and Dickinson, 2000; Sul et al., 2010) and associative representations (Bechara et al., 1997; Bechara et al., 2001). The activation of the occipital fusiform gyrus is usually not associated with response inhibition specifically, but does play a role in colour processing (Bartels and Zeki, 2000). This finding may reflect the presentation of the red stop signal in the SST, as it is the only aspect of the two tasks that differ in colour.

The findings presented here paint a picture of largely divergent networks underlying interference resolution and response inhibition in humans. This demonstrates the need for more intra-individual studies when comparing psychological constructs, owing to the minimization in measurement differences, physiological differences (as all task data is derived on the same day) and the possible impact of large individual variation when using different groups. The extent to which these findings provide evidence for the canonical cortico-basal-ganglia loop is

mixed. For the SST, this study provides evidence against the recruitment of the indirect or hyperdirect pathway during successful response inhibition, as both would implicate increased activity in the STN. These results are in contention to both older and more recent models of response inhibition implementation (Aron et al., 2014; Diesburg and Wessel, 2021; Schmidt and Berke, 2017). Resolution of the combined Simon and Flanker effect does appear to recruit nodes of the indirect and hyperdirect pathways. The IFG, rSTN, lSN, and Tha are active during interference resolution, but we do not find evidence of the GPe/GPi or striatum in the network, both at a whole-brain and ROI level. Our model-based analysis of the MSIT revealed that the drift rate difference between INC and CON conditions positively correlated with the difference in activity between INC and CON conditions in the right ACC and right IFG. Since a larger difference in drift rate between the two trial types indicates a greater level of susceptibility to the Simon or Flanker effect, it appears that activity in these two regions somewhat indicate the degree to which participants resolve conflicting stimuli. The ACC has long been suggested to play a role in conflict monitoring (Van Veen and Carter, 2005; Wiecki and Frank, 2013) and these results may indicate that the region encodes the degree of detected conflict. The IFG has been implicated in many roles, but the evidence of drift rate encoding found here suggests it and the ACC are a major requirement for interference resolution. Interestingly, we did not find any evidence of regions encoding for our behavioural measure of response inhibition (SSRT).

Bringing the findings of this study together, it appears that interference resolution and response inhibition recruit markedly separate neural systems. On top of this, the lack of correlation between modelling parameter estimations supports the dissimilarity between processes on a behavioural level. There is therefore little evidence that we should see these two phenomena as two sides of the same inhibition coin. Despite that, the IFG and pSG appear to play a pivotal role in some aspect of both tasks. In view of previous literature, it is likely that the IFG plays a more domain general role in specific types of signal/conflict detection and that it is needed to make the choice of what behavioural step to perform. The continued lack of evidence that the hyperdirect and indirect pathway are solely engaged in successful response inhibition raises serious concerns. We therefore argue that the pathways involved in successful stopping and successful going are integrated and that the nodes constituting these pathways play task-general roles. Considering that regions of basal ganglia display greater activation for failed stopping, this points towards a general network not specific to global response inhibition.

Chapter 6

The canonical stopping network: Revisiting the role of the subcortex in response inhibition

This chapter is submitted as:
S. J. S. Isherwood, S. Kemp, S. Miletić, N. R. Stevenson, P.-L. Bazin, and B. U. Forstmann (2023b). The canonical stopping network: Revisiting the role of the subcortex in response inhibition. *submitted*.

Abstract

This study investigates the functional network underlying response inhibition in the human brain, particularly the role of the basal ganglia in successful response inhibition. We provide evidence that the canonical inhibition pathways may not be recruited during successful response inhibition during the stop signal task (SST). Instead, subcortical nodes including the substantia nigra, subthalamic nucleus, thalamus, and ventral tegmental area are more likely to be activated during failed stop trials, suggesting that successful inhibition does not rely on the recruitment of these nodes. The findings challenge previous functional magnetic resonance imaging (fMRI) studies of the SST and suggest the need to ascribe a separate function to these networks. We also highlight the substantial effect smoothing can have on the conclusions drawn from task-specific GLMs. This study presents a proof of concept for meta-analytical methods that enable the merging of extensive, unprocessed or unreduced datasets. It demonstrates the significant potential that open-access data sharing can offer to the research community. With an increasing number of datasets being shared publicly, researchers will have the ability to conduct meta-analyses on more than just summary data.

6.1 Introduction

Response inhibition, generally defined as the ability to suppress a planned or already-initiated response (Logan, 1985), is an essential part of everyday motor control, and underpinned by a series of cortical and subcortical pathways. Defining the neural mechanisms underlying response inhibition in the neurotypical population has important consequences in the clinical neurosciences, where impairment in these pathways has been associated with a number of neurological and psychiatric diseases including Parkinson's Disease, addiction and schizophrenia (Chowdhury et al., 2018; Claassen et al., 2015; Congdon et al., 2014; Noël et al., 2016; Rømer Thomsen et al., 2018; Seeley et al., 2009).

Response inhibition has been behaviourally examined using the stop signal task (SST) for more than four decades. In the SST, participants make a motor response as quickly as possible in response to a go signal. In a minority of trials (usually around 25% of all trials), a stop signal appears shortly after the onset of the go signal, indicating that the participant should not respond to the go signal in that trial. The stop signal's onset is normally adjusted after each stop signal trial based on stopping success, such that each participant will be able to stop successfully on approximately 50% of trials (Verbruggen et al., 2019). Behavioural dynamics during the SST are interpreted under the framework of the horse race model (Logan and Cowan, 1984). This model proposes that on each stop trial, the presentation of the go stimulus triggers the go process, which races towards a threshold that results in a response. Upon the presentation of the stop signal, a stop process is similarly triggered, which races towards an independent threshold. Depending on whether the go or stop process finishes first, the response is respectively performed or inhibited. Performance on go trials and failed stop (FS) trials (where the participant makes an inappropriate response) is quantified by reaction time (RT). Performance on successful stop (SS) trials (where the stop signal appears and the participant gives no response) is quantified by the stop signal reaction time (SSRT), which estimates the speed of the latent stopping process (Verbruggen et al., 2019).

Contemporary models of response inhibition propose that inhibition is realised via three cortico-basal-ganglia pathways; the *direct*, *indirect*, and *hyperdirect* pathways. While all three are involved in response inhibition and movement, the *hyperdirect* pathway has been theorized to be the pathway through which action is ultimately cancelled (Aron and Poldrack, 2006). The signalling cascade originates from the prefrontal cortex and is thought to implement stopping upon

detection of a stop signal by inhibition of the thalamus (Tha) via the subthalamic nucleus (STN), substantia nigra (SN) and globus pallidus interna (GPi; Coudé et al., 2018; Diesburg and Wessel, 2021). This pathway was originally identified in rodents and non-human primates, but its anatomical plausibility in humans was demonstrated by Chen and colleagues, who measured firing in the frontal cortex 1-2 ms after stimulation of the STN (Chen et al., 2020). The connectivity of these cortico-basal-ganglia tracts have also been demonstrated to be correlated with stopping behaviour (Forstmann et al., 2012; Singh et al., 2021; Xu et al., 2016; Zhang and Iwaki, 2020). Clinical studies have also demonstrated the importance of subcortical regions, particularly the STN, in relation to stopping. Evidence from Parkinson's disease patients undergoing deep brain stimulation has associated the STN with (successful) stopping behaviour (Alegre et al., 2013; Ray et al., 2009; Ray et al., 2012) and demonstrated that bilateral stimulation of this region can improve performance in the SST (Mancini et al., 2019).

Functional imaging research has been used extensively to elucidate which regions are associated with action cancellation. These images are frequently acquired at 3 Tesla (T) and the BOLD response during go (GO), FS, and SS trials is assessed. Contrasts of interest are often FS > GO, SS > GO, and FS > SS. Cortically, three regions have been consistently implicated: the right inferior frontal gyrus (rIFG), pre-supplementary motor area (preSMA) and anterior insula (Aron et al., 2014; Hollander et al., 2017; Isherwood et al., 2023a; Miletić et al., 2020; Swick et al., 2011). In the subcortex, functional evidence is inconsistent. Contrasts of FS > GO or SS > GO have intermittently implicated the STN in the SST (Aron and Poldrack, 2006; Coxon et al., 2016; Yoon et al., 2019), but few studies have detected differences in the BOLD response between FS and SS trials. Notably, many studies have not detected differences in subcortical BOLD activity for these contrasts (see e.g., Bloemendaal et al., 2016; Boehler et al., 2010; Chang and Guenther, 2020; Gaillard et al., 2020; Xu et al., 2015. At higher field strengths (7T), a different pattern emerges. FS > GO and FS > SS contrasts have consistently shown a widespread subcortical BOLD response, with clusters of activation evident in the STN, SN, Tha, GPi, and globus pallidus externa (GPe; Hollander et al., 2017; Isherwood et al., 2023a; Miletić et al., 2020).

These disparities may arise due to the difficulty of imaging the human subcortex in vivo with MRI. Due to its distance from the MR head coils, proximity of sub-regions and varying biophysical properties, the subcortex can have limited inter-regional contrast and a low signal-to-noise ratio (Bazin et al., 2020; Hollander et al., 2017; Isaacs et al., 2018; Isherwood et al., 2021a; Keuken et al., 2018; Miletić et al.,

2022). The subcortical regions are also relatively small structures. For example, the STN has a volume of approximately 82 mm3; 3mm isotropic resolutions therefore provide only 3 - 4 voxels for analysis of a relatively complex structure (Alkemade et al., 2020a). Attaining sufficient signal in the deep brain for accurate statistical analysis is therefore particularly difficult at lower field strengths (Murphy et al., 2007).

Here, we reprocess and reanalyse five functional SST datasets to shed light on the discrepancies in subcortical BOLD responses. Canonical methods of meta-analysis have the tendency to lose information when compiling multiple sources of data, due to reliance on summary statistics and a lack of raw data accessibility. Taking advantage of the recent surge in open access data, we aimed to improve upon these methods by using the raw data now available instead of relying on simple summary measures (e.g., MNI coordinates). Though computationally expensive, the gain in power from reanalysing multiple functional datasets without this loss of information is of huge benefit. In addition, using raw data as a starting point for datasets acquired separately allows one to minimize differences in preprocessing and analyses pipelines. We chose datasets that used similar go stimuli (left or right pointing arrows) to maintain as much consistency across the datasets as possible. Stop signals during the SST are generally either of the auditory or visual type; we opted to use both types in this study with the assumption that they rely on the same underlying inhibition network (Ramautar et al., 2006).

6.2 Methods

6.2.1 Participants

This study combined data from five datasets, two acquired at 3T and three at 7T: *Aron_3T* (Aron and Poldrack, 2006), *Poldrack_3T* (Poldrack et al., 2016), *deHollander_7T* (Hollander et al., 2017), *Isherwood_7T* (Isherwood et al., 2023a), and *Miletic_7T* (Miletić et al., 2020). The number of participants and their relevant demographics for each dataset are as follows: *Aron_3T* - 14 participants (4 female; mean age 28.1 ± 4.1), *Poldrack_3T* - 130 participants (62 female; mean age 31 ± 8.7; age range 21 - 50), *deHollander_7T* - 20 participants (10 female; mean age 26 ± 2.6; age range 22 - 32), *Isherwood_7T* - 37 participants (20 female; mean age 26.3 ± 5.6; age range 19 - 39), and *Miletic_7T* - 17 participants (9 female; mean age 23.7 ± 3.2).

Table 6.1: The principal MR acquisition parameters of the functional scans for each dataset.

Dataset	TR (ms)	TE (ms)	Voxel size (mm)	FOV (mm)	No. slices	GRAPPA
Aron_3T	2000	30	3.125 x 3.125 x 4	200 x 200 x 132	33	N/A
Poldrack_3T	2000	30	3 x 3 x 4	192 x 192 x 136	34	N/A
deHollander_7T	2000	14	1.5 x 1.5 x 1.5	192 x 192 x 97	60	3
Isherwood_7T	1380	14	1.5 x 1.5 x 1.5	192 x 192 x 128	82	3
Miletic_7T	3000	14	1.6 x 1.6 x 1.6	192 x 192 x 112	70	3

6.2.2 Scanning protocols

This section describes the MR acquisition procedure for each dataset. The main acquisition parameters of the functionals scans can be found in Table 6.1, with a detailed account of each dataset's structural and functional scans in the following paragraphs.

For the *Aron_3T* dataset, each participant was scanned on a Siemens Allegra 3T scanner. The session consisted of three functional runs of the SST and an anatomical T1w image. The functional data was collected using a single echo 2D-echo planar imaging (EPI) BOLD sequence (TR = 2000 ms; TE = 30 ms; voxel size = 3.125 x 3.125 x 4 mm; flip angle = 90°; Field of View (FOV) = 200 x 200 x 132 mm; matrix size = 64 x 64; slices = 33; phase encoding direction = A » P). A 1 mm isotropic T1w image was acquired during each session using the MPRAGE sequence (TR = 2300 ms; TE = 2.1 ms; matrix size = 192 x 192).

For the *Poldrack_3T* dataset, each participant was scanned on a Siemens Trio 3T scanner. The session consisted of one functional run of the SST and an anatomical T1w image. The functional data was collected using a single echo 2D-EPI BOLD sequence (TR = 2000 ms; TE = 30 ms; voxel size = 3 x 3 x 4 mm; flip angle = 90°; FOV = 192 x 192 x 136 mm; matrix size = 64 x 64; slices = 34; phase encoding direction = A » P). A 1 mm isotropic T1w image was acquired during each session using the MPRAGE sequence (TR = 1900 ms; TE = 2.26 ms; matrix size = 256 x 256).

For the *deHollander_7T* dataset, each participant was scanned on a Siemens MAGNETOM 7 Tesla (7T) scanner with a 32-channel head coil. The session consisted of three functional runs of the SST, B0 field map acquisition (TR = 1500 ms, TE_1 = 6 ms, TE_2 = 7.02 ms), and an anatomical T1w image. The functional data was collected using a single echo 2D-EPI BOLD sequence (TR = 2000 ms; TE = 14 ms; GRAPPA = 3; voxel size = 1.5 mm isotropic; partial Fourier = 6/8; flip angle = 60°; FOV = 192 x 192 x 97 mm; matrix size = 128 x 128; BW = 1446Hz/Px; slices = 60; phase encoding direction = A » P; echo spacing = 0.8ms). Each run had

an acquisition time of 13:27 min, totalling 40:21 min of functional scanning. A 0.7 mm isotropic T1w image was acquired during each session using the MP2RAGE sequence (TR = 5000 ms; TE = 2.45 ms; inversions TI_1 = 900 ms, TI_2 = 2750 ms; flip angle 1 = 5°; flip angle 2 = 3°; Marques et al., 2010).

For the *Isherwood_7T* dataset, each participant was scanned on a Siemens MAGNETOM TERRA 7T scanner with a 32-channel head coil. The session consisted of two functional runs of the SST, top-up acquisition, and an anatomical T1w image. The functional data was collected using a single echo 2D-EPI BOLD sequence (TR = 1380 ms; TE = 14 ms; MB = 2; GRAPPA = 3; voxel size = 1.5 mm isotropic; partial Fourier = 6/8; flip angle = 60°; FOV = 192 x 192 x 128 mm; matrix size = 128 x 128; BW = 1446 Hz/Px; slices = 82; phase encoding direction = A » P; echo spacing = 0.8 ms). Each run had an acquisition time of 13:27 min, totalling 26:54 min of functional scanning. Subsequently to each run, five volumes of the same protocol with opposite phase encoding direction (P » A) were collected (top-up) for distortion correction. A 1 mm isotropic T1w image was acquired during each session using the MP2RAGE sequence (TR = 4300 ms; TE = 1.84 ms; inversions TI_1 = 840 ms, TI_2 = 2370 ms; flip angle 1 = 5°; flip angle 2 = 6°; Marques et al., 2010).

For the *Miletic_7T* dataset, each participant was scanned on a Siemens MAGNETOM 7T scanner with a 32-channel head coil. The session consisted of three functional runs of the SST, B0 field map acquisition (TR = 1500 ms, TE_1= 6 ms, TE_2 = 7.02 ms), and an anatomical T1w image. The functional data was collected using a single echo 2D-EPI BOLD sequence (TR = 3000 ms; TE = 14 ms; GRAPPA = 3; voxel size = 1.6 mm isotropic; partial Fourier = 6/8; flip angle = 70°; FOV = 192 x 192 x 112 mm; matrix size = 120 x 120; BW = 1436 Hz/Px; slices = 70; phase encoding direction = A » P; echo spacing = 0.8 ms). A 0.7 mm isotropic T1w image was acquired during each session using the MP2RAGE sequence (TR = 5000 ms; TE = 2.45 ms; inversions TI_1 = 900 ms, TI_1 = 2750 ms; flip angle 1 = 5°; flip angle 2 = 3°; Marques et al., 2010).

6.2.3 Procedure and exclusions

Participants that were not accompanied by a T1w anatomical image were automatically excluded from the study as the image is required for registration during preprocessing. In addition, the behavioural data of each participant from each database were quality controlled on the basis of a specific set of exclusion criteria. These criteria include (1) more than 10% go-omissions across all functional runs; (2) a stopping accuracy of less than 35% or more than 65%; (3) a go-accuracy of less than 95%; (4) mean signal respond RTs that were longer on average than

go RTs (inconsistent with the standard race model). Based on these criteria, no subjects were excluded from the *Aron_3T* dataset, 24 from the *Poldrack_3T* dataset, three from the *deHollander_7T* dataset, five from the *Isherwood_7T* dataset, and two from the *Miletic_7T* dataset. A further nine participants were excluded from the *Poldrack_3T* dataset due to a lack of T1w image or a lack of SST data. As the specific genders and ages of each participant in each dataset are not all available due to General Data Protection Regulations (GDPR), we were unable to recalculate participant demographics after exclusions. The final number of participants in each dataset after screening is as follows: *Aron_3T*, 14 participants; *Poldrack_3T*, 97 participants; *deHollander_7T*, 17 participants; *Isherwood_7T*, 31 participants; *Miletic_7T*, 15 participants. Therefore, the analyses in this paper are based on stop signal data from 5 datasets, 174 participants and 293 runs.

6.2.4 Stop signal task (SST)

All datasets used a simple, two alternative choice stop signal paradigm. This paradigm consists of two trial types, go trials, and stop trials. On each trial, an arrow is presented on the screen in either the left or right direction (the go stimulus). The participant presses the button corresponding to the direction of the arrow. On a subset of trials (25%), a stop signal appears shortly after go signal onset, indicating the participant should try to inhibit their movement and not respond in that trial. In the auditory SST, this stop signal is presented as a 'beep' sound. In the visual SST, this stop signal is presented as a change in visual stimulus; for example, in the *Isherwood_7T* dataset, the circle surrounding the arrow would change from white to red. The time between the presentation of the go stimulus and the stop signal is defined by the stop signal delay (SSD). The SSD is adapted iteratively during the task. Generally, if the participant responds during a stop trial, the SSD is reduced by 50 ms on the next stop trial, meaning the stop signal will appear earlier in the next trial and it will be easier for the participant to inhibit their response. Conversely, if the participant stops successfully, the SSD will increase by 50 ms and the stop signal will appear later in the next trial This method of SSD adaptation is known as a staircase procedure and ensures that each participant is able to inhibit their actions approximately 50% of the time. Task performance in this paradigm is characterized by the race model (Logan and Cowan, 1984). The model assumes a go process and a stop process race independently and whichever finishes first defines whether a participant responds or inhibits their actions. The go process is characterized by the observable go RT,

Table 6.2: Task details for the SST in each dataset.

Dataset	Response modality	Type	Stop signal duration (ms)	No. staircases	SSD range (ms)	Total no. trials	Stop trials (%)
Aron_3T	Hand, R	Auditory	500	4	100 - 250	384	25
Poldrack_3T	Hand, R	Auditory	250	2	N/A	128	25
deHollander_7T	Hand, L/R	Auditory	62	4	0 – 2000	384	25
Isherwood_7T	Hand, L/R	Visual	300	1	50 – 900	200	25
Miletic_7T	Hand, L/R	Auditory	62	2	0 – 2000	342	25

whereas the stop process is characterized by the latent SSRT, which is estimated based on the effects of the SSD throughout the task.

Although the SST employed in each dataset is similar, there are some differences which are detailed in Table 6.2. We note here the most important differences in design aspects of the SSTs, these include (1) Response modality, describing the manual response and whether left (L), right (R) or both (L/R) hands were used; (2) Type, describing whether the stop signal was auditory or visual; (3) Stop signal duration, how long the auditory or visual stop signal was presented for; (4) Number of staircases, describing the number of staircases used to track the SSD of each participant during the task; (5) SSD range, describing the minimum and maximum values that the SSD could be during the task; (6) total trial number, the number of trials each participant performed over all runs; (7) Stop trials, the percentage of overall trials that were stop trials (as opposed to go trials).

6.2.5 Behavioural analyses

For all runs within each dataset, median RTs on go and stop trials, the mean SSD and proportion of successful stops were calculated. For each participant, the SSRT was calculated using the mean method, estimated by subtracting the mean SSD from median go RT (Aron and Poldrack, 2006; Logan and Cowan, 1984). Both frequentist and Bayesian analyses methods were used to calculate the correlation between mean SSRTs and median go RTs, as well as to test the statistical difference between median failed stop RTs and median go RTs.

6.2.6 fMRIprep preprocessing pipeline

fMRIPrep was used to preprocess all acquired anatomical and functional data (Esteban et al., 2020; Esteban et al., 2018). The following two sections describe, in detail, the preprocessing steps that fMRIPrep performed on each dataset.

6.2.6.1 Anatomical data preprocessing

A total of 1 T1-weighted (T1w) images was found within the input for each subject of each BIDS dataset. The T1-weighted (T1w) image was corrected for intensity non-uniformity (INU) with N4BiasFieldCorrection (Tustison et al., 2010), distributed with ANTs 2.3.3 (Avants et al., 2008, RRID:SCR_004757), and used as T1w-reference throughout the workflow. The T1w-reference was then skull-stripped with a Nipype implementation of the antsBrainExtraction.sh workflow (from ANTs), using OASIS30ANTs as target template. Brain tissue segmentation of cerebrospinal fluid (CSF), white matter (WM) and grey matter (GM) was performed on the brain-extracted T1w using fast (FSL 5.0.9, RRID:SCR_002823, Zhang et al., 2001). Brain surfaces were reconstructed using recon-all (FreeSurfer 6.0.1, RRID:SCR_001847, Dale et al., 1999), and the brain mask previously estimated was refined with a custom variation of the method to reconcile ANTs-derived and FreeSurfer-derived segmentations of the cortical grey matter of Mindboggle (RRID:SCR_002438, Klein et al., 2017). Volume-based spatial normalization to one standard space (MNI152NLin2009cAsym) was performed through nonlinear registration with antsRegistration (ANTs 2.3.3) using brain-extracted versions of both T1w reference and the T1w template. The following template was selected for spatial normalization: ICBM 152 Nonlinear Asymmetrical template version 2009c (Fonov et al., 2009, RRID:SCR_008796; TemplateFlow ID: MNI152NLin2009cAsym).

6.2.6.2 Functional data preprocessing

For each of the BOLD runs per subject (across all datasets), the following preprocessing was performed. First, a reference volume and its skull-stripped version were generated using a custom methodology of fMRIPrep. For datasets where a distortion correction image was not acquired (*Aron_3T* and *Poldrack_3T*), a deformation field to correct for susceptibility distortions was estimated based on fMRIPrep's fieldmap-less approach. The deformation field is that resulting from co-registering the BOLD reference to the same-subject T1w-reference with its intensity inverted (Wang et al., 2017). Registration is performed with antsRegistration (ANTs 2.3.3), and the process regularized by constraining deformation to be nonzero along the phase-encoding direction, and modulated with an average fieldmap template (Treiber et al., 2016). For the *deHollander_7T* and *Miletic_7T* datasets, a B0-nonuniformity map (or fieldmap) was estimated based on a phase-difference map calculated with a dual-echo gradient-recall echo sequence, processed with a custom workflow of SDCFlows inspired by the epidewarp.fsl script

with further improvements in HCP Pipelines (Uğurbil et al., 2013). The fieldmap was then co-registered to the target EPI reference run and converted to a displacements field map (amenable to registration tools such as ANTs) with FSL's fugue and other SDCflows tools. For the *Isherwood_7T* dataset, a B0-nonuniformity map (or fieldmap) was estimated based on two EPI references with opposing phase-encoding directions, with 3dQwarp (Cox and Hyde, 1997; AFNI 20160207). Based on the estimated susceptibility distortion, a corrected EPI reference was calculated for a more accurate co-registration with the anatomical reference. The BOLD reference was then co-registered to the T1w reference using bbregister (FreeSurfer) which implements boundary-based registration (Greve and Fischl, 2009). Co-registration was configured with six degrees of freedom. Head-motion parameters with respect to the BOLD reference (transformation matrices, and six corresponding rotation and translation parameters) were estimated before any spatiotemporal filtering using mcflirt (FSL 5.0.9, Jenkinson et al., 2002). BOLD runs were slice-time corrected using 3dTshift from AFNI 20160207 (Cox and Hyde, 1997; RRID:SCR_005927). The BOLD time-series (including slice-timing correction when applied) were resampled onto their original, native space by applying a single, composite transform to correct for head-motion and susceptibility distortions. These resampled BOLD time-series will be referred to as preprocessed BOLD in original space, or just preprocessed BOLD. Several confounding time-series were calculated based on the preprocessed BOLD: framewise displacement (FD), DVARS and three region-wise global signals. FD was computed using two formulations following Power (absolute sum of relative motions, Power et al., 2014) and Jenkinson (relative root mean square displacement between affines, Jenkinson et al., 2002). FD and DVARS are calculated for each functional run, both using their implementations in Nipype (following the definitions by Power et al., 2014). The three global signals are extracted within the CSF, the WM, and the whole-brain masks. Additionally, a set of physiological regressors were extracted to allow for component-based noise correction (CompCor, Behzadi et al., 2007). Principal components are estimated after high-pass filtering the preprocessed BOLD time-series (using a discrete cosine filter with 128 s cut-off) for the two CompCor variants: temporal (tCompCor) and anatomical (aCompCor). tCompCor components are then calculated from the top 2% variable voxels within the brain mask. For aCompCor, three probabilistic masks (CSF, WM and combined CSF+WM) are generated in anatomical space. The implementation differs from that of Behzadi et al. in that instead of eroding the masks by 2 pixels on BOLD space, the aCompCor masks are subtracted a mask of pixels that likely contain a

volume fraction of GM. This mask is obtained by dilating a GM mask extracted from the FreeSurfer's aseg segmentation, and it ensures components are not extracted from voxels containing a minimal fraction of GM. Finally, these masks are resampled into BOLD space and binarized by thresholding at .99 (as in the original implementation). Components are also calculated separately within the WM and CSF masks. For each CompCor decomposition, the k components with the largest singular values are retained, such that the retained components' time series are sufficient to explain 50 percent of variance across the nuisance mask (CSF, WM, combined, or temporal). The remaining components are dropped from consideration. The head-motion estimates calculated in the correction step were also placed within the corresponding confounds file. The confound time series derived from head motion estimates and global signals were expanded with the inclusion of temporal derivatives and quadratic terms for each (Satterthwaite et al., 2013). Frames that exceeded a threshold of .5 mm FD or 1.5 standardised DVARS were annotated as motion outliers. All resamplings can be performed with a single interpolation step by composing all the pertinent transformations (i.e. head-motion transform matrices, susceptibility distortion correction when available, and co-registrations to anatomical and output spaces). Gridded (volumetric) resamplings were performed using antsApplyTransforms (ANTs), configured with Lanczos interpolation to minimize the smoothing effects of other kernels (Lanczos, 1964). Non-gridded (surface) resamplings were performed using mri_vol2surf (FreeSurfer).

6.2.7 Temporal signal to noise ratios (tSNRs)

Sequence sensitivity in BOLD fMRI can be approximated by the calculation of the temporal signal to noise ratio (tSNR). While it is not possible discriminate the exact source of noise causing temporal fluctuations in measured signal, they are thought to arise from either thermal or physiological interference. To get a feel for the image quality in different regions of the brain between datasets, we here compared region of interest (ROI)-wise tSNRs. Using probabilistic atlases, we took the mean of the ROI signal and divided by its standard deviation across time. Each voxels contribution to the mean signal of the region was weighted by its probability of belonging to the region While simple to calculate, tSNR comparison between data of differing acquisition methods is less trivial. Here, we only correct for the differences in voxel size between datasets. As spatial resolution is directly proportional to MR signal, we divided these tSNR values by the volume of a single voxel (Edelstein et al., 1986). tSNR was calculated using the exact same data

used in the ROI-wise GLMs. That is, unsmoothed but preprocessed data from fMRIprep.

6.2.8 fMRI analysis – general linear models (GLMs)

GLM analyses were computed at both a whole-brain voxel-wise and region-specific level. A canonical double gamma hemodynamic response function (HRF) with temporal derivative was used as the basis set for both methods of analysis (Glover, 1999). The design matrix consisted of the three task-specific regressors for each of the three experimental conditions; failed stop (FS) trials, successful stop (SS) trials and go (GO) trials, six motion parameters (three translational and three rotational) as well as DVARS and framewise displacement estimated during preprocessing. The first 20 aCompCor components from fMRIPrep were used to account for physiological noise (Behzadi et al., 2007). Following data preprocessing through fMRIPrep, all data were high-pass filtered (cut-off 1/128 Hz) to remove slow drift. Three SST contrasts were computed for both the whole-brain and region of interest (ROI) GLMs: FS > GO, FS > SS and SS > GO.

6.2.8.1 Voxel-wise

Whole-brain analyses were computed using the FILM method from FSL FEAT (version 6.0.5.2; Jenkinson et al., 2012; Woolrich et al., 2001 as implemented in the Python package wrapper Nipype (version 1.7.0; Gorgolewski et al., 2011). Run-level GLMs accounting for autocorrelated residuals were computed, the results warped to MNI152NLin2009cAsym space, and subsequently combined per subject using fixed effects analyses. Data for the whole-brain GLMs were spatially smoothed using the SUSAN method with a full width half maximum (FWHM) equal to the voxel size of the functional image (Smith and Brady, 1997). Therefore, a 3.125 mm kernel was applied to the *Aron_3T* dataset, a 3 mm kernel to the *Poldrack_3T* dataset, a 1.5 mm kernel to the *deHollander_7T* and *Isherwood_7T* datasets, and a 1.6 mm kernel to the *Miletic_7T* dataset. These base-level kernels were applied to the data used for the main statistical analyses. Group-level models were subsequently estimated using FMRIB Local Analysis of Mixed Effects (FLAME) 1 and FLAME 2 from FSL (Woolrich et al., 2001), taking advantage of the fact that FLAME allows the estimation of different variances for each dataset. Dummy variables were used as regressors to allow the categorization of data into different datasets so that they could be estimated separately and then combined. Statistical parametric maps (SPMs) were generated to visualize the resulting group-

level models. The maps were corrected for the false discovery rate (FDR) using critical value of q < .05 (Yekutieli and Benjamini, 1999).

6.2.8.2 ROI-wise

ROI analyses were then performed. Timeseries were extracted from each subcortical region of interest using probabilistic masks provided by MASSP (Bazin et al., 2020), except in the case of the putamen and caudate nucleus, which were provided by the Harvard-Oxford subcortical atlas (Rizk-Jackson et al., 2011). Each voxels contribution to the mean signal of the region was therefore weighted by its probability of belonging to the region. Cortical regions parcellations were provided by the Harvard-Oxford cortical atlas (Rizk-Jackson et al., 2011). These timeseries were extracted from unsmoothed data so to ensure regional specificity. ROI analyses were computed using the FILM method of FSL FEAT. To do this, we inputted each run for each participant in MNI152NLin2009cAsym space, where the signal of each region was replaced with its mean extracted timeseries. Hence, the signal within each region was homogenous on each given volume. ROIs were therefore defined before implementing the ROI analyses. The regions include the inferior frontal gyrus (IFG), primary motor cortex (M1), pre-supplementary motor area (preSMA), caudate nucleus (caudate), GPe, GPi, putamen, SN, STN, Tha, and VTA. Due to the restricted FOV of the *deHollander_7T* dataset, this dataset was not used in the ROI-wise analysis of the M1 and preSMA regions. M1 and preSMA ROI-wise results are therefore based only on the *Aron_3T*, *Poldrack_3T*, *Isherwood_7T*, and *Miletic_7T* datasets. After the run-level GLMs were computed using FILM, the same fixed effects analyses and subsequent mixed-effects analyses used in the voxel-wise GLMs were performed.

6.2.9 Smoothing comparison

To further understand the impact of preprocessing on fMRI analyses, we computed voxel-wise GLM results based on a more lenient smoothing kernel. To observe the effect of smoothing on these analyses, we compared the results of our main statistical analyses, using base-level kernel sizes, to the same data when all datasets were smoothed using a 5 mm FWHM kernel. We chose to compared base-level smoothing kernels to 5 mm as this was the kernel sized used in the Aron and Poldrack (2006) study. To do this, the same voxel-wise GLM method was used as described above.

Table 6.3: Descriptive statistics of behaviour in the SST across each dataset. Standard errors are given.

Dataset	Median go RT (ms)	Median failed stop RT (ms)	Go omissions (%)	Go errors (%)	Mean SSRT (ms)	Median SSD (ms)	Mean stopping accuracy (%)
Aron_3T	423 ± 18	382 ± 11	.7 ± .4	.6 ± .2	196 ± 10	227 ± 17	53 ± 1
Poldrack_3T	466 ± 9	426 ± 8	.1 ± .04	.9 ± .1	187 ± 5	279 ± 11	52 ± .6
deHollander_7T	472 ± 24	439 ± 22	1.6 ± .5	.3 ± .1	222 ± 9	250 ± 22	54 ± 2
Isherwood_7T	626 ± 25	543 ± 22	1.9 ± .4	2.2 ± .4	251 ± 6	350 ± 30	54 ± 1
Miletic_7T	445 ± 17	414 ± 15	1.1 ± .5	.7 ± .2	215 ± 18	230 ± 23	50 ± 1

6.3 Results

6.3.1 Behavioural analyses

Table 6.3 summarizes the descriptive statistics of the behavioural data from each dataset. The median failed stop RT is significantly faster within all datasets than the median go RT (*Aron_3T*: p = 4.44e-5, BF = 590.75; *Poldrack_3T*: p < 2.2e-16, BF = 3.06e+23; *deHollander_7T*: p = 1.21e-11, BF = 7.57e+8; *Isherwood_7T*: p = 2.75e-5, BF = 897.41; *Miletic_7T*: p = .0019, BF = 22.39), consistent with assumptions of the standard horse-race model (Logan and Cowan, 1984). Mean SSRT was calculated using the mean method and are all within normal range across the datasets. The mean stopping accuracy (near 50%) across all datasets indicates that the staircasing procedure operated accordingly and successfully kept SSDs tailored to the SSRT of participants during the task. In addition, median go RTs did not correlate with mean SSRTs within datasets (*Aron_3T*: r = .411, p = .10, BF = 1.41; *Poldrack_3T*: r = .011, p = .91, BF = .23; *deHollander_7T*: r = -.30, p = .09, BF = 1.30; *Isherwood_7T*: r = .13, p = .65, BF = .57; *Miletic_7T*: r = .37, p = .19, BF = 1.02), indicating independence between the stop and go processes, an important assumption of the horse-race model (Logan and Cowan, 1984).

6.3.2 tSNRs

To observe quantitative differences in signal quality between the datasets, we first calculated ROI-wise tSNR maps of the unsmoothed data. In Fig. 6.1 we show both the corrected and uncorrected tSNR values for five ROIs. As the tSNR values across each hemisphere were similar, we opted to take the mean across both. The corrected tSNR values display the clear benefit of 7T acquisition compared to 3T in terms of data quality. In the cortical ROIs, the 7T datasets appear to perform equally well, though when zooming in on subcortical ROIs, the *deHollander_7T* and *Miletic_7T* datasets display superiority. The uncorrected tSNR values paint a different picture. These tSNRs are even across all the datasets, with the exception

Figure 6.1: Corrected and uncorrected tSNR values for five ROIs over all datasets. The values are derived from the mean tSNR values of both hemispheres. Error bars are standard errors. Corrected tSNRs are equal to the uncorrected tSNRs divided by the volume of a single voxel. IFG, inferior frontal gyrus; SN, substantia nigra; STN, subthalamic nucleus; Tha, thalamus; VTA, ventral tegmental area.

of the *Isherwood_7T* dataset which appears to suffer, most likely due to its increased multiband factor (Chen et al., 2015). It should be noted that interpretation of the uncorrected tSNR values is difficult, due to the inherent proportionality of tSNR and voxel volume (Edelstein et al., 1986). That is, the 3T datasets acquire data with a voxel volume approximately ten times smaller than that of the 7T datasets and therefore have an advantage when not correcting for this difference.

6.3.3 Voxel-wise GLMs

We calculated whole-brain voxel-wise GLMs using the canonical HRF with a temporal derivative to statistically observe the brain areas underlying behaviour in the SST. The three trial types result in three possible contrasts: FS > GO, FS > SS, and SS > GO. Due to the restricted FOV of the images acquired in the *deHollander_7T* dataset, group-level SPMs display a limited activation pattern at the most superior part of the cortex, as no data were acquired there for one dataset. We first show the group-level SPMs of the overall contrasts of the SST across all datasets (see Fig. 6.2), the SPMs for each contrast of each individual dataset can be found in the appendix (supplementary Figs. E.1, E.2 & E.3). Significant BOLD responses for the FS > GO contrast were found in the bilateral IFG, preSMA, SN,

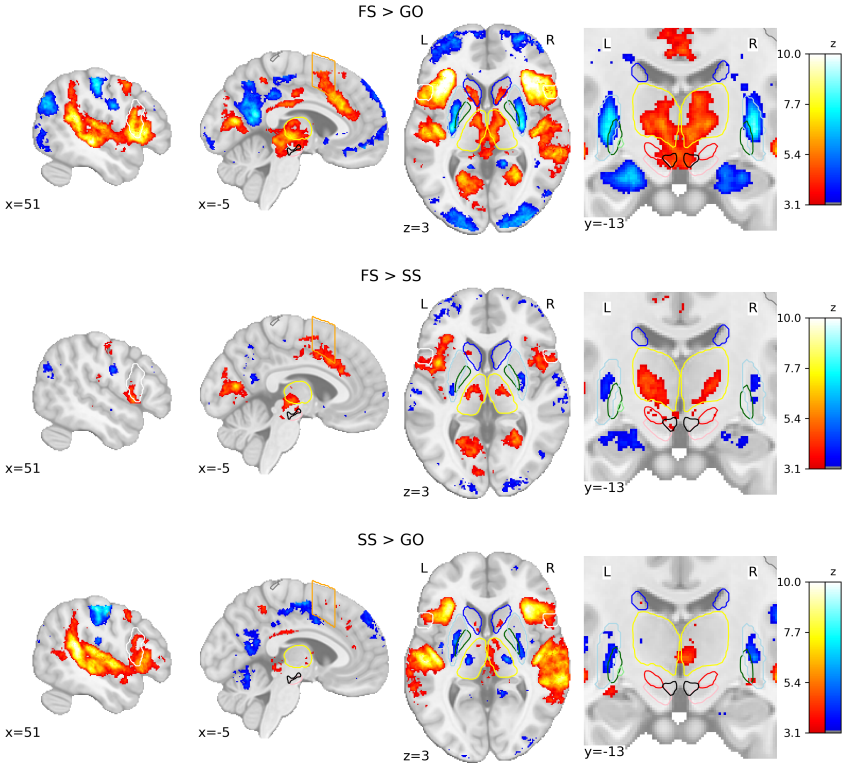

Figure 6.2: Group-level SPMs of the three main contrasts of the SST. Activation colours indicate FDR thresholded (q < .05) z-values. Two sagittal, one axial, and one zoomed in coronal view are shown. Coloured contour lines indicate regions of interest (IFG in white, M1 in grey, preSMA in orange, Caudate in dark blue, Putamen in light blue, GPe in dark green, GPi in light green, SN in pink, STN in red, thalamus in yellow, and VTA in black). The background template and coordinates are in MNI2009c (1mm). FS, failed stop; SS, successful stop.

STN and VTA. It can be clearly seen that this contrast elicits the largest subcortical response out of the three. The FS > SS contrast shows significant bilateral activation in the IFG, STN, Tha and VTA. The SS > GO contrast shows significant activation in the bilateral IFG and Tha.

6.3.4 ROI-wise GLMs

To further statistically compare the functional results between datasets, we then fit a set of GLMs using the canonical HRF with a temporal derivative to the timeseries extracted from each ROI. Below we show the results of the group-level ROI analyses over all datasets (Fig. 6.3). Overall, these results are in line with the group-level voxel-wise GLMs. To account for multiple comparisons, threshold values were set using the FDR method, with a minimum z-score of 3.1 to ensure

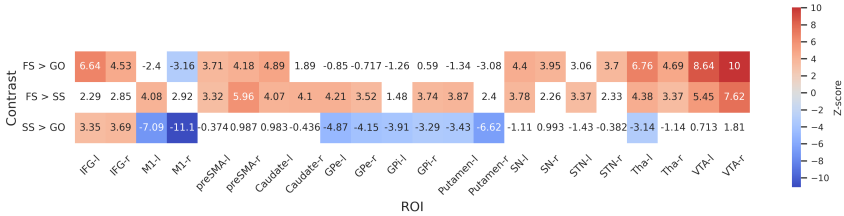

Figure 6.3: Group-level z-scores from the ROI-wise GLM analysis of included datasets. Thresholds are set using FDR correction (q < .05), with a minimum threshold of 3.1. Regions that do not reach significance are coloured white. Left and right hemispheres are shown separately, denoted by '-l' or '-r', respectively. IFG, inferior frontal gyrus; M1, primary motor cortex; preSMA, pre-supplementary motor area; GPe, globus pallidus externa; GPi, globus pallidus interna; SN, substantia nigra; STN, subthalamic nucleus; Tha, thalamus; VTA, ventral tegmental area.

conservatism. For the FS > GO contrast, we found significant positive z-scores in the bilateral IFG, preSMA, SN, Tha, VTA, left caudate, and right STN as well as significant negative z-scores in the right M1. For the FS > SS contrast we found significant positive z-scores in the bilateral preSMA, caudate, GPe, Tha, VTA, left M1, putamen, SN, STN, and right GPi. None of our ROIs were significantly more recruited during SS trials than FS trials. For the SS > GO contrast we found a significant positive z-scores in the bilateral IFG and significant negative z-scores in bilateral M1, GPe, GPi, putamen, and left Tha. Left/right differences in M1 may be explained by the differences in response modality between datasets (the *Aron_3T* and *Poldrack_3T* datasets only used the right hand for responses). Upon further inspection of the group-level data, left/right differences in M1 appears to be driven by larger variance estimates of the left M1.

6.3.5 Smoothing comparison

To visualize the effect of spatial smoothing on voxel-wise GLMs, we computed SST contrasts using base-level kernels and a kernel of 5 mm. The difference in group-level SPMs for SS > GO contrast is prominent (see Fig 6.4). Comparisons for the contrasts of FS > GO and FS > SS contrasts can be found in Supplementary Figure E.4. If we were to make inferences based on the group-level SPMs calculated using the 5 mm kernel, this study could potentially incorrectly conclude that both the SN and VTA are significantly activated in SS trials compared to GO trials. Much larger regions of significant activation can be seen in the 5 mm smoothed SPMs, both cortically and subcortically. This comparison demonstrates the prominent consequences that preprocessing pipelines can have on the overall analysis of functional data.

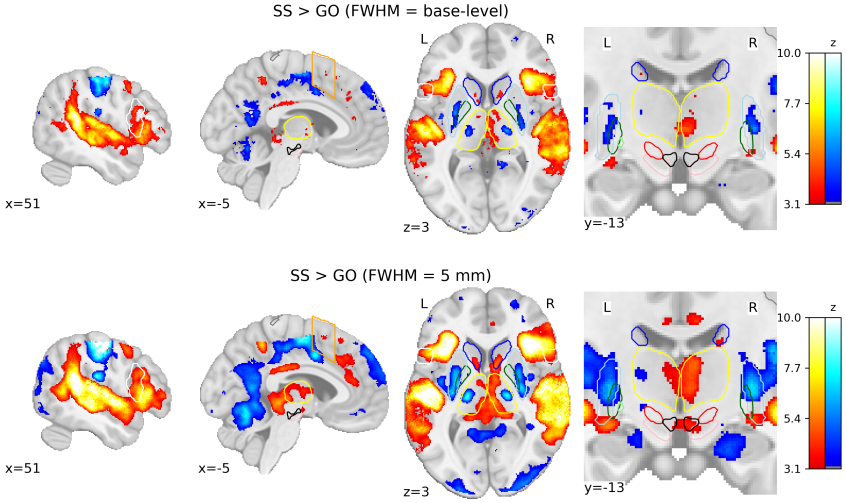

Figure 6.4: Comparison of group-level SPMs for the SS > GO contrast using different smoothing kernels. SPMs resulting from GLMs computed on base-level spatially smoothed data can be seen on the top row, with SPMs resulting from GLMs computed on data spatially smoothed with a FHWM of 5 mm. Activation colours indicate FDR thresholded (q < .05) z-values. Two sagittal, one axial, and one zoomed in coronal view are shown. Coloured contour lines indicate regions of interest (IFG in white, M1 in grey, preSMA in orange, Caudate in dark blue, Putamen in light blue, GPe in dark green, GPi in light green, SN in pink, STN in red, thalamus in yellow, and VTA in black). The background template and coordinates are in MNI2009c (1mm). FS, failed stop; SS, successful stop.

6.4 Discussion

The functional network underlying response inhibition in the human brain has been a pinnacle research question in the cognitive neurosciences for decades. The basal ganglia specifically have been implicated in broad movement control since the early twentieth century (Wilson, 1912). However, the role of these subcortical structures in successful response inhibition is unclear. Evidence for the role of the basal ganglia in response inhibition comes from a multitude of studies citing significant activation of either the SN, STN or GPe during successful inhibition trials (Aron, 2007; Aron and Poldrack, 2006; Mallet et al., 2016; Nambu et al., 2002; Zhang et al., 2019). Here, we provide evidence that the canonical inhibition pathways, both *indirect* and *hyperdirect*, may not be recruited during successful response inhibition during the SST. We expected to find increased activation in the nodes of the *indirect* pathway (e.g., the STN, SN, GPe) during successful stop compared to go or failed stop trials, but we could not find evidence for this. Instead, we find a large recruitment of subcortical nodes, including the SN, STN, Tha, and VTA during failed stop trials (when compared to go trials). Due to the larger degree of positive BOLD responses in subcortical structures (SN, STN, Tha, and VTA) in the FS > GO and FS > SS contrasts, there is an indication that successful inhibition does not rely on the recruitment of these nodes. Moreover, it appears that failing to inhibit one's action drives the utilisation of these nodes, pointing to the need to ascribe a separate function to these networks.

These results are in contention to previous fMRI studies of the stop signal task as well as an array of studies using different measurement techniques such as local field potential recordings (Alegre et al., 2013; Benis et al., 2014; Wessel et al., 2016c). Furthermore, FS trials have been relatively understudied, as they do not cleanly reflect the inhibition network that is rightly the main area of attention. It is likely that the inhibition network is at least partially active even when inhibition is unsuccessful. From both the voxel-wise and ROI-wise analyses it is clear that the VTA plays a role in the mechanisms underlying FS trials. Investigation into the specific role of the VTA and dopaminergic system in response inhibition has led to conflicting results (Aron et al., 2003; Boonstra et al., 2005). Inhibition of the VTA has been seen to increase the number of premature responses in a five-choice serial reaction time task in rats (Flores-Dourojeanni et al., 2021), the VTA appears to degenerate in Parkinson's Disease (Alberico et al., 2015), and is associated with reward uncertainty in response inhibition tasks (Tennyson et al., 2018). Feedback in the SST is inherent in its design; a failure to stop simultaneously triggers the

realization that an error was made, without the need for explicit task feedback. Speculatively, a failure to stop could trigger nodes of the mesolimbic pathway in response to this action error, as the VTA is known to respond to reward prediction errors (Bayer and Glimcher, 2005; Eshel et al., 2015; Schultz et al., 1997).

This is not the first aggregatory study that has found limited activation of basal ganglia regions when specifically looking at successful response inhibition (Hung et al., 2018; Isherwood et al., 2021b; Zhang et al., 2017). Although, from our literature search, this is the first study to take advantage of an array of unprocessed open-access data. Now that it is becoming increasingly common for researchers to make such detailed data available, it is beneficial for the research field to move on from meta-analytical methods that use only summary measures of activation profiles. Although, it should be noted, that canonical methods of meta-analysis still provide advantages over more processing-intensive methods such as applied here. Firstly, on the scale of five datasets, this methodology was applied and completed relatively quickly, but standard meta-analyses can include tens if not hundreds of studies, a feat that would be difficult to manage for the method described here. Secondly, the sample reported here is somewhat biased, it includes only data that were openly accessible in full, it is likely there are many more studies that would be useful to answer the research question posited here. Simpler methods of meta-analysis, where only coordinates or summary measures are needed to aggregate data, benefit from having access to a much wider range of potential sources of data. What we have been able to do here, even with a limited number of datasets, is process all the data with the same set of criteria. We therefore benefitted from sets of extremely well-vetted behavioural and functional data, that can have all aspects of the datasets compared to one another. This allowed us to tightly control aspects of the preprocessing pipeline that can affect later analyses steps, such as distortion correction and smoother kernel sizes.

The consequences of spatial smoothing on statistical analyses are well known and can have huge effects on group or subject-level inferences (Chen et al., 2018; Mikl et al., 2008). Here, we have shown again the substantial effect smoothing can have on the conclusions drawn from task-specific GLMs. Based on the results of the smoothing comparison and the differences in optimal kernel sizes for each dataset, ROI-analyses may offer superior statistical testing to that of voxel-wise methods as you do not introduce a loss of specificity. ROI-wise methods also have the added benefit of not needing to warp images from individual space to common or group templates, which may also introduce a loss of specificity when looking at smaller structures, such as those in the subcortex. However, ROI-wise

methods are only as good as the predefined atlases used in the analysis. MRI may benefit from high spatial resolution in comparison to other neuroimaging methods, but there are still subpopulations of nuclei, such as those within the STN, that may have different roles in response inhibition and are not easily distinguishable (Mosher et al., 2021). MRI is of course also disadvantaged by its poor temporal resolution, a dimension that hinders the ability to dissociate different mechanisms occurring during the course of a trial (e.g., attention, detection of salient events; Benis et al., 2016). Methodologies with enhanced temporal resolution, such as electroencephalography (EEG), will also benefit from the wave of open-access data and can focus on research questions that MRI currently cannot, including disentangling the mixed cognitive processes underlying response inhibition.

The results presented here add to a growing literature exposing inconsistencies in our understanding of the networks underlying successful response inhibition. Based on the five datasets analysed, neither the *indirect* nor *hyperdirect* pathways show a greater degree of activation on SS trials compared to GO trials, or indeed compared to FS trials. It is evident that how response inhibition is implemented in the human brain requires more attention. Adaptations of the classical SST are already being deployed to aid in disentangling the role attention and signal detection in overall response inhibition (Boecker et al., 2013; Bryden and Roesch, 2015). This paper serves as a proof of concept for methods of meta-analysis that allow the unification of largely unprocessed or unreduced datasets and exemplifies the huge opportunities that open-access data sharing can bring to the research field. As more and more datasets are made publicly available, researchers will be able to perform meta-analyses not only on summary data, but datasets with a rich body of parameters and data points.

Chapter 7

General discussion

This thesis aimed to advance our knowledge of the human subcortex, with a specific focus on functions related to motor and cognitive inhibition. I chose to approach this research question in a holistic manner, by first focusing on the structure of the deep brain, and fine tuning our understanding and maps of the nuclei we aim to investigate.

Firstly, in **chapter 2** we brought together the anatomical findings of twenty different MRI archives to better understand the quality of data across the field. We provided the first quantitative assessment of MR image quality across a range of open-access structural MRI databases. The results demonstrated the extraordinary performance of UHF MRI and the image quality it can provide. Although, image quality is not the only factor researchers should look at when acquiring data of their own; sample size, age-range and the number or type of contrasts are just some of the many aspects one should consider. The chapter also highlights the importance and necessity of open-access data in furthering our knowledge of the structural properties of the human brain.

Chapter 3 builds on our interest in the anatomical properties of the human subcortex. We explored the aging patterns of 17 subcortical regions, both large and small using quantitative UHF MRI. Specifically, we investigated the size, shape, and biophysical properties of these structures over the adult lifespan using advanced modelling techniques that allowed us to estimate both their iron and myelin content. This knowledge is of huge importance for tailoring MR sequences to specific structures, accurately delineating structures at different ages and understanding which biophysical properties are part of normal aging and which are potentially pathological. We found that some of these structures exhibited large locational changes with increasing age, a factor that must be considered when using generalized atlases. These studies focused on regions that constitute part of the basal ganglia, a collection of nuclei evidenced to be involved in an array of cognitive, motor, and limbic processes. Indeed, the number of studies implicating its role in cognitive and motor inhibition is abundant (Albin et al.,

1989; Aron, 2007; Aron et al., 2016; Aron and Poldrack, 2006; Chambers et al., 2009; Guitart-Masip et al., 2011; Mink, 1996; Ridderinkhof and Van Der Molen, 1997; Salami et al., 2014; Schmidt et al., 2020; Utter and Basso, 2008; Wessel and Aron, 2017; Wiecki and Frank, 2013). Iron accumulation and myelin degradation may be a part of the normal aging process but they are also a common pathophysiology of multiple neurodegenerative disorders such as Parkinson's Disease and Huntington's Disease (Andersen et al., 2014; Ward et al., 2014). Cognitive decline and age also go hand in hand, but the causal relationship between these changes in biophysical properties of the brain and cognition is difficult to quantify.

In **chapter 4**, we collate all the functional imaging results we could find within a specific set of criteria pertaining to inhibition-related functions. The criteria included a minimum spatial resolution, so to ensure voxels fit within smaller subcortical structures; isotropic or near-isotropic data only, as anisotropy negatively impacts anatomical accuracy; 3T imaging or above, as lower field strengths do not supply the necessary signal at higher resolutions. Our results were unexpected, the meta-analyses revealed little overlap between response inhibition and interference resolution across all samples. We were surprised to find an absence of consistent subcortical activation across both inhibition subtypes, which speaks to the difficulty of high sensitivity scanning of the human subcortex. Due to the suboptimality of lower field strengths, it appears that increasing statistical power by means of data aggregation may not be enough to find consistent subcortical activation. The results of this study left many questions unanswered, in addition to raising even more. We knew we could do more to answer these questions. After this study, we thought we had taken inter-individual comparisons of inhibition-related functions as far as they could go. In addition, we were motivated to build upon the analysis by using both the neural and behavioural data to their full extent. We believed using a model-based framework in an intra-individual manner would allow us to fill the remaining knowledge gap.

In **chapter 5** we explored response inhibition and interference resolution in our own UHF MRI study, tailoring our imaging protocols to maximize data quality in the subcortex. Both **chapters 2** and **3** indicated that researchers should take age-related structural changes in brain organization into account when investigating the deep brain. As such, we ensured our sample comprised only of young adults, aiming to minimize any deviations in structural locations of biophysical properties that may arise from age-related differences. Combining cognitive modelling with high-resolution functional MRI we set out to find the overlaps and differences between response inhibition and interference resolution, both

in terms of observed behaviour and their neural implementations. Our results indicate a disparity between the two cognitive processes, a finding that mirrors previous inter-individual efforts investigating response inhibition and interference resolution (Huang et al., 2020; Hung et al., 2018; Isherwood et al., 2021b; Tobia et al., 2016). Interference resolution appeared to rely on nodes of the *indirect* and *hyperdirect* pathway, whereas successful response inhibition did not. Considering the array of studies implicating these pathways in successful response inhibition, we were puzzled by the results.

Focusing on the contradictory imaging results of response inhibition we found in **chapters 4** and **5**, **chapter 6** used a novel method of meta-analysis to aggregate stop signal data from five open-access datasets. We discussed the pitfalls of standard meta-analytical methods, including the fact that they commonly use only summary measures of activation profiles. Although this allows the unification of data from a much larger sample of separate datasets, it misses out on a crucial wealth of detailed and useful data points. We show that it is possible to gain substantial power from using raw data, though this is limited by the rate at which datasets are made open-access. This chapter again finds little evidence of *indirect* or *hyperdirect* pathway activation during successful inhibition. Three chapters of this thesis highlight a dissonance between current theories of response inhibition and fMRI evidence.

Collectively, this work emphasizes the importance of data quality and both inter- and intra-individual research. We have highlighted the difficulties of studying the human subcortex *in vivo*, extended our structural understanding of the deep brain across the adult lifespan, shown the benefits of tailored sequences for functional investigation into the basal ganglia as well as underlined a knowledge gap in our functional understanding of deep brain structures. Even though we are increasing the percentage of subcortical nodes represented in MR atlases, it seems we have a long way to go to fully understand the extent to which these regions are involved in inhibition-related functions. In the discussion below, we build upon the results of the studies in this thesis and consider their implications in light of other findings in the research field.

In the first section I discuss how we have made strides towards charting the uncharted, with a focus on the complexity of deep brain subregions and data quality. In the second section, I return to our main research question: how are inhibition-related functions implemented in the brain? I discuss where response inhibition and interference resolution overlap, how standard paradigms can limit the scope of our understanding of complicated psychological constructs, and the

difficulty in the interpretation of functional imaging. In the section following, I bridge the gap between our neural and behavioural findings by discussing how latent modelling parameters can aid our interpretation of neural data and vice versa. This discussion ends with a conversation on exciting new avenues of research that complement the methods and findings of this thesis.

The structure of the human subcortex

Our understanding of the human subcortex is ever evolving. For now, the 455 structures cited throughout this thesis are our best estimate of how to separate these densely packed regions. But this number is not set in stone. In the past, structures have been defined by their visual differences and cytohistochemical properties. We are now finding new ways of delineating these structures, including using multi-modal approaches. Chapters 2 and 3 take advantage of this multi-modal method to obtain novel insights into how some structures change over the adult lifespan. Despite all of this, and other recent advancements in understanding the structure of the human subcortex (Huang et al., 2022; Tian et al., 2020; Yu et al., 2021), we are still left with a vast expanse of uncharted territory. Not only is the representation of subcortical nuclei in MR atlases still at around 8% of the total number of subcortical structures, but the number of regional subcomponents is likely to continue to increase as our understanding grows.

For example, the thalamus is the largest structure in the subcortex, comprising anywhere between five and 60 substructures, depending whether divisions are based on functional or cytoarchitectural definitions (Fama and Sullivan, 2015; Schmahmann, 2003). We are still far from representing this range of possible subdivisions through MR atlases, with 26 being the largest number characterized so far (Iglesias et al., 2018). Defining regional subcomponents is not an easy feat. What even defines a functional subdivision and how we can orthogonalize this is also subject to debate (Karachi et al., 2009; Miletić et al., 2022). Given the number of studies investigating both structural and functional subdivisions of the thalamus, it is easy to wonder why the structure is generally treated as a single unit throughout the field of neuroscience, as we did here in Chapters 3, 4, 5 & 6. The thalamus is a diencephalic structure with connections to almost the entire cerebral cortex that transcends almost all domains of cognition, motor, or limbic functioning. There are two main reasons for why the thalamus, and other subcortical structures, are treated as a single structure.

One principal reason behind treating it as a single structure is most likely the same reason as why the entire subcortex is difficult to image: contrast. At the microscopic level, delineation of subcortical structures and substructures becomes much easier due to obvious differences in cytohistochemical makeup. But, at the mesoscopic level and with only a handful on MR contrasts to choose from, it is near impossible to delineate (manually or automatically) these structures, although QSM, T2* and other quantitative methods, like those used in chapter 3, make this delineation easier. On a standard T1w image it would not be obvious that many of the structures are heterogenous. For the future then, *in vivo* MRI would benefit from being informed by histological or other *ex vivo* methods (e.g., *post mortem* MRI). This type of methodology has already resulted in atlases that progress our segmentation capacity of the human subcortex (Bazin et al., 2020; Iglesias et al., 2018).

A second reason for this underrepresentation of thalamic subnuclei is also a practical one: the sheer number of possible analyses. Voxel-based analyses may still be the gold standard in the field, where the number of statistical tests for a single contrast range from tens of thousands to millions, but this does not come without its drawbacks. With increasing statistical tests comes an increased sensitivity loss due to multiple comparison correction. We may be able to lower the chance of type I errors with this method, but we also increase the likelihood of type II errors. Our sensitivity to BOLD changes in the subcortex is already low, we must therefore be careful to maintain as much sensitivity as possible, by avoiding excessive comparisons. Luckily, with region of interest analysis (ROI) we can easily reduce the number of statistical tests. In our study in chapter 5, 16 regions (32 when including both hemispheres) were used in the ROI analysis. These 16 regions were selected due to previous research implicating their roles in one or both tasks. With little previous research into the role of thalamic substructures in inhibition-related functions, it was difficult to justify the addition of between 10 (both hemispheres) and 52 extra regions that we did not have specific hypotheses on. We wanted to be conservative with the number of regions in our ROI analysis, to preserve statistical power. This avenue of research is admittedly an exciting one and with more time, a research line that would have benefitted the ambition of this thesis. Indeed, in our voxel-based analysis in chapter 5 we did find evidence that distinct substructures of the thalamus are involved in interference resolution (see Fig 5.9). With chapter 5 being the first 7T comparison of response inhibition and interference resolution, we have only just started casting light on subcortical involvement in these processes. And with human subcortical research still in

its infancy, the role of thalamic substructures in inhibition-related functions or decision making in general constitutes very exploratory work. My hope is that future work on this topic, which would be far more than a singular thesis in itself, would allow a more confirmatory analysis of some thalamic substructures in inhibition-related functions.

On the topic of conservatism, the work in chapter 2 could have benefitted from a greater number of regional comparisons and larger sample size from each database – a point made by reviewers in the submission phase of the paper. A separate, equally accurate method would have been to take a percentage of the sample size (e.g., 10%), and a minimum number of samples (e.g., five), for each database. In practice however, this number of samples would become infeasible for a singular rater such as myself. This was the same reasoning for why only two regions from each individual were sampled, two regions (three when splitting the caudate nucleus into hemispheres) already meant that 2010 regions were manually localized, without including the test-retest analyses. In light of the test-retest analyses validating our results, and the results of other papers showing a similar trend across 3T and 7T imaging, you might be left wondering: Is there space for lower field imaging in subcortical research? It should be obvious now that the gain in signal from higher field imaging outweighs the cost to B_0 inhomogeneities, motion artefacts and specific absorption rate (SAR). In my opinion, there is only one reason why standard neuroimaging research would benefit from 3T acquisition over 7T, and it is an indirect one: cost. For some research lines the need for a large quantity of data offsets the need for the highest data quality. As long as the data quality is *sufficient*, capturing individual differences from an increased quantity of data, especially in the human brain, can have its benefits. For example, the industry standard for brain templates in the neuroscience field is the Montreal Neurological Institute and Hospital (MNI) coordinate system. One could easily argue that the advantages of using 152 individuals to create a template is more applicable to the general structure of brain across the population than using higher resolution data from a smaller sample. The cost of 7T is currently just too high to maintain a large cohort where quantity can be prioritized.

The implementation of inhibition-related functions

A core finding of the work in this thesis is the apparent distinction between response inhibition and interference resolution on the implementation-level in the human brain, as evidenced in Chapters 4 and 5. Based on theoretical consid-

erations we were expecting much more of an overlap between the two (Dempster, 1993; Friedman and Miyake, 2004; Nigg, 2000). Our findings revealed that neural overlap between the two inhibition-related functions was limited to the bilateral insula, presupplementary motor area (preSMA), and right inferior frontal gyrus (rIFG). These nodes are unlikely to be involved in response inhibition or interference resolution specifically, but instead partake in more general roles.

The insula for example, has many potential functions, which are likely not mutually exclusive. The region has been implicated in the maintenance of task-specific rules (Dosenbach et al., 2008), maintenance of attention (Nelson et al., 2010), salience processing (Uddin, 2015), and interoception (Craig, 2009). For response inhibition specifically, the insula is thought to either aid through salience detection or by slowing responses after salient events (Cai et al., 2014). Similarly for interference resolution, the insula is most likely to aid in the detection of stimuli that cause interference (Deng et al., 2018). A more specific role is theorized for the preSMA, namely that it underlies the ability to adjust response thresholds (Cavanagh et al., 2011; Mulder et al., 2014). Indeed, model-based efforts have shown that trial-to-trial changes in decision threshold estimates correlate with trial-to-trial fluctuations in BOLD activity in the preSMA (Maanen et al., 2011). Wolpe et al. (2022) compared the SST performance of an adult male with a preSMA lesion to a group of healthy volunteers. They found that the lesioned patient had a slower SSRT than healthy controls, but a faster go RT. Although only a case-study, it provides further compelling evidence for the role of the preSMA in the setting of response thresholds. In response inhibition, the preSMA could adjust the thresholds defining the finishing times of the go and stop processes, while during interference resolution it could do the same for the different choice options. The IFG has been the region most implicated in response inhibition, though its exact function has been the subject of debate for almost two decades (Aron et al., 2004; Hampshire, 2015). Although consistently cited as a node of the response inhibition network, it is implicated in a wide-range of tasks (Duncan et al., 2000; Hampshire et al., 2007; Shallice et al., 2008).

I would like to tell you that our results have given an unequivocal answer to the role of these nodes in inhibition-related functions. But alas, we too here are hindered by the limited temporal resolution of fMRI, and for response inhibition, limited by the experimental design of the classical SST. The disentangling of within-trial cognitive or motor processes is not something fMRI lends itself well to; temporal resolution in this method has quite a way to go. Since we cannot disentangle processes of the classical SST during a single trial, we have another option: change

the paradigm. As previously mentioned, attentional and inhibitory processes are muddled during the classical SST. An alternative is a related paradigm called the stimulus-selective SST (Sebastian et al., 2016; Sebastian et al., 2017; Sharp et al., 2010). As well as the usual *go* and *stop* trials, an additional attentional capture (*ac*) trial type is presented. If on a *stop* trial, participants are instructed to inhibit their actions when they see a coloured circle (e.g., red), on an *ac* trial, participants are instructed to continue responding when they see a differently coloured circle (e.g., blue). The point of this setup is to induce the detection of a salient signal (which occurs on any trial that is not a *go* trial), but not induce the inhibition mechanism. This class of SSTs are not novel, but unfortunately are difficult for functional imaging studies due to the number of trials required to acquire sufficient data points for all trials. The sweet spot of classical SST configuration is around 3:1 of *go*:*stop* trials (Verbruggen et al., 2019). Many studies using the stimulus-selective SST have configured their tasks as roughly 2:1:1 of *go*:*stop*:*ac* trials (Sebastian et al., 2016; Sebastian et al., 2017; Sharp et al., 2010). While this may seem in line with recommendations, it removes an important aspect of the classical SST: the overall salience of non-*go* trials. The more often *stop* trials are presented within an SST, the more likely it is for unfavourable strategies to arise, such as waiting for the stop signal to occur to increase the likelihood of successfully inhibiting one's actions (Verbruggen et al., 2013). Such a strategy biases SSRT estimates and violates the assumptions of the horse-race model. It is not a massive leap to assume that this rationale would apply to dynamics within a stimulus-selective type SST as well. Until a time where fMRI repetition times are low enough and our methods of signal deconvolution are advanced enough that we can align the speed of trial lengths to that of standard behavioural experiments, it is difficult to employ such variants to the same extent as the classical SST. Even so, I have high hopes that such variants will aid our understanding of the core mechanisms underlying the full spread of cognitive and motor processes occurring during response inhibition.

It could be said that due to the sheer amount of research suggesting the contrary, our results of response inhibition may be invalid. But these results are not an isolated event, they are in fact replicating the results of two previous 7T studies (Hollander et al., 2017; Miletić et al., 2020). I see two possible interpretations of the results presented here. The first, is that subcortical constituents of the *hyperdirect* pathway (e.g., STN, SN and GPe) are just *not* required for successful motor inhibition, and that previous fMRI research has found aberrant activation here. The second, is that these regions within the subcortex have an incomparable hemodynamic response function to that of the cortex, and we are missing a key

piece of information leading to an abnormal activation pattern in our data. As shown in our smoothing kernel comparison in chapter 6, it is possible that liberal preprocessing steps could explain at least some of the subcortical activation patterns seen in previous studies. This of course though does not explain the ocean of research implicating the STN in successful response inhibition, either directly through single unit or LFP recordings in humans and animals or indirectly through DBS in Parkinson's patients (Alegre et al., 2013; Bastin et al., 2014; Benis et al., 2014; Obeso et al., 2011; Ray et al., 2009; Schmidt and Berke, 2017; Wessel et al., 2016c; Wildenberg et al., 2006; Wouwe et al., 2017).

These conflicting results are difficult to explain. While we do not provide evidence that the *hyperdirect* pathway is involved in successful response inhibition, we also cannot rule it out. We, as cognitive neuroscientists, are left with the complex task of interpreting the BOLD response of fMRI. Where, an increase in BOLD signal *most likely* reflects underlying neural activation, but a lack of observed BOLD signal (especially in the subcortex), in no way suggests a lack of underlying neuronal activation (Lowe et al., 2000). Even at 1.5 mm isotropic resolution we are certainly missing patches of activation of entire structures or their subcomponents, due to a lack of observable signal. There is no obvious statistical answer to how many voxels you need within a structure to be able to say you have a valid signal, that is specific to that region. Attempting to answer this question becomes even more difficult when you take partial voluming or anisotropic voxels into account. What we can say, is that four voxels are not sufficient. To make progress on this problem, future work validating the correlation between BOLD signal in the subcortex and neural activity is necessary, in addition to validating the correlation between BOLD signal and LFP recordings.

The findings pertaining to failed response inhibition trials are similarly difficult to interpret. Indeed, the mechanisms behind, and the limbic or cognitive consequences of failed stops are difficult to define. Which BOLD response patterns reflect which psychological construct is the difficult question. Most simply, the neural activation may just reflect a stop process that does not reach fruition. In my opinion, while neural activation may partly reflect this mechanism, it is likely muddled with more complex processes, such as error processing, frustration, or some type of updating mechanism. This may explain the observed activation of the VTA during failed stop trials, which is known to be involved in prediction and error processing (Fiorillo et al., 2003; Schultz et al., 1997). Even though the stop signal in the SST is pseudo-randomized and cannot be accurately predicted, the brain is a predictive machine (Friston, 2010). It may be that individuals do

in some way attempt to predict the presentation of the stop signal, and failure to stop or failure to prime the stop process properly results in some type of prediction error. In addition to failed response inhibition, we also found that the VTA was active during interference resolution, a novel finding. Although the VTA has not previously been implicated using fMRI specifically, the impact of the dopamine system on interference resolution has been investigated before, albeit mostly indirectly. Using a dopamine antagonist, Rabella et al. (2016) found that hindering the dopamine system negatively impacted performance in a Flanker task. Additionally, electrophysiological recordings in monkeys have explicitly implicated the VTA during interference resolution (Matsumoto and Takada, 2013). How exactly the VTA moderates aspects of attention, reward or error processing is unknown. The involvement of the dopaminergic system in interference resolution and in failed response inhibition is therefore a key finding of this thesis, and points to an underlying mechanism not concretely explored in the research field.

The computation of inhibition-related functions

It is evident from chapters 4 through 6 that inhibition-related functions are divergent on an implementational level. Based on the results in chapter 5, it is also evident that there is no obvious association between them on a computational level. We presented here the first formal model of behaviour during the MSIT, as well as the first model-based approach to this paradigm. We also built upon previous model-based efforts for the SST (Aron and Poldrack, 2006; Logan and Cowan, 1984; Matzke et al., 2013). A key finding was evidence for the involvement of the anterior cingulate cortex (ACC) and IFG in resolving interference. Activation in both regions has long been seen (Botvinick et al., 1999; Bush et al., 1998; Jimura et al., 2009; Nee et al., 2007), but their correlation with drift rate parameters is novel. But does this mean that these two regions, or one of these two regions, is *actually* encoding evidence accumulation? Unfortunately, such a question is out of the realms of the methods used in this thesis. The correlation does indicate to us that the regions are involved in the process of evidence accumulation. This could mean that one, or both, regions implement the accumulation of evidence towards a specific choice or that they are part of a network that supports different aspects of the accumulation process. It could also be that via the transfer of information during the decision-process, that parts of the accumulation process are reflected in nodes downstream to the accumulation region, which can perform their function based on the evidence passed to them. The choice that is in the end made, is likely

a result of a combination of multiple processes, some co-occurring, some sequential. The ACC specifically, may play a role in the tracking of uncertainty in which response to select (Heekeren et al., 2008; Shenhav et al., 2018). Within our cognitive model, higher differences in drift rate between the congruent and incongruent conditions of the MSIT suggest more susceptibility to cognitive interference. In this sense, our results are in line with previous research suggesting that the ACC in some way signals the presentation of interference, and the interference intensity (Botvinick et al., 2001). It is however becoming apparent that different subregions of the ACC may have distinct functions (Buchsbaum et al., 2013; Shenhav et al., 2018). Future work will hopefully uncover the specific contribution of each ACC subcomponent to the decision-process, where methods such as joint modelling could provide assistance.

Generally, associations between neural and behavioural data (even behavioural-behavioural data) are established through a two-stage process (Forstmann et al., 2008). Firstly, we calculate summary measures of individual behaviour and their neural counterpart separately, and then, we apply statistical tests to relate the two. Moving away from this two-stage approach, Purcell et al., 2010 demonstrated that neurophysiological data can be used to predict behavioural data. In a sense, this approach was still one-way and does not allow neural and behavioural data to be mutually informative on the holistic model. *True* joint modelling provides a means to combine both sets of data into a single-model analysis, as well as permitting models to be mutually informative. For example, by allowing parameters of the model to covary, Turner et al. (2017b) constructed a framework where behavioural and neural data could influence each other's parameters in a bidirectional manner. Therefore, instead of merely correlating the parameters estimated for each cognitive model of the MSIT and SST, and their respectful neural data, their relation could be estimated by means of a variance-covariance matrix. This method provides a way to add another level of constraint to both the neural and behavioural models. What results is a single model that estimates parameters that are a compromise to each individual model, the best fit is defined through the influence of both sets of data. Turner et al. (2017a) further provided an additional advantage to this framework: dimensionality reduction. Estimating the entire variance-covariance matrix has the advantage of estimating every and all possible associations between parameters, allowing for exploratory analyses, but in many cases can be redundant. Using a factor analysis on top of this approach, can help remove a dimension within the estimated parameters by collapsing related elements into single latent factors. These methods are not yet easily implementable. My

hope is that as the detail of experimentally recorded information grows, methods such as these will aid in finding the currently unobservable structures within.

In contrast to the MSIT, estimated latent parameters within the SST did not correlate with any brain regions previously implicated in response inhibition. An obvious question one might ask themselves is: is SSRT reliable? Or, useful? Are there other methods to estimate the latent behaviour of successful response inhibition? The answer to this is complex. Accurate estimation of SSRT is based on whole list of assumptions and practical considerations (Verbruggen et al., 2019). There are many ways to estimate this latent parameter, but traditional non-parametric methods likely produce biased estimates. For example, an important aspect often overlooked is the necessity to take trigger failures into account. Failure to do so often causes an overestimation of SSRT (Band et al., 2003; Matzke et al., 2017). Trigger failures, times at which the stop process is not triggered on a stop trial, are notoriously difficult to estimate. SSRT and trigger failures are thought to underlie subtly different aspects of inhibitory control (Schachar and Logan, 1990; Tannock et al., 1989). While we did take trigger failures into account in chapter 5, this aspect of response inhibition was not intensely touched upon within this thesis. Recent work has attempted to dissociate between the concepts of SSRT and trigger failures more reliably, finding that although SSRT itself did not correlate with behavioural measures of impulsivity, impulsivity did correlate with the estimated probability of trigger failure (Skippen et al., 2019). This two process computational outlook of response inhibition, together with the two process implementational outlook of response inhibition (Diesburg and Wessel, 2021), adds to the growing literature pointing to the complexity of global inhibitory control.

On top of these methods of SSRT estimation through cognitive modelling, recent work has found a new way to estimate the latency of the stop process. Using a more direct method, Raud and Huster, 2017 measured electromyography (EMG) activity during the SST and observed the moment at which EMG activity collapsed in the hand on a successful stop trial. This shows that it is possible to measure the muscle related activity associated with a successful stop trial. This in a sense, is a direct measurement of SSRT, as it shows the moment that stopping was determined in the motor domain. Not only could this eventually provide trial to trial estimations of SSRT directly, but this could help dissociate between the motor and cognitive components of successful stopping.

Future directions

In addition to the variations of the SST, issues with BOLD signal and joint modelling techniques described above, there are further steps the field can take to aid in the understanding of inhibition-related functions in the human subcortex. We have come a long way since Karl Pearson's first use of formal techniques to combine data *en masse* (Pearson, 1904). Although this endeavor was modest compared to modern standards and without the integration of uncertainty estimates, it was the first step in the development of a noteworthy statistical practice. It was not until the late 70's that the term 'meta-analysis' was coined (Glass, 1976). Even with all the progress made since then (e.g., activation likelihood estimation, multivariate pattern analysis, seed-based d mapping, to name a few), I believe we are heading towards an even larger leap forward in methodology. As shown in chapter 6, with suitable hardware and access to pre-acquired research data it is now possible to aggregate full datasets, as opposed to only summary measures, which has been the norm within the field of functional imaging for over 20 years (Farah and Aguirre, 1999). This method was only the first example, much methodological research is required to optimize the use of GLM-based meta-anlayses. We will of course never be able to get around the issues of differences in data quality, inconsistencies in analyses pipelines or acquisition parameters, or other variabilities in experimental design between samples. Still, the possibility of accounting for the full wealth of data is appealing, moving on from its mere central tendency to the entire distribution. With enough data, the variability within datasets might actually be a good thing. Any one acquisition method, experimental design or preprocessing pipeline comes with a range of biases. By aggregating complete datasets from various sources, we likely find results closer to the ground truth, or at least our best estimate of it. This thesis depended on such aggregation and would not have been possible without the movement towards data sharing. Three of the five chapters presented here necessitated the accessibility of previously acquired datasets. Although the current standard of meta-analyses has been extraordinarily helpful to the field, it is my hope that we will continue to develop meta-analytical methods such as those used in chapter 6, where we can take full advantage of the dense research data collected globally.

Another fruitful direction of research is the advancement of acquisition techniques for imaging the subcortex. Structural imaging of the subcortex has made leaps forwards in recent years, as evidenced in this thesis. Functional imaging on the other hand, still has a longer way to go. Further increases in field strength is

a clear contender for advancing both imaging types. 9.4T systems are likely the next set of scanners to be clinically certified, even if this step is not yet around the corner. The increase from 7T to 9.4T has the propensity to double the BOLD contrast-to-noise ratio, allowing for unprecedented spatial resolutions (Budde et al., 2014). The downside is that radio frequency inhomogeneities becomes a serious problem above 3T (Van de Moortele et al., 2005). Additionally, although changes in magnetic susceptibility and relaxation times have their advantages at higher field strengths, they also cause more complex issues (e.g., signal loss, distortions; Frahm et al., 1994; Jezzard and Balaban, 1995). While we here have raised the cortico-centric nature of the field of neuroscience, it is important to note that we must find methods that focus on the brain holistically and not just shift our focus onto the other. Problematically, methods that allow accurate characterization of the subcortex can negatively impact the acquisition of cortical regions, and vice versa. Customized coil designs do show promise here though (Wiggins et al., 2012). Since increasing the number of detector elements or size of surface coils has shown little promise in the deep brain, the development of dipole antennas may provide hope by delivering greater signal penetration (Raaijmakers et al., 2011).

On top of increasing the efficiency of our imaging acquisition methods, another exciting avenue is opening: focused ultrasound. Due to the location of the subcortex, cortical methods of brain stimulation and inhibition do not work. Therefore, cortical studies of inhibition-related functions that make use of transcranial magnetic stimulation or transcranial direct current stimulation are numerous (Kwon and Kwon, 2013; Wildenberg et al., 2010; Yu et al., 2022), while the subcortex has been limited to only invasive methods such as deep brain stimulation or optogenetics (Bari et al., 2020; Ray et al., 2009). With the advent of focused ultrasound, there comes a way to stimulate or inhibit spatially specific areas of neural tissue from afar (Blackmore et al., 2019), as well as the opportunity to study healthy populations *in vivo*. The ability to modulate specific regions of the brain while performing a task gives an immensely useful dimension of information about the regions function. I hope that future research will drive the use of methodologies such as these to finally allow the modulation of subcortical structures *in vivo* in a non-invasive way.

With this thesis I have made steps in the right direction, but how exactly the brain implements inhibition-related functions still eludes us. I am optimistic that the future will bring methodologies that allow us to understand all three levels of analysis of both response inhibition and interference resolution. My hope is

that the work presented here aids in the understanding of these functions and in a historically underrepresented area of the brain: the subcortex.

Appendices

Appendix A

Supplementary Materials to Chapter 2

A.1 Supplementary results

Table A.1: **Websites, descriptor papers and download process for all presented databases.** N, no; Y, yes; U, unprocessed; P, processed; N/A, not applicable; NITRC, Neuroimaging Tools & Resources Collaboratory.

Index	Database	Link to Database homepage	Reference for database descriptor paper	How to access	Application process	Data type
1	250	(1) http://hiresmri.ovgu.de/ (2) http://dx.doi.org/10.5061/dryad.38s74	Lüsebrink, F., Sciarra, A., Mattern, H., .. (2017). T1-weighted in vivo human whole brain MRI dataset with an ultra-high isotropic resolution of 250 μm. Sci Data, 4, 170032. doi: 10.1038/sdata.2017.32	(1) Database homepage. (2) Data download link sent after a valid email address is given. Immediate download not available.	N	U & P
2	AHEAD	https://uvaauas.figshare.com/articles/AHEAD_structural_MRI_Data/8332325	Alkemade, A., Mulder, M.J., Groot, J.M., .. (submitted). The Amsterdam Ultra-high field adult lifespan database (AHEAD): A freely available multimodal magnetic resonance imaging database.	Data immediately downloadable from database link.	N	U
3	Age-ility	https://www.nitrc.org/projects/age-ility/	Karayanidis, F., Keuken, M.C., Wong, S.A., .. (2015). The Age-ility Project (Phase 1): Structural and functional imaging and electrophysiological data repository. Neuroimage.	Data immediately downloadable from 'Downloads' tab in database link.	N	U

Index	Database	Link to Database homepage	Reference for database descriptor paper	How to access	Application process	Data type
4	ATAG	https://www.nitrc.org/projects/atag_mri_scans	Forstmann, B.U., Keuken, M.C., Schafer, A., .. (2014). Multi-modal ultra-high resolution structural 7-Tesla MRI data repository. Sci Data.	NITRC account required. Data immediately available from download tab in database link after login.	N	U
5	GSP	https://www.neuroinfo.org/gsp/	Holmes, A.J., Hollinshead, M.O., O'Keefe, T.M., .. (2015). Brain Genomics Superstruct Project initial data release with structural, functional, and behavioral measures. Sci Data.	Dataverse account required and access to database must be requested. A data usage agreement must be agreed to. There are no institutional barriers. Data is accessible after a valid email address is confirmed.	Y	U
6	Cam-Can	http://www.cam-can.org/	Taylor, J.R., Williams, N., Cusack, R., .. (2015). The Cambridge Centre for Ageing and Neuroscience (Cam-CAN) data repository: Structural and functional MRI, MEG, and cognitive data from a cross-sectional adult lifespan sample. Neuroimage, 144, 262-269.	A data usage agreement must be agreed to. Details of institutional affiliation and a research proposal must be provided. The applicant must wait for approval to gain access to the database.	Y	U

Index	Database	Link to Database homepage	Reference for database descriptor paper	How to access	Application process	Data type
7	DLBS	http://fcon_1000.projects.nitrc.org/indi/retro/dlbs.html	N/A	Data immediately downloadable from database link.	N	U
8	HCP-YA	https://www.humanconnectome.org/study/hcp-young-adult	Van Essen, D.C., Smith, S.M., Barch, D.M., .. (2013). The WU-Minn Human Connectome Project: An overview. NeuroImage, 80, 62-79.	ConnectomeDB account is required. Valid email addresss and institution information is required to create account. Data usage terms must be agreed to. Aspera connect plugin must be downloaded and used to aid with data transfer of the large database.	Y	U & P
9	IXI	http://brain-development.org/ixi-dataset/	N/A	Data immediately downloadable from database link.	N	U
10	Kirby 21	https://www.nitrc.org/projects/multimodal	Landman, B.A., Huang, A.J., Gifford, A., .. "Multi- Parametric Neuroimaging Reproducibility: A 3T Resource Study". (2010). NeuroImage.	Data immediately available from 'Downloads' tab in database link.	N	U

Index	Database	Link to Database homepage	Reference for database descriptor paper	How to access	Application process	Data type
11	MAASTRICHT	https://zenodo.org/record/1206163	Gulban, O.F., Schneider, M., Marquardt, I., .. (2018). A scalable method to improve gray matter segmentation at ultra high field MRI. PLoS One, 13, 6, e0198335. doi: 10.1371/journal.pone.0198335.	Data immediately downloadable from database link.	N	U
12	MASSIVE	http://massive-data.org/index.html	Froeling, M., Tax, C.M.W., Vos, S.B., .. (2016). "MASSIVE" Brain Dataset: Multiple Acquisitions for Standardization of Structural Imaging Validation and Evaluation. Magnetic Resonance in Medicine, 77(5), 1797-1809.	Data immediately available from 'Downloads' tab in database link.	N	U
13	MSC	https://openneuro.org/datasets/ds000224/versions/00002	Gordon, E.M., Laumann, T.O., Gilmore, A.W., .. (2017). Precision Functional Mapping of Individual Human Brains. Neuron, 95, 791–807.	Data immediately downloadable from database link.	N	U
14	MPI-CBS	https://www.nitrc.org/frs/?group_id=606	Tardif, C.L., Schäfer, A., Trampel, R., .. (2016). Open Science CBS Neuroimaging Repository: Sharing ultra-high-field MR images of the brain. Neuroimage, 124, 1143-1148.	License agreement must be agreed to. Data available from 'Downloads' tab in database link after agreement.	N	P

Index	Database	Link to Database homepage	Reference for database descriptor paper	How to access	Application process	Data type
15	MPI-LMBB	(1) https://www.nitrc.org/projects/mpilmbb/ (2) https://www.openfmri.org/dataset/ds000221/ http://fcon_1000.projects.nitrc.org/indi/enhanced/	Mendes, N., Oligschlaeger, S., Lauckner, M.E., .. (2017). A functional connectome phenotyping dataset including cognitive state and personality measures. BioRxiv.	(1) Homepage link (2) Data download link. Data immediately available for download.	N	U
16	NKI-RS		Nooner, K. B., Colcombe, S. J., Tobe, R. H., .. (2012). The NKI-Rockland Sample: A Model for Accelerating the Pace of Discovery Science in Psychiatry. Frontiers in Neuroscience, 6, 152.	Data immediately available from the 'Data' tab of the database homepage. NITRC account and login required.	N	U
17	PTBP	https://figshare.com/articles/PTBP_Nifti/1190933	Avants, B.B., Duda, J.T., Kilroy, E., .. (2015). The pediatric template of brain perfusion. Sci Data, 2, 150003. doi: 10.1038/sdata.2015.3.	Data immediately downloadable from database link.	N	U
18	RAIDERS	http://datasets.datalad.org/?dir=/labs/haxby/raiders	Haxby, J.V., Guntupalli, J.S., Connolly, A.C., .. (2011). A Common, High-Dimensional Model of the Representational Space in Human Ventral Temporal Cortex. Neuron, 72, 404 - 416. DOI10.1016/j.neuron.2011.08.026	Data immediately downloadable from database link.	N	U

Index	Database	Link to Database homepage	Reference for database descriptor paper	How to access	Application process	Data type
19	SALD	http://fcon_1000.projects.nitrc.org/indi/retro/sald.html	Wei, D., Zhuang, K., Ai, L., .. (2018). Structural and functional brain scans from the cross-sectional Southwest University adult lifespan dataset. Scientific Data, 5, 180134.	Data immediately downloadable from database link.	N	U
20	StudyForrest	http://studyforrest.org/about.html	Hanke, M., Baumgartner, F. J., Ibe, P., .. (2014). A high-resolution 7-Tesla fMRI dataset from complex natural stimulation with an audio movie. Scientific Data, 1, 1–18.	Data immediately downloadable from 'Access' tab in database link.	N	U

Table A.2: **High-profile databases that do not adhere to all of our inclusion criteria.** + indicates that this database meets this inclusion criteria, - indicates that this database does not meet this inclusion criteria.

Database	Exclusively normative data	All data of similar Composition	Accessible to the worldwide scientific community	No institutional/ positional barriers	Free of charge
ABCD	+	+	+	-	+
ABIDE	-	-	+	+	+
ADHD 200	-	-	+	+	+
ADNI	-	+	+	+	+
AIBL	-	+	+	+	+
BRAINS	+	-	+	+	+
CMI-HBN	+	-	+	+	+
COBRE	-	+	+	+	+
CoRR	+	-	+	+	+
fBIRN	-	-	+	+	+
FCP	+	-	+	+	+
Mindboggle	+	-	+	+	+
MIRIAD	-	+	+	+	+
NACC	-	-	+	+	+
NCANDA	+	+	+	-	+
OASIS	+	-	+	+	+
OpenNeuro	-	-	+	+	+
PING	+	+	+	-	+
PNC	+	+	+	-	+
SchizConnect	-	-	+	+	+
UK Biobank	+	+	+	+	-

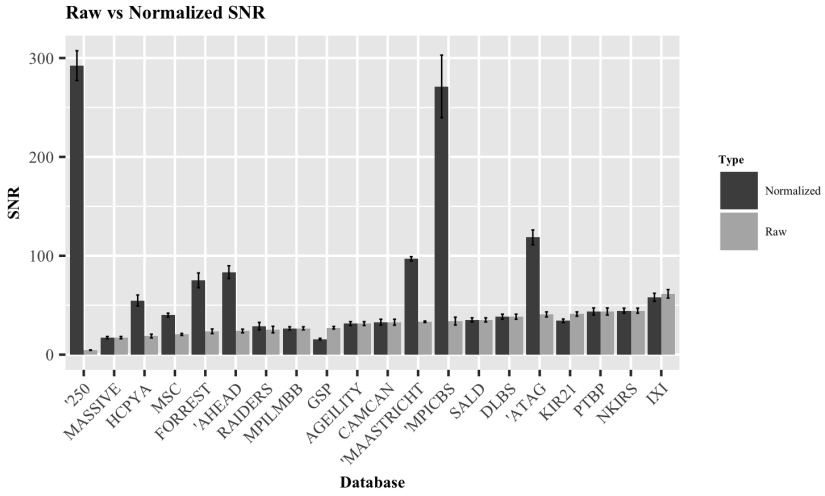

Figure A.1: Bar chart comparing the raw and normalized SNR measurements. Values are ordered from lowest to highest, based on the raw SNR measurements. Error bars indicate standard error of the mean.

Table A.3: **SNR and CNR estimations for the contrasts offered by each database.** All qualitative images are reported as normalized values, all quantitative images are reported as raw. SNR_{CC} indicates the SNR of the corpus callosum and SNR_{CN} indicates the mean SNR of both caudate nuclei. n, number of participants used for calculation; MPRAGE, magnetization prepared rapid gradient echo; MP2RAGE, magnetization prepared 2 rapid acquisition gradient echoes; ME, multiple echo; FLASH, fast low angle shot; SPACE, sampling perfection with application of optimized contrasts using different flip angle evolutions; FLAIR, fluid attenuation inversion recovery; IR, inversion recovery; TSE, turbo spin echo; TFE, turbo field echo; sb, slab; un, unprocessed; pro, processed; T1w, T1-weighted; qT1, quantitative T1 map; T2w, T2-weighted; PDw, proton density-weighted; T2*w, T2*-weighted; qT2*, quantitative T2* map; QSM, quantitative susceptibility mapping; SWI, susceptibility weighted image.

Database	Sequence	Contrast	SNR_{CC} (± SEM)	SNR_{CN} (± SEM)	CNR (± SEM)	n	Resolution (mm)
250	MPRAGE	T1w-un	292.3 ± 15.0	198.3 ± 14.6	93.5 ± 6.7	1	0.25 x 0.25 x 0.25
	MPRAGE	T1w-pro	570.4 ± 123.5	368.0 ± 53.5	93.7 ± 14.6	1	0.25 x 0.25 x 0.25
Age-ility	MPRAGE	T1w	31.4 ± 2.0	20.4 ± 2.0	5.8 ± 0.9	5	1 x 1 x 1
AHEAD	MP2RAGEME	T1w	83.4 ± 6.5	39.5 ± 1.3	28.5 ± 1.3	15	0.64 x 0.64 x 0.7
	MP2RAGEME	qT1	24.2 ± 2.4	19.6 ± 1.1	6.0 ± 0.6	15	0.64 x 0.64 x 0.7
	MP2RAGEME	QSM	10.0 ± 2.6	16.0 ± 1.5	8.7 ± 1.8	15	0.64 x 0.64 x 0.7
	MP2RAGEME	PDw	97.5 ± 6.2	29.5 ± 2.4	1.7 ± 0.5	15	0.64 x 0.64 x 0.7
	MP2RAGEME	T2*w	77.7 ± 12.0	25.3 ± 2.6	0.3 ± 0.5	15	0.64 x 0.64 x 0.7
	MP2RAGEME	qT2*	10.6 ± 0.6	6.3 ± 0.4	0.3 ± 0.1	15	0.64 x 0.64 x 0.7
	MP2RAGEME	T1w-sb	157.1 ± 7.5	103.1 ± 5.7	37.4 ± 1.3	15	0.5 x 0.5 x 0.5
	MP2RAGEME	qT1-sb	15.4 ± 0.7	14.4 ± 0.7	4.3 ± 0.2	15	0.5 x 0.5 x 0.5
	MP2RAGEME	PDw-sb	147.8 ± 8.2	79.5 ± 6.4	8.3 ± 2.5	15	0.5 x 0.5 x 0.5
	MP2RAGEME	T2*w-sb	138.1 ± 21.1	83.8 ± 9.8	5.0 ± 1.7	15	0.5 x 0.5 x 0.5
	MP2RAGEME	qT2*-sb	8 ± 0.3	6.2 ± 0.4	0.8 ± 0.2	15	0.5 x 0.5 x 0.5
ATAG	MP2RAGE	T1w	118.6 ± 6.5	29.6 ± 1.4	19.6 ± 0.7	15	0.7 x 0.7 x 0.7
	MP2RAGE	qT1	23.7 ± 0.9	17.8 ± 0.6	6.2 ± 0.2	15	0.7 x 0.7 x 0.7
	ME-3D-FLASH	T2*w	128.5 ± 11.4	85.5 ± 10.6	2.8 ± 1.9	15	0.5 x 0.5 x 0.5
	MP2RAGE	T1w-sb	146.2 ± 9.1	47.9 ± 2.1	23.3 ± 1.3	15	0.6 x 0.6 x 0.6
	MP2RAGE	qT1-sb	23.8 ± 1.1	19.6 ± 0.7	4.9 ± 0.3	15	0.6 x 0.6 x 0.6
Cam-Can	MPRAGE	T1w	32.8 ± 2.7	24.1 ± 1.2	6.1 ± 0.5	15	1 x 1 x 1
	SPACE	T2w	11.8 ± 1.0	14.3 ± 0.7	2.7 ± 0.2	15	1 x 1 x 1
GSP	MEMPRAGE	T1w	15.8 ± 0.8	8.8 ± 0.7	3.6 ± 0.2	5	1.2 x 1.2 x 1.2
DLBS	MPRAGE	T1w	38.3 ± 4.2	19.4 ± 2.7	4.8 ± 0.7	15	1 x 1 x 1
HCPYA	MPRAGE	T1w-un	54.7 ± 5.6	40.4 ± 1.8	9.1 ± 1.3	5	0.7 x 0.7 x 0.7
	SPACE	T2w-un	26.7 ± 2.6	37.7 ± 3	11.5 ± 0.3	5	0.7 x 0.7 x 0.7
	MPRAGE	T1w-pro	87.8 ± 13.0	72.9 ± 12.9	16.3 ± 2.8	5	0.7 x 0.7 x 0.7
	SPACE	T2w-pro	32.8 ± 2.1	57.1 ± 8.5	14.6 ± 3.1	5	0.7 x 0.7 x 0.7
IXI	-	T1w	58.0 ± 3.6	33.7 ± 1.8	4.2 ± 0.4	15	0.94 x 0.94 x 1.2
	-	T2w	15.5 ± 1.4	17.7 ± 1	4.0 ± 0.2	15	0.9 x 0.9 x 1.2
	-	PDw	58.0 ± 3.9	35.1 ± 2	8.3 ± 0.4	15	0.9 x 0.9 x 1.2
Kirby 21	MPRAGE	T1w	34.2 ± 1.8	16.7 ± 1.1	6.9 ± 0.6	5	1 x 1 x 1.2
	FLAIR	FLAIR	14.0 ± 1.6	8.0 ± 1.1	1.7 ± 0.3	5	1.1 x 1.1 x 1.1
MAASTRICHT	MPRAGE	T1w	96.9 ± 2.2	36.6 ± 3.3	18.5 ± 2.1	5	0.7 x 0.7 x 0.7
	MPRAGE	PDw	129.0 ± 11.0	85.3 ± 22.1	2.6 ± 0.9	5	0.7 x 0.7 x 0.7
	MPRAGE	T2*w	55.3 ± 8.9	37 ± 5	4.0 ± 1.6	5	0.7 x 0.7 x 0.7
MPI-CBS	MP2RAGE	T1w	271.3 ± 31.7	93.1 ± 15.9	42.4 ± 5.4	5	0.5 x 0.5 x 0.5
	MP2RAGE	qT1	24.7 ± 3.2	18.9 ± 2.9	5 ± 0.7	5	0.5 x 0.5 x 0.5
	ME-FLASH	T2*w	129.6 ± 24.1	83.9 ± 22	6.4 ± 2.5	5	0.5 x 0.5 x 0.5
	ME-FLASH	qT2*	9.1 ± 0.6	4.7 ± 0.8	0.1 ± 0.2	5	0.5 x 0.5 x 0.5
MPI-LMBB	MP2RAGE	T1w	26.6 ± 1.3	12.7 ± 0.3	6.4 ± 0.3	15	1 x 1 x 1
	MP2RAGE	qT1	17.2 ± 0.8	17 ± 0.4	5.9 ± 0.2	15	1 x 1 x 1
	-	FLAIR	81.7 ± 7.0	82 ± 5 .0	16.5 ± 1.4	10	0.49 x 0.49 x 1
MASSIVE	3D-TFE	T1w	17.2 ± 1.2	10.6 ± 0.3	6.4 ± 0.3	1	1 x 1 x 1
	3D-TSE	T2w	21.9 ± 2.0	13.8 ± 1.8	2.2 ± 0.4	1	1 x 1 x 1
	3D-IR-TSE	FLAIR	15.9 ± 1.4	13 ± 1.2	2.6 ± 0.2	1	1 x 1 x 1
MSC	-	T1w	40.0 ± 2.0	26.6 ± 1.3	9.3 ± 0.2	5	0.8 x 0.8 x 0.8
	-	T2w	16.0 ± 1.5	23 ± 2.3	5.2 ± 0.7	5	0.8 x 0.8 x 0.8
NKI-RS	MPRAGE	T1w	44.5 ± 2.7	28.1 ± 1.0	7.8 ± 0.4	15	1 x 1 x 1
PTBP	MPRAGE	T1w	43.6 ± 3.6	28.2 ± 1.8	9.2 ± 0.7	5	1 x 1 x 1
RAIDERS	MPRAGE	T1w	28.9 ± 3.8	16.9 ± 1.6	8.8 ± 0.9	5	0.938 x 0.938 x 1
SALD	MPRAGE	T1w	35.1 ± 2.0	23.9 ± 0.8	6.0 ± 0.2	15	1 x 1 x 1
StudyForrest	3D-TFE	T1w	75.2 ± 7.5	43.5 ± 4.1	18.5 ± 1.1	5	0.67 x 0.67 x 0.7
	3D-TSE	T2w	51.6 ± 7.8	66.0 ± 3.0	10.2 ± 1.0	5	0.67 x 0.67 x 0.7
	3D Presto FFE	SWI	72.0 ± 11.2	40.3 ± 1.9	1.2 ± 1.2	5	0.43 x 0.43 x 0.35

Appendix B

Supplementary Materials to Chapter 3

B.1 Supplementary results

CNR comparisons

Under the assumption of mono-exponential signal decay, the expected contrast-to-noise ratio (CNR) of an T2*-weighted single echo, echo planar imaging protocol, per unit change in T2*, is given by (e.g. Poser et al., 2006; Posse et al., 1999):

$$CNR(TE, T2^*) = \frac{S_0}{\sigma_0} TE \exp \frac{-TE}{T2^*} \tag{B.1}$$

where S_0 and σ_0 are the signal and (temporal) variance, respectively, at echo time $TE = 0$. In the following comparisons, we assume that S_0 and σ_0 are the same across structures and protocols. This assumption is unlikely to be true for between-region CNR comparisons, as S_0/σ_0 is typically lower in subcortical regions compared to cortical regions in part due to the larger distance to the MRI receiver coils. We ignore any potential between-region differences in the size of the T2* changes that result from changes in the oxygenation levels. Under these assumptions, CNR ratios can be used to compare the expected CNRs when using echo time A to study region n with the expected CNR when using echo time B to study region m:

$$\frac{CNR(TE_A, T2^*_m)}{CNR(TE_B, T2^*_n)} = \frac{TE_A \exp \frac{-TE_A}{T2^*_m}}{TE_B \exp \frac{-TE_B}{T2^*_n}} \tag{B.2}$$

First, we can compare the expected CNR in the red nucleus with the CNR in the amygdala, both in 19 years old participants, using T2* values obtained through our app (`https://subcortex.eu/app`). Filling in $TE_A = TE_B = T2^*_{amg} = 0.04248$ s (i.e., in both protocols, we use an echo time optimized for the amygdala at 19 years old), and $T2^*_{rn} = 0.01825$ s, we find $\frac{CNR(TE_A, T2^*_{rn})}{CNR(TE_B, T2^*_{amg})} = 0.265$, implying the CNR in the red nucleus is approximately 73.5% lower than in the amygdala with this echo time. In practice, since S_0/σ_0 is also likely to be lower in the red nucleus than in the amygdala, the CNR ratio will be even lower.

Second, we can estimate the effect of age-related decreases in T2*. The red nucleus has an approximate $T2^* = 0.01825$ s at 19 years old, and $T2^* = 0.0131$ s at 50 years old. If an echo time of $TE_A = TE_B = 0.01825$ s is used for a participant of 50 years old, then $\frac{CNR(0.01825,0.0131)}{CNR(0.01825,0.01825)} = 0.6765$, showing an approximately 32% loss in CNR compared to the CNR that would be obtained with this echo time in a participant of 19 years old.

Third, we can compare the expected CNR in the red nucleus at 19 years old ($T2^* = 0.01825$ s) when using the optimal echo time $TE_A = 0.01825$ s with the CNR that would be obtained if an echo time is used that is optimal for the amygdala: $TE_B = 0.04248$ s. The ratio $\frac{CNR(0.01825,0.01825)}{CNR(0.04248,0.01825)} = 1.621$, showing that a substantial CNR gain can be expected from optimising the echo time to meet the specific requirements of that region.

Finally, we can compare the effect of adapting echo times to adjust for age-related changes in T2*. Taking again the red nucleus as an example, the T2* decreases from 0.01825 s to 0.0131 s between 19 and 50 years old. Suppose we analyze the red nucleus in a 50 year old participant using the corresponding optimal echo time (hence, $TE_A = T2^* = 0.0131$ s), then, compared with using an echo time optimal for young participants $TE_B = 0.01825$ s, we find that $\frac{CNR(0.0131,0.0131)}{CNR(0.01825,0.0131)} = 1.063$. Hence, adjusting for the age-related decrease in T2* leads to modest CNR gains.

In practice, changing the echo time may not always be possible due to hardware limitations (e.g., the slew rate of the MRI gradients limits the minimum echo time that can be achieved), and potentially requires undersampling of k-space (e.g., using GRAPPA, SENSE, or partial Fourier) or bandwidth changes. These additional changes will affect the protocols' S_0/σ_0, complicating direct comparison between the expected performance of two candidate MRI protocols. Another option is to use multi echo protocols, in which data is acquired at multiple echo times, which can be optimized for multiple regions at the same time (Gowland and Bowtell, 2007; Kundu et al., 2017; Miletić et al., 2020; Puckett et al., 2018). These additional factors should be taken into account when developing an MRI protocol in order to find the optimal trade-off between echo time settings and S_0/σ_0.

B.2 Supplementary figures and tables

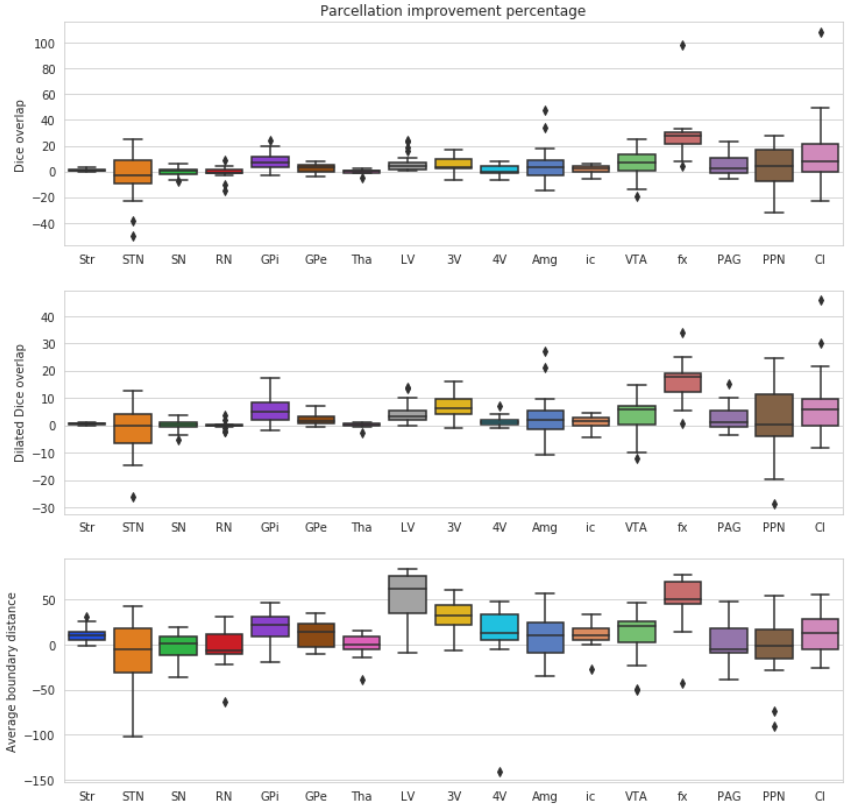

Figure B.1: Leave-one-out re-validation of the MASSP algorithm. The boxplots show the percentage of improvement in parcellation accuracy of the version of MASSP in the current study (with a second co-registration and an intensity normalization step) compared to the original MASSP Positive values indicate better values for the current version. The dilated Dice overlap coefficient is the Dice coefficient after dilating the masks by 1 voxel; as such, it provides a measure of overlap while allowing for 1 voxel of uncertainty. For full details on these metrics, see Bazin et al. (2020).

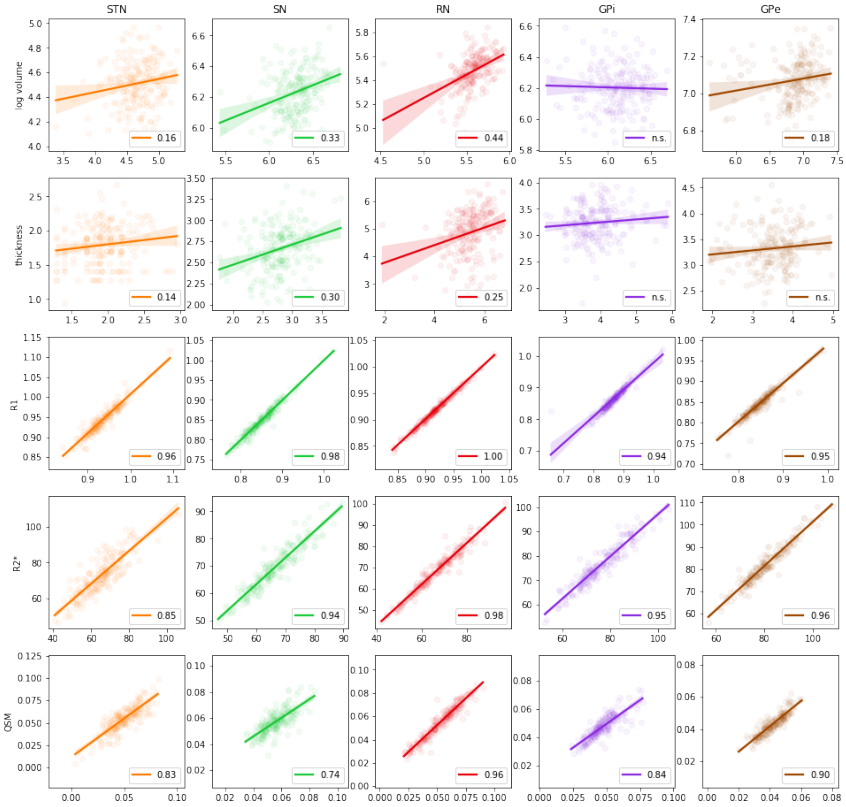

Figure B.2: Comparison between metrics obtained by manual delineation (x-axes) with metrics obtained when using the improved version of MASSP to delineate structures. Rows indicate volume, thickness, R1, R2*, and QSM. Circles are individual data points, straight lines are regression lines with 95% confidence intervals as the shaded area. Pearson's correlation coefficients are shown when the correlation was significant.

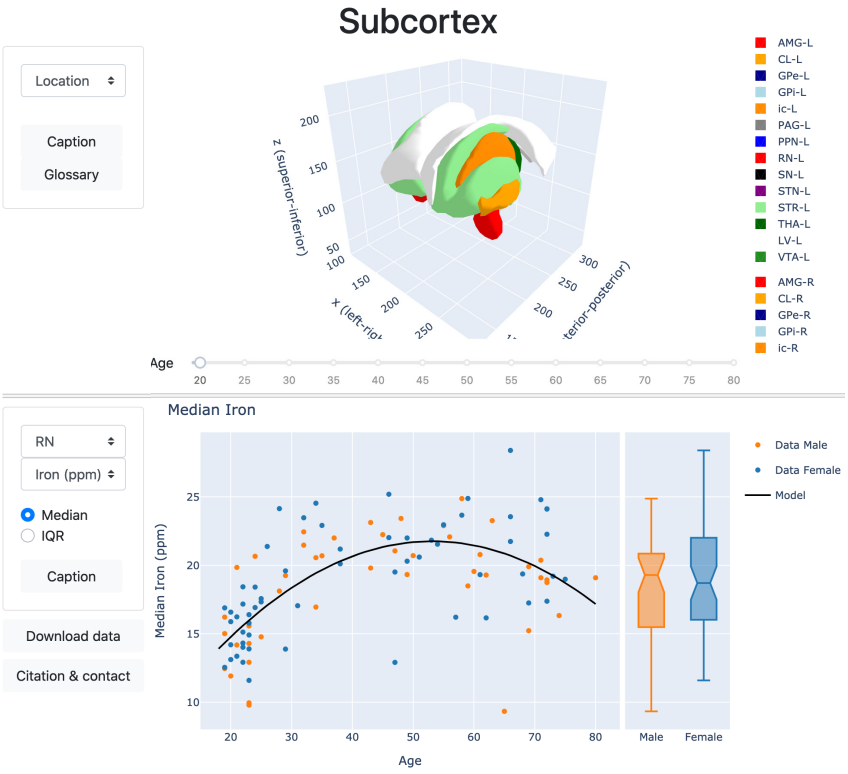

Figure B.3: Illustration of the interactive app which allows for visualizing all data and age-related change models. Top panel features a 3D mesh plot that includes all 17 subcortical structures under investigation. The age slider can be used to visualize the age-related changes in center of mass location (currently visible), or the median or interquartile range of iron, myelin, R1, R2*, and QSM values, color-coded on the structures. Bottom panel features scatterplots of the relation between age and twelve measures (median and interquartile range of myelin, iron, R1, R2*, QSM, and thickness) for all structures. Optional captions are included, and the data underlying the bottom panel can readily be downloaded as a csv file. The app can be accessed via `https://subcortex.eu/app`

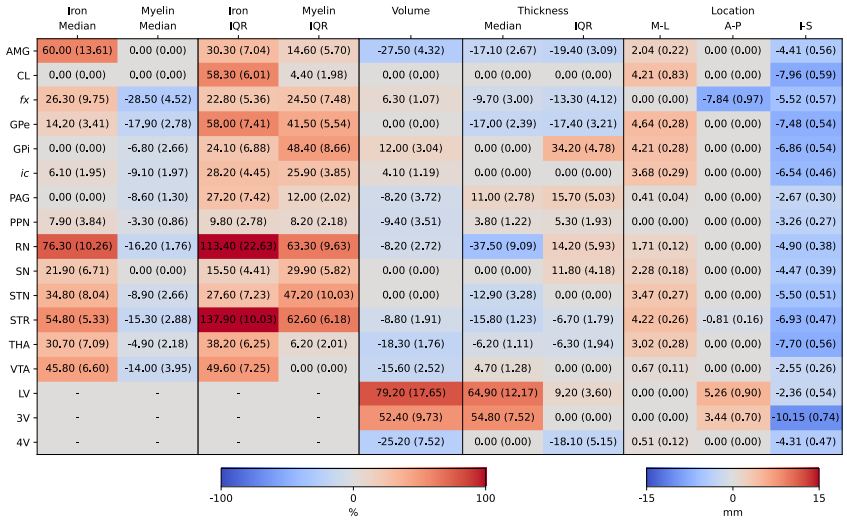

Figure B.4: Matrix of total age-related change in all dependent variables (columns) for individual structures (rows). Values indicate the summed absolute change between 19-75 years old. Negative values indicate decreases. Standard errors were obtained by bootstrapping with 10,000 iterations and are shown in parentheses. The ventricular system is assumed to have no iron or myelin concentration and is excluded from analysis.

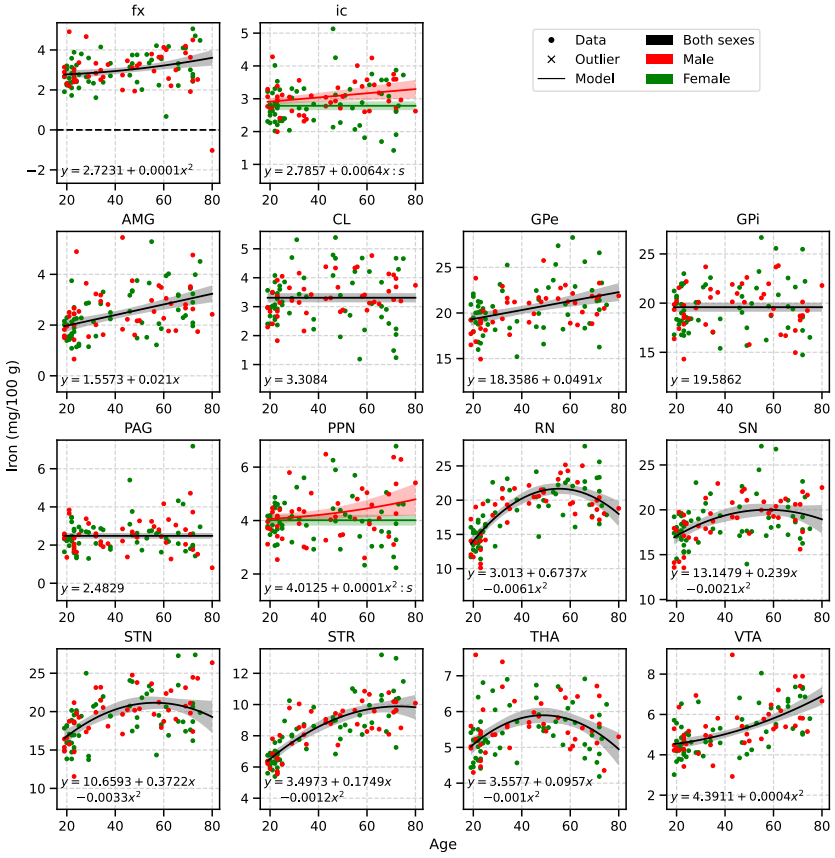

Figure B.5: Age-related change in median iron for all structures. Equations are the parameterized winning models, with x referring to age, and s to sex (dummy coded; 0 = female, 1 = male), and colons indicate interactions. Shaded areas indicate 95% confidence intervals of the winning model predictions

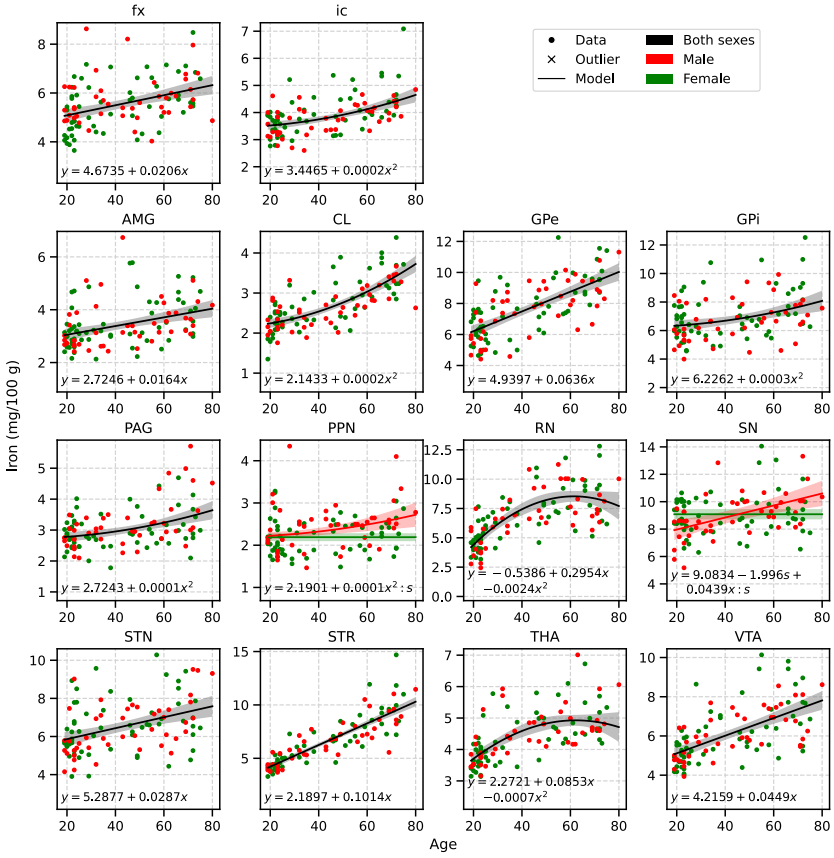

Figure B.6: Age-related change in IQR iron for all structures. Equations are the parameterized winning models, with x referring to age, and s to sex (dummy coded; 0 = female, 1 = male), and colons indicate interactions. Shaded areas indicate 95% confidence intervals of the winning model predictions

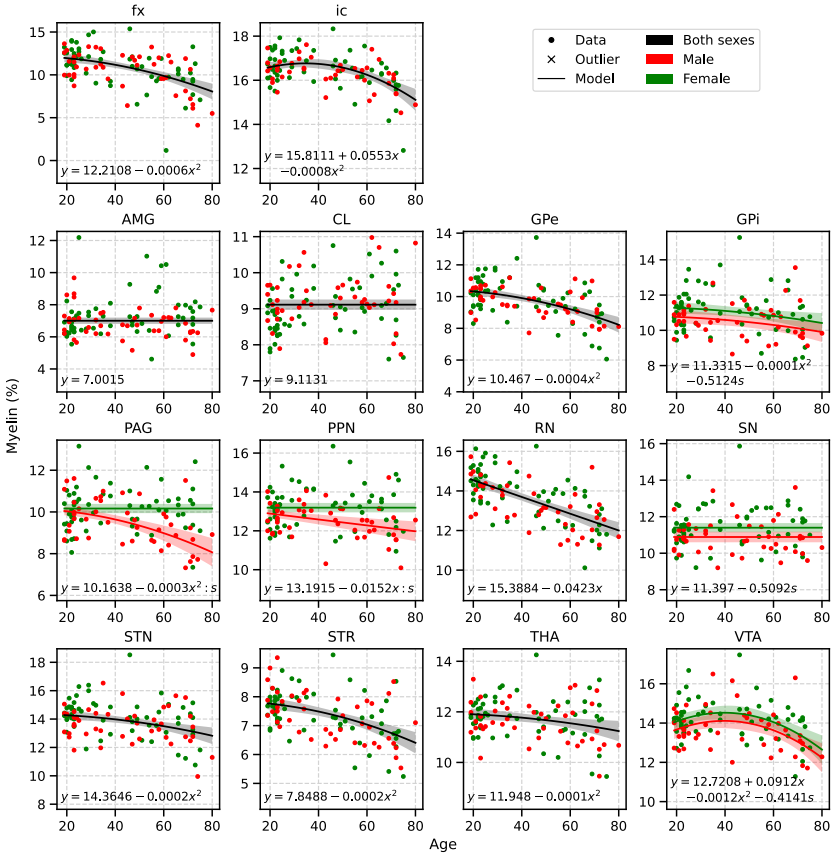

Figure B.7: Age-related change in median myelin for all structures. Equations are the parameterized winning models, with x referring to age, and s to sex (dummy coded; 0 = female, 1 = male), and colons indicate interactions. Shaded areas indicate 95% confidence intervals of the winning model predictions

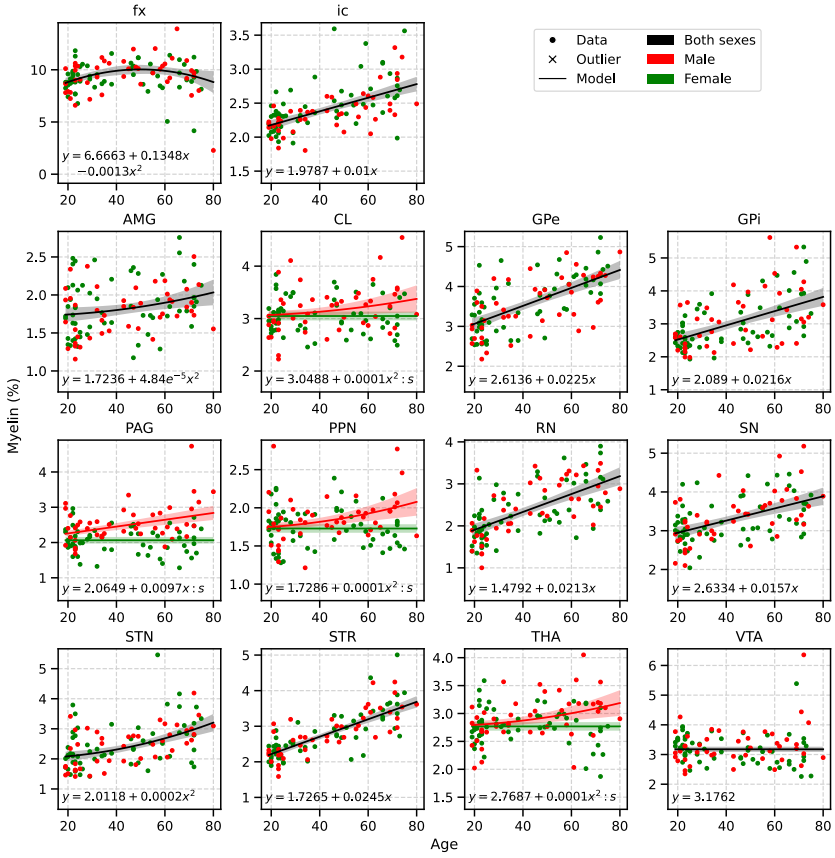

Figure B.8: Age-related change in IQR myelin for all structures. Equations are the parameterized winning models, with x referring to age, and s to sex (dummy coded; 0 = female, 1 = male), and colons indicate interactions. Shaded areas indicate 95% confidence intervals of the winning model predictions

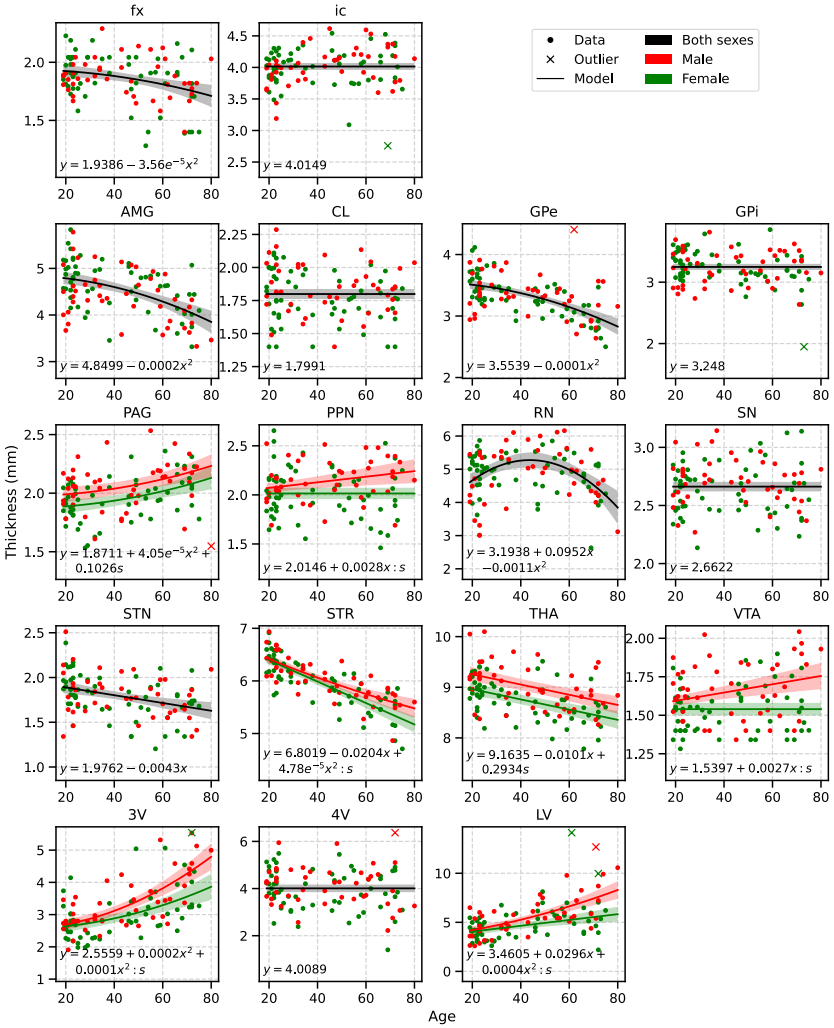

Figure B.9: Age-related change in median thickness for all structures. Equations are the parameterized winning models, with x referring to age, and s to sex (dummy coded; 0 = female, 1 = male), and colons indicate interactions. Shaded areas indicate 95% confidence intervals of the winning model predictions

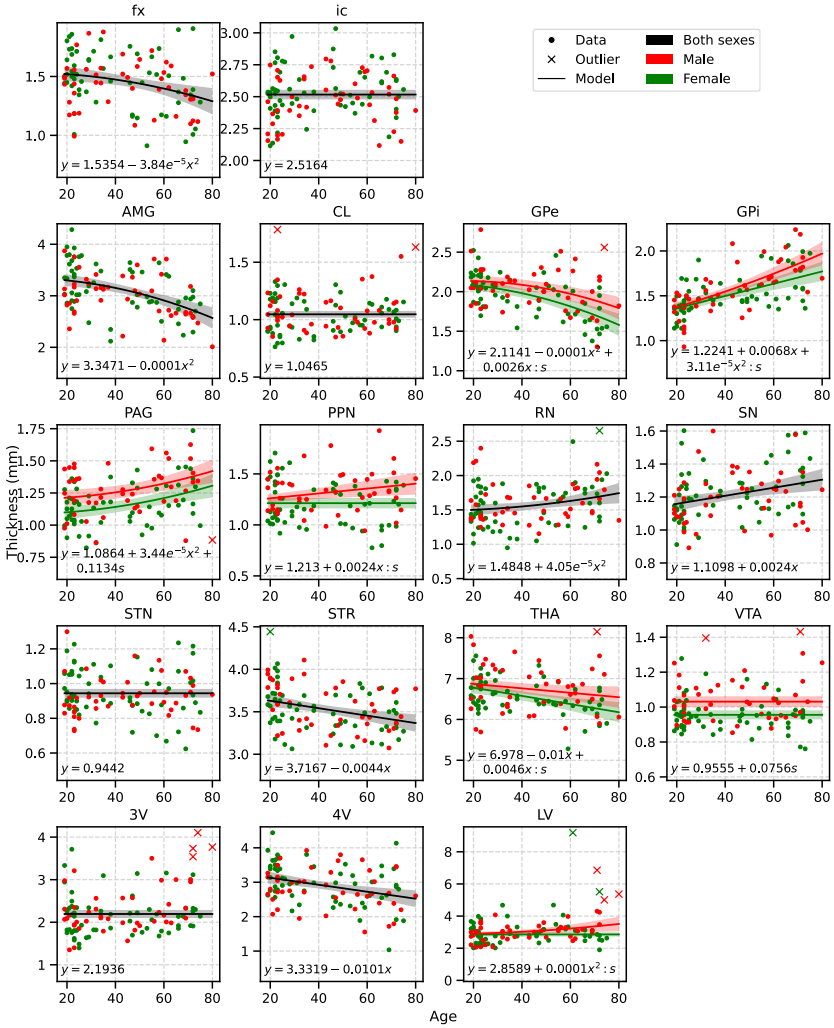

Figure B.10: Age-related change in IQR thickness for all structures. Equations are the parameterized winning models, with x referring to age, and s to sex (dummy coded; 0 = female, 1 = male), and colons indicate interactions. Shaded areas indicate 95% confidence intervals of the winning model predictions

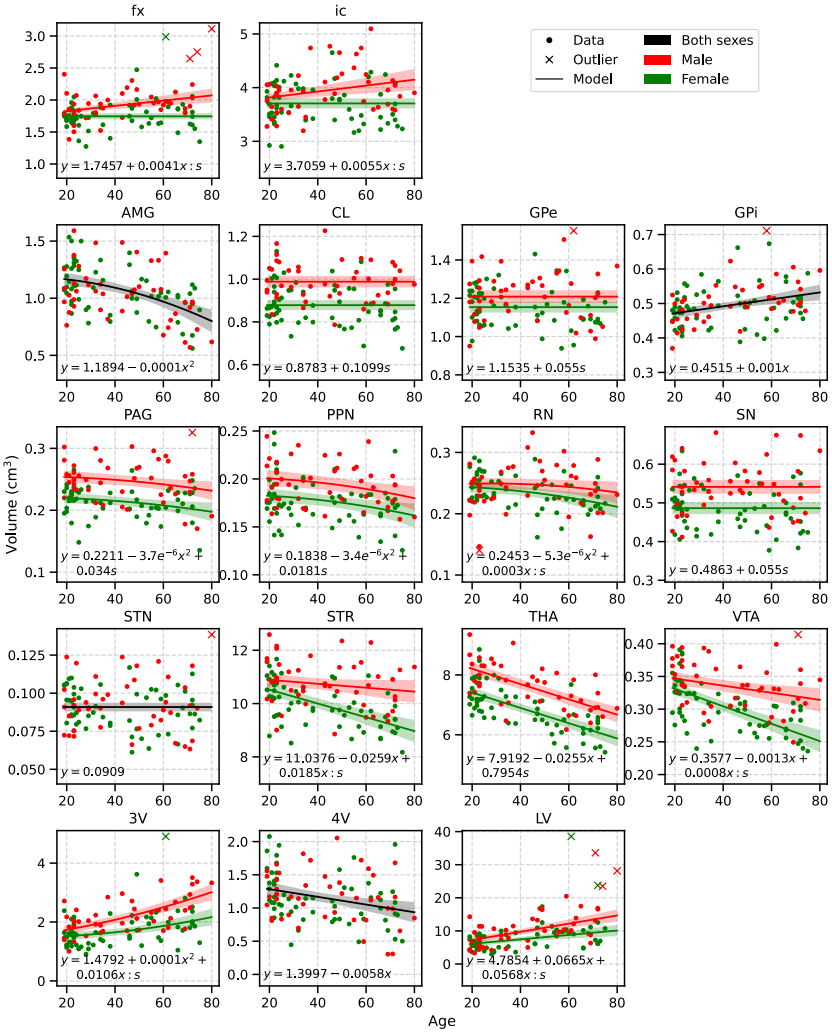

Figure B.11: Age-related change in volume for all structures. Equations are the parameterized winning models, with x referring to age, and s to sex (dummy coded; 0 = female, 1 = male), and colons indicate interactions. Shaded areas indicate 95% confidence intervals of the winning model predictions

Table B.1: Iron estimates and corresponding qMRI values used for estimating linear model Equation 3.1. For all regions that were divided in subregions in one but not the other source (i.e. GP vs GPi/GPe; STR vs PUT/CAU; brain stem vs medulla oblongata; and cortical areas), we entered all subregions in the OLS model, using the more specific values where possible, and the global values otherwise. E.g., both GPe and GPi were in the model and shared iron values (Hallgren and Sourander report only GP), but different qMRI values. To obtain qMRI values for cortex, brain stem, and cerebellum, we parcellated our qMRI data using MGDM and CRUISE Bazin et al. (2014) [a]From Hallgren and Sourander (1958); [b]From Metere and Möller (2018); [c]We used the qMRI metrics of the internal capsule here.

	Iron (mg/100 g)	**QSM (ppm)**	**R1 (Hz)**	**R2* (Hz)**
Brainstem	1.4[a]	−0.000 486	0.808	37.959
Caudate	9.28[a]	0.012 768	0.66	48.64
Cerebellum	3.35[a]	−0.000 078	0.505	34.069
Frontal cortex	2.92[a]	−0.000 004	0.537	32.722
Frontal white	4.24[a]	−0.020 322[c]	0.895[c]	36.294[c]
Globus pallidus externa	21.3[a]	0.042 671	0.848	85.107
Globus pallidus interna	21.3[a]	0.047 246	0.869	77.739
Motor cortex	5.03[a]	−0.000 004	0.537	32.722
Occipital cortex	4.55[a]	−0.000 004	0.537	32.722
Putamen	13.32[a]	0.012 768	0.655	48.644
Parietal cortex	3.81[a]	−0.000 004	0.537	32.722
Red Nucleus	19.48[a]	0.063 051	0.922	74.041
Substantia nigra	18.46[a]	0.058 915	0.862	72.284
Sensory cortex	4.32[a]	−0.000 004	0.537	32.722
Thalamus	4.76[a]	0.002 828	0.758	38.228
Temporal cortex	3.13[a]	−0.000 004	0.537	32.722
Ventricles	0.062[b]	0.005 553	0.341	6.259

Table B.2: For all regions that were divided in subregions in one but not the other source (i.e. GP vs GPi/GPe; STR vs PUT/CAU; brain stem vs medulla oblongata; and cortical areas), we entered all subregions in the OLS model, using the more specific values where possible, and the global values otherwise. E.g., both CAU and PUT were in the model with separate myelin values, but identical qMRI values since the MASSP parcellation only reports STR. To obtain qMRI values for cortex, brain stem, and cerebellum, we parcellated our qMRI data using MGDM and CRUISE Bazin et al. (2014). [a]From Randall (1938); [b]From Metere and Möller (2018); [c]Estimated based on the *post mortem* specimen; [d]We used the qMRI metrics of the internal capsule here.

	Myelin (%)	**QSM (ppm)**	**R1 (Hz)**	**R2* (Hz)**
Brainstem	15.36[a]	−0.000 486	0.808	37.959
Caudate	6.21[a]	0.012 768	0.655	48.644
Frontal cortex	5.08[a]	−0.000 004	0.537	32.722
Frontal white	16.26[a]	−0.020 322[d]	0.895[d]	36.294[d]
Globus pallidus externa	10.404[c]	0.044 293	0.813	84.875
Globus pallidus interna	10.404[c]	0.046 384	0.838	75.216
Parietal cortex	5.42[a]	−0.000 004	0.537	32.722
Putamen	5.611[c]	0.012 768	0.655	48.644
Red nucleus	13.442[c]	0.059 001	0.894	72.979
Substantia nigra	7.404[c]	0.056 24	0.846	71.532
Subthalamic nucleus	14.423[c]	0.058 185	0.935	78.924
Thalamus	11.4[a]	0.002 828	0.758	38.228
Ventricles	0.002[b]	0.005 553	0.232	6.259

Appendix C

Supplementary Materials to Chapter 4

C.1 Supplementary results

Table C.1: The percentage overlap of each of the structures within the significant clusters. The AAL2, Harvard Oxford and Julich atlases were used.

Contrast	Cluster ID	COM X	COM Y	COM Z	Cluster Z-value	Volume (mm3)	aal	harvard oxford	juelich
Interference	1	2	12	48	3.71902	4144	55.02% Supp Motor Area L; 24.52% Supp Motor Area R; 14.86% Cingulate Mid R; 5.02% Frontal Sup Medial R	39.00% Right Paracingulate Gyrus; 24.71% Left Juxtapositional Lobule Cortex (formerly Supplementary Motor Cortex); 21.24% Left Paracingulate Gyrus; 7.14% Right Superior Frontal Gyrus	49.81% GM Premotor cortex BA6 R; 41.89% GM Premotor cortex BA6 L; 8.30% no label
	2	38	20	0	3.71902	3112	80.46% Insula R; 8.48% no label	49.36% Right Insular Cortex; 36.25% Right Frontal Operculum Cortex; 14.14% Right Frontal Orbital Cortex	59.64% no label; 17.99% WM Inferior occipito-frontal fascicle R; 11.31% GM Broca's area BA45 R; 11.05% GM Broca's area BA44 R
	3	-44	-64	-12	3.71902	2760	46.96% Occipital Inf L; 31.30% Temporal Inf L; 20.00% Fusiform L	44.35% Left Lateral Occipital Cortex inferior division; 30.14% Left Inferior Temporal Gyrus temporooccipital part; 16.81% Left Temporal Occipital Fusiform Cortex; 8.70% Left Occipital Fusiform Gyrus	73.62% no label; 22.03% GM Visual cortex V5 L
	4	-38	-42	40	3.54008	1400	84.57% Parietal Inf L; 9.71% no label; 5.71% Postcentral L	34.86% Left Supramarginal Gyrus posterior division; 26.29% Left Superior Parietal Lobule; 23.43% Left Supramarginal Gyrus anterior division; 15.43% Left Postcentral Gyrus	37.14% GM Anterior intra-parietal sulcus hIP1 L; 31.43% GM Anterior intra-parietal sulcus hIP3 L; 24.00% GM Anterior intra-parietal sulcus hIP2 L; 6.86% GM Primary somatosensory cortex BA2 L
	5	-44	4	30	3.23888	1200	86.67% Precentral L; 13.33% Frontal Inf Oper L	80.67% Left Precentral Gyrus; 14.67% Left Middle Frontal Gyrus	80.67% GM Broca's area BA44 L; 11.33% WM Corticospinal tract L; 6.67% GM Premotor cortex BA6 L
	6	-26	-6	56	3.09023	1160	51.72% Frontal Sup 2 L; 35.86% Precentral L; 12.41% Frontal Mid 2 L	38.62% Left Superior Frontal Gyrus; 32.41% Left Precentral Gyrus; 28.97% Left Middle Frontal Gyrus	94.48% GM Premotor cortex BA6 L; 5.52% WM Corticospinal tract L
	7	-14	-70	52	3.09023	1160	70.34% Parietal Sup L; 29.66% Precuneus L	96.55% Left Lateral Occipital Cortex superior division	73.79% GM Superior parietal lobule 7A L; 26.21% GM Superior parietal lobule 7P L
	8	-30	-58	56	2.80703	1056	88.64% Parietal Sup L; 11.36% Parietal Inf L	65.15% Left Superior Parietal Lobule; 34.85% Left Lateral Occipital Cortex superior division	78.79% GM Superior parietal lobule 7A L; 18.94% GM Superior parietal lobule 7PC L
	9	-30	20	4	2.36152	856	97.20% Insula L	82.24% Left Insular Cortex; 17.76% Left Frontal Operculum Cortex	90.65% no label; 6.54% GM Broca's area BA45 L
Inhibition	1	36	18	-4	3.71902	9920	36.85% Insula R; 21.29% no label; 15.00% Putamen R; 14.92% Frontal Inf Orb 2 R; 8.06% Frontal Inf Tri R	34.03% Right Insular Cortex; 29.84% Right Frontal Orbital Cortex; 14.27% Right Putamen; 10.08% Right Frontal Operculum Cortex; 6.05% Right Inferior Frontal Gyrus pars triangularis	52.58% no label; 26.05% WM Inferior occipito-frontal fascicle R; 15.24% GM Broca's area BA45 R
	2	50	-48	28	3.71902	9256	25.67% SupraMarginal R; 19.01% Temporal Mid R; 17.03% Temporal Sup R; 14.69% Parietal Inf R; 9.33% Angular R; 6.40% Parietal Sup R	43.04% Right Supramarginal Gyrus posterior division; 19.79% Right Lateral Occipital Cortex superior division; 16.68% Right Middle Temporal Gyrus temporooccipital part; 11.50% Right Angular Gyrus; 8.21% Right Superior Parietal Lobule	30.16% GM Inferior parietal lobule PFm R; 13.92% GM Inferior parietal lobule Pga R; 12.88% GM Inferior parietal lobule PF R; 12.79% GM Anterior intra-parietal sulcus hIP3 R; 11.15% no label; 7.35% GM Superior parietal lobule 7A R; 6.57% GM Anterior intra-parietal sulcus hIP1 R
	3	46	8	36	3.71902	8960	37.32% Precentral R; 26.96% Frontal Inf Oper R; 18.75% Frontal Mid 2 R; 10.71% Frontal Inf Tri R	39.73% Right Middle Frontal Gyrus; 30.45% Right Precentral Gyrus; 25.18% Right Inferior Frontal Gyrus pars opercularis	46.52% GM Broca's area BA44 R; 35.54% GM Premotor cortex BA6 R; 10.62% GM Broca's area BA45 R; 6.07% no label

Contrast	Cluster ID	COM X	COM Y	COM Z	Cluster Z-value	Volume (mm3)	aal	harvard oxford	juelich
	4	-32	18	-2	3.71902	5544	67.53% Insula L; 12.41% Frontal Inf Tri L; 9.81% no label; 8.95% Frontal Inf Orb 2 L	53.25% Left Insular Cortex; 21.36% Left Frontal Orbital Cortex; 19.62% Left Frontal Operculum Cortex	70.56% no label; 14.14% GM Broca's area BA44 L; 8.66% WM Inferior occipito-frontal fascicle L; 6.64% GM Broca's area BA45 L
	5	42	-62	-10	3.71902	4312	41.37% Temporal Inf R; 33.77% Fusiform R; 12.99% Occipital Inf R; 8.16% Temporal Mid R	32.28% Right Lateral Occipital Cortex inferior division; 30.43% Right Temporal Occipital Fusiform Cortex; 18.92% Right Inferior Temporal Gyrus temporooccipital part; 18.37% Right Occipital Fusiform Gyrus	51.02% no label; 26.72% GM Visual cortex V5 R; 17.63% GM Visual cortex V4 R
	6	-40	-70	-8	3.71902	4032	34.52% Fusiform L; 32.94% Occipital Mid L; 26.39% Occipital Inf L	53.17% Left Lateral Occipital Cortex inferior division; 26.59% Left Temporal Occipital Fusiform Cortex; 16.07% Left Occipital Fusiform Gyrus	39.68% GM Visual cortex V5 L; 37.50% no label; 14.68% GM Visual cortex V4 L; 8.13% WM Optic radiation L
	7	8	14	54	3.71902	3824	58.58% Supp Motor Area R; 29.92% Supp Motor Area L; 8.58% Frontal Sup 2 R	57.53% Right Superior Frontal Gyrus; 14.64% Right Paracingulate Gyrus; 13.81% Left Superior Frontal Gyrus; 12.55% Left Paracingulate Gyrus	78.87% GM Premotor cortex BA6 R; 19.04% GM Premotor cortex BA6 L
	8	-60	-48	34	3.71902	1704	43.66% SupraMarginal L; 33.80% no label; 20.66% Parietal Inf L	88.73% Left Supramarginal Gyrus posterior division; 9.39% Left Angular Gyrus	56.34% GM Inferior parietal lobule PF L; 23.00% GM Inferior parietal lobule PFm L; 20.66% no label
	9	50	-24	-6	3.35279	1488	61.83% Temporal Sup R; 21.51% Temporal Mid R; 16.67% no label	50.00% Right Superior Temporal Gyrus posterior division; 48.39% Right Middle Temporal Gyrus posterior division	50.54% GM Insula Id1 R; 30.65% no label; 9.14% WM Acoustic radiation R; 8.06% WM Optic radiation R
	10	-30	-90	6	3.23888	1456	100.00% Occipital Mid L	43.41% Left Occipital Pole; 40.11% Left Lateral Occipital Cortex inferior division; 16.48% Left Lateral Occipital Cortex superior division	48.35% GM Visual cortex V3V L; 18.13% no label; 17.03% GM Visual cortex V2 BA18 L; 9.34% WM Optic radiation L; 7.14% GM Visual cortex V4 L
	11	-40	-2	42	2.57583	1136	99.30% Precentral L	92.96% Left Precentral Gyrus; 7.04% Left Middle Frontal Gyrus	71.83% GM Premotor cortex BA6 L; 16.20% no label; 8.45% WM Corticospinal tract L
	12	36	-88	2	2.47833	1088	94.85% Occipital Mid R; 5.15% Occipital Inf R	65.44% Right Lateral Occipital Cortex inferior division; 33.09% Right Occipital Pole	39.71% no label; 35.29% GM Visual cortex V4 R; 17.65% GM Visual cortex V3V R; 7.35% WM Optic radiation R
	13	34	40	24	2.28013	1000	86.40% Frontal Mid 2 R; 13.60% Frontal Sup 2 R	99.20% Right Frontal Pole	100.00% no label
	14	8	22	34	1.65463	768	97.92% Cingulate Mid R	78.12% Right Paracingulate Gyrus; 21.88% Right Cingulate Gyrus anterior division	75.00% no label; 14.58% WM Cingulum R; 10.42% GM Premotor cortex BA6 R
Interference >Inhibition	1	-36	-32	36	3.54412	1976	44.53% no label; 32.79% Parietal Inf L; 22.67% Postcentral L	45.75% Left Postcentral Gyrus; 29.96% Left Supramarginal Gyrus anterior division; 23.89% no label	23.48% GM Inferior parietal lobule PFt L; 15.38% WM Superior longitudinal fascicle L; 13.77% WM Corticospinal tract L; 12.96% GM Anterior intra-parietal sulcus hIP2 L; 10.53% GM Primary somatosensory cortex BA3a L; 8.91% GM Anterior intra-parietal sulcus hIP3 L; 6.48% GM Primary somatosensory cortex BA2 L; 6.48% GM Anterior intra-parietal sulcus hIP1 L
	2	0	-70	52	3.44817	680	92.94% Precuneus L	96.47% Left Precuneous Cortex	37.65% GM Superior parietal lobule 7A L; 36.47% GM Superior parietal lobule 7P L; 22.35% GM Superior parietal lobule 7P R

Contrast	Cluster ID	COM X	COM Y	COM Z	Cluster Z-value	Volume (mm3)	aal	harvard oxford	juelich
	3	-8	-50	38	3.37412	592	51.35% Precuneus L; 37.84% Cingulate Mid L; 8.11% Precuneus R	60.81% Left Precuneous Cortex; 31.08% Left Cingulate Gyrus posterior division; 8.11% Right Precuneous Cortex	54.05% GM Superior parietal lobule 5M L; 18.92% no label; 12.16% GM Superior parietal lobule 5M R; 6.76% WM Cingulum L; 5.41% GM Superior parietal lobule 5Ci L
Inhibition >interference	1	56	-52	18	3.58756	21792	38.33% Temporal Mid R; 24.71% Temporal Sup R; 11.12% SupraMarginal R; 9.07% Parietal Inf R; 8.85% Angular R; 7.71% no label	35.35% Right Angular Gyrus; 18.32% Right Middle Temporal Gyrus temporooccipital part; 17.95% Right Supramarginal Gyrus posterior division; 10.94% Right Superior Temporal Gyrus posterior division; 6.13% Right Middle Temporal Gyrus posterior division; 6.02% Right Lateral Occipital Cortex inferior division	28.60% GM Inferior parietal lobule Pga R; 24.78% no label; 20.78% GM Inferior parietal lobule PFm R; 7.78% GM Inferior parietal lobule PGp R
	2	-34	26	-14	3.72735	12496	27.46% Frontal Inf Orb 2 L; 20.23% OFCpost L; 15.43% Insula L; 13.70% no label; 6.85% OFClat L	63.51% Left Frontal Orbital Cortex; 16.01% Left Frontal Pole; 11.01% Left Insular Cortex	79.19% no label; 9.03% GM Broca's area BA45 L; 6.91% WM Inferior occipito-frontal fascicle L
	3	46	2	44	3.59027	9128	55.13% Frontal Mid 2 R; 37.95% Precentral R	62.05% Right Middle Frontal Gyrus; 37.07% Right Precentral Gyrus	40.05% no label; 35.85% GM Premotor cortex BA6 R; 18.23% GM Broca's area BA44 R
	4	22	48	22	3.49556	4160	79.04% Frontal Sup 2 R; 12.12% no label; 8.85% Frontal Mid 2 R	98.65% Right Frontal Pole	100.00% no label
	5	-58	-54	38	3.52706	3880	39.18% no label; 23.71% SupraMarginal L; 22.27% Parietal Inf L; 8.04% Temporal Sup L	65.15% Left Supramarginal Gyrus posterior division; 32.37% Left Angular Gyrus	41.44% GM Inferior parietal lobule PFm L; 28.87% GM Inferior parietal lobule PF L; 24.54% no label; 5.15% GM Inferior parietal lobule Pga L
	6	26	20	-6	3.6251	3504	35.84% no label; 35.62% Putamen R; 13.01% Insula R; 10.96% Caudate R	40.18% Right Putamen; 25.34% Right Frontal Orbital Cortex; 20.09% Right Insular Cortex; 8.68% Right Caudate	49.09% no label; 34.47% WM Inferior occipito-frontal fascicle R; 8.68% WM Callosal body
	7	-52	-80	12	3.28042	744	74.19% Occipital Mid L; 25.81% no label	100.00% Left Lateral Occipital Cortex inferior division	49.46% GM Visual cortex V5 L; 26.88% no label; 22.58% GM Visual cortex V4 L
	8	-20	-98	18	3.32455	616	57.14% Occipital Mid L; 33.77% Occipital Sup L; 9.09% no label	85.71% Left Occipital Pole; 14.29% Left Lateral Occipital Cortex superior division	76.62% GM Visual cortex V2 BA18 L; 14.29% GM Visual cortex V1 BA17 L; 6.49% WM Optic radiation L

Table C.2: Additional control analyses testing the robustness of inhibition contrasts

Contrast	Cluster ID	COM X	COM Y	COM Z	Cluster Z-value	Volume (mm3)	aal	harvard oxford	juelich
Inhibition (salient events != 50/50)	1	36	18	-4	3.7190	9976	36.89% Insula R; 21.17% no label; 15.16% Putamen R; 14.92% Frontal Inf Orb 2 R; 8.02% Frontal Inf Tri R	34.00% Right Insular Cortex; 29.75% Right Frontal Orbital Cortex; 14.43% Right Putamen; 10.10% Right Frontal Operculum Cortex; 6.01% Right Inferior Frontal Gyrus pars triangularis	52.77% no label; 25.90% WM Inferior occipito-frontal fascicle R; 15.16% GM Broca's area BA45 R
	2	50	-50	30	3.7190	9416	25.66% SupraMarginal R; 17.76% Temporal Mid R; 17.16% Temporal Sup R; 14.95% Parietal Inf R; 9.52% Angular R; 6.80% Parietal Sup R	43.50% Right Supramarginal Gyrus posterior division; 20.56% Right Lateral Occipital Cortex superior division; 15.38% Right Middle Temporal Gyrus temporooccipital part; 11.64% Right Angular Gyrus; 8.16% Right Superior Parietal Lobule	30.25% GM Inferior parietal lobule PFm R; 14.02% GM Inferior parietal lobule Pga R; 12.91% GM Inferior parietal lobule PF R; 12.74% GM Anterior intra-parietal sulcus hIP3 R; 9.94% no label; 7.65% GM Superior parietal lobule 7A R; 6.88% GM Anterior intra-parietal sulcus hIP1 R
	3	46	8	36	3.7190	8704	36.86% Precentral R; 27.11% Frontal Inf Oper R; 19.58% Frontal Mid 2 R; 9.74% Frontal Inf Tri R	41.54% Right Middle Frontal Gyrus; 29.96% Right Precentral Gyrus; 24.63% Right Inferior Frontal Gyrus pars opercularis	47.15% GM Broca's area BA44 R; 35.48% GM Premotor cortex BA6 R; 9.56% GM Broca's area BA45 R; 6.71% no label
	4	-32	18	-2	3.7190	5600	67.14% Insula L; 12.71% Frontal Inf Tri L; 9.86% no label; 9.00% Frontal Inf Orb 2 L	53.00% Left Insular Cortex; 21.43% Left Frontal Orbital Cortex; 19.57% Left Frontal Operculum Cortex	70.29% no label; 14.29% GM Broca's area BA44 L; 8.71% WM Inferior occipito-frontal fascicle L; 6.71% GM Broca's area BA45 L
	5	42	-62	-10	3.7190	4360	41.10% Temporal Inf R; 34.13% Fusiform R; 13.03% Occipital Inf R; 8.07% Temporal Mid R	32.11% Right Lateral Occipital Cortex inferior division; 30.83% Right Temporal Occipital Fusiform Cortex; 18.72% Right Inferior Temporal Gyrus temporooccipital part; 18.35% Right Occipital Fusiform Gyrus	50.83% no label; 26.61% GM Visual cortex V5 R; 17.80% GM Visual cortex V4 R
	6	-40	-70	-8	3.7190	4120	34.56% Fusiform L; 32.82% Occipital Mid L; 26.02% Occipital Inf L	52.82% Left Lateral Occipital Cortex inferior division; 26.99% Left Temporal Occipital Fusiform Cortex; 15.92% Left Occipital Fusiform Gyrus	39.61% GM Visual cortex V5 L; 37.48% no label; 14.37% GM Visual cortex V4 L; 8.54% WM Optic radiation L
	7	6	14	54	3.7190	3568	56.73% Supp Motor Area R; 32.06% Supp Motor Area L; 8.07% Frontal Sup 2 R	55.16% Right Superior Frontal Gyrus; 15.70% Right Paracingulate Gyrus; 14.80% Left Superior Frontal Gyrus; 13.45% Left Paracingulate Gyrus	77.35% GM Premotor cortex BA6 R; 20.40% GM Premotor cortex BA6 L
	8	-60	-48	34	3.7190	1720	44.19% SupraMarginal L; 33.49% no label; 20.47% Parietal Inf L	88.84% Left Supramarginal Gyrus posterior division; 9.30% Left Angular Gyrus	56.74% GM Inferior parietal lobule PF L; 22.79% GM Inferior parietal lobule PFm L; 20.47% no label
	9	50	-24	-6	3.3528	1488	61.83% Temporal Sup R; 21.51% Temporal Mid R; 16.67% no label	50.00% Right Superior Temporal Gyrus posterior division; 48.39% Right Middle Temporal Gyrus posterior division	50.54% GM Insula Id1 R; 30.65% no label; 9.14% WM Acoustic radiation R; 8.06% WM Optic radiation R
	10	-30	-90	6	3.1559	1472	100.00% Occipital Mid L	43.48% Left Occipital Pole; 40.22% Left Lateral Occipital Cortex inferior division; 16.30% Left Lateral Occipital Cortex superior division	48.37% GM Visual cortex V3V L; 17.93% no label; 17.39% GM Visual cortex V2 BA18 L; 9.24% WM Optic radiation L; 7.07% GM Visual cortex V4 L

Contrast	Cluster ID	COM X	COM Y	COM Z	Cluster Z-value	Volume (mm3)	aal	harvard oxford	juelich
	11	-40	-2	42	2.6356	1152	99.31% Precentral L	93.06% Left Precentral Gyrus; 6.94% Left Middle Frontal Gyrus	71.53% GM Premotor cortex BA6 L; 15.97% no label; 9.03% WM Corticospinal tract L
	12	36	-88	2	2.5556	1112	94.96% Occipital Mid R; 5.04% Occipital Inf R	64.75% Right Lateral Occipital Cortex inferior division; 33.81% Right Occipital Pole	39.57% no label; 34.53% GM Visual cortex V4 R; 17.99% GM Visual cortex V3V R; 7.91% WM Optic radiation R
	13	34	40	24	2.3867	1032	86.82% Frontal Mid 2 R; 13.18% Frontal Sup 2 R	98.45% Right Frontal Pole	100.00% no label
	14	8	22	34	1.6902	776	97.94% Cingulate Mid R	78.35% Right Paracingulate Gyrus; 21.65% Right Cingulate Gyrus anterior division	75.26% no label; 14.43% WM Cingulum R; 10.31% GM Premotor cortex BA6 R
	15	-54	-60	8	1.6646	768	98.96% Temporal Mid L	71.88% Left Middle Temporal Gyrus temporooccipital part; 17.71% Left Lateral Occipital Cortex inferior division	46.88% GM Inferior parietal lobule PGp L; 33.33% no label; 14.58% GM Inferior parietal lobule Pga L
Inhibition ((salient events != 50/50) & (Max Trial duration <= 4 seconds))	1	34	18	-4	3.7190	8848	37.88% Insula R; 20.07% no label; 17.63% Putamen R; 13.65% Frontal Inf Orb 2 R; 6.24% Frontal Inf Tri R	35.90% Right Insular Cortex; 27.03% Right Frontal Orbital Cortex; 16.82% Right Putamen; 8.41% Right Frontal Operculum Cortex; 5.42% Right Inferior Frontal Gyrus pars triangularis	56.96% no label; 25.86% WM Inferior occipito-frontal fascicle R; 11.93% GM Broca's area BA45 R
	2	46	6	36	3.7190	7976	39.92% Precentral R; 25.88% Frontal Inf Oper R; 19.06% Frontal Mid 2 R; 8.43% Frontal Inf Tri R; 5.92% Frontal Sup 2 R	38.82% Right Middle Frontal Gyrus; 34.50% Right Precentral Gyrus; 23.47% Right Inferior Frontal Gyrus pars opercularis	49.45% GM Broca's area BA44 R; 37.01% GM Premotor cortex BA6 R; 7.02% no label; 5.82% GM Broca's area BA45 R
	3	42	-62	-10	3.7190	4992	39.42% Temporal Inf R; 36.06% Fusiform R; 12.98% Occipital Inf R; 7.69% Temporal Mid R	32.53% Right Lateral Occipital Cortex inferior division; 30.77% Right Temporal Occipital Fusiform Cortex; 19.07% Right Occipital Fusiform Gyrus; 17.63% Right Inferior Temporal Gyrus temporooccipital part	49.68% no label; 25.96% GM Visual cortex V5 R; 19.55% GM Visual cortex V4 R
	4	-40	-70	-8	3.7190	4696	34.41% Fusiform L; 30.49% Occipital Mid L; 27.77% Occipital Inf L	51.79% Left Lateral Occipital Cortex inferior division; 26.41% Left Temporal Occipital Fusiform Cortex; 17.38% Left Occipital Fusiform Gyrus	38.16% GM Visual cortex V5 L; 37.82% no label; 16.01% GM Visual cortex V4 L; 8.01% WM Optic radiation L
	5	-32	18	-2	3.7190	4584	74.17% Insula L; 9.77% Frontal Inf Tri L; 8.38% no label; 7.33% Frontal Inf Orb 2 L	60.73% Left Insular Cortex; 18.32% Left Frontal Operculum Cortex; 17.63% Left Frontal Orbital Cortex	71.73% no label; 15.18% GM Broca's area BA44 L; 8.03% WM Inferior occipito-frontal fascicle L; 5.06% GM Broca's area BA45 L
	6	8	14	54	3.7190	3832	57.83% Supp Motor Area R; 29.02% Supp Motor Area L; 9.81% Frontal Sup 2 R	57.41% Right Superior Frontal Gyrus; 15.45% Right Paracingulate Gyrus; 13.99% Left Superior Frontal Gyrus; 11.90% Left Paracingulate Gyrus	78.50% GM Premotor cortex BA6 R; 19.21% GM Premotor cortex BA6 L
	7	58	-44	8	3.7190	2488	64.31% Temporal Mid R; 35.69% Temporal Sup R	57.23% Right Middle Temporal Gyrus temporooccipital part; 34.08% Right Supramarginal Gyrus posterior division; 8.36% Right Angular Gyrus	38.26% GM Inferior parietal lobule Pga R; 32.80% no label; 27.65% GM Inferior parietal lobule PFm R

Contrast	Cluster ID	COM X	COM Y	COM Z	Cluster Z-value	Volume (mm3)	aal	harvard oxford	juelich
	8	34	-60	46	3.7190	2160	28.52% Angular R; 27.78% Parietal Inf R; 24.07% Parietal Sup R; 16.30% Occipital Sup R	59.63% Right Lateral Occipital Cortex superior division; 32.22% Right Superior Parietal Lobule; 8.15% Right Angular Gyrus	46.67% GM Anterior intra-parietal sulcus hIP3 R; 22.59% GM Superior parietal lobule 7A R; 11.48% GM Superior parietal lobule 7P R; 10.37% GM Anterior intra-parietal sulcus hIP1 R; 5.56% GM Inferior parietal lobule PGp R
	9	62	-42	26	3.7190	1816	76.65% SupraMarginal R; 23.35% Temporal Sup R	81.50% Right Supramarginal Gyrus posterior division; 14.98% Right Angular Gyrus	55.07% GM Inferior parietal lobule PFm R; 43.61% GM Inferior parietal lobule PF R
	10	-30	-90	4	3.7190	1528	98.95% Occipital Mid L	45.03% Left Lateral Occipital Cortex inferior division; 40.31% Left Occipital Pole; 14.66% Left Lateral Occipital Cortex superior division	45.55% GM Visual cortex V3V L; 16.23% no label; 15.71% GM Visual cortex V2 BA18 L; 13.09% GM Visual cortex V4 L; 9.42% WM Optic radiation L
	11	-60	-46	34	3.5401	1480	41.62% SupraMarginal L; 31.35% no label; 27.03% Parietal Inf L	95.68% Left Supramarginal Gyrus posterior division	63.24% GM Inferior parietal lobule PF L; 21.62% no label; 15.14% GM Inferior parietal lobule PFm L
	12	36	-88	2	3.4316	1432	85.47% Occipital Mid R; 9.50% Occipital Inf R	62.01% Right Lateral Occipital Cortex inferior division; 32.40% Right Occipital Pole	33.52% no label; 30.73% GM Visual cortex V4 R; 24.02% GM Visual cortex V3V R; 8.38% WM Optic radiation R
	13	52	-24	-6	3.1947	1320	60.61% Temporal Sup R; 21.82% Temporal Mid R; 17.58% no label	50.91% Right Superior Temporal Gyrus posterior division; 48.48% Right Middle Temporal Gyrus posterior division	46.67% GM Insula Id1 R; 33.94% no label; 10.30% WM Acoustic radiation R; 7.88% WM Optic radiation R
	14	50	-40	46	3.0902	1304	63.80% Parietal Inf R; 36.20% SupraMarginal R	94.48% Right Supramarginal Gyrus posterior division; 5.52% Right Supramarginal Gyrus anterior division	44.17% GM Inferior parietal lobule PFm R; 34.97% GM Inferior parietal lobule PF R; 13.50% GM Anterior intra-parietal sulcus hIP1 R
	15	-52	-60	8	2.1444	904	99.12% Temporal Mid L	66.37% Left Middle Temporal Gyrus temporooccipital part; 16.81% Left Lateral Occipital Cortex inferior division; 10.62% Left Angular Gyrus	40.71% GM Inferior parietal lobule PGp L; 38.94% no label; 13.27% GM Inferior parietal lobule Pga L; 5.31% GM Inferior parietal lobule PFm L
	16	8	22	34	1.8606	800	97.00% Cingulate Mid R	80.00% Right Paracingulate Gyrus; 20.00% Right Cingulate Gyrus anterior division	79.00% no label; 12.00% GM Premotor cortex BA6 R; 9.00% WM Cingulum R

Appendix D

Supplementary Materials to Chapter 5

D.1 Supplementary results

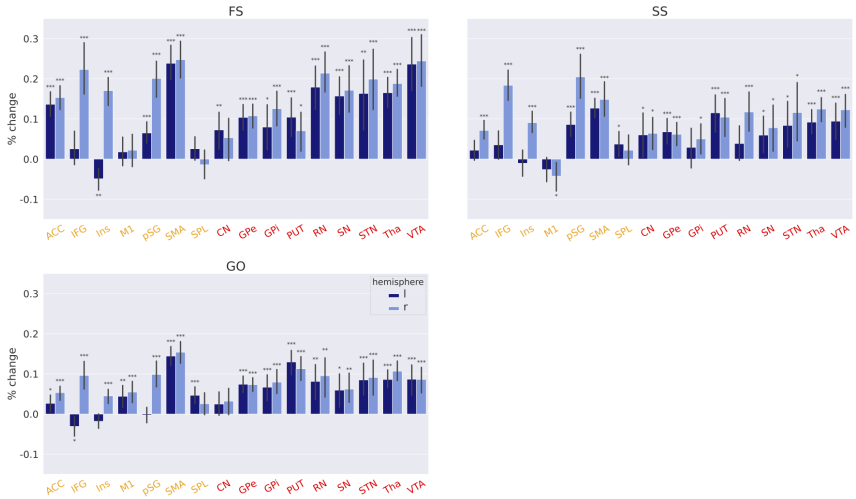

Figure D.1: ROI analyses for all individual trial types in the SST. T-value significance are FDR corrected ($q < 0.05$). Left hemisphere is shown in dark blue, and right in light blue. Asterisks denotes significance. FS, failed stops; SS, successful stops; ACC, anterior cingulate cortex; IFG, inferior frontal gyrus; Ins, insula; M1, motor cortex 1; pSG, posterior supramarginal gyrus; SMA, pre-supplementary motor area; SPL, superior parietal lobule; CN, caudate nucleus; GPe, globus pallidus externa; GPi, globus pallidus interna; PUT, putamen; RN, red nucleus; SN, substantia nigra; STN, subthalamic nucleus; Tha, thalamus; VTA, ventral tegmental area. Orange denotes cortical regions, red, subcortical.

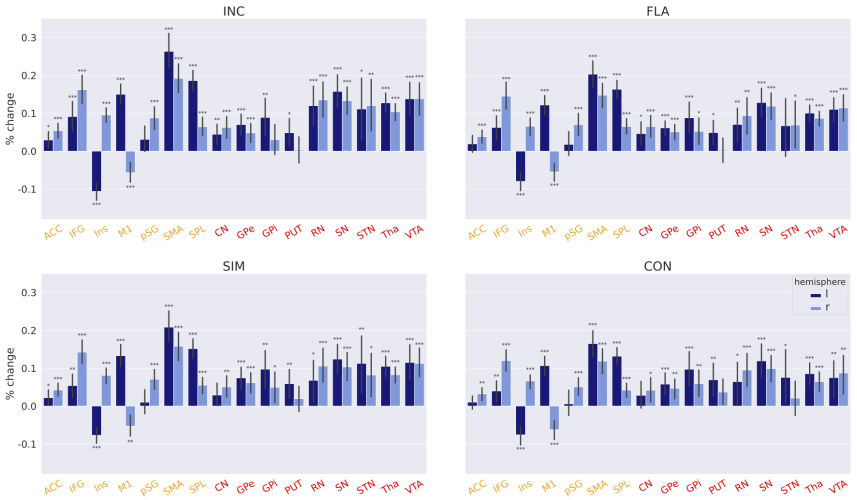

Figure D.2: ROI analyses for all individual trial types in the MSIT. Left hemisphere is shown in dark blue, and right in light blue. Asterisks denotes significance. INC, incongruent; FLA, Flanker; SIM, Simon; CON, congruent; ACC, anterior cingulate cortex; IFG, inferior frontal gyrus; Ins, insula; M1, motor cortex 1; pSG, posterior supramarginal gyrus; SMA, pre-supplementary motor area; SPL, superior parietal lobule; CN, caudate nucleus; GPe, globus pallidus externa; GPi, globus pallidus interna; PUT, putamen; RN, red nucleus; SN, substantia nigra; STN, subthalamic nucleus; Tha, thalamus; VTA, ventral tegmental area. Orange denotes cortical regions, red, subcortical.

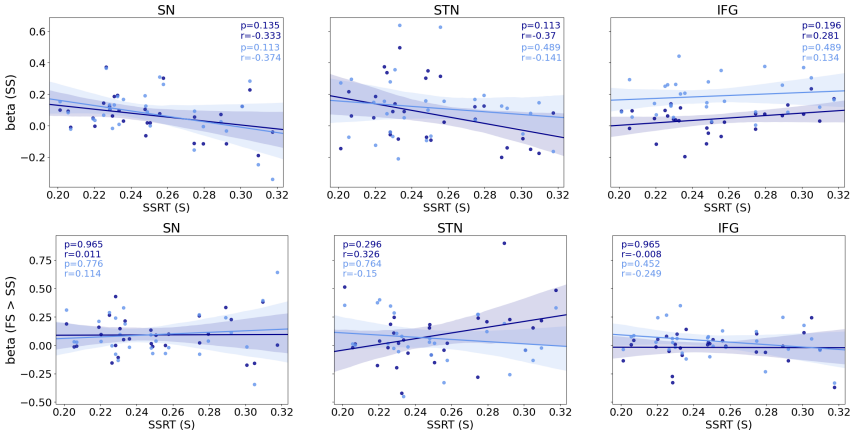

Figure D.3: Group-level correlations between GLM betas on SS trials and SSRTs (top) and the FS > SS contrast and SSRTs (bottom) in the SST when using the BEESTS method for SSRT estimation. Significance is FDR corrected. r denotes the Pearson correlation, with p the corresponding p-value. Left hemisphere is shown in dark blue. Right hemisphere is shown in light blue.

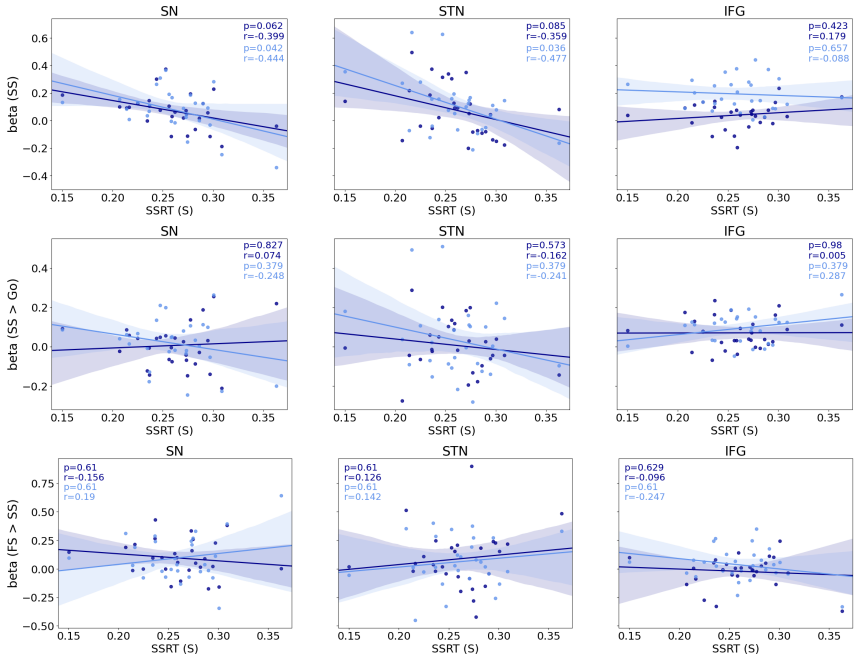

Figure D.4: Group-level correlations between GLM betas on SS trials and SSRTs (top), the SS > GO contrast and SSRTs (middle), and the FS > SS contrast and SSRTs (bottom) in the SST when using the mean method for SSRT estimation. Significance is FDR corrected. r denotes the Pearson correlation, with p the corresponding p-value. Left hemisphere is shown in dark blue. Right hemisphere is shown in light blue.

Appendix E

Supplementary Materials to Chapter 6

E.1 Supplementary results

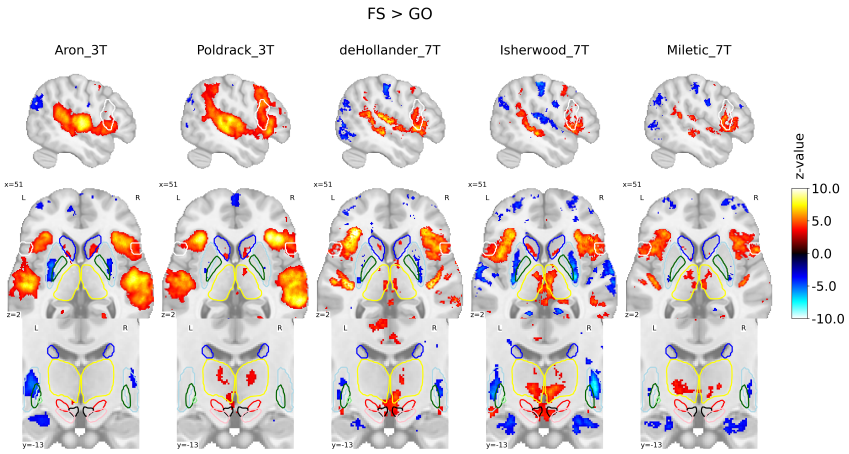

Figure E.1: Group-level SPMs of the FS > GO contrast of the SST for each dataset. Activation colours indicate FDR thresholded (q < .05) z-values. Sagittal (top), axial (middle) and a zoomed in coronal (bottom) view are shown. Coloured contour lines indicate regions of interest (IFG in white, M1 in grey, preSMA in orange, Caudate in dark blue, Putamen in light blue, GPe in dark green, GPi in light green, SN in pink, STN in red, thalamus in yellow, and VTA in black). The background template and coordinates are in MNI2009c (1mm); slices are drawn through x = 51 (top), y = -13 (bottom), and z = 2 (middle).

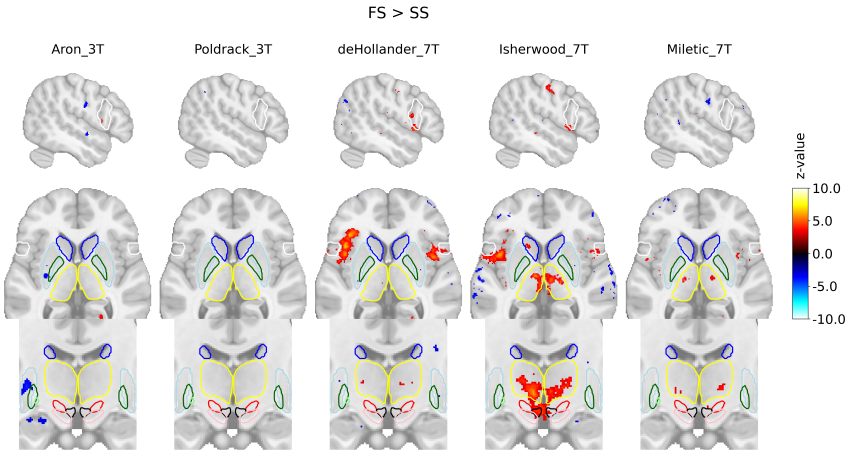

Figure E.2: Group-level SPMs of the FS > SS contrast of the SST for each dataset. Activation colours indicate FDR thresholded (q < .05) z-values. Sagittal (top), axial (middle) and a zoomed in coronal (bottom) view are shown. Coloured contour lines indicate regions of interest (IFG in white, M1 in grey, preSMA in orange, Caudate in dark blue, Putamen in light blue, GPe in dark green, GPi in light green, SN in pink, STN in red, thalamus in yellow, and VTA in black). The background template and coordinates are in MNI2009c (1mm); slices are drawn through x = 51 (top), y = -13 (bottom), and z = 2 (middle).

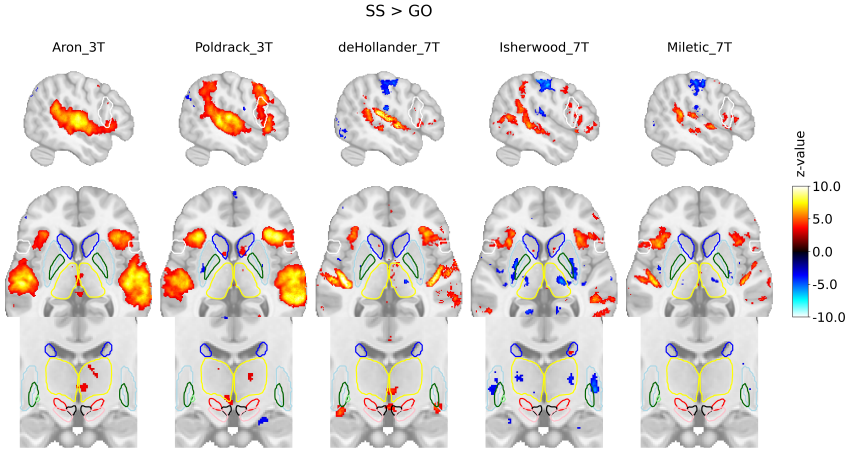

Figure E.3: Group-level SPMs of the SS > GO contrast of the SST for each dataset. Activation colours indicate FDR thresholded (q < .05) z-values. Sagittal (top), axial (middle) and a zoomed in coronal (bottom) view are shown. Coloured contour lines indicate regions of interest (IFG in white, M1 in grey, preSMA in orange, Caudate in dark blue, Putamen in light blue, GPe in dark green, GPi in light green, SN in pink, STN in red, thalamus in yellow, and VTA in black). The background template and coordinates are in MNI2009c (1mm); slices are drawn through x = 51 (top), y = -13 (bottom), and z = 2 (middle).

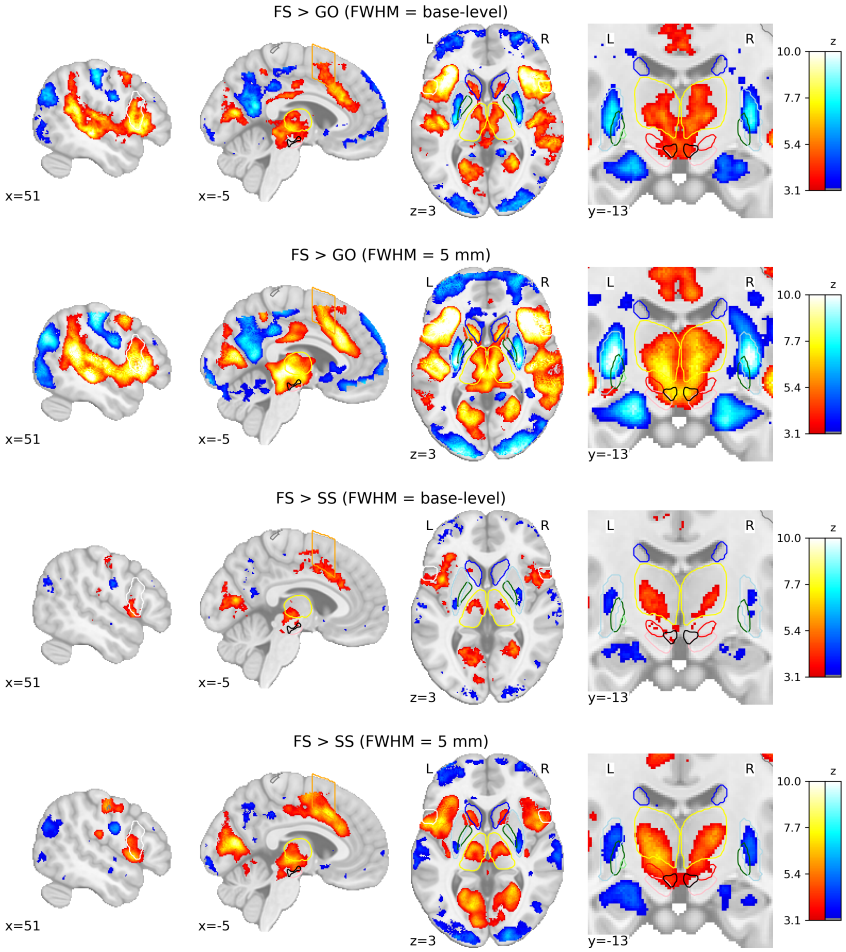

Figure E.4: Group-level SPMs of the FS > GO and FS > SS contrasts using different smoothing kernels. Activation colours indicate FDR thresholded (q < .05) z-values. Two sagittal, one axial, and one zoomed in coronal view are shown. Coloured contour lines indicate regions of interest (IFG in white, M1 in grey, preSMA in orange, Caudate in dark blue, Putamen in light blue, GPe in dark green, GPi in light green, SN in pink, STN in red, thalamus in yellow, and VTA in black). The background template and coordinates are in MNI2009c (1mm). FS, failed stop; SS, successful stop.

Bibliography

Abraham, A., Pedregosa, F., Eickenberg, M., Gervais, P., Mueller, A., Kossaifi, J., Gramfort, A., Thirion, B., and Varoquaux, G. (2014). Machine learning for neuroimaging with scikit-learn. *Frontiers in neuroinformatics* 8, p. 14. DOI: 10.3389/fninf.2014.00014.

Abutalebi, J., Della Rosa, P. A., Green, D. W., Hernandez, M., Scifo, P., Keim, R., Cappa, S. F., and Costa, A. (2012). Bilingualism tunes the anterior cingulate cortex for conflict monitoring. *Cerebral cortex* 22, pp. 2076–2086.

Acosta-Cabronero, J., Betts, M. J., Cardenas-Blanco, A., Yang, S., and Nestor, P. J. (2016). In vivo MRI mapping of brain iron deposition across the adult lifespan. *Journal of Neuroscience* 36, pp. 364–374. DOI: 10.1523/JNEUROSCI.1907-15.2016.

Adnan Majid, D. S., Cai, W., Corey-Bloom, J., and Aron, A. R. (2013). Proactive selective response suppression is implemented via the basal ganglia. *Journal of Neuroscience*. DOI: 10.1523/JNEUROSCI.5651-12.2013.

Akaike, H. (1973). "Information theory and an extension of the maximum likelihood principle." In: *Proceedings of the Second International Symposium on Information Theory*. Ed. by B. Petrov and F. Caski. Budapest: Akademiai Kiado, pp. 267–281.

Albanese, A., Bhatia, K., Bressman, S. B., DeLong, M. R., Fahn, S., Fung, V. S., Hallett, M., Jankovic, J., Jinnah, H. A., Klein, C., et al. (2013). Phenomenology and classification of dystonia: a consensus update. *Movement disorders* 28, pp. 863–873.

Alberico, S. L., Cassell, M. D., and Narayanan, N. S. (2015). The vulnerable ventral tegmental area in Parkinson's disease. en. *Basal Ganglia* 5, pp. 51–55.

Albin, R. L., Young, A. B., and Penney, J. B. (1989). The functional anatomy of basal ganglia disorders. *Trends in neurosciences* 12, pp. 366–375. DOI: 10.1016/0166-2236(89)90074-X.

Alegre, M., Lopez-Azcarate, J., Obeso, I., Wilkinson, L., Rodriguez-Oroz, M. C., Valencia, M., Garcia-Garcia, D., Guridi, J., Artieda, J., Jahanshahi, M., and Obeso, J. A. (2013). The subthalamic nucleus is involved in successful inhibition in the stop-signal task: A local field potential study in Parkinson's disease. *Experimental Neurology* 239, pp. 1–12. DOI: https://doi.org/10.1016/j.expneurol.2012.08.027.

Alexander, G. E., DeLong, M. R., and Strick, P. L. (1986). Parallel organization of functionally segregated circuits linking basal ganglia and cortex. *Annual Review of Neuroscience*. DOI: 10.1146/annurev.ne.09.030186.002041.

Alexander, L. M., Escalera, J., Ai, L., Andreotti, C., Febre, K., Mangone, A., Vega-Potler, N., Langer, N., Alexander, A., Kovacs, M., Litke, S., O'Hagan, B., Andersen, J., Bronstein, B., Bui, A., Bushey, M., Butler, H., Castagna, V., Camacho, N., Chan, E., Citera, D., Clucas, J., Cohen, S., Dufek, S., Eaves, M., Fradera, B., Gardner, J., Grant-Villegas, N., Green, G., Gregory, C., Hart, E., Harris, S., Horton, M., Kahn, D., Kabotyanski, K., Karmel, B., Kelly, S. P., Kleinman, K., Koo, B., Kramer, E., Lennon, E., Lord, C., Mantello, G., Margolis, A., Merikangas, K. R., Milham, J., Minniti, G., Neuhaus, R., Levine, A., Osman, Y., Parra, L. C., Pugh, K. R., Racanello, A., Restrepo, A., Saltzman, T., Septimus, B., Tobe, R., Waltz, R., Williams, A., Yeo, A., Castellanos, F. X., Klein, A., Paus, T., Leventhal, B. L., Craddock, R. C., Koplewicz, H. S., and Milham, M. P. (2017). Data Descriptor: An open resource

for transdiagnostic research in pediatric mental health and learning disorders. *Scientific Data*. DOI: 10.1038/sdata.2017.181.

Alkemade, A., Forstmann, B. U., Schwarz, J., Kotz, S. A., Keuken, M. C., Weise, D., Schäfer, A., Hollander, G. de, and Ott, D. V. M. (2017). Comparison of T2*-weighted and QSM contrasts in Parkinson's disease to visualize the STN with MRI. *PLOS ONE*. DOI: 10.1371/journal.pone.0176130.

Alkemade, A., Keuken, M. C., and Forstmann, B. U. (2013). A perspective on terra incognita: uncovering the neuroanatomy of the human subcortex. *Frontiers in Neuroanatomy*. DOI: 10.3389/fnana.2013.00040.

Alkemade, A., Mulder, M. J., Groot, J. M., Isaacs, B. R., Berendonk, N. van, Lute, N., Isherwood, S. J. S., Bazin, P.-L., and Forstmann, B. U. (2020a). The Amsterdam Ultra-high field adult lifespan database (AHEAD): A freely available multimodal 7 Tesla submillimeter magnetic resonance imaging database. *NeuroImage*. DOI: 10.1016/j.neuroimage.2020.117200.

Alkemade, A., Mulder, M. J., Trutti, A. C., and Forstmann, B. U. (2021). Manual delineation approaches for direct imaging of the subcortex. *Brain Structure and Function*. DOI: 10.1007/s00429-021-02400-x.

Alkemade, A., Pine, K., Kirilina, E., Keuken, M. C., Mulder, M. J., Balesar, R., Groot, J. M., Bleys, R. L. A. W., Trampel, R., Weiskopf, N., Herrler, A., Möller, H. E., Bazin, P.-l., and Forstmann, B. U. (2020b). 7 Tesla MRI Followed by Histological 3D Reconstructions in Whole-Brain Specimens. *Frontiers in Neuroanatomy* 14, pp. 1–11. DOI: 10.3389/fnana.2020.536838.

Andersen, H. H., Johnsen, K. B., and Moos, T. (2014). Iron deposits in the chronically inflamed central nervous system and contributes to neurodegeneration. *Cellular and Molecular Life Sciences* 71, pp. 1607–1622. DOI: 10.1007/s00018-013-1509-8.

Andrew, D. et al. (2015). Risk taking, response inhibition and the right inferior frontal gyrus. *Journal of Neurology, Neurosurgery & Psychiatry* 86, e3–e3.

Aquino, D., Bizzi, A., Grisoli, M., Garavaglia, B., Bruzzone, M. G., Nardocci, N., Savoiardo, M., and Chiapparini, L. (2009). Age-related iron deposition in the basal ganglia: Quantitative analysis in healthy subjects. *Radiology*. DOI: 10.1148/radiol.2522081399.

Aron, A. R., Dowson, J. H., Sahakian, B. J., and Robbins, T. W. (2003). Methylphenidate improves response inhibition in adults with attention-deficit/hyperactivity disorder. en. *Biol. Psychiatry* 54, pp. 1465–1468.

Aron, A. R. (2007). *The neural basis of inhibition in cognitive control*. DOI: 10.1177/1073858407299288.

– (2011). From reactive to proactive and selective control: developing a richer model for stopping inappropriate responses. *Biological psychiatry* 69, e55. DOI: 10.1016/J.BIOPSYCH.2010.07.024.

Aron, A. R., Herz, D. M., Brown, P., Forstmann, B. U., and Zaghloul, K. (2016). Frontosubthalamic circuits for control of action and cognition. In: *Journal of Neuroscience*. DOI: 10.1523/JNEUROSCI.2348-16.2016.

Aron, A. R. and Poldrack, R. A. (2006). Cortical and subcortical contributions to Stop signal response inhibition: role of the subthalamic nucleus. *The Journal of neuroscience : the official journal of the Society for Neuroscience* 26, pp. 2424–2433. DOI: 10.1523/JNEUROSCI.4682-05.2006.

Aron, A. R., Robbins, T. W., and Poldrack, R. A. (2004). *Inhibition and the right inferior frontal cortex*. DOI: 10.1016/j.tics.2004.02.010.

– (2014). *Inhibition and the right inferior frontal cortex: One decade on*. DOI: 10.1016/j.tics.2013.12.003.

Arshad, M., Stanley, J. A., and Raz, N. (2016). Adult age differences in subcortical myelin content are consistent with protracted myelination and unrelated to diffusion tensor imaging indices. *NeuroImage* 143, pp. 26–39. DOI: 10.1016/j.neuroimage.2016.08.047.

Avants, B., Epstein, C., Grossman, M., and Gee, J. (2008). Symmetric diffeomorphic image registration with cross-correlation: Evaluating automated labeling of elderly and neurodegenerative brain. *Medical Image Analysis* 12, pp. 26–41. DOI: 10.1016/j.media.2007.06.004.

Avants, B. B., Duda, J. T., Kilroy, E., Krasileva, K., Jann, K., Kandel, B. T., Tustison, N. J., Yan, L., Jog, M., Smith, R., Wang, Y., Dapretto, M., and Wang, D. J. (2015). The pediatric template of brain perfusion. *Scientific data*. DOI: 10.1038/sdata.2015.3.

Band, G. P., Molen, M. W. v. d., and Logan, G. D. (2003). Horse-race model simulations of the stop-signal procedure. *Acta Psychologica* 112, pp. 105–142. DOI: 10.1016/S0001-6918(02)00079-3.

Bari, A., Xu, S., Pignatelli, M., Takeuchi, D., Feng, J., Li, Y., and Tonegawa, S. (2020). Differential attentional control mechanisms by two distinct noradrenergic coeruleo-frontal cortical pathways. *Proceedings of the National Academy of Sciences* 117, pp. 29080–29089. DOI: 10.1073/pnas.2001748117.

Bartels, A. and Zeki, S. (2000). The architecture of the colour centre in the human visual brain: new results and a review. *The European journal of neuroscience* 12, pp. 172–193. DOI: 10.1046/J.1460-9568.2000.00905.X.

Bastin, J., Polosan, M., Benis, D., Goetz, L., Bhattacharjee, M., Piallat, B., Krainik, A., Bougerol, T., Chabardès, S., and David, O. (2014). Inhibitory control and error monitoring by human subthalamic neurons. *Translational psychiatry* 4, e439–e439.

Bates, D., Maechler, M., Bolker, B., and Walker, S. (2014). lme4: Linear mixed-effects models using Eigen and S4. R package version 1.1-7, http://CRAN.R-project.org/package=lme4. *R package version*.

Bayer, H. M. and Glimcher, P. W. (2005). Midbrain dopamine neurons encode a quantitative reward prediction error signal. *Neuron* 47, pp. 129–141. DOI: 10.1016/j.neuron.2005.05.020.

Bazin, P. L., Alkemade, A., Mulder, M. J., Henry, A. G., and Forstmann, B. U. (2020). Multi-contrast anatomical subcortical structures parcellation. *eLife*. DOI: 10.7554/ELIFE.59430.

Bazin, P.-L., Alkemade, A., van der Zwaag, W., Caan, M., Mulder, M. J., and Forstmann, B. U. (2019). Denoising High-Field Multi-Dimensional MRI With Local Complex PCA. *Frontiers in Neuroscience* 13, pp. 1–10. DOI: 10.3389/fnins.2019.01066.

Bazin, P.-L., Weiss, M., Dinse, J., Schäfer, A., Trampel, R., and Turner, R. (2014). A computational framework for ultra-high resolution cortical segmentation at 7 Tesla. *NeuroImage* 93, pp. 201–209. DOI: 10.1016/j.neuroimage.2013.03.077.

Beauregard, M. and Lévesque, J. (2006). Functional magnetic resonance imaging investigation of the effects of neurofeedback training on the neural bases of selective attention and response inhibition in children with attention-deficit/hyperactivity disorder. *Applied Psychophysiology Biofeedback*. DOI: 10.1007/s10484-006-9001-y.

Bechara, A., Damasio, H., Tranel, D., and Damasio, A. R. (1997). Deciding advantageously before knowing the advantageous strategy. *Science (New York, N.Y.)* 275, pp. 1293–1295. DOI: 10.1126/SCIENCE.275.5304.1293.

Bechara, A., Dolan, S., Denburg, N., Hindes, A., Anderson, S. W., and Nathan, P. E. (2001). Decision-making deficits, linked to a dysfunctional ventromedial prefrontal cortex, revealed in alcohol and stimulant abusers. *Neuropsychologia* 39, pp. 376–389. DOI: 10.1016/S0028-3932(00)00136-6.

Behzadi, Y., Restom, K., Liau, J., and Liu, T. T. (2007). A Component Based Noise Correction Method (CompCor) for BOLD and Perfusion Based fMRI. *NeuroImage* 37, p. 90. DOI: 10.1016/J.NEUROIMAGE.2007.04.042.

Bellec, P., Chu, C., Chouinard-Decorte, F., Benhajali, Y., Margulies, D. S., and Craddock, R. C. (2017). The Neuro Bureau ADHD-200 Preprocessed repository. *NeuroImage*. DOI: 10.1016/j.neuroimage.2016.06.034.

Benis, D., David, O., Lachaux, J.-P., Seigneuret, E., Krack, P., Fraix, V., Chabardès, S., and Bastin, J. (2014). Subthalamic nucleus activity dissociates proactive and reactive inhibition in patients with Parkinson's disease. *NeuroImage* 91, pp. 273–281. DOI: https://doi.org/10.1016/j.neuroimage.2013.10.070.

Benis, D., David, O., Piallat, B., Kibleur, A., Goetz, L., Bhattacharjee, M., Fraix, V., Seigneuret, E., Krack, P., Chabardès, S., and Bastin, J. (2016). Response inhibition rapidly increases single-neuron responses in the subthalamic nucleus of patients with Parkinson's disease. *Cortex* 84, pp. 111–123. DOI: 10.1016/j.cortex.2016.09.006.

Bergstrom, J. A. (1894). The Relation of the Interference to the Practice Effect of an Association. *The American Journal of Psychology*. DOI: 10.2307/1411651.

Bettio, L. E., Rajendran, L., and Gil-Mohapel, J. (2017). The effects of aging in the hippocampus and cognitive decline. *Neuroscience and Biobehavioral Reviews* 79, pp. 66–86. DOI: 10.1016/j.neubiorev.2017.04.030.

Betts, M. J., Acosta-Cabronero, J., Cardenas-Blanco, A., Nestor, P. J., and Düzel, E. (2016). High-resolution characterisation of the aging brain using simultaneous quantitative susceptibility mapping (QSM) and R2* measurements at 7 T. *NeuroImage* 138, pp. 43–63. DOI: 10.1016/j.neuroimage.2016.05.024.

Betzel, R. F., Byrge, L., He, Y., Goñi, J., Zuo, X. N., and Sporns, O. (2014). Changes in structural and functional connectivity among resting-state networks across the human lifespan. *NeuroImage*. DOI: 10.1016/j.neuroimage.2014.07.067.

Birkl, C., Langkammer, C., Golob-Schwarzl, N., Leoni, M., Haybaeck, J., Goessler, W., Fazekas, F., and Ropele, S. (2016). Effects of formalin fixation and temperature on MR relaxation times in the human brain. *NMR in Biomedicine* 29, pp. 458–465. DOI: 10.1002/nbm.3477.

Birn, R. M., Smith, M. A., Jones, T. B., and Bandettini, P. A. (2008). The respiration response function: The temporal dynamics of fMRI signal fluctuations related to changes in respiration. *NeuroImage* 40, pp. 644–654. DOI: 10.1016/j.neuroimage.2007.11.059.

Bischof, G. N. and Park, D. C. (2015). *Obesity and Aging: Consequences for Cognition, Brain Structure, and Brain Function*. DOI: 10.1097/PSY.0000000000000212.

Bischoff-Grethe, A., Ozyurt, I. B., Busa, E., Quinn, B. T., Fennema-Notestine, C., Clark, C. P., Morris, S., Bondi, M. W., Jernigan, T. L., Dale, A. M., Brown, G. G., and Fischl, B. (2007). A technique for the deidentification of structural brain MR images. *Human Brain Mapping*. DOI: 10.1002/hbm.20312.

Blackmore, J., Shrivastava, S., Sallet, J., Butler, C. R., and Cleveland, R. O. (2019). Ultrasound Neuromodulation: A Review of Results, Mechanisms and Safety. *Ultrasound in Medicine and Biology* 45, pp. 1509–1536. DOI: 10.1016/j.ultrasmedbio.2018.12.015.

Blesa, M., Serag, A., Wilkinson, A. G., Anblagan, D., Telford, E. J., Pataky, R., Sparrow, S. A., Macnaught, G., Semple, S. I., Bastin, M. E., and Boardman, J. P. (2016). Parcellation of the healthy neonatal brain into 107 Regions using atlas propagation through intermediate time points in childhood. *Frontiers in Neuroscience*. DOI: 10.3389/fnins.2016.00220.

Bloemendaal, M., Zandbelt, B., Wegman, J., Rest, O. van de, Cools, R., and Aarts, E. (2016). Contrasting neural effects of aging on proactive and reactive response inhibition. en. *Neurobiol. Aging* 46, pp. 96–106.

Boecker, M., Gauggel, S., and Drueke, B. (2013). Stop or stop-change–does it make any difference for the inhibition process? en. *Int. J. Psychophysiol.* 87, pp. 234–243.

Boehler, C. N., Appelbaum, L. G., Krebs, R. M., Hopf, J. M., and Woldorff, M. G. (2010). Pinning down response inhibition in the brain - Conjunction analyses of the Stop-signal task. *NeuroImage*. DOI: 10.1016/j.neuroimage.2010.04.276.

Boehler, C. N., Bunzeck, N., Krebs, R. M., Noesselt, T., Schoenfeld, M. A., Hans-Jochen, H., Münte, T. F., Woldorff, M. G., and Hopf, J. M. (2011). Substantia nigra activity level predicts trial-to-trial adjustments in cognitive control. *Journal of Cognitive Neuroscience*. DOI: 10.1162/jocn.2010.21473.

Boonstra, A. M., Kooij, J. J. S., Oosterlaan, J., Sergeant, J. A., and Buitelaar, J. K. (2005). Does methylphenidate improve inhibition and other cognitive abilities in adults with childhood-onset ADHD? en. *J. Clin. Exp. Neuropsychol.* 27, pp. 278–298.

Bottomley, P. A., Foster, T. H., Argersinger, R. E., and Pfeifer, L. M. (1984). A review of normal tissue hydrogen NMR relaxation times and relaxation mechanisms from 100 MHz: Dependence on tissue type, NMR frequency, temperature, species, excision, and age. *Medical Physics*. DOI: 10.1118/1.595535.

Botvinick, M., Nystrom, L. E., Fissell, K., Carter, C. S., and Cohen, J. D. (1999). Conflict monitoring versus selection-for-action in anterior cingulate cortex. *Nature* 402, pp. 179–181. DOI: 10.1038/46035.

Botvinick, M. M., Carter, C. S., Braver, T. S., Barch, D. M., and Cohen, J. D. (2001). Conflict monitoring and cognitive control. *Psychological Review*. DOI: 10.1037/0033-295X.108.3.624.

Brammerloh, M., Morawski, M., Friedrich, I., Reinert, T., Lange, C., Pelicon, P., Vavpetič, P., Jankuhn, S., Jäger, C., Alkemade, A., Balesar, R., Pine, K., Gavriilidis, F., Trampel, R., Reimer, E., Arendt, T., Weiskopf, N., and Kirilina, E. (2021). Measuring the iron content of dopaminergic neurons in substantia nigra with MRI relaxometry. *NeuroImage* 239. DOI: 10.1016/j.neuroimage.2021.118255.

Brand, A., Allen, L., Altman, M., Hlava, M., and Scott, J. (2015). Beyond authorship: Attribution, contribution, collaboration, and credit. *Learned Publishing* 28, pp. 151–155. DOI: 10.1087/20150211.

Brittain, J.-S., Watkins, K. E., Joundi, R. A., Ray, N. J., Holland, P., Green, A. L., Aziz, T. Z., and Jenkinson, N. (2012). A Role for the Subthalamic Nucleus in Response Inhibition during Conflict. *Journal of Neuroscience* 32, pp. 13396–13401. DOI: 10.1523/JNEUROSCI.2259-12.2012. eprint: https://www.jneurosci.org/content/32/39/13396.full.pdf.

Brooks, D. J., Luthert, P., Gadian, D., and Marsden, C. D. (1989). Does signal-attenuation of high-field T2-weighted MRI of the brain reflect regional cerebral iron deposition? Observations on the relationship between regional cerebral water proton T2 values and iron levels. *Journal of Neurology Neurosurgery and Psychiatry*. DOI: 10.1136/jnnp.52.1.108.

Brown, S. A., Brumback, T., Tomlinson, K., Cummins, K., Thompson, W. K., Nagel, B. J., De Bellis, M. D., Hooper, S. R., Clark, D. B., Chung, T., Hasler, B. P., Colrain, I. M., Baker, F. C., Prouty, D., Pfefferbaum, A., Sullivan, E. V., Pohl, K. M., Rohlfing, T., Nichols, B. N., Chu, W., and Tapert, S. F. (2015). The national consortium on alcohol and neuro-development in adolescence (NCANDA): A multisite study of adolescent development and substance use. *Journal of Studies on Alcohol and Drugs*. DOI: 10.15288/jsad.2015.76.895.

Bryden, D. W. and Roesch, M. R. (2015). Executive control signals in orbitofrontal cortex during response inhibition. en. *J. Neurosci.* 35, pp. 3903–3914.

Buchsbaum, B. R., Erickson, D. T., and Kayser, A. S. (2013). Decomposing effects of time on task reveals an anteroposterior gradient of perceptual decision regions. *PLoS ONE* 8, e72074. DOI: 10.1371/journal.pone.0072074.

Budde, J., Shajan, G., Zaitsev, M., Scheffler, K., and Pohmann, R. (2014). Functional MRI in human subjects with gradient-echo and spin-echo EPI at 9.4 T. *Magnetic Resonance in Medicine* 71, pp. 209–218. DOI: 10.1002/mrm.24656.

Bullitt, E., Zeng, D., Mortamet, B., Ghosh, A., Aylward, S. R., Lin, W., Marks, B. L., and Smith, K. (2010). The effects of healthy aging on intracerebral blood vessels visualized by magnetic resonance angiography. *Neurobiology of Aging*. DOI: 10.1016/j.neurobiolaging.2008.03.022.

Burke, R. E. and O'Malley, K. (2013). Axon degeneration in Parkinson's disease. *Experimental neurology* 246, pp. 72–83.

Bush, G., Shin, L. M., Holmes, J., Rosen, B. R., and Vogt, B. A. (2003). The Multi-Source Interference Task: validation study with fMRI in individual subjects. *Molecular psychiatry* 8, pp. 60–70. DOI: 10.1038/SJ.MP.4001217.

Bush, G. and Shin, L. M. (2006). The Multi-Source Interference Task: an fMRI task that reliably activates the cingulo-frontal-parietal cognitive/attention network. *Nature protocols* 1, pp. 308–313. DOI: 10.1038/NPROT.2006.48.

Bush, G., Whalen, P. J., Rosen, B. R., Jenike, M. A., McInerney, S. C., and Rauch, S. L. (1998). The counting Stroop: an interference task specialized for functional neuroimaging: validation study with functional MRI. *Human Brain Mapping* 6, pp. 270–282. DOI: 10.1002/(SICI)1097-0193(1998)6:4<270::AID-HBM6>3.0.CO;2-0.

Bystron, I., Blakemore, C., and Rakic, P. (2008). Development of the human cerebral cortex: Boulder Committee revisited. *Nature Reviews Neuroscience* 9, pp. 110–122.

Caan, M. W. A., Bazin, P.-L., Marques, J. P., Hollander, G., Dumoulin, S. O., and van der Zwaag, W. (2019). MP2RAGEME: T1, T2, and QSM mapping in one sequence at 7 tesla. *Human Brain Mapping* 40, pp. 1786–1798. DOI: 10.1002/hbm.24490.

Caballol, N., Marti, M. J., and Tolosa, E. (2007). Cognitive dysfunction and dementia in Parkinson disease. *Movement disorders: official journal of the Movement Disorder Society* 22, S358–S366.

Cai, W., Ryali, S., Chen, T., Li, C.-S. R., and Menon, V. (2014). Dissociable roles of right inferior frontal cortex and anterior insula in inhibitory control: evidence from intrinsic and task-related functional parcellation, connectivity, and response profile analyses across multiple datasets. *Journal of Neuroscience* 34, pp. 14652–14667.

Callaghan, M. F., Freund, P., Draganski, B., Anderson, E., Cappelletti, M., Chowdhury, R., Diedrichsen, J., FitzGerald, T. H., Smittenaar, P., Helms, G., Lutti, A., and Weiskopf, N. (2014). Widespread age-related differences in the human brain microstructure revealed by quantitative magnetic resonance imaging. *Neurobiology of Aging* 35, pp. 1862–1872. DOI: 10.1016/j.neurobiolaging.2014.02.008.

Casey, B. J., Cannonier, T., Conley, M. I., Cohen, A. O., Barch, D. M., Heitzeg, M. M., Soules, M. E., Teslovich, T., Dellarco, D. V., Garavan, H., Orr, C. A., Wager, T. D., Banich, M. T., Speer, N. K., Sutherland, M. T., Riedel, M. C., Dick, A. S., Bjork, J. M., Thomas, K. M., Chaarani, B., Mejia, M. H., Hagler, D. J., Daniela Cornejo, M., Sicat, C. S., Harms, M. P., Dosenbach, N. U., Rosenberg, M., Earl, E., Bartsch, H., Watts, R., Polimeni, J. R., Kuperman, J. M., Fair, D. A., and Dale, A. M. (2018). *The Adolescent Brain Cognitive Development (ABCD) study: Imaging acquisition across 21 sites*. DOI: 10.1016/j.dcn.2018.03.001.

Cavanagh, J. F., Wiecki, T. V., Cohen, M. X., Figueroa, C. M., Sherman, S. J., and Frank, M. J. (2011). Subthalamic Nucleus Stimulation reverses Influence Over Decision Threshold. *Nature Neuroscience* 14, pp. 1462–1467. DOI: 10.1038/nn.2925.Subthalamic.

Cavanagh, J. F., Sanguinetti, J. L., Allen, J. J. B., Sherman, S. J., and Frank, M. J. (2014). The Subthalamic Nucleus Contributes to Post-error Slowing. *Journal of Cognitive Neuroscience* 26, pp. 2637–2644. DOI: 10.1162/jocn_a_00659. eprint: https://direct.mit.edu/jocn/article-pdf/26/11/2637/1947909/jocn_a_00659.pdf.

Chambers, C. D., Garavan, H., and Bellgrove, M. A. (2009). *Insights into the neural basis of response inhibition from cognitive and clinical neuroscience*. DOI: 10.1016/j.neubiorev.2008.08.016.

Chan, D., Shafto, M., Kievit, R., Matthews, F., Spink, M., Valenzuela, M., and Henson, R. N. (2018). Lifestyle activities in mid-life contribute to cognitive reserve in late-life, independent of education, occupation, and late-life activities. *Neurobiology of Aging*. DOI: 10.1016/j.neurobiolaging.2018.06.012.

Chang, C., Cunningham, J. P., and Glover, G. H. (2009). Influence of heart rate on the BOLD signal: The cardiac response function. *NeuroImage* 44, pp. 857–869. DOI: 10.1016/j.neuroimage.2008.09.029.

Chang, S.-E. and Guenther, F. H. (2020). Involvement of the cortico-basal ganglia-thalamocortical loop in developmental stuttering. *Frontiers in Psychology* 10, p. 3088.

Chen, L., Vu, A. T., Xu, J., Moeller, S., Uğurbil, K., Yacoub, E., and Feinberg, D. A. (2015). Evaluation of highly accelerated simultaneous multi-slice EPI for fMRI. *NeuroImage* 104, pp. 452–459. DOI: 10.1016/j.neuroimage.2014.10.027.

Chen, T., Becker, B., Camilleri, J., Wang, L., Yu, S., Eickhoff, S. B., and Feng, C. (2018). A domain-general brain network underlying emotional and cognitive interference processing: evidence from coordinate-based and functional connectivity meta-analyses. *Brain Structure and Function*. DOI: 10.1007/s00429-018-1727-9.

Chen, W., Hemptinne, C. de, Miller, A. M., Leibbrand, M., Little, S. J., Lim, D. A., Larson, P. S., and Starr, P. A. (2020). Prefrontal-subthalamic hyperdirect pathway modulates movement inhibition in humans. en. *Neuron* 106, 579–588.e3.

Cheng, S., Wu, C., Qi, X., Liu, L., Ma, M., Zhang, L., Cheng, B., Liang, C., Li, P., Kafle, O. P., Wen, Y., and Zhang, F. (2020). A Large-Scale Genetic Correlation Scan Between Intelligence and Brain Imaging Phenotypes. *Cerebral cortex (New York, N.Y. : 1991)*. DOI: 10.1093/cercor/bhaa043.

Cherubini, A., Péran, P., Caltagirone, C., Sabatini, U., and Spalletta, G. (2009). Aging of subcortical nuclei: Microstructural, mineralization and atrophy modifications measured in vivo using MRI. *NeuroImage* 48, pp. 29–36. DOI: 10.1016/j.neuroimage.2009.06.035.

Cho, Z. H., Oh, S. H., Kim, J. M., Park, S. Y., Kwon, D. H., Jeong, H. J., Kim, Y. B., Chi, J. G., Park, C. W., Huston, J., Lee, K. H., and Jeon, B. S. (2011). Direct visualization of Parkinson's disease by in vivo human brain imaging using 7.0T magnetic resonance imaging. *Movement Disorders*. DOI: 10.1002/mds.23465.

Cho, Z.-H., Kim, Y.-B., Han, J.-Y., Min, H.-K., Kim, K.-N., Choi, S.-H., Veklerov, E., and Shepp, L. A. (2008). New brain atlas—mapping the human brain in vivo with 7.0 T MRI and comparison with postmortem histology: will these images change modern medicine? *International Journal of Imaging Systems and Technology* 18, pp. 2–8.

Chowdhury, N. S., Livesey, E. J., Blaszczynski, A., and Harris, J. A. (2018). Variations in response control within at-risk gamblers and non-gambling controls explained by GABAergic inhibition in the motor cortex. en. *Cortex* 103, pp. 153–163.

Chudasama, Y. and Robbins, T. (2006). Functions of frontostriatal systems in cognition: comparative neuropsychopharmacological studies in rats, monkeys and humans. *Biological psychology* 73, pp. 19–38.

Cieslik, E. C., Mueller, V. I., Eickhoff, C. R., Langner, R., and Eickhoff, S. B. (2015). *Three key regions for supervisory attentional control: Evidence from neuroimaging meta-analyses*. DOI: 10.1016/j.neubiorev.2014.11.003.

Claassen, D. O., Wildenberg, W. P. M. van den, Harrison, M. B., Wouwe, N. C. van, Kanoff, K., Neimat, J. S., and Wylie, S. A. (2015). Proficient motor impulse control in Parkinson disease patients with impulsive and compulsive behaviors. en. *Pharmacol. Biochem. Behav.* 129, pp. 19–25.

Colizoli, O., Gee, J. W. de, van der Zwaag, W., and Donner, T. H. (2020). *Comparing fMRI responses measured at 3 versus 7 Tesla across human cortex, striatum, and brainstem*. DOI: 10.1101/2020.05.12.090175.

Collingwood, J. F. and Davidson, M. R. (2014). The role of iron in neurodegenerative disorders: Insights and opportunities with synchrotron light. *Frontiers in Pharmacology* 5 AUG, pp. 1–19. DOI: 10.3389/fphar.2014.00191.

Collins, C. M. and Smith, M. B. (2001). Signal-to-noise ratio and absorbed power as functions of main magnetic field strength, and definition of "90°" RF pulse for the head in the birdcage coil. *Magnetic Resonance in Medicine*. DOI: 10.1002/mrm.1091.

Congdon, E., Altshuler, L. L., Mumford, J. A., Karlsgodt, K. H., Sabb, F. W., Ventura, J., McGough, J. J., London, E. D., Cannon, T. D., Bilder, R. M., and Poldrack, R. A. (2014). Neural activation during response inhibition in adult attention-deficit/hyperactivity disorder: preliminary findings on the effects of medication and symptom severity. en. *Psychiatry Res.* 222, pp. 17–28.

Coudé, D., Parent, A., and Parent, M. (2018). Single-axon tracing of the corticosubthalamic hyperdirect pathway in primates. *Brain Structure and Function* 223, pp. 3959–3973.

Coupé, P., Catheline, G., Lanuza, E., and Manjón, J. V. (2017). Towards a unified analysis of brain maturation and aging across the entire lifespan: A MRI analysis. *Human Brain Mapping* 38, pp. 5501–5518. DOI: 10.1002/hbm.23743.

Courchesne, E., Chisum, H. J., Townsend, J., Cowles, A., Covington, J., Egaas, B., Harwood, M., Hinds, S., and Press, G. A. (2000). Normal brain development and aging: Quantitative analysis at in vivo MR imaging in healthy volunteers. *Radiology* 216, pp. 672–682. DOI: 10.1148/radiology.216.3.r00au37672.

Cox, R. W. and Hyde, J. S. (1997). Software tools for analysis and visualization of fMRI data. *NMR in Biomedicine* 10, pp. 171–178. DOI: 10.1002/(SICI)1099-1492(199706/08)10:4/5<171::AID-NBM453>3.0.CO;2-L.

Coxon, J. P., Goble, D. J., Leunissen, I., Van Impe, A., Wenderoth, N., and Swinnen, S. P. (2016). Functional brain activation associated with inhibitory control deficits in older adults. en. *Cereb. Cortex* 26, pp. 12–22.

Craig, A. D. (2009). *How do you feel - now? The anterior insula and human awareness*. DOI: 10.1038/nrn2555.

Criaud, M. and Boulinguez, P. (2013). *Have we been asking the right questions when assessing response inhibition in go/no-go tasks with fMRI? A meta-analysis and critical review*. DOI: 10.1016/j.neubiorev.2012.11.003.

Dagli, M. S., Ingeholm, J. E., and Haxby, J. V. (1999). Localization of cardiac-induced signal change in fMRI. *NeuroImage* 9, pp. 407–415. DOI: 10.1006/nimg.1998.0424.

Dale, A. M., Fischl, B., and Sereno, M. I. (1999). Cortical Surface-Based Analysis. *NeuroImage* 9, pp. 179–194. DOI: 10.1006/nimg.1998.0395.

Daugherty, A. and Raz, N. (2013). Age-related differences in iron content of subcortical nuclei observed in vivo: A meta-analysis. *NeuroImage*. DOI: 10.1016/j.neuroimage.2012.12.040.

Daugherty, A. M. and Raz, N. (2015). Appraising the Role of Iron in Brain Aging and Cognition: Promises and Limitations of MRI Methods. *Neuropsychology Review* 25, pp. 272–287. DOI: 10.1007/s11065-015-9292-y.

– (2016). Accumulation of iron in the putamen predicts its shrinkage in healthy older adults: A multi-occasion longitudinal study. *NeuroImage* 128, pp. 11–20. DOI: 10.1016/j.neuroimage.2015.12.045.

De Graaf, W. L., Kilsdonk, I. D., Lopez-Soriano, A., Zwanenburg, J. J. M., Visser, F., Polman, C. H., Castelijns, J. A., Geurts, J. J. G., Pouwels, P. J. W., Luijten, P. R., Barkhof, F., and Wattjes, M. P. (2013).

Clinical application of multi-contrast 7-T MR imaging in multiple sclerosis: Increased lesion detection compared to 3 T confined to grey matter. *European Radiology*. DOI: 10.1007/s00330-012-2619-7.

De Hollander, G., Keuken, M. C., and Forstmann, B. U. (2015). The subcortical cocktail problem; Mixed signals from the subthalamic nucleus and substantia nigra. *PLoS ONE* 10. DOI: 10.1371/journal.pone.0120572.

Deistung, A., Schäfer, A., Schweser, F., Biedermann, U., Turner, R., and Reichenbach, J. R. (2013). Toward in vivo histology: A comparison of quantitative susceptibility mapping (QSM) with magnitude-, phase-, and R2*-imaging at ultra-high magnetic field strength. *NeuroImage*. DOI: 10.1016/j.neuroimage.2012.09.055.

DeLong, M. R. (1990). Primate models of movement disorders of basal ganglia origin. *Trends in neurosciences* 13, pp. 281–285. DOI: 10.1016/0166-2236(90)90110-V.

Dempster, F. N. (1993). "Resistance to interference: Developmental changes in a basic processing dimension." In: *Emerging Themes in Cognitive Development*. Vol. 1. Springer, pp. 3–27. DOI: 10.1007/978-1-4615-2854-8_1.

Deng, Y., Wang, X., Wang, Y., and Zhou, C. (2018). Neural correlates of interference resolution in the multi-source interference task: a meta-analysis of functional neuroimaging studies. *Behavioral and brain functions : BBF* 14. DOI: 10.1186/S12993-018-0140-0.

Desikan, R. S., Ségonne, F., Fischl, B., Quinn, B. T., Dickerson, B. C., Blacker, D., Buckner, R. L., Dale, A. M., Maguire, R. P., Hyman, B. T., Albert, M. S., and Killiany, R. J. (2006). An automated labeling system for subdividing the human cerebral cortex on MRI scans into gyral based regions of interest. *NeuroImage*. DOI: 10.1016/j.neuroimage.2006.01.021.

Devlin, J. T. and Poldrack, R. A. (2007). In praise of tedious anatomy. *NeuroImage* 37, pp. 1033–1041. DOI: 10.1016/j.neuroimage.2006.09.055.

Di, X., Rypma, B., and Biswal, B. B. (2014). Correspondence of executive function related functional and anatomical alterations in aging brain. *Progress in Neuro-Psychopharmacology and Biological Psychiatry*. DOI: 10.1016/j.pnpbp.2013.09.001.

Di Martino, A., Yan, C.-G., Li, Q., Denio, E., Castellanos, F. X., Alaerts, K., Anderson, J. S., Assaf, M., Bookheimer, S. Y., Dapretto, M., et al. (2014). The autism brain imaging data exchange: towards a large-scale evaluation of the intrinsic brain architecture in autism. *Molecular psychiatry* 19, pp. 659–667.

Di Pellegrino, G., Ciaramelli, E., and Làdavas, E. (2007). The regulation of cognitive control following rostral anterior cingulate cortex lesion in humans. *Journal of Cognitive Neuroscience*. DOI: 10.1162/jocn.2007.19.2.275.

Diesburg, D. A. and Wessel, J. R. (2021). The Pause-then-Cancel model of human action-stopping: Theoretical considerations and empirical evidence. *Neuroscience and biobehavioral reviews* 129, pp. 17–34. DOI: 10.1016/J.NEUBIOREV.2021.07.019.

Dima, D. et al. (2021). Subcortical volumes across the lifespan: Data from 18,605 healthy individuals aged 3–90 years. *Human Brain Mapping*, pp. 1–18. DOI: 10.1002/hbm.25320.

Ding, L. and Gold, J. I. (2013). The basal ganglia's contributions to perceptual decision making. *Neuron* 79, pp. 640–649. DOI: 10.1016/j.neuron.2013.07.042.

Donders, F. C. (1969). On the speed of mental processes. *Acta Psychologica*. DOI: 10.1016/0001-6918(69)90065-1.

Dosenbach, N. U., Fair, D. A., Cohen, A. L., Schlaggar, B. L., and Petersen, S. E. (2008). A dual-networks architecture of top-down control. *Trends in Cognitive Sciences* 12, pp. 99–105. DOI: 10.1016/j.tics.2008.01.001.

Duann, J. R., Ide, J. S., Luo, X., and Li, C. S. R. (2009). Functional connectivity delineates distinct roles of the inferior frontal cortex and presupplementary motor area in stop signal inhibition. *Journal of Neuroscience*. DOI: 10.1523/JNEUROSCI.1300-09.2009.

Duncan, J., Seitz, R. J., Kolodny, J., Bor, D., Herzog, H., Ahmed, A., Newell, F. N., and Emslie, H. (2000). A Neural Basis for General Intelligence. *Science* 289, pp. 457–460. DOI: 10.1126/science.289.5478.457.

DuPre, E. and Spreng, R. N. (2017). Structural covariance networks across the life span, from 6 to 94 years of age. *Network Neuroscience*. DOI: 10.1162/netn_a_00016.

Duvernoy, H. M. (1999). *Human brain stem vessels: Including the pineal gland and information on brain stem infarction*. Springer.

Eagle, D. M., Bari, A., and Robbins, T. W. (2008). The neuropsychopharmacology of action inhibition: cross-species translation of the stop-signal and go/no-go tasks. *Psychopharmacology* 199, pp. 439–456. DOI: 10.1007/S00213-008-1127-6.

Edelstein, W., Glover, G., Hardy, C., and Redington, R. (1986). The intrinsic signal-to-noise ratio in NMR imaging. *Magnetic resonance in medicine* 3, pp. 604–618.

Ehrenberg, A. J., Nguy, A. K., Theofilas, P., Dunlop, S., Suemoto, C. K., Di Lorenzo Alho, A. T., Leite, R. P., Diehl Rodriguez, R., Mejia, M. B., Rüb, U., Farfel, J. M., de Lucena Ferretti-Rebustini, R. E., Nascimento, C. F., Nitrini, R., Pasquallucci, C. A., Jacob-Filho, W., Miller, B., Seeley, W. W., Heinsen, H., and Grinberg, L. T. (2017). Quantifying the accretion of hyperphosphorylated tau in the locus coeruleus and dorsal raphe nucleus: the pathological building blocks of early Alzheimer's disease. *Neuropathology and Applied Neurobiology* 43, pp. 393–408. DOI: 10.1111/nan.12387.

Eickhoff, S. B., Bzdok, D., Laird, A. R., Kurth, F., and Fox, P. T. (2012). Activation likelihood estimation revisited. *NeuroImage*.

Eickhoff, S., Nichols, T. E., Van Horn, J. D., and Turner, J. A. (2016). Sharing the wealth: Neuroimaging data repositories. *NeuroImage*. DOI: 10.1016/j.neuroimage.2015.10.079.

Eickhoff, S. B., Bzdok, D., Laird, A. R., Roski, C., Caspers, S., Zilles, K., and Fox, P. T. (2011). Co-activation patterns distinguish cortical modules, their connectivity and functional differentiation. *NeuroImage*. DOI: 10.1016/j.neuroimage.2011.05.021.

Eickhoff, S. B., Heim, S., Zilles, K., and Amunts, K. (2006). Testing anatomically specified hypotheses in functional imaging using cytoarchitectonic maps. *NeuroImage*. DOI: 10.1016/j.neuroimage.2006.04.204.

Eickhoff, S. B., Laird, A. R., Fox, P. M., Lancaster, J. L., and Fox, P. T. (2017). Implementation errors in the GingerALE Software: Description and recommendations. *Human Brain Mapping*. DOI: 10.1002/hbm.23342.

Eickhoff, S. B., Paus, T., Caspers, S., Grosbras, M. H., Evans, A. C., Zilles, K., and Amunts, K. (2007). Assignment of functional activations to probabilistic cytoarchitectonic areas revisited. *NeuroImage*. DOI: 10.1016/j.neuroimage.2007.03.060.

Eickhoff, S. B., Stephan, K. E., Mohlberg, H., Grefkes, C., Fink, G. R., Amunts, K., and Zilles, K. (2005). A new SPM toolbox for combining probabilistic cytoarchitectonic maps and functional imaging data. *NeuroImage*. DOI: 10.1016/j.neuroimage.2004.12.034.

Ellis, K. A., Bush, A. I., Darby, D., De Fazio, D., Foster, J., Hudson, P., Lautenschlager, N. T., Lenzo, N., Martins, R. N., Maruff, P., Masters, C., Milner, A., Pike, K., Rowe, C., Savage, G., Szoeke, C., Taddei, K., Villemagne, V., Woodward, M., Ames, D., Acosta, O., Ames, J., Agarwal, M., Bahar-Fuchs, A., Baxendale, D., Bechta-Metti, K., Bevage, C., Bevege, L., Bourgeat, P., Brown, B., Bush, A., Clarnette, R., Cowie, T., Crowley, K., Currie, A., El-Sheikh, D., Ellis, K., Dickinson, K., Farrow, M., Faux, N., Fripp, J., Fowler, C., Gupta, V., Jones, G., Khoo, J., Killedar, A., Killeen, N., Tae, W. K., Kotsopoulos,

E., Lachovitzki, R., Lautenschlager, N., Li, Q. X., Liang, X., Lucas, K., Lui, J., Martins, G., Montague, C., Moore, L., Muir, A., O'Halloran, C., O'Keefe, G., Panayiotou, A., Paton, A., Paton, J., Peiffer, J., Pejoska, S., Pertile, K., Porter, L., Price, R., Raniga, P., Rees, G., Rembach, A., Rimajova, M., Robins, P., Ronsisvalle, E., Rumble, R., Rodrigues, M., Salvado, O., Sach, J., Samuel, M., Sittironnarit, G., Taddei, T., Trivedi, D., Trounson, B., Tsikkos, M., Walker, S., Ward, V., and Yastrubetskaya, O. (2009). The Australian Imaging, Biomarkers and Lifestyle (AIBL) study of aging: Methodology and baseline characteristics of 1112 individuals recruited for a longitudinal study of Alzheimer's disease. *International Psychogeriatrics*. DOI: 10.1017/S1041610209009405.

Eriksen, B. A. and Eriksen, C. W. (1974). Effects of noise letters upon the identification of a target letter in a nonsearch task. *Perception and Psychophysics*. DOI: 10.3758/BF03203267.

Eshel, N., Bukwich, M., Rao, V., Hemmelder, V., Tian, J., and Uchida, N. (2015). Arithmetic and local circuitry underlying dopamine prediction errors. en. *Nature* 525, pp. 243–246.

Esteban, O., Ciric, R., Finc, K., Blair, R. W., Markiewicz, C. J., Moodie, C. A., Kent, J. D., Goncalves, M., DuPre, E., Gomez, D. E., et al. (2020). Analysis of task-based functional MRI data preprocessed with fMRIPrep. *Nature protocols* 15, pp. 2186–2202.

Esteban, O., Markiewicz, C. J., Blair, R. W., Moodie, C. A., Isik, A. I., Erramuzpe, A., Kent, J. D., Goncalves, M., DuPre, E., Snyder, M., Oya, H., Ghosh, S. S., Wright, J., Durnez, J., Poldrack, R. A., and Gorgolewski, K. J. (2018). fMRIPrep: a robust preprocessing pipeline for functional MRI. *Nature Methods 2018 16:1* 16, pp. 111–116. DOI: 10.1038/s41592-018-0235-4.

Evans, A. C., Janke, A. L., Collins, D. L., and Baillet, S. (2012). *Brain templates and atlases*. DOI: 10.1016/j.neuroimage.2012.01.024.

Fama, R. and Sullivan, E. V. (2015). Thalamic structures and associated cognitive functions: Relations with age and aging. *Neuroscience and Biobehavioral Reviews* 54, pp. 29–37. DOI: 10.1016/j.neubiorev.2015.03.008.

Farah, M. J. and Aguirre, G. K. (1999). Imaging visual recognition: PET and fMRI studies of the functional anatomy of human visual recognition. *Trends in Cognitive Sciences* 3, pp. 179–186. DOI: 10.1016/s1364-6613(99)01309-1.

Fasano, A. and Lozano, A. M. (2015). Deep brain stimulation for movement disorders. *Current Opinion in Neurology* 28, pp. 423–436. DOI: 10.1097/WCO.0000000000000226.

Federative Committee on Anatomical Terminology (1998). *Terminologia Anatomica – International Anatomical Terminology*. Stuttgart, Germany: Thieme.

Federau, C. and Gallichan, D. (2016). Motion-correction enabled ultra-high resolution in-vivo 7T-MRI of the brain. *PLoS ONE*. DOI: 10.1371/journal.pone.0154974.

Fellows, L. K. and Farah, M. J. (2005). Is anterior cingulate cortex necessary for cognitive control? *Brain*. DOI: 10.1093/brain/awh405.

Fields, R. D. (2015). A new mechanism of nervous system plasticity: Activity-dependent myelination. *Nature Reviews Neuroscience* 16, pp. 756–767. DOI: 10.1038/nrn4023.

Fiorillo, C. D., Tobler, P. N., and Schultz, W. (2003). Discrete Coding of Reward Dopamine Neurons. *Science* 299, pp. 1898–1902.

Fischer, P., Pogosyan, A., Herz, D. M., Cheeran, B., Green, A. L., Fitzgerald, J., Aziz, T. Z., Hyam, J., Little, S., Foltynie, T., Limousin, P., Zrinzo, L., Brown, P., and Tan, H. (2017). Subthalamic nucleus gamma activity increases not only during movement but also during movement inhibition. *eLife* 6. Ed. by E. Vaadia, e23947. DOI: 10.7554/eLife.23947.

Fjell, A. M., Westlye, L. T., Amlien, I., Espeseth, T., Reinvang, I., Raz, N., Agartz, I., Salat, D. H., Greve, D. N., Fischl, B., Dale, A. M., and Walhovd, K. B. (2009). High consistency of regional cortical thinning in aging across multiple samples. *Cerebral Cortex*. DOI: 10.1093/cercor/bhn232.

Fjell, A. M., Westlye, L. T., Grydeland, H., Amlien, I., Espeseth, T., Reinvang, I., Raz, N., Holland, D., Dale, A. M., and Walhovd, K. B. (2013). Critical ages in the life course of the adult brain: Nonlinear subcortical aging. *Neurobiology of Aging* 34, pp. 2239–2247. DOI: 10.1016/j.neurobiolaging.2013.04.006.

Flores-Dourojeanni, J. P., Rijt, C. van, Munkhof, M. H. van den, Boekhoudt, L., Luijendijk, M. C. M., Vanderschuren, L. J. M. J., and Adan, R. A. H. (2021). Temporally specific roles of ventral tegmental area projections to the nucleus accumbens and prefrontal cortex in attention and impulse control. en. *J. Neurosci.* 41, pp. 4293–4304.

Fonov, V., Evans, A. C., Botteron, K., Almli, C. R., McKinstry, R. C., and Collins, D. L. (2011). Unbiased average age-appropriate atlases for pediatric studies. *NeuroImage*. DOI: 10.1016/j.neuroimage.2010.07.033.

Fonov, V., Evans, A., McKinstry, R., Almli, C., and Collins, D. (2009). Unbiased nonlinear average age-appropriate brain templates from birth to adulthood. *NeuroImage*. DOI: 10.1016/s1053-8119(09)70884-5.

Forstmann, B. U., De Hollander, G., Van Maanen, L., Alkemade, A., and Keuken, M. C. (2016). *Towards a mechanistic understanding of the human subcortex*. DOI: 10.1038/nrn.2016.163.

Forstmann, B. U., Isaacs, B. R., and Temel, Y. (2017). *Ultra High Field MRI-Guided Deep Brain Stimulation*. DOI: 10.1016/j.tibtech.2017.06.010.

Forstmann, B. U., Jahfari, S., Scholte, H. S., Wolfensteller, U., Van Den Wildenberg, W. P., and Ridderinkhof, K. R. (2008). Function and structure of the right inferior frontal cortex predict individual differences in response inhibition: A model-based approach. *Journal of Neuroscience*. DOI: 10.1523/JNEUROSCI.1465-08.2008.

Forstmann, B. U., Keuken, M. C., Jahfari, S., Bazin, P.-L., Neumann, J., Schäfer, A., Anwander, A., and Turner, R. (2012). Cortico-subthalamic white matter tract strength predicts interindividual efficacy in stopping a motor response. *NeuroImage* 60, pp. 370–375. DOI: https://doi.org/10.1016/j.neuroimage.2011.12.044.

Forstmann, B. U., Keuken, M. C., Schafer, A., Bazin, P. L., Alkemade, A., and Turner, R. (2014). Multi-modal ultra-high resolution structural 7-Tesla MRI data repository. *Scientific Data*. DOI: 10.1038/sdata.2014.50.

Fortin, N. J., Agster, K. L., and Eichenbaum, H. B. (2002). Critical role of the hippocampus in memory for sequences of events. *Nature neuroscience* 5, pp. 458–462.

Frahm, J., Merboldt, K.-D., and Hanicke, W. (1994). The influence of the slice-selection gradient on functional MRI of human brain activation. *Journal of Magnetic Resonance, Series B* 103, pp. 91–93. DOI: 10.1006/jmrb.1994.1035.

Frank, M. J. (2006). Hold your horses: A dynamic computational role for the subthalamic nucleus in decision making. *Neural Networks*. DOI: 10.1016/j.neunet.2006.03.006.

Frässle, S., Aponte, E. A., Bollmann, S., Brodersen, K. H., Do, C. T., Harrison, O. K., Harrison, S. J., Heinzle, J., Iglesias, S., Kasper, L., Lomakina, E. I., Mathys, C., Müller-Schrader, M., Pereira, I., Petzschner, F. H., Raman, S., Schöbi, D., Toussaint, B., Weber, L. A., Yao, Y., and Stephan, K. E. (2021). TAPAS: An Open-Source Software Package for Translational Neuromodeling and Computational Psychiatry. *Frontiers in Psychiatry* 12, p. 857. DOI: 10.3389/FPSYT.2021.680811/BIBTEX.

Frazier, J. A., Chiu, S., Breeze, J. L., Makris, N., Lange, N., Kennedy, D. N., Herbert, M. R., Bent, E. K., Koneru, V. K., Dieterich, M. E., Hodge, S. M., Rauch, S. L., Grant, P. E., Cohen, B. M., Seidman, L. J., Caviness, V. S., and Biederman, J. (2005). Structural brain magnetic resonance imaging of limbic and thalamic volumes in pediatric bipolar disorder. *American Journal of Psychiatry*. DOI: 10.1176/appi.ajp.162.7.1256.

Friedman, N. P. and Miyake, A. (2004). The relations among inhibition and interference control functions: a latent-variable analysis. *Journal of experimental psychology. General* 133, pp. 101–135. DOI: 10.1037/0096-3445.133.1.101.

Friston, K. J. (2010). The free-energy principle: a unified brain theory? *Nature Reviews Neuroscience* 11, pp. 127–138. DOI: 10.1038/nrn2787.

Froeling, M., Tax, C. M., Vos, S. B., Luijten, P. R., and Leemans, A. (2017). "MASSIVE" brain dataset: Multiple acquisitions for standardization of structural imaging validation and evaluation. *Magnetic Resonance in Medicine*. DOI: 10.1002/mrm.26259.

Gaillard, A., Rossell, S. L., Carruthers, S. P., Sumner, P. J., Michie, P. T., Woods, W., Neill, E., Phillipou, A., Toh, W. L., and Hughes, M. E. (2020). Greater activation of the response inhibition network in females compared to males during stop signal task performance. *Behavioural Brain Research*. DOI: 10.1016/j.bbr.2020.112586.

Gallichan, D., Marques, J. P., and Gruetter, R. (2016). Retrospective correction of involuntary microscopic head movement using highly accelerated fat image navigators (3D FatNavs) at 7T. *Magnetic Resonance in Medicine*. DOI: 10.1002/mrm.25670.

Garrison, J. R., Done, J., and Simons, J. S. (2019). *Interpretation of published meta-analytical studies affected by implementation errors in the GingerALE software*. DOI: 10.1016/j.neubiorev.2017.10.027.

Gauggel, S., Rieger, M., and Feghoff, T.-A. (2004). Inhibition of ongoing responses in patients with Parkinson's disease. *Journal of Neurology, Neurosurgery and Psychiatry* 75, pp. 539–544. DOI: 10.1136/jnnp.2003.016469.

Gavazzi, G., Giovannelli, F., Currò, T., Mascalchi, M., and Viggiano, M. P. (2020). *Contiguity of proactive and reactive inhibitory brain areas: a cognitive model based on ALE meta-analyses*. DOI: 10.1007/s11682-020-00369-5.

Geerligs, L., Rubinov, M., Cam-CAN, and Henson, R. N. (2015). State and Trait Components of Functional Connectivity: Individual Differences Vary with Mental State. *Journal of Neuroscience*. DOI: 10.1523/jneurosci.1324-15.2015.

Gelman, A. and Hill, J. (2006). Data Analysis Using Regression and Multilevel/Hierarchical Models. *Data Analysis Using Regression and Multilevel/Hierarchical Models*. DOI: 10.1017/CBO9780511790942.

Gelman, A. and Rubin, D. B. (1992). Inference from Iterative Simulation Using Multiple Sequences. *https://doi.org/10.1214/ss/1177011136* 7, pp. 457–472. DOI: 10.1214/SS/1177011136.

German, D. C., White, C. L., and Sparkman, D. R. (1987). Alzheimer's disease: Neurofibrillary tangles in nuclei that project to the cerebral cortex. *Neuroscience* 21, pp. 305–312. DOI: 10.1016/0306-4522(87)90123-0.

Gilks, W. R., Richardson, S., and Spiegelhalter, D. J. (2003). *Markok Chain Monte Carlo In Practice*, pp. 1–18.

Glass, G. V. (1976). Primary, secondary and meta-analysis of research. *Educational Research* 5.

Glasser, M. F. and Van Essen, D. C. (2011). Mapping Human Cortical Areas In Vivo Based on Myelin Content as Revealed by T1- and T2-Weighted MRI. *Journal of Neuroscience*. DOI: 10.1523/jneurosci.2180-11.2011.

Glasser, M. F., Coalson, T. S., Robinson, E. C., Hacker, C. D., Harwell, J., Yacoub, E., Ugurbil, K., Andersson, J., Beckmann, C. F., Jenkinson, M., Smith, S. M., and Van Essen, D. C. (2016). A multi-modal parcellation of human cerebral cortex. *Nature*. DOI: 10.1038/nature18933.

Glimcher, P. W. (2004). *Decisions, uncertainty, and the brain: The science of neuroeconomics*. MIT press.

Glover, G. H., Li, T.-Q., and Ress, D. (2000). Image-Based Method for Retrospective Correction of Physiological Motion Effects in fMRI: RETROICOR. DOI: 10.1002/1522-2594.

Glover, G. H. (1999). Deconvolution of impulse response in event-related BOLD fMRI. *NeuroImage* 9, pp. 416–429. DOI: 10.1006/NIMG.1998.0419.

Goldstein, J. M., Seidman, L. J., Makris, N., Ahern, T., O'Brien, L. M., Caviness, V. S., Kennedy, D. N., Faraone, S. V., and Tsuang, M. T. (2007). Hypothalamic Abnormalities in Schizophrenia: Sex Effects and Genetic Vulnerability. *Biological Psychiatry*. DOI: 10.1016/j.biopsych.2006.06.027.

Good, C. D., Johnsrude, I. S., Ashburner, J., Henson, R. N., Friston, K. J., and Frackowiak, R. S. (2001). A Voxel-Based Morphometric Study of Ageing in 465 Normal Adult Human Brains. *NeuroImage* 14, pp. 21–36. DOI: 10.1006/nimg.2001.0786.

Goodro, M., Sameti, M., Patenaude, B., and Fein, G. (2012). Age effect on subcortical structures in healthy adults. *Psychiatry Research - Neuroimaging* 203, pp. 38–45. DOI: 10.1016/j.pscychresns.2011.09.014.

Gordon, E. M., Laumann, T. O., Gilmore, A. W., Newbold, D. J., Greene, D. J., Berg, J. J., Ortega, M., Hoyt-Drazen, C., Gratton, C., Sun, H., Hampton, J. M., Coalson, R. S., Nguyen, A. L., McDermott, K. B., Shimony, J. S., Snyder, A. Z., Schlaggar, B. L., Petersen, S. E., Nelson, S. M., and Dosenbach, N. U. (2017). Precision Functional Mapping of Individual Human Brains. *Neuron* 95, 791–807.e7. DOI: 10.1016/j.neuron.2017.07.011.

Gorgolewski, K. J., Burns, C. D., Madison, C., Clark, D., Halchenko, Y. O., Waskom, M. L., and Ghosh, S. S. (2011). Nipype: A Flexible, Lightweight and Extensible Neuroimaging Data Processing Framework in Python. *Frontiers in Neuroinformatics* 5. DOI: 10.3389/fninf.2011.00013.

Gorgolewski, K. J., Varoquaux, G., Rivera, G., Schwarz, Y., Ghosh, S. S., Maumet, C., Sochat, V. V., Nichols, T. E., Poldrack, R. A., Poline, J. B., Yarkoni, T., and Margulies, D. S. (2015). NeuroVault.Org: A web-based repository for collecting and sharing unthresholded statistical maps of the human brain. *Frontiers in Neuroinformatics*. DOI: 10.3389/fninf.2015.00008.

Gowland, P. A. and Bowtell, R. (2007). Theoretical optimization of multi-echo fMRI data acquisition. *Physics in Medicine and Biology* 52, pp. 1801–1813. DOI: 10.1088/0031-9155/52/7/003.

Gratton, C., Laumann, T. O., Nielsen, A. N., Greene, D. J., Gordon, E. M., Gilmore, A. W., Nelson, S. M., Coalson, R. S., Snyder, A. Z., Schlaggar, B. L., Dosenbach, N. U., and Petersen, S. E. (2018). Functional Brain Networks Are Dominated by Stable Group and Individual Factors, Not Cognitive or Daily Variation. *Neuron*. DOI: 10.1016/j.neuron.2018.03.035.

Greenberg, D. L., Messer, D. F., Payne, M. E., MacFall, J. R., Provenzale, J. M., Steffens, D. C., and Krishnan, R. R. (2008). Aging, gender, and the elderly adult brain: An examination of analytical strategies. *Neurobiology of Aging*. DOI: 10.1016/j.neurobiolaging.2006.09.016.

Greve, D. N. and Fischl, B. (2009). Accurate and robust brain image alignment using boundary-based registration. *NeuroImage* 48, pp. 63–72. DOI: 10.1016/J.NEUROIMAGE.2009.06.060.

Grydeland, H., Vértes, P. E., Váša, F., Romero-Garcia, R., Whitaker, K., Alexander-Bloch, A. F., Bjørnerud, A., Patel, A. X., Sederevičius, D., Tamnes, C. K., Westlye, L. T., White, S. R., Walhovd, K. B., Fjell, A. M., and Bullmore, E. T. (2019). Waves of maturation and senescence in micro-structural MRI markers of human cortical myelination over the lifespan. *Cerebral Cortex* 29, pp. 1369–1381. DOI: 10.1093/cercor/bhy330.

Guan, X., Xu, X., and Zhang, M. (2017). Region-Specific Iron Measured by MRI as a Biomarker for Parkinson's Disease. *Neuroscience Bulletin* 33, pp. 561–567. DOI: 10.1007/s12264-017-0138-x.

Guitart-Masip, M., Fuentemilla, L., Bach, D. R., Huys, Q. J., Dayan, P., Dolan, R. J., and Duzel, E. (2011). Action dominates valence in anticipatory representations in the human striatum and dopaminergic midbrain. *Journal of Neuroscience*. DOI: 10.1523/JNEUROSCI.6376-10.2011.

Gulban, O. F., Schneider, M., Marquardt, I., Haast, R. A., and De Martino, F. (2018). A scalable method to improve gray matter segmentation at ultra high field MRI. *PLoS ONE*. DOI: 10.1371/journal.pone.0198335.

Guo, Y., Schmitz, T. W., Mur, M., Ferreira, C. S., and Anderson, M. C. (2018). A supramodal role of the basal ganglia in memory and motor inhibition: Meta-analytic evidence. *Neuropsychologia*. DOI: 10.1016/j.neuropsychologia.2017.11.033.

Haacke, E. M., Cheng, N. Y., House, M. J., Liu, Q., Neelavalli, J., Ogg, R. J., Khan, A., Ayaz, M., Kirsch, W., and Obenaus, A. (2005). Imaging iron stores in the brain using magnetic resonance imaging. *Magnetic Resonance Imaging*. DOI: 10.1016/j.mri.2004.10.001.

Haacke, E. M. and Patrick, J. L. (1986). Reducing motion artifacts in two-dimensional Fourier transform imaging. *Magnetic Resonance Imaging*. DOI: 10.1016/0730-725X(86)91046-5.

Haast, R. A., Ivanov, D., Formisano, E., and Uludağ, K. (2016). Reproducibility and reliability of quantitative and weighted T1 and T2* mapping for myelin-based cortical parcellation at 7 tesla. *Frontiers in Neuroanatomy* 10, pp. 1–17. DOI: 10.3389/fnana.2016.00112.

Hahn, G. J. (1977). The Hazards of Extrapolation in Regression Analysis. *Journal of Quality Technology* 9, pp. 159–165. DOI: 10.1080/00224065.1977.11980791.

Hallett, M. (1998). The neurophysiology of dystonia. *Archives of Neurology* 55, pp. 601–603.

– (2006). Pathophysiology of dystonia. *Parkinson's Disease and Related Disorders*, pp. 485–488.

Hallgren, B. and Sourander, P. (1958). THE EFFECT OF AGE ON THE NON-HAEMIN IRON IN THE HUMAN BRAIN. *Journal of Neurochemistry*. DOI: 10.1111/j.1471-4159.1958.tb12607.x.

Hametner, S., Endmayr, V., Deistung, A., Palmrich, P., Prihoda, M., Haimburger, E., Menard, C., Feng, X., Haider, T., Leisser, M., Köck, U., Kaider, A., Höftberger, R., Robinson, S., Reichenbach, J. R., Lassmann, H., Traxler, H., Trattnig, S., and Grabner, G. (2018). The influence of brain iron and myelin on magnetic susceptibility and effective transverse relaxation - A biochemical and histological validation study. *NeuroImage* 179, pp. 117–133. DOI: 10.1016/j.neuroimage.2018.06.007.

Hampshire, A. (2015). Putting the brakes on inhibitory models of frontal lobe function. *NeuroImage* 113, pp. 340–355.

Hampshire, A., Chamberlain, S. R., Monti, M. M., Duncan, J., and Owen, A. M. (2010). The role of the right inferior frontal gyrus: inhibition and attentional control. *NeuroImage* 50, pp. 1313–1319. DOI: 10.1016/J.NEUROIMAGE.2009.12.109.

Hampshire, A., Duncan, J., and Owen, A. M. (2007). Selective tuning of the blood oxygenation level-dependent response during simple target detection dissociates human frontoparietal subregions. *Journal of neuroscience* 27, pp. 6219–6223.

Hampshire, A., Thompson, R., Duncan, J., and Owen, A. M. (2009). Selective tuning of the right inferior frontal gyrus during target detection. *Cognitive, affective and behavioral neuroscience* 9, p. 103. DOI: 10.3758/CABN.9.1.103.

Hanes, D. P., Patterson, W. F., and Schall, J. D. (1998). Role of frontal eye fields in countermanding saccades: visual, movement, and fixation activity. *Journal of neurophysiology* 79, pp. 817–834.

Hanke, M., Baumgartner, F. J., Ibe, P., Kaule, F. R., Pollmann, S., Speck, O., Zinke, W., and Stadler, J. (2014). A high-resolution 7-Tesla fMRI dataset from complex natural stimulation with an audio movie. *Scientific Data*. DOI: 10.1038/sdata.2014.3.

Harrison, S. J., Bianchi, S., Heinzle, J., Stephan, K. E., Iglesias, S., and Kasper, L. (2021). A Hilbert-based method for processing respiratory timeseries. *NeuroImage* 230, p. 117787. DOI: 10.1016/j.neuroimage.2021.117787.

Harvey, A. K., Pattinson, K. T., Brooks, J. C., Mayhew, S. D., Jenkinson, M., and Wise, R. G. (2008). Brainstem functional magnetic resonance imaging: Disentangling signal from physiological noise. *Journal of Magnetic Resonance Imaging* 28, pp. 1337–1344. DOI: 10.1002/jmri.21623.

Havsteen, I., Ohlhues, A., Madsen, K. H., Nybing, J. D., Christensen, H., and Christensen, A. (2017). *Are movement artifacts in magnetic resonance imaging a real problem?-a narrative review*. DOI: 10.3389/fneur.2017.00232.

Haxby, J. V., Guntupalli, J. S., Connolly, A. C., Halchenko, Y. O., Conroy, B. R., Gobbini, M. I., Hanke, M., and Ramadge, P. J. (2011). A common, high-dimensional model of the representational space in human ventral temporal cortex. *Neuron*. DOI: 10.1016/j.neuron.2011.08.026.

Heathcote, A., Lin, Y. S., Reynolds, A., Strickland, L., Gretton, M., and Matzke, D. (2019). Dynamic models of choice. *Behavior Research Methods* 51, pp. 961–985. DOI: 10.3758/S13428-018-1067-Y/FIGURES/15.

Heekeren, H. R., Marrett, S., and Ungerleider, L. G. (2008). The neural systems that mediate human perceptual decision making. *Nature reviews. Neuroscience* 9, pp. 467–479. DOI: 10.1038/nrn2374.

Hernández, M., Costa, A., Fuentes, L. J., Vivas, A. B., and Sebastián-Gallés, N. (2010). The impact of bilingualism on the executive control and orienting networks of attention. *Bilingualism: Language and Cognition* 13, pp. 315–325.

Herting, M. M., Johnson, C., Mills, K. L., Vijayakumar, N., Dennison, M., Liu, C., Goddings, A. L., Dahl, R. E., Sowell, E. R., Whittle, S., Allen, N. B., and Tamnes, C. K. (2018). Development of subcortical volumes across adolescence in males and females: A multisample study of longitudinal changes. *NeuroImage* 172, pp. 194–205. DOI: 10.1016/j.neuroimage.2018.01.020.

Hill, R. A., Li, A. M., and Grutzendler, J. (2018). Lifelong cortical myelin plasticity and age-related degeneration in the live mammalian brain. *Nature Neuroscience* 21, pp. 683–695. DOI: 10.1038/s41593-018-0120-6.

Hirsch, E. C., Graybiel, A. M., and Agid, Y. (1988). Melanized dopaminergic neurons are differentially affected in Parkinson's disease. *Nature* 334, pp. 345–348.

Ho, T. C., Gutman, B., Pozzi, E., Grabe, H. J., Hosten, N., Wittfeld, K., Völzke, H., Baune, B., Dannlowski, U., Förster, K., Grotegerd, D., Redlich, R., Jansen, A., Kircher, T., Krug, A., Meinert, S., Nenadic, I., Opel, N., Dinga, R., Veltman, D. J., Schnell, K., Veer, I., Walter, H., Gotlib, I. H., Sacchet, M. D., Aleman, A., Groenewold, N. A., Stein, D. J., Li, M., Walter, M., Ching, C. R., Jahanshad, N., Ragothaman, A., Isaev, D., Zavaliangos-Petropulu, A., Thompson, P. M., Sämann, P. G., and Schmaal, L. (2020). Subcortical shape alterations in major depressive disorder: Findings from the ENIGMA major depressive disorder working group. *Human Brain Mapping*, pp. 1–11. DOI: 10.1002/hbm.24988.

Hollander, G. de, Keuken, M. C., van der Zwaag, W., Forstmann, B. U., and Trampel, R. (2017). Comparing functional MRI protocols for small, iron-rich basal ganglia nuclei such as the subthalamic nucleus at 7 T and 3 T. *Human Brain Mapping*. DOI: 10.1002/hbm.23586.

Holmes, A. J., Lee, P. H., Hollinshead, M. O., Bakst, L., Roffman, J. L., Smoller, J. W., and Buckner, R. L. (2012). Individual Differences in Amygdala-Medial Prefrontal Anatomy Link Negative Affect, Impaired Social Functioning, and Polygenic Depression Risk. *Journal of Neuroscience* 32, pp. 18087–18100. DOI: 10.1523/jneurosci.2531-12.2012.

Holmes, A. J., Hollinshead, M. O., O'Keefe, T. M., Petrov, V. I., Fariello, G. R., Wald, L. L., Fischl, B., Rosen, B. R., Mair, R. W., Roffman, J. L., Smoller, J. W., and Buckner, R. L. (2015). Brain Genomics Superstruct Project initial data release with structural, functional, and behavioral measures. *Scientific Data*. DOI: 10.1038/sdata.2015.31.

Holroyd, C. B. and Coles, M. G. (2008). Dorsal anterior cingulate cortex integrates reinforcement history to guide voluntary behavior. *Cortex*. DOI: 10.1016/j.cortex.2007.08.013.

Huang, C.-C., Rolls, E. T., Feng, J., and Lin, C.-P. (2022). An extended Human Connectome Project multimodal parcellation atlas of the human cortex and subcortical areas. *Brain Structure and Function* 227, pp. 763–778.

Huang, Y., Su, L., and Ma, Q. (2020). The Stroop effect: An activation likelihood estimation meta-analysis in healthy young adults. *Neuroscience Letters*. DOI: 10.1016/j.neulet.2019.134683.

Hung, Y., Gaillard, S. L., Yarmak, P., and Arsalidou, M. (2018). Dissociations of cognitive inhibition, response inhibition, and emotional interference: Voxelwise ALE meta-analyses of fMRI studies. *Human Brain Mapping*. DOI: 10.1002/hbm.24232.

Huntenburg, J. M., Bazin, P. L., Goulas, A., Tardif, C. L., Villringer, A., and Margulies, D. S. (2017). A Systematic Relationship Between Functional Connectivity and Intracortical Myelin in the Human Cerebral Cortex. *Cerebral cortex (New York, N.Y. : 1991)*. DOI: 10.1093/cercor/bhx030.

Iglesias, J. E., Insausti, R., Lerma-Usabiaga, G., Bocchetta, M., Van Leemput, K., Greve, D. N., Kouwe, A. van der, Fischl, B., Caballero-Gaudes, C., and Paz-Alonso, P. M. (2018). A probabilistic atlas of the human thalamic nuclei combining ex vivo MRI and histology. *NeuroImage* 183, pp. 314–326. DOI: 10.1016/j.neuroimage.2018.08.012.

Inano, S., Takao, H., Hayashi, N., Yoshioka, N., Mori, H., Kunimatsu, A., Abe, O., and Ohtomo, K. (2013). Effects of age and gender on neuroanatomical volumes. *Journal of Magnetic Resonance Imaging* 37, pp. 1072–1076. DOI: 10.1002/jmri.23910.

Isaacs, B. R., Mulder, M. J., Groot, J. M., Berendonk, N. van, Lute, N., Bazin, P.-L., Forstmann, B. U., and Alkemade, A. (2020). 3 versus 7 Tesla magnetic resonance imaging for parcellations of subcortical brain structures in clinical settings. *PloS one* 15, e0236208.

Isaacs, B. R., Forstmann, B. U., Temel, Y., and Keuken, M. C. (2018). The Connectivity Fingerprint of the Human Frontal Cortex, Subthalamic Nucleus, and Striatum. *Frontiers in Neuroanatomy*. DOI: 10.3389/fnana.2018.00060.

Isherwood, S. J. S., Bazin, P.-L., Alkemade, A., and Forstmann, B. U. (2021a). Quantity and quality: Normative open-access neuroimaging databases. *PLOS ONE* 16, pp. 1–30. DOI: 10.1371/journal.pone.0248341.

Isherwood, S. J. S., Bazin, P.-L., Miletić, S., Stevenson, N. R., Trutti, A. C., Tse, D. H. Y., Heathcote, A., Matzke, D., Innes, R. J., Habli, S., Sokolowski, D. R., Alkemade, A., Håberg, A. K., and Forstmann, B. U. (2023a). Investigating Intra-Individual Networks of Response Inhibition and Interference Resolution using 7T MRI. *NeuroImage*, p. 119988.

Isherwood, S. J. S., Kemp, S., Miletić, S., Stevenson, N. R., Bazin, P.-L., and Forstmann, B. U. (2023b). The canonical stopping network: Revisiting the role of the subcortex in response inhibition. *submitted*.

Isherwood, S. J. S., Keuken, M. C., Bazin, P.-L., and Forstmann, B. U. (2021b). Cortical and subcortical contributions to interference resolution and inhibition - An fMRI ALE meta-analysis. *Neuroscience and biobehavioral reviews* 129, pp. 245–260. DOI: 10.1016/J.NEUBIOREV.2021.07.021.

Jahanshahi, M., Obeso, I., Baunez, C., Alegre, M., and Krack, P. (2015). Parkinson's Disease, the Subthalamic Nucleus, Inhibition, and Impulsivity. *Movement Disorders* 30, pp. 128–140. DOI: 10.1002/MDS.26049.

Jahfari, S., Waldorp, L., Wildenberg, W. P. van den, Scholte, H. S., Ridderinkhof, K. R., and Forstmann, B. U. (2011). Effective Connectivity Reveals Important Roles for Both the Hyperdirect (Fronto-Subthalamic) and the Indirect (Fronto-Striatal-Pallidal) Fronto-Basal Ganglia Pathways during Response Inhibition. *The Journal of Neuroscience* 31, p. 6891. DOI: 10.1523/JNEUROSCI.5253-10.2011.

Jauregi, A., Kessler, K., and Hassel, S. (2018). Linking cognitive measures of response inhibition and reward sensitivity to trait impulsivity. *Frontiers in psychology* 9, p. 2306.

Jeffreys, H. (1935). Some Tests of Significance, Treated by the Theory of Probability. *Mathematical Proceedings of the Cambridge Philosophical Society*. DOI: 10.1017/S030500410001330X.

Jenkinson, M., Bannister, P., Brady, M., and Smith, S. (2002). Improved optimization for the robust and accurate linear registration and motion correction of brain images. *NeuroImage* 17, pp. 825–841. DOI: 10.1016/S1053-8119(02)91132-8.

Jenkinson, M., Beckmann, C. F., Behrens, T. E., Woolrich, M. W., and Smith, S. M. (2012). FSL. *NeuroImage* 62, pp. 782–790. DOI: 10.1016/J.NEUROIMAGE.2011.09.015.

Jensen-Campbell, L. A., Adams, R., Perry, D. G., Workman, K. A., Furdella, J. Q., and Egan, S. K. (2002). Agreeableness, extraversion, and peer relations in early adolescence: Winning friends and deflecting aggression. *Journal of Research in Personality* 36, pp. 224–251.

Jernigan, T. L., Archibald, S. L., Fennema-Notestine, C., Gamst, A. C., Stout, J. C., Bonner, J., and Hesselink, J. R. (2001). Effects of age on tissues and regions of the cerebrum and cerebellum. *Neurobiology of Aging*. DOI: 10.1016/S0197-4580(01)00217-2.

Jernigan, T. L., Brown, T. T., Hagler, D. J., Akshoomoff, N., Bartsch, H., Newman, E., Thompson, W. K., Bloss, C. S., Murray, S. S., Schork, N., Kennedy, D. N., Kuperman, J. M., McCabe, C., Chung, Y., Libiger, O., Maddox, M., Casey, B. J., Chang, L., Ernst, T. M., Frazier, J. A., Gruen, J. R., Sowell, E. R., Kenet, T., Kaufmann, W. E., Mostofsky, S., Amaral, D. G., and Dale, A. M. (2016). The Pediatric Imaging, Neurocognition, and Genetics (PING) Data Repository. *NeuroImage*. DOI: 10.1016/j.neuroimage.2015.04.057. arXiv: 15334406.

Jezzard, P. and Balaban, R. S. (1995). Correction for geometric distortion in echo planar images from B0 field variations. *Magnetic Resonance in Medicine* 34, pp. 65–73. DOI: 10.1002/mrm.1910340111.

Jimura, K., Yamashita, K., Chikazoe, J., Hirose, S., Miyashita, Y., and Konishi, S. (2009). A critical component that activates the left inferior prefrontal cortex during interference resolution. *The European Journal of Neuroscience* 29, pp. 1915–1920. DOI: 10.1111/j.1460-9568.2009.06731.x.

Job, D. E., Dickie, D. A., Rodriguez, D., Robson, A., Danso, S., Pernet, C., Bastin, M. E., Boardman, J. P., Murray, A. D., Ahearn, T., Waiter, G. D., Staff, R. T., Deary, I. J., Shenkin, S. D., and Wardlaw, J. M. (2017). A brain imaging repository of normal structural MRI across the life course: Brain Images of Normal Subjects (BRAINS). *NeuroImage* 144, pp. 299–304. DOI: 10.1016/j.neuroimage.2016.01.027.

Johansen-Berg, H. (2013). Human connectomics - What will the future demand? *NeuroImage*. DOI: 10.1016/j.neuroimage.2013.05.082.

Kapur, S. (2003). Psychosis as a state of aberrant salience: a framework linking biology, phenomenology, and pharmacology in schizophrenia. *American journal of Psychiatry* 160, pp. 13–23.

Karachi, C., Grabli, D., Baup, N., Mounayar, S., Tandé, D., François, C., and Hirsch, E. C. (2009). Dysfunction of the subthalamic nucleus induces behavioral and movement disorders in monkeys. *Movement Disorders* 24, pp. 1183–1192. DOI: 10.1002/mds.22547.

Karayanidis, F., Keuken, M. C., Wong, A., Rennie, J. L., Hollander, G. de, Cooper, P. S., Ross Fulham, W., Lenroot, R., Parsons, M., Phillips, N., Michie, P. T., and Forstmann, B. U. (2016). The Age-ility Project (Phase 1): Structural and functional imaging and electrophysiological data repository. *NeuroImage*. DOI: 10.1016/j.neuroimage.2015.04.047.

Kasper, L., Bollmann, S., Diaconescu, A. O., Hutton, C., Heinzle, J., Iglesias, S., Hauser, T. U., Sebold, M., Manjaly, Z. M., Pruessmann, K. P., and Stephan, K. E. (2017). The PhysIO Toolbox for Modeling Physiological Noise in fMRI Data. *Journal of neuroscience methods* 276, pp. 56–72. DOI: 10.1016/J.JNEUMETH.2016.10.019.

Keator, D. B., Erp, T. G. van, Turner, J. A., Glover, G. H., Mueller, B. A., Liu, T. T., Voyvodic, J. T., Rasmussen, J., Calhoun, V. D., Lee, H. J., Toga, A. W., McEwen, S., Ford, J. M., Mathalon, D. H., Diaz,

M., O'Leary, D. S., Jeremy Bockholt, H., Gadde, S., Preda, A., Wible, C. G., Stern, H. S., Belger, A., McCarthy, G., Ozyurt, B., and Potkin, S. G. (2016). The Function Biomedical Informatics Research Network Data Repository. *NeuroImage*. DOI: 10.1016/j.neuroimage.2015.09.003.

Kelley, R., Flouty, O., Emmons, E. B., Kim, Y., Kingyon, J., Wessel, J. R., Oya, H., Greenlee, J. D., and Narayanan, N. S. (2018). A human prefrontal-subthalamic circuit for cognitive control. *Brain* 141, pp. 205–216. DOI: 10.1093/brain/awx300. eprint: https://academic.oup.com/brain/article-pdf/141/1/205/24175616/awx300.pdf.

Kerl, H. U., Gerigk, L., Pechlivanis, I., Al-Zghloul, M., Groden, C., and Nölte, I. S. (2012). The subthalamic nucleus at 7.0 Tesla: Evaluation of sequence and orientation for deep-brain stimulation. *Acta Neurochirurgica*. DOI: 10.1007/s00701-012-1476-0.

Keuken, M. C., Bazin, P. L., Backhouse, K., Beekhuizen, S., Himmer, L., Kandola, A., Lafeber, J. J., Prochazkova, L., Trutti, A., Schäfer, A., Turner, R., and Forstmann, B. U. (2017). Effects of aging on T1 , T2 , and QSM MRI values in the subcortex. *Brain Structure and Function*. DOI: 10.1007/s00429-016-1352-4.

Keuken, M. C., Bazin, P. L., Crown, L., Hootsmans, J., Laufer, A., Müller-Axt, C., Sier, R., Putten, E. J. van der, Schäfer, A., Turner, R., and Forstmann, B. U. (2014). Quantifying inter-individual anatomical variability in the subcortex using 7T structural MRI. *NeuroImage*. DOI: 10.1016/j.neuroimage.2014.03.032.

Keuken, M. C., Bazin, P.-L., Schafer, A., Neumann, J., Turner, R., and Forstmann, B. U. (2013). Ultra-High 7T MRI of Structural Age-Related Changes of the Subthalamic Nucleus. *Journal of Neuroscience* 33, pp. 4896–4900. DOI: 10.1523/jneurosci.3241-12.2013.

Keuken, M. C., Isaacs, B. R., Trampel, R., van der Zwaag, W., and Forstmann, B. U. (2018). *Visualizing the Human Subcortex Using Ultra-high Field Magnetic Resonance Imaging*. DOI: 10.1007/s10548-018-0638-7.

Keuken, M. C. and Forstmann, B. U. (2015). A probabilistic atlas of the basal ganglia using 7 T MRI. *Data in Brief*. DOI: 10.1016/j.dib.2015.07.028.

Khattar, N., Triebswetter, C., Kiely, M., Ferrucci, L., Resnick, S. M., Spencer, R. G., and Bouhrara, M. (2021). Investigation of the association between cerebral iron content and myelin content in normative aging using quantitative magnetic resonance neuroimaging. *NeuroImage* 239, p. 118267. DOI: 10.1016/j.neuroimage.2021.118267.

Kim, J.-H. and Ress, D. (2017). Reliability of the depth-dependent high-resolution BOLD hemodynamic response in human visual cortex and vicinity. *Magnetic Resonance Imaging* 39, pp. 53–63. DOI: 10.1016/j.mri.2017.01.019.

Kim, J.-H., Taylor, A. J., Himmelbach, M., Hagberg, G. E., Scheffler, K., and Ress, D. (2022). Characterization of the blood oxygen level dependent hemodynamic response function in human subcortical regions with high spatiotemporal resolution. *Frontiers in Neuroscience* 16. DOI: 10.3389/fnins.2022.834244.

Kitajima, M., Korogi, Y., Kakeda, S., Moriya, J., Ohnari, N., Sato, T., Hayashida, Y., Hirai, T., Okuda, T., and Yamashita, Y. (2008). Human subthalamic nucleus: Evaluation with high-resolution MR imaging at 3.0 T. *Neuroradiology* 50, pp. 675–681. DOI: 10.1007/s00234-008-0388-4.

Klein, A., Ghosh, S. S., Bao, F. S., Giard, J., Häme, Y., Stavsky, E., Lee, N., Rossa, B., Reuter, M., Chaibub Neto, E., and Keshavan, A. (2017). Mindboggling morphometry of human brains. *PLOS Computational Biology* 13. Ed. by D. Schneidman, e1005350. DOI: 10.1371/journal.pcbi.1005350.

Klein, A. and Tourville, J. (2012). 101 labeled brain images and a consistent human cortical labeling protocol. *Frontiers in Neuroscience*. DOI: 10.3389/fnins.2012.00171.

Krasnow, B., Tamm, L., Greicius, M. D., Yang, T. T., Glover, G. H., Reiss, A. L., and Menon, V. (2003). Comparison of fMRI activation at 3 and 1.5 T during perceptual, cognitive, and affective processing. *NeuroImage*. DOI: 10.1016/S1053-8119(03)00002-8.

Kringelbach, M. L. and Rolls, E. T. (2004). The functional neuroanatomy of the human orbitofrontal cortex: evidence from neuroimaging and neuropsychology. *Progress in neurobiology* 72, pp. 341–372. DOI: 10.1016/J.PNEUROBIO.2004.03.006.

Krüger, G. and Glover, G. H. (2001). Physiological noise in oxygenation-sensitive magnetic resonance imaging. *Magnetic Resonance in Medicine* 46, pp. 631–637. DOI: 10.1002/mrm.1240.

Kühn, A. A., Williams, D., Kupsch, A., Limousin, P., Hariz, M., Schneider, G.-H., Yarrow, K., and Brown, P. (2004). Event-related beta desynchronization in human subthalamic nucleus correlates with motor performance. *Brain* 127, pp. 735–746. DOI: 10.1093/brain/awh106. eprint: https://academic.oup.com/brain/article-pdf/127/4/735/17869637/awh106.pdf.

Kundu, P., Voon, V., Balchandani, P., Lombardo, M. V., Poser, B. A., and Bandettini, P. A. (2017). Multi-echo fMRI: A review of applications in fMRI denoising and analysis of BOLD signals. *NeuroImage* 154, pp. 59–80. DOI: 10.1016/j.neuroimage.2017.03.033.

Kwon, Y. H. and Kwon, J. W. (2013). Response Inhibition Induced in the Stop-signal Task by Transcranial Direct Current Stimulation of the Pre-supplementary Motor Area and Primary Sensoriomotor Cortex. *Journal of Physical Therapy Science* 25, pp. 1083–1086. DOI: 10.1589/jpts.25.1083.

Laird, A. R., Fox, P. M., Price, C. J., Glahn, D. C., Uecker, A. M., Lancaster, J. L., Turkeltaub, P. E., Kochunov, P., and Fox, P. T. (2005). ALE meta-analysis: Controlling the false discovery rate and performing statistical contrasts. In: *Human Brain Mapping*. DOI: 10.1002/hbm.20136.

Lancaster, J. L., Tordesillas-Gutiérrez, D., Martinez, M., Salinas, F., Evans, A., Zilles, K., Mazziotta, J. C., and Fox, P. T. (2007). Bias between MNI and talairach coordinates analyzed using the ICBM-152 brain template. *Human Brain Mapping*. DOI: 10.1002/hbm.20345.

Lanczos, C. (1964). Evaluation of Noisy Data. *Journal of the Society for Industrial and Applied Mathematics Series B Numerical Analysis* 1, pp. 76–85. DOI: 10.1137/0701007.

Landis, J. R. and Koch, G. G. (1977). The Measurement of Observer Agreement for Categorical Data. *Biometrics* 33, pp. 159–174.

Landman, B. A., Huang, A. J., Gifford, A., Vikram, D. S., Lim, I. A. L., Farrell, J. A., Bogovic, J. A., Hua, J., Chen, M., Jarso, S., Smith, S. A., Joel, S., Mori, S., Pekar, J. J., Barker, P. B., Prince, J. L., and Zijl, P. C. van (2011). Multi-parametric neuroimaging reproducibility: A 3-T resource study. *NeuroImage*. DOI: 10.1016/j.neuroimage.2010.11.047.

Langkammer, C., Bredies, K., Poser, B. A., Barth, M., Reishofer, G., Fan, A. P., Bilgic, B., Fazekas, F., Mainero, C., and Ropele, S. (2015). Fast quantitative susceptibility mapping using 3D EPI and total generalized variation. *NeuroImage* 111, pp. 622–630. DOI: 10.1016/j.neuroimage.2015.02.041.

Langkammer, C., Schweser, F., Krebs, N., Deistung, A., Goessler, W., Scheurer, E., Sommer, K., Reishofer, G., Yen, K., Fazekas, F., Ropele, S., and Reichenbach, J. R. (2012). Quantitative susceptibility mapping (QSM) as a means to measure brain iron? A post mortem validation study. *NeuroImage* 62, pp. 1593–1599. DOI: 10.1016/j.neuroimage.2012.05.049.

Lau, J. C., Xiao, Y., Haast, R. A., Gilmore, G., Uludağ, K., MacDougall, K. W., Menon, R. S., Parrent, A. G., Peters, T. M., and Khan, A. R. (2020). Direct visualization and characterization of the human zona incerta and surrounding structures. *Human Brain Mapping* 41, pp. 4500–4517. DOI: 10.1002/hbm.25137.

Lebel, C., Gee, M., Camicioli, R., Wieler, M., Martin, W., and Beaulieu, C. (2012). Diffusion tensor imaging of white matter tract evolution over the lifespan. *NeuroImage* 60, pp. 340–352. DOI: 10.1016/j.neuroimage.2011.11.094.

Lee, C. C., Jack, C. R., Grimm, R. C., Rossman, P. J., Felmlee, J. P., Ehman, R. L., and Riederer, S. J. (1996). Real-time adaptive motion correction in functional MRI. *Magnetic Resonance in Medicine*. DOI: 10.1002/mrm.1910360316.

Lemaitre, H., Goldman, A. L., Sambataro, F., Verchinski, B. A., Meyer-Lindenberg, A., Weinberger, D. R., and Mattay, V. S. (2012). Normal age-related brain morphometric changes: Nonuniformity across cortical thickness, surface area and gray matter volume? *Neurobiology of Aging* 33, 617.e1–617.e9. DOI: 10.1016/j.neurobiolaging.2010.07.013.

LeVine, S. M., Wulser, M. J., and Lynch, S. G. (1998). Iron quantification in cerebrospinal fluid. *Analytical Biochemistry* 265, pp. 74–78. DOI: 10.1006/abio.1998.2903.

Levitt, J. J., Rosow, L. K., Nestor, P. G., Pelavin, P. E., Swisher, T. M., McCarley, R. W., and Shenton, M. E. (2013). A volumetric MRI study of limbic, associative and sensorimotor striatal subregions in schizophrenia. *Schizophrenia Research*. DOI: 10.1016/j.schres.2012.08.032.

Lewis, L. D., Setsompop, K., Rosen, B. R., and Polimeni, J. R. (2018). Stimulus-dependent hemodynamic response timing across the human subcortical-cortical visual pathway identified through high spatiotemporal resolution 7T fMRI. *NeuroImage* 181, pp. 279–291. DOI: 10.1016/j.neuroimage.2018.06.056.

Li, C. S. R., Huang, C., Constable, R. T., and Sinha, R. (2006). Imaging response inhibition in a stop-signal task: neural correlates independent of signal monitoring and post-response processing. *The Journal of neuroscience : the official journal of the Society for Neuroscience* 26, pp. 186–192. DOI: 10.1523/JNEUROSCI.3741-05.2006.

Li, Q., Yang, G., Li, Z., Qi, Y., Cole, M. W., and Liu, X. (2017). Conflict detection and resolution rely on a combination of common and distinct cognitive control networks. *Neuroscience and biobehavioral reviews* 83, pp. 123–131. DOI: 10.1016/J.NEUBIOREV.2017.09.032.

Li, W., Tol, M. J. van, Li, M., Miao, W., Jiao, Y., Heinze, H. J., Bogerts, B., He, H., and Walter, M. (2014). Regional specificity of sex effects on subcortical volumes across the lifespan in healthy aging. *Human Brain Mapping* 35, pp. 238–247. DOI: 10.1002/hbm.22168.

Li, Y., Sethi, S. K., Zhang, C., Miao, Y., Yerramsetty, K. K., Palutla, V. K., Gharabaghi, S., Wang, C., He, N., Cheng, J., Yan, F., and Haacke, E. M. (2021). Iron Content in Deep Gray Matter as a Function of Age Using Quantitative Susceptibility Mapping: A Multicenter Study. *Frontiers in Neuroscience* 14, pp. 1–13. DOI: 10.3389/fnins.2020.607705.

Li, Z., Chen-Roetling, J., and Regan, R. F. (2009). Increasing expression of H- or L-ferritin protects cortical astrocytes from hemin toxicity. *Free Radical Research* 43, pp. 613–621. DOI: 10.1080/10715760902942808.

Liberati, A., Altman, D. G., Tetzlaff, J., Mulrow, C., Gøtzsche, P. C., Ioannidis, J. P., Clarke, M., Devereaux, P. J., Kleijnen, J., and Moher, D. (2009). The PRISMA statement for reporting systematic reviews and meta-analyses of studies that evaluate healthcare interventions: explanation and elaboration. *BMJ (Clinical research ed.)* DOI: 10.1136/bmj.b2700.

Limousin, P., Pollak, P., Benazzouz, A., Hoffmann, D., Le Bas, J.-F., Perret, J., Benabid, A.-L., and Broussolle, E. (1995). Effect on parkinsonian signs and symptoms of bilateral subthalamic nucleus stimulation. *The Lancet* 345, pp. 91–95. DOI: 10.1016/S0140-6736(95)90062-4.

Liu, C., Li, W., Tong, K. A., Yeom, K. W., and Kuzminski, S. (2015). Susceptibility-weighted imaging and quantitative susceptibility mapping in the brain. *Journal of Magnetic Resonance Imaging* 42, pp. 23–41. DOI: 10.1002/jmri.24768.

Liu, Z., Rios, C., Zhang, N., Yang, L., Chen, W., and He, B. (2010). Linear and nonlinear relationships between visual stimuli, EEG and BOLD fMRI signals. *Neuroimage* 50, pp. 1054–1066.

Logan, G. D. (1985). Executive control of thought and action. en. *Acta Psychol. (Amst.)* 60, pp. 193–210.

Logan, G. D. and Cowan, W. B. (1984). On the ability to inhibit thought and action: A theory of an act of control. *Psychological Review* 91, pp. 295–327. DOI: 10.1037/0033-295X.91.3.295.

Logan, G. D., Van Zandt, T., Verbruggen, F., and Wagenmakers, E. J. (2014). On the ability to inhibit thought and action: General and special theories of an act of control. *Psychological Review* 121, pp. 66–95. DOI: 10.1037/a0035230.

Logothetis, N. K., Pauls, J., Augath, M., Trinath, T., and Oeltermann, A. (2001). Neurophysiological investigation of the basis of the fMRI signal. *Nature* 412, pp. 150–157. DOI: 10.1038/35084005.

Lorincz, M. T. (2010). Neurologic Wilson's disease. *Annals of the New York Academy of Sciences* 1184, pp. 173–187.

Lorio, S., Kherif, F., Ruef, A., Melie-Garcia, L., Frackowiak, R., Ashburner, J., Helms, G., Lutti, A., and Draganski, B. (2016). Neurobiological origin of spurious brain morphological changes: A quantitative MRI study. *Human Brain Mapping* 37, pp. 1801–1815. DOI: 10.1002/hbm.23137.

Lowe, M. J., Lurito, J. T., Mathews, V. P., Phillips, M. D., and Hutchins, G. D. (2000). Quantitative comparison of functional contrast from BOLD-weighted spin-echo and gradient-echo echoplanar imaging at 1.5 Tesla and H215O PET in the whole brain. *Journal of Cerebral Blood Flow & Metabolism* 20, pp. 1331–1340. DOI: 10.1097/00004647-200009000-00012.

Lozano, A. M., Lipsman, N., Bergman, H., Brown, P., Chabardes, S., Chang, J. W., Matthews, K., McIntyre, C. C., Schlaepfer, T. E., Schulder, M., Temel, Y., Volkmann, J., and Krauss, J. K. (2019). Deep brain stimulation: current challenges and future directions. *Nature Reviews Neurology* 15, pp. 148–160. DOI: 10.1038/s41582-018-0128-2.

Lüsebrink, F., Sciarra, A., Mattern, H., Yakupov, R., and Speck, O. (2017). T 1 -weighted in vivo human whole brain MRI dataset with an ultrahigh isotropic resolution of 250 μm. *Scientific Data*. DOI: 10.1038/sdata.2017.32.

Lüsebrink, F., Wollrab, A., and Speck, O. (2013). Cortical thickness determination of the human brain using high resolution 3T and 7T MRI data. *NeuroImage*. DOI: 10.1016/j.neuroimage.2012.12.016.

Lyu, B., Tsvetanov, K. A., Tyler, L. K., Clarke, A., Cam-CAN, and Amos, W. (2020). Genetic signatures of human brain structure: A comparison between GWAS and relatedness-based regression. *bioRxiv*.

Maanen, L. van, Brown, S. D., Eichele, T., Wagenmakers, E.-J., Ho, T., Serences, J., and Forstmann, B. U. (2011). Neural Correlates of Trial-to-Trial Fluctuations in Response Caution. *Journal of Neuroscience* 31, pp. 17488–17495. DOI: 10.1523/JNEUROSCI.2924-11.2011.

Maanen, L. van, Turner, B., and Forstmann, B. U. (2015). From model-based perceptual decision-making to spatial interference control. *Current Opinion in Behavioral Sciences* 1, pp. 72–77. DOI: 10.1016/J.COBEHA.2014.10.010.

MacKay, A., Whittall, K., Adler, J., Li, D., Paty, D., and Graeb, D. (1994). In vivo visualization of myelin water in brain by magnetic resonance. *Magnetic Resonance in Medicine* 31, pp. 673–677. DOI: 10.1002/mrm.1910310614.

Madan, C. R. (2017). Advances in Studying Brain Morphology: The Benefits of Open-Access Data. *Frontiers in Human Neuroscience*. DOI: 10.3389/fnhum.2017.00405.

Madden, D. J., Bennett, I. J., Burzynska, A., Potter, G. G., Chen, N. kuei, and Song, A. W. (2012). Diffusion tensor imaging of cerebral white matter integrity in cognitive aging. *Biochimica et Biophysica Acta - Molecular Basis of Disease* 1822, pp. 386–400. DOI: 10.1016/j.bbadis.2011.08.003.

Makris, N., Goldstein, J. M., Kennedy, D., Hodge, S. M., Caviness, V. S., Faraone, S. V., Tsuang, M. T., and Seidman, L. J. (2006). Decreased volume of left and total anterior insular lobule in schizophrenia. *Schizophrenia Research*. DOI: 10.1016/j.schres.2005.11.020.

Mallet, N., Schmidt, R., Leventhal, D., Chen, F., Amer, N., Boraud, T., and Berke, J. D. (2016). Arkypallidal cells send a Stop signal to striatum. en. *Neuron* 89, pp. 308–316.

Malone, I. B., Cash, D., Ridgway, G. R., MacManus, D. G., Ourselin, S., Fox, N. C., and Schott, J. M. (2013). MIRIAD-Public release of a multiple time point Alzheimer's MR imaging dataset. *NeuroImage*. DOI: 10.1016/j.neuroimage.2012.12.044.

Mancini, C., Modugno, N., Santilli, M., Pavone, L., Grillea, G., Morace, R., and Mirabella, G. (2019). Unilateral stimulation of subthalamic nucleus does not affect inhibitory control. *Frontiers in Neurology* 9, p. 1149.

Mancini, M., Karakuzu, A., Cohen-Adad, J., Cercignani, M., Nichols, T. E., and Stikov, N. (2020). An interactive meta-analysis of MRI biomarkers of Myelin. *eLife* 9, pp. 1–23. DOI: 10.7554/eLife.61523.

Mangeat, G., Govindarajan, S. T., Mainero, C., and Cohen-Adad, J. (2015). Multivariate combination of magnetization transfer, T2* and B0 orientation to study the myelo-architecture of the in vivo human cortex. *NeuroImage* 119, pp. 89–102. DOI: 10.1016/j.neuroimage.2015.06.033.

Mansouri, F. A., Tanaka, K., and Buckley, M. J. (2009). *Conflict-induced behavioural adjustment: A clue to the executive functions of the prefrontal cortex*. DOI: 10.1038/nrn2538.

Marcus, D. S., Fotenos, A. F., Csernansky, J. G., Morris, J. C., and Buckner, R. L. (2010). Open access series of imaging studies: Longitudinal MRI data in nondemented and demented older adults. *Journal of Cognitive Neuroscience*. DOI: 10.1162/jocn.2009.21407.

Marcus, D. S., Wang, T. H., Parker, J., Csernansky, J. G., Morris, J. C., and Buckner, R. L. (2007). Open Access Series of Imaging Studies (OASIS): Cross-sectional MRI data in young, middle aged, nondemented, and demented older adults. *Journal of Cognitive Neuroscience*. DOI: 10.1162/jocn.2007.19.9.1498.

Marner, L. and Pakkenberg, B. (2003). Total length of nerve fibers in prefrontal and global white matter of chronic schizophrenics. *Journal of Psychiatric Research*. DOI: 10.1016/S0022-3956(03)00069-4.

Marques, J. P., Khabipova, D., and Gruetter, R. (2017). Studying cyto and myeloarchitecture of the human cortex at ultra-high field with quantitative imaging: R1, R2* and magnetic susceptibility. *NeuroImage* 147, pp. 152–163. DOI: 10.1016/j.neuroimage.2016.12.009.

Marques, J. P., Kober, T., Krueger, G., van der Zwaag, W., Van de Moortele, P. F., and Gruetter, R. (2010). MP2RAGE, a self bias-field corrected sequence for improved segmentation and T1-mapping at high field. *NeuroImage* 49, pp. 1271–1281. DOI: 10.1016/J.NEUROIMAGE.2009.10.002.

Marr, D. (1982). *Vision: a computational investigation into the human representation and processing of visual information*. DOI: 10.1016/0022-2496(83)90030-5.

Martin, W. R., Wieler, M., and Gee, M. (2008). Midbrain iron content in early Parkinson disease: A potential biomarker of disease status. *Neurology* 70, pp. 1411–1417. DOI: 10.1212/01.wnl.0000286384.31050.b5.

Matsumoto, M. and Takada, M. (2013). Distinct representations of cognitive and motivational signals in midbrain dopamine neurons. *Neuron* 79, pp. 1011–1024. DOI: 10.1016/j.neuron.2013.07.002.

Matzke, D., Love, J., and Heathcote, A. (2017). A Bayesian approach for estimating the probability of trigger failures in the stop-signal paradigm. *Behavior research methods* 49, pp. 267–281. DOI: 10.3758/S13428-015-0695-8.

Matzke, D., Love, J., Wiecki, T. V., Brown, S. D., Logan, G. D., and Wagenmakers, E. J. (2013). Release the BEESTS: Bayesian Estimation of Ex-Gaussian STop-Signal reaction time distributions. *Frontiers in psychology* 4. DOI: 10.3389/FPSYG.2013.00918.

Matzke, D., Verbruggen, F., and Logan, G. D. (2018). The Stop-Signal Paradigm. *Stevens' Handbook of Experimental Psychology and Cognitive Neuroscience*, pp. 1–45. DOI: 10.1002/9781119170174.EPCN510.

Matzke, D. and Wagenmakers, E. J. (2009). Psychological interpretation of the ex-Gaussian and shifted Wald parameters: A diffusion model analysis. *Psychonomic Bulletin and Review 2009 16:5* 16, pp. 798–817. DOI: 10.3758/PBR.16.5.798.

Mayer, A. R., Teshiba, T. M., Franco, A. R., Ling, J., Shane, M. S., Stephen, J. M., and Jung, R. E. (2012). Modeling conflict and error in the medial frontal cortex. *Human Brain Mapping*. DOI: 10.1002/hbm.21405.

McAuliffe, M. J., Lalonde, F. M., McGarry, D., Gandler, W., Csaky, K., and Trus, B. L. (2001). Medical image processing, analysis and visualization in clinical research. In: *Proceedings of the IEEE Symposium on Computer-Based Medical Systems*. DOI: 10.1109/cbms.2001.941749.

McCoy, R. C., Wakefield, J., and Akey, J. M. (2017). Impacts of Neanderthal-introgressed sequences on the landscape of human gene expression. *Cell* 168, pp. 916–927.

Mendes, N., Oligschlaeger, S., Lauckner, M. E., Golchert, J., Huntenburg, J. M., Falkiewicz, M., Ellamil, M., Krause, S., Baczkowski, B. M., Cozatl, R., Osoianu, A., Kumral, D., Pool, J., Golz, L., Dreyer, M., Haueis, P., Jost, R., Kramarenko, Y., Engen, H., Ohrnberger, K., Gorgolewski, K. J., Farrugia, N., Babayan, A., Reiter, A., Schaare, H. L., Reinelt, J., Roebbig, J., Uhlig, M., Erbey, M., Gaebler, M., Smallwood, J., Villringer, A., and Margulies, D. S. (2017). A functional connectome phenotyping dataset including cognitive state and personality measures. *bioRxiv*. DOI: 10.1038/sdata.2018.307.

Mennes, M., Biswal, B. B., Castellanos, F. X., and Milham, M. P. (2013). Making data sharing work: The FCP/INDI experience. *NeuroImage*. DOI: 10.1016/j.neuroimage.2012.10.064.

Metere, R. and Möller, H. E. (2018). Quantifying the myelin and iron contents of the brain in vivo using a linear model of relaxation. *Proceedings of the International Society for Magnetic Resonance in Medicine* 26, p. 5505.

Mewes, A. U. J., Huppi, P. S., Als, H., Rybicki, F. J., Inder, T. E., McAnulty, G. B., Mulkern, R. V., Robertson, R. L., Rivkin, M. J., Warfield, S. K., and Hüppi, P. S. (2006). Regional Brain Development in Serial Magnetic Resonance Imaging of Low-Risk Preterm Infants. *Pediatrics*. DOI: 10.1542/peds.2005-2675.

Michaely, H. J., Kramer, H., Dietrich, O., Nael, K., Lodemann, K.-P., Reiser, M. F., and Schoenberg, S. O. (2007). Intraindividual Comparison of High-Spatial-Resolution Abdominal MR Angiography at 1.5 T and 3.0 T: Initial Experience. *Radiology* 244. PMID: 17709837, pp. 907–913. DOI: 10.1148/radiol.2443061647. eprint: https://doi.org/10.1148/radiol.2443061647.

Middleton, F. A. and Strick, P. L. (1994). Anatomical evidence for cerebellar and basal ganglia involvement in higher cognitive function. *Science* 266, pp. 458–461.

Mikhael, S., Hoogendoorn, C., Valdes-Hernandez, M., and Pernet, C. (2018). A critical analysis of neuroanatomical software protocols reveals clinically relevant differences in parcellation schemes. *NeuroImage*. DOI: 10.1016/j.neuroimage.2017.02.082.

Mikl, M., Mareček, R., Hluštík, P., Pavlicová, M., Drastich, A., Chlebus, P., Brázdil, M., and Krupa, P. (2008). Effects of spatial smoothing on fMRI group inferences. *Magnetic Resonance Imaging*. DOI: 10.1016/j.mri.2007.08.006.

Milchenko, M. and Marcus, D. (2013). Obscuring surface anatomy in volumetric imaging data. *Neuroinformatics*. DOI: 10.1007/s12021-012-9160-3.

Miletić, S., Bazin, P. L., Weiskopf, N., van der Zwaag, W., Forstmann, B. U., and Trampel, R. (2020). fMRI protocol optimization for simultaneously studying small subcortical and cortical areas at 7T. *NeuroImage*. DOI: 10.1016/j.neuroimage.2020.116992.

Miletić, S., Bazin, P.-L., Isherwood, S. J. S., Keuken, M. C., Alkemade, A., and Forstmann, B. U. (2022). Charting human subcortical maturation across the adult lifespan with in vivo 7 T MRI. *NeuroImage* 249, p. 118872. DOI: 10.1016/j.neuroimage.2022.118872.

Milham, M. P., Craddock, R. C., Son, J. J., Fleischmann, M., Clucas, J., Xu, H., Koo, B., Krishnakumar, A., Biswal, B. B., Castellanos, F. X., Colcombe, S., Di Martino, A., Zuo, X. N., and Klein, A. (2018). Assessment of the impact of shared brain imaging data on the scientific literature. *Nature Communications*. DOI: 10.1038/s41467-018-04976-1.

Miller, E. K. and Cohen, J. D. (2001). An integrative theory of prefrontal cortex function. *Annual review of neuroscience* 24, pp. 167–202. DOI: 10.1146/ANNUREV.NEURO.24.1.167.

Mink, J. W. (1996). The basal ganglia: Focused selection and inhibition of competing motor programs. *Progress in Neurobiology*. DOI: 10.1016/S0301-0082(96)00042-1.

Montague, P. R. and Berns, G. S. (2002). Neural economics and the biological substrates of valuation. *Neuron* 36, pp. 265–284. DOI: 10.1016/S0896-6273(02)00974-1.

Moon, H. C., Baek, H.-M., and Park, Y. S. (2016). Comparison of 3 and 7 Tesla Magnetic Resonance Imaging of Obstructive Hydrocephalus Caused by Tectal Glioma. *Brain Tumor Research and Treatment*. DOI: 10.14791/btrt.2016.4.2.150.

Morey, R. D. and Rouder, J. N. (2015). Bayesfactor: Computation of Bayes factors for common designs. R package version 0.9.12-2. *BayesFactor: Computation of Bayes Factors for Common Designs*. DOI: 10.1007/978-3-642-21037-2.

Morris, C. M., Candy, J. M., Oakley, A. E., Bloxham, C. A., and Edwardson, J. A. (1992). Histochemical distribution of non-haem iron in the human brain. *Acta Anatomica*. DOI: 10.1159/000147312.

Morris, J. C., Weintraub, S., Chui, H. C., Cummings, J., DeCarli, C., Ferris, S., Foster, N. L., Galasko, D., Graff-Radford, N., Peskind, E. R., Beekly, D., Ramos, E. M., and Kukull, W. A. (2006). The Uniform Data Set (UDS): Clinical and cognitive variables and descriptive data from Alzheimer disease centers. *Alzheimer Disease and Associated Disorders*. DOI: 10.1097/01.wad.0000213865.09806.92.

Mosher, C. P., Mamelak, A. N., Malekmohammadi, M., Pouratian, N., and Rutishauser, U. (2021). Distinct roles of dorsal and ventral subthalamic neurons in action selection and cancellation. en. *Neuron* 109, 869–881.e6.

Mueller, S. G., Weiner, M. W., Thal, L. J., Petersen, R. C., Jack, C. R., Jagust, W., Trojanowski, J. Q., Toga, A. W., and Beckett, L. (2005). *Ways toward an early diagnosis in Alzheimer's disease: The Alzheimer's Disease Neuroimaging Initiative (ADNI)*. DOI: 10.1016/j.jalz.2005.06.003.

Mulder, M. J., Maanen, L. van, and Forstmann, B. U. (2014). Perceptual decision neurosciences - a model-based review. *Neuroscience* 277, pp. 872–884. DOI: 10.1016/j.neuroscience.2014.07.031.

Mulder, M. J., Keuken, M. C., Bazin, P. L., Alkemade, A., and Forstmann, B. U. (2019). Size and shape matter: the impact of voxel geometry on the identification of small nuclei. *PLoS ONE*. DOI: 10.1371/journal.pone.0215382.

Müller, V. I., Cieslik, E. C., Laird, A. R., Fox, P. T., Radua, J., Mataix-Cols, D., Tench, C. R., Yarkoni, T., Nichols, T. E., Turkeltaub, P. E., Wager, T. D., and Eickhoff, S. B. (2018). Ten simple rules for neuroimaging meta-analysis. *Neuroscience and Biobehavioral Reviews* 84, pp. 151–161. DOI: 10.1016/j.neubiorev.2017.11.012.

Murphy, K., Bodurka, J., and Bandettini, P. A. (2007). How long to scan? The relationship between fMRI temporal signal to noise ratio and necessary scan duration. en. *Neuroimage* 34, pp. 565–574.

Nachev, P., Kennard, C., and Husain, M. (2008). *Functional role of the supplementary and pre-supplementary motor areas*. DOI: 10.1038/nrn2478.

Nambu, A., Tokuno, H., and Takada, M. (2002). Functional significance of the cortico-subthalamo-pallidal 'hyperdirect' pathway. *Neuroscience research* 43, pp. 111–117. DOI: 10.1016/S0168-0102(02)00027-5.

Narvacan, K., Treit, S., Camicioli, R., Martin, W., and Beaulieu, C. (2017). Evolution of deep gray matter volume across the human lifespan. *Human Brain Mapping* 38, pp. 3771–3790. DOI: 10.1002/hbm.23604.

Nee, D. E., Wager, T. D., and Jonides, J. (2007). Interference resolution: Insights from a meta-analysis of neuroimaging tasks. *Cognitive, Affective, and Behavioral Neuroscience 2007 7:1* 7, pp. 1–17. DOI: 10.3758/CABN.7.1.1.

Nelson, S. M., Dosenbach, N. U., Cohen, A. L., Wheeler, M. E., Schlaggar, B. L., and Petersen, S. E. (2010). Role of the anterior insula in task-level control and focal attention. *Brain structure and function* 214, pp. 669–680.

Neumann, W. J., Schroll, H., De Almeida Marcelino, A. L., Horn, A., Ewert, S., Irmen, F., Krause, P., Schneider, G. H., Hamker, F., and Kühn, A. A. (2018). Functional segregation of basal ganglia pathways in Parkinson's disease. *Brain*. DOI: 10.1093/brain/awy206.

Niendam, T. A., Laird, A. R., Ray, K. L., Dean, Y. M., Glahn, D. C., and Carter, C. S. (2012). Meta-analytic evidence for a superordinate cognitive control network subserving diverse executive functions. *Cognitive, Affective and Behavioral Neuroscience*. DOI: 10.3758/s13415-011-0083-5.

Nigg, J. T. (2001). Is ADHD a disinhibitory disorder? *Psychological bulletin* 127, p. 571.

– (2000). On Inhibition/Disinhibition in Developmental Psychopathology: Views from Cognitive and Personality Psychology and a Working Inhibition Taxonomy. *Psychological Bulletin*. DOI: 10.1037/0033-2909.126.2.220.

Noebauer-Huhmann, I. M., Szomolanyi, P., Kronnerwetter, C., Widhalm, G., Weber, M., Nemec, S., Juras, V., Ladd, M. E., Prayer, D., and Trattnig, S. (2015). Brain tumours at 7T MRI compared to 3T—contrast effect after half and full standard contrast agent dose: initial results. *European Radiology*. DOI: 10.1007/s00330-014-3351-2.

Noël, X., Brevers, D., Hanak, C., Kornreich, C., Verbanck, P., and Verbruggen, F. (2016). On the automaticity of response inhibition in individuals with alcoholism. en. *J. Behav. Ther. Exp. Psychiatry* 51, pp. 84–91.

Nooner, K. B., Colcombe, S. J., Tobe, R. H., Mennes, M., Benedict, M. M., Moreno, A. L., Panek, L. J., Brown, S., Zavitz Stephen, T. T., Li, Q., Sikka, S., Gutman, D., Bangaru, S., Schlachter, R. T., Anwar, S. M., Hinz, C. M., Kaplan, M. S., Rachlin, A. B., Adelsberg, S., Cheung, B., Khanuja, R., Yan, C., Courtney, C. C., King, M., Wood, D., Cox, C. L., Kelly, A. M., Petkova, E., Reiss, P. T., Duan, N., Thomsen, D., Biswal, B., Coffey, B., Hoptman, M. J., Javitt, D. C., Pomara, N., Sidtis, J. J., Koplewicz, H. S., Castellanos, F. X., Leventhal, B. L., and Milham, M. P. (2012). *The NKI-Rockland sample: A model for accelerating the pace of discovery science in psychiatry*. DOI: 10.3389/fnins.2012.00152.

Notter, M., Gale, D., Herholz, P., Markello, R., Notter-Bielser, M.-L., and Whitaker, K. (2019). Atlas-Reader: A Python package to generate coordinate tables, region labels, and informative figures from statistical MRI images. *Journal of Open Source Software*. DOI: 10.21105/joss.01257.

O'Callaghan, C., Bertoux, M., and Hornberger, M. (2014). *Beyond and below the cortex: The contribution of striatal dysfunction to cognition and behaviour in neurodegeneration*. DOI: 10.1136/jnnp-2012-304558.

O'Doherty, J. P. (2014). The problem with value. *Neuroscience and biobehavioral reviews* 43, pp. 259–268. DOI: 10.1016/J.NEUBIOREV.2014.03.027.

O'Doherty, J. P., Dayan, P., Schultz, J., Deichmann, R., Friston, K. J., and Dolan, R. J. (2004). Dissociable Roles of Ventral and Dorsal Striatum in Instrumental Conditioning. *Science* 304, pp. 452–454. DOI: 10.1126/science.1094285.

Obeso, I., Wilkinson, L., Casabona, E., Bringas, M. L., Álvarez, M., Álvarez, L., Pavón, N., Rodríguez-Oroz, M. C., Macías, R., Obeso, J. A., and Jahanshahi, M. (2011). Deficits in inhibitory control and

conflict resolution on cognitive and motor tasks in Parkinson's disease. *Experimental Brain Research* 212, pp. 371–384. DOI: 10.1007/s00221-011-2758-7.

Obeso, J. A., Marin, C., Rodriguez-Oroz, C., Blesa, J., Benitez-Temiño, B., Mena-Segovia, J., Rodríguez, M., and Olanow, C. W. (2008). The basal ganglia in Parkinson's disease: Current concepts and unexplained observations. *Annals of Neurology* 64, pp. 30–46. DOI: 10.1002/ana.21481.

Ogg, R. J. and Steen, R. G. (1998). Age-related changes in brain T1 are correlated with iron concentration. *Magnetic Resonance in Medicine* 40, pp. 749–753. DOI: 10.1002/mrm.1910400516.

Oguz, I., Yaxley, R., Budin, F., Hoogstoel, M., Lee, J., Maltbie, E., Liu, W., and Crews, F. T. (2013). Comparison of Magnetic Resonance Imaging in Live vs. Post Mortem Rat Brains. *PLoS ONE*. DOI: 10.1371/journal.pone.0071027.

Okada, N., Fukunaga, M., Yamashita, F., Koshiyama, D., Yamamori, H., Ohi, K., Yasuda, Y., Fujimoto, M., Watanabe, Y., Yahata, N., et al. (2016). Abnormal asymmetries in subcortical brain volume in schizophrenia. *Molecular psychiatry* 21, pp. 1460–1466.

Pagani, E., Agosta, F., Rocca, M. A., Caputo, D., and Filippi, M. (2008). Voxel-based analysis derived from fractional anisotropy images of white matter volume changes with aging. *NeuroImage*. DOI: 10.1016/j.neuroimage.2008.03.021.

Pagliaccio, D., Barch, D. M., Bogdan, R., Wood, P. K., Lynskey, M. T., Heath, A. C., and Agrawal, A. (2015). Shared predisposition in the association between cannabis use and subcortical brain structure. *JAMA Psychiatry*. DOI: 10.1001/jamapsychiatry.2015.1054.

Pajula, J. and Tohka, J. (2014). Effects of spatial smoothing on inter-subject correlation based analysis of FMRI. *Magnetic Resonance Imaging*. DOI: 10.1016/j.mri.2014.06.001.

Pardoe, H. R., Kucharsky Hiess, R., and Kuzniecky, R. (2016). Motion and morphometry in clinical and nonclinical populations. *NeuroImage*. DOI: 10.1016/j.neuroimage.2016.05.005.

Pauli, W. M., Nili, A. N., and Tyszka, J. M. (2018). A high-resolution probabilistic in vivo atlas of human subcortical brain nuclei. *Scientific Data* 5, p. 180063. DOI: 10.1038/sdata.2018.63.

Pearson, K. (1895). Correlation coefficient. In: *Royal Society Proceedings*. Vol. 58, p. 214.

– (1904). Report on Certain Enteric Fever Inoculation Statistics. *British Medical Journal* 2, pp. 1243–1246. DOI: 10.1136/bmj.2.2309.1243.

Pham, D. L. and Bazin, P. L. (2009). *Unsupervised tissue classification*. Second Edi. Elsevier Inc., pp. 209–222. DOI: 10.1016/B978-012373904-9.50020-9.

Poldrack, R. A., Congdon, E., Triplett, W., Gorgolewski, K. J., Karlsgodt, K. H., Mumford, J. A., Sabb, F. W., Freimer, N. B., London, E. D., Cannon, T. D., and Bilder, R. M. (2016). A phenome-wide examination of neural and cognitive function. en. *Sci. Data* 3, p. 160110.

Poldrack, R. A., Barch, D. M., Mitchell, J. P., Wager, T. D., Wagner, A. D., Devlin, J. T., Cumba, C., Koyejo, O., and Milham, M. P. (2013). Towards open sharing of task-based fMRI data: The OpenfMRI project. *Frontiers in Neuroinformatics*. DOI: 10.3389/fninf.2013.00012.

Poldrack, R. A. and Gorgolewski, K. J. (2014). *Making big data open: Data sharing in neuroimaging*. DOI: 10.1038/nn.3818.

Poser, B. A., Versluis, M. J., Hoogduin, J. M., and Norris, D. G. (2006). BOLD contrast sensitivity enhancement and artifact reduction with multiecho EPI: Parallel-acquired inhomogeneity-desensitized fMRI. *Magnetic Resonance in Medicine* 55, pp. 1227–1235. DOI: 10.1002/mrm.20900.

Posse, S., Wiese, S., Gembris, D., Mathiak, K., Kessler, C., Grosse-Ruyken, M. L., Elghahwagi, B., Richards, T., Dager, S. R., and Kiselev, V. G. (1999). Enhancement of BOLD-Contrast Sensitivity by Single-Shot Multi-Echo Functional MR Imaging. *Magnetic resonance in medicine* 42, pp. 87–97.

Potvin, O., Mouiha, A., Dieumegarde, L., and Duchesne, S. (2016). Normative data for subcortical regional volumes over the lifetime of the adult human brain. *NeuroImage* 137, pp. 9–20. DOI: 10.1016/j.neuroimage.2016.05.016.

Power, J. D., Mitra, A., Laumann, T. O., Snyder, A. Z., Schlaggar, B. L., and Petersen, S. E. (2014). Methods to detect, characterize, and remove motion artifact in resting state fMRI. *NeuroImage* 84, pp. 320–341. DOI: 10.1016/j.neuroimage.2013.08.048.

Priovoulos, N., Jacobs, H. I., Ivanov, D., Uludağ, K., Verhey, F. R., and Poser, B. A. (2018). High-resolution in vivo imaging of human locus coeruleus by magnetization transfer MRI at 3T and 7T. *NeuroImage*. DOI: 10.1016/j.neuroimage.2017.07.045.

Pruessmann, K. P., Weiger, M., Scheidegger, M. B., and Boesiger, P. (1999). SENSE: Sensitivity encoding for fast MRI. *Magnetic Resonance in Medicine*. DOI: 10.1002/(SICI)1522-2594(199911)42:5<952::AID-MRM16>3.0.CO;2-S.

Puckett, A. M., Bollmann, S., Poser, B. A., Palmer, J., Barth, M., and Cunnington, R. (2018). Using multi-echo simultaneous multi-slice (SMS) EPI to improve functional MRI of the subcortical nuclei of the basal ganglia at ultra-high field (7T). *NeuroImage* 172, pp. 886–895. DOI: 10.1016/j.neuroimage.2017.12.005.

Purcell, B. A., Heitz, R. P., Cohen, J. Y., Schall, J. D., Logan, G. D., and Palmeri, T. J. (2010). Neurally constrained modeling of perceptual decision making. *Psychological Review* 117, pp. 1113–1143. DOI: 10.1037/a0020311.

Qiu, A., Crocetti, D., Adler, M., Mahone, E. M., Denckla, M. B., Miller, M. I., and Mostofsky, S. H. (2009). Basal ganglia volume and shape in children with attention deficit hyperactivity disorder. *American Journal of Psychiatry* 166, pp. 74–82.

Raaijmakers, A. J., Ipek, O., Klomp, D. W., Possanzini, C., Harvey, P. R., Lagendijk, J. J., and Van Den Berg, C. A. (2011). Design of a radiative surface coil array element at 7 T: The single-side adapted dipole antenna. *Magnetic Resonance in Medicine* 66, pp. 1488–1497. DOI: 10.1002/mrm.22886.

Rabella, M., Grasa, E., Corripio, I., Romero, S., Mananas, M. A., Antonijoan, R. M., and al., et (2016). Neurophysiological evidence of impaired self-monitoring in schizotypal personality disorder and its reversal by dopaminergic antagonism. *NeuroImage: Clinical* 11, pp. 770–779. DOI: 10.1016/j.nicl.2016.05.019.

Rae, C. L., Hughes, L. E., Weaver, C., Anderson, M. C., and Rowe, J. B. (2014). Selection and stopping in voluntary action: A meta-analysis and combined fMRI study. *NeuroImage*. DOI: 10.1016/j.neuroimage.2013.10.012.

Raj, D., Anderson, A. W., and Gore, J. C. (2001). Respiratory effects in human functional magnetic resonance imaging due to bulk susceptibility changes. *Physics in Medicine and Biology* 46, pp. 3331–3340. DOI: 10.1088/0031-9155/46/12/318.

Ramautar, J. R., Kok, A., and Ridderinkhof, K. R. (2006). Effects of stop-signal modality on the N2/P3 complex elicited in the stop-signal paradigm. en. *Biol. Psychol.* 72, pp. 96–109.

Ramos, P., Santos, A., Pinto, N. R., Mendes, R., Magalhães, T., and Almeida, A. (2014). Iron levels in the human brain: A post-mortem study of anatomical region differences and age-related changes. *Journal of Trace Elements in Medicine and Biology* 28, pp. 13–17. DOI: 10.1016/j.jtemb.2013.08.001.

Randall, L. O. (1938). Chemical Topography of the Brain. *Journal of Biological Chemistry* 124, pp. 481–488.

Ratcliff, R. and Murdock, B. B. (1976). Retrieval processes in recognition memory. *Psychological Review* 83, pp. 190–214. DOI: 10.1037/0033-295X.83.3.190.

Raud, L. and Huster, R. J. (2017). The temporal dynamics of response inhibition and their modulation by cognitive control. *Brain Topography* 30, pp. 486–501. DOI: 10.1007/s10548-017-0554-8.

Rawlings, J. O., Pantula, S. G., and Dickey, D. A. (1998). *Applied Regression Analysis*. Ed. by J. O. Rawlings, S. G. Pantula, and D. A. Dickey. Springer Texts in Statistics. New York: Springer-Verlag. DOI: 10.1007/b98890.

Ray, N. J., Jenkinson, N., Brittain, J., Holland, P., Joint, C., Nandi, D., Bain, P. G., Yousif, N., Green, A., Stein, J. S., and Aziz, T. Z. (2009). The role of the subthalamic nucleus in response inhibition: evidence from deep brain stimulation for Parkinson's disease. *Neuropsychologia* 47, pp. 2828–2834. DOI: 10.1016/J.NEUROPSYCHOLOGIA.2009.06.011.

Ray, N. J., Brittain, J.-S., Holland, P., Joundi, R. A., Stein, J. F., Aziz, T. Z., and Jenkinson, N. (2012). The role of the subthalamic nucleus in response inhibition: Evidence from local field potential recordings in the human subthalamic nucleus. *NeuroImage* 60, pp. 271–278. DOI: https://doi.org/10.1016/j.neuroimage.2011.12.035.

Ray Li, C. S., Yan, P., Sinha, R., and Lee, T. W. (2008). Subcortical processes of motor response inhibition during a stop signal task. *NeuroImage* 41, pp. 1352–1363. DOI: 10.1016/J.NEUROIMAGE.2008.04.023.

Raz, N. (2004). "The Aging Brain Observed in Vivo." In: *Cognitive Neuroscience of Aging*. Vol. 15. Oxford University Press, pp. 19–57. DOI: 10.1093/acprof:oso/9780195156744.003.0002.

Raz, N., Lindenberger, U., Rodrigue, K. M., Kennedy, K. M., Head, D., Williamson, A., Dahle, C., Gerstorf, D., and Acker, J. D. (2005). Regional brain changes in aging healthy adults: General trends, individual differences and modifiers. *Cerebral Cortex* 15, pp. 1676–1689. DOI: 10.1093/cercor/bhi044.

Raz, N. and Rodrigue, K. M. (2006). Differential aging of the brain: Patterns, cognitive correlates and modifiers. *Neuroscience and Biobehavioral Reviews* 30, pp. 730–748. DOI: 10.1016/j.neubiorev.2006.07.001.

Raz, N., Rodrigue, K. M., Kennedy, K. M., Head, D., Gunning-Dixon, F., and Acker, J. D. (2003). Differential Aging of the Human Striatum: Longitudinal Evidence. *American Journal of Neuroradiology*. DOI: 10.1016/S0140-6736(94)92338-8.

Raznahan, A., Shaw, P. W., Lerch, J. P., Clasen, L. S., Greenstein, D., Berman, R., Pipitone, J., Chakravarty, M. M., and Giedd, J. N. (2014). Longitudinal four-dimensional mapping of subcortical anatomy in human development. *Proceedings of the National Academy of Sciences* 111, pp. 1592–1597. DOI: 10.1073/pnas.1316911111.

Resnick, S. M., Pham, D. L., Kraut, M. A., Zonderman, A. B., and Davatzikos, C. (2003). Longitudinal magnetic resonance imaging studies of older adults: a shrinking brain. *The Journal of neuroscience : the official journal of the Society for Neuroscience*. DOI: 23/8/3295 [pii].

Ridderinkhof, K. R. and Van Der Molen, M. W. (1997). Mental resources, processing speed, and inhibitory control: a developmental perspective. *Biological Psychology* 45, pp. 241–261.

Rizk-Jackson, A., Stoffers, D., Sheldon, S., Kuperman, J., Dale, A., Goldstein, J., Corey-Bloom, J., Poldrack, R. A., and Aron, A. R. (2011). Evaluating imaging biomarkers for neurodegeneration in pre-symptomatic Huntington's disease using machine learning techniques. *NeuroImage* 56, pp. 788–796. DOI: 10.1016/J.NEUROIMAGE.2010.04.273.

Rolls, E. T., Joliot, M., and Tzourio-Mazoyer, N. (2015). Implementation of a new parcellation of the orbitofrontal cortex in the automated anatomical labeling atlas. *NeuroImage*. DOI: 10.1016/j.neuroimage.2015.07.075.

Rømer Thomsen, K., Blom Osterland, T., Hesse, M., and Feldstein Ewing, S. W. (2018). The intersection between response inhibition and substance use among adolescents. en. *Addict. Behav.* 78, pp. 228–230.

Rooney, W. D., Johnson, G., Li, X., Cohen, E. R., Kim, S.-G., Ugurbil, K., and Springer, C. S. (2007). Magnetic field and tissue dependencies of human brain longitudinal1H2O relaxation in vivo. *Magnetic Resonance in Medicine* 57, pp. 308–318. DOI: 10.1002/mrm.21122.

Salami, A., Rieckmann, A., Fischer, H., and Bäckman, L. (2014). A multivariate analysis of age-related differences in functional networks supporting conflict resolution. *Neuroimage* 86, pp. 150–163.

Salmon, D. P. and Filoteo, J. V. (2007). Neuropsychology of cortical versus subcortical dementia syndromes. In: *Seminars in neurology*. Vol. 27. Copyright© 2007 by Thieme Medical Publishers, Inc., 333 Seventh Avenue, New, pp. 007–021.

Salo, T., Yarkoni, T., Nichols, T. E., Poline, J.-B., Kent, J. D., Gorgolewski, K. J., Glerean, E., Bottenhorn, K. L., Bilgel, M., Wright, J., Reeders, P., Kimbler, A., Nielson, D. N., Yanes, J. A., Pérez, A., Oudyk, K. M., Jarecka, D., and Laird, A. R. (2020). neurostuff/NiMARE: 0.0.4. DOI: 10.5281/ZENODO.4396091.

Samanez-Larkin, G. R. and D'Esposito, M. (2008). Group comparisons: Imaging the aging brain. *Social Cognitive and Affective Neuroscience* 3, pp. 290–297. DOI: 10.1093/scan/nsn029.

Satterthwaite, T. D., Elliott, M. A., Gerraty, R. T., Ruparel, K., Loughead, J., Calkins, M. E., Eickhoff, S. B., Hakonarson, H., Gur, R. C., Gur, R. E., and Wolf, D. H. (2013). An improved framework for confound regression and filtering for control of motion artifact in the preprocessing of resting-state functional connectivity data. *NeuroImage* 64, pp. 240–256. DOI: 10.1016/j.neuroimage.2012.08.052.

Satterthwaite, T. D., Elliott, M. A., Ruparel, K., Loughead, J., Prabhakaran, K., Calkins, M. E., Hopson, R., Jackson, C., Keefe, J., Riley, M., Mentch, F. D., Sleiman, P., Verma, R., Davatzikos, C., Hakonarson, H., Gur, R. C., and Gur, R. E. (2014). *Neuroimaging of the Philadelphia Neurodevelopmental Cohort*. DOI: 10.1016/j.neuroimage.2013.07.064.

Savalia, N. K., Agres, P. F., Chan, M. Y., Feczko, E. J., Kennedy, K. M., and Wig, G. S. (2017). Motion-related artifacts in structural brain images revealed with independent estimates of in-scanner head motion. *Human Brain Mapping*. DOI: 10.1002/hbm.23397.

Schachar, R. and Logan, G. D. (1990). Impulsivity and inhibitory control in normal development and childhood psychopathology. *Developmental Psychology* 26, pp. 710–720. DOI: 10.1037/0012-1649.26.5.710.

Schäfer, A., Forstmann, B. U., Neumann, J., Wharton, S., Mietke, A., Bowtell, R., and Turner, R. (2012). Direct visualization of the subthalamic nucleus and its iron distribution using high-resolution susceptibility mapping. *Human Brain Mapping*. DOI: 10.1002/hbm.21404.

Schenck, J. F. and Zimmerman, E. A. (2004). High-field magnetic resonance imaging of brain iron: Birth of a biomarker? *NMR in Biomedicine* 17, pp. 433–445. DOI: 10.1002/nbm.922.

Schmahmann, J. D. (2003). Vascular syndromes of the thalamus. *Stroke* 34, pp. 2264–2278. DOI: 10.1161/01.STR.0000087786.38997.9E.

Schmidt, C. C., Timpert, D. C., Arend, I., Vossel, S., Dovern, A., Saliger, J., Karbe, H., Fink, G. R., Henik, A., and Weiss, P. H. (2018). Preserved but less efficient control of response interference after unilateral lesions of the striatum. *Frontiers in Human Neuroscience*. DOI: 10.3389/fnhum.2018.00414.

Schmidt, C. C., Timpert, D. C., Arend, I., Vossel, S., Fink, G. R., Henik, A., and Weiss, P. H. (2020). Control of response interference: caudate nucleus contributes to selective inhibition. *Scientific Reports*. DOI: 10.1038/s41598-020-77744-1.

Schmidt, R. and Berke, J. D. (2017). A Pause-then-Cancel model of stopping: evidence from basal ganglia neurophysiology. *Philosophical Transactions of the Royal Society B: Biological Sciences* 372. DOI: 10.1098/RSTB.2016.0202.

Schmierer, K., Wheeler-Kingshott, C. A., Tozer, D. J., Boulby, P. A., Parkes, H. G., Yousry, T. A., Scaravilli, F., Barker, G. J., Tofts, P. S., and Miller, D. H. (2008). Quantitative magnetic resonance of postmortem multiple sclerosis brain before and after fixation. *Magnetic Resonance in Medicine* 59, pp. 268–277. DOI: 10.1002/mrm.21487.

Schridde, U., Khubchandani, M., Motelow, J. E., Sanganahalli, B. G., Hyder, F., and Blumenfeld, H. (2008). Negative BOLD with large increases in neuronal activity. *Cerebral cortex* 18, pp. 1814–1827.

Schultz, W., Dayan, P., and Montague, P. R. (1997). A neural substrate of prediction and reward. *Science* 275, pp. 1593–1599. DOI: 10.1126/science.275.5306.1593.

Schultz, W. and Dickinson, A. (2000). Neuronal coding of prediction errors. *Annual review of neuroscience* 23, pp. 473–500. DOI: 10.1146/ANNUREV.NEURO.23.1.473.

Schwarz, G. (1978). Estimating the dimension of a model. *The Annals of Statistics* 6, pp. 461–464. DOI: 10.1214/aos/1176344136.

Seabold, S. and Perktold, J. (2010). Statsmodels: econometric and statistical modeling with Python. *9th Python in Science Conference*, pp. 57–61.

Sebastian, A., Baldermann, C., Feige, B., Katzev, M., Scheller, E., Hellwig, B., Lieb, K., Weiller, C., Tüscher, O., and Klöppel, S. (2013). Differential effects of age on subcomponents of response inhibition. *Neurobiology of Aging*. DOI: 10.1016/j.neurobiolaging.2013.03.013.

Sebastian, A., Forstmann, B. U., and Matzke, D. (2018). Towards a model-based cognitive neuroscience of stopping – a neuroimaging perspective. *Neuroscience and Biobehavioral Reviews* 90, pp. 130–136. DOI: 10.1016/J.NEUBIOREV.2018.04.011.

Sebastian, A., Jung, P., Neuhoff, J., Wibral, M., Fox, P. T., Lieb, K., Fries, P., Eickhoff, S. B., Tüscher, O., and Mobascher, A. (2016). Dissociable attentional and inhibitory networks of dorsal and ventral areas of the right inferior frontal cortex: a combined task-specific and coordinate-based meta-analytic fMRI study. *Brain Structure and Function*. DOI: 10.1007/s00429-015-0994-y.

Sebastian, A., Rössler, K., Wibral, M., Mobascher, A., Lieb, K., Jung, P., and Tüscher, O. (2017). Neural architecture of selective stopping strategies: distinct brain activity patterns are associated with attentional capture but not with outright stopping. *Journal of Neuroscience* 37, pp. 9785–9794.

Seeley, W. W., Crawford, R. K., Zhou, J., Miller, B. L., and Greicius, M. D. (2009). Neurodegenerative diseases target large-scale human brain networks. en. *Neuron* 62, pp. 42–52.

Sengupta, A., Kaule, F. R., Guntupalli, J. S., Hoffmann, M. B., Häusler, C., Stadler, J., and Hanke, M. (2016). A studyforrest extension, retinotopic mapping and localization of higher visual areas. *Scientific Data*. DOI: 10.1038/sdata.2016.93.

Serrien, D. J. and Sovijärvi-Spapé, M. M. (2013). Cognitive control of response inhibition and switching: Hemispheric lateralization and hand preference. *Brain and Cognition*. DOI: 10.1016/j.bandc.2013.04.013.

Shafto, M. A., Tyler, L. K., Dixon, M., Taylor, J. R., Rowe, J. B., Cusack, R., Calder, A. J., Marslen-Wilson, W. D., Duncan, J., Dalgleish, T., Henson, R. N., Brayne, C., Bullmore, E., Campbell, K., Cheung, T., Davis, S., Geerligs, L., Kievit, R., McCarrey, A., Price, D., Samu, D., Treder, M., Tsvetanov, K., Williams, N., Bates, L., Emery, T., Erzinçlioglu, S., Gadie, A., Gerbase, S., Georgieva, S., Hanley, C., Parkin, B., Troy, D., Allen, J., Amery, G., Amunts, L., Barcroft, A., Castle, A., Dias, C., Dowrick, J., Fair, M., Fisher, H., Goulding, A., Grewal, A., Hale, G., Hilton, A., Johnson, F., Johnston, P., Kavanagh-Williamson, T., Kwasniewska, M., McMinn, A., Norman, K., Penrose, J., Roby, F., Rowland, D., Sargeant, J., Squire, M., Stevens, B., Stoddart, A., Stone, C., Thompson, T., Yazlik, O., Barnes, D., Hillman, J., Mitchell, J., Villis, L., and Matthews, F. E. (2014). The Cambridge Centre for Ageing and Neuroscience (Cam-CAN) study protocol: A cross-sectional, lifespan, multidisciplinary examination of healthy cognitive ageing. *BMC Neurology*. DOI: 10.1186/s12883-014-0204-1.

Shaklee, P. M. (2014). *Data in brief - making your data count*. DOI: 10.1016/j.dib.2014.09.001.

Shallice, T., Stuss, D. T., Alexander, M. P., Picton, T. W., and Derkzen, D. (2008). The multiple dimensions of sustained attention. *Cortex* 44, pp. 794–805. DOI: 10.1016/J.CORTEX.2007.04.002.

Sharp, D. J., Bonnelle, V., De Boissezon, X., Beckmann, C. F., James, S. G., Patel, M. C., and Mehta, M. A. (2010). Distinct frontal systems for response inhibition, attentional capture, and error processing. *Proceedings of the National Academy of Sciences of the United States of America* 107, pp. 6106–6111. DOI: 10.1073/PNAS.1000175107.

Shen, S., Sandoval, J., Swiss, V. A., Li, J., Dupree, J., Franklin, R. J., and Casaccia-Bonnefil, P. (2008). Age-dependent epigenetic control of differentiation inhibitors is critical for remyelination efficiency. *Nature Neuroscience* 11, pp. 1024–1034. DOI: 10.1038/nn.2172.

Shenhav, A., Straccia, M. A., Musslick, S., and al., et (2018). Dissociable neural mechanisms track evidence accumulation for selection of attention versus action. *Nature Communications* 9, p. 2485. DOI: 10.1038/s41467-018-04841-1.

Shepherd, G. M. (2013). Corticostriatal connectivity and its role in disease. *Nature Reviews Neuroscience* 14, pp. 278–291. DOI: 10.1038/nrn3469.

Shepherd, T. M., Flint, J. J., Thelwall, P. E., Stanisz, G. J., Mareci, T. H., Yachnis, A. T., and Blackband, S. J. (2009). Postmortem interval alters the water relaxation and diffusion properties of rat nervous tissue - Implications for MRI studies of human autopsy samples. *NeuroImage* 44, pp. 820–826. DOI: 10.1016/j.neuroimage.2008.09.054.

Shroff, M. M., Babyn, P. S., Chavhan, G. B., Thomas, B., and Haacke, E. M. (2009). Principles, Techniques, and Applications of T2*-based MR Imaging and Its Special Applications. *RadioGraphics*. DOI: 10.1148/rg.295095034.

Siegert, S., Herrojo Ruiz, M., Brücke, C., Huebl, J., Schneider, G.-H., Ullsperger, M., and Kühn, A. A. (2014). Error signals in the subthalamic nucleus are related to post-error slowing in patients with Parkinson's disease. *Cortex* 60. Special issue: What does human intracerebral recording tell us about emotions? pp. 103–120. DOI: https://doi.org/10.1016/j.cortex.2013.12.008.

Siemonsen, S., Finsterbusch, J., Matschke, J., Lorenzen, A., Ding, X. Q., and Fiehler, J. (2008). Age-dependent normal values of T2 and T2 in brain parenchyma. In: *American Journal of Neuroradiology*. DOI: 10.3174/ajnr.A0951.

Simon, J. R. (1969). Reactions toward the source of stimulation. *Journal of experimental psychology* 81, p. 174.

Simon, J. R. and Rudell, A. P. (1967). Auditory S-R compatibility: The effect of an irrelevant cue on information processing. *Journal of Applied Psychology*. DOI: 10.1037/h0020586.

Singh, M., Fuelscher, I., He, J., Anderson, V., Silk, T. J., and Hyde, C. (2021). Inter-individual performance differences in the stop-signal task are associated with fibre-specific microstructure of the fronto-basal-ganglia circuit in healthy children. en. *Cortex* 142, pp. 283–295.

Singh, V., Pfeuffer, J., Zhao, T., and Ress, D. (2018). Evaluation of spiral acquisition variants for functional imaging of human superior colliculus at 3T field strength. *Magnetic Resonance in Medicine* 79, pp. 1931–1940.

Skippen, P., Matzke, D., Heathcote, A., Fulham, W. R., Michie, P., and Karayanidis, F. (2019). Reliability of triggering inhibitory process is a better predictor of impulsivity than SSRT. *Acta Psychologica* 192, pp. 104–117. DOI: 10.1016/j.actpsy.2018.12.010.

Slater-Hammel, A. T. (1960). Reliability, Accuracy, and Refractoriness of a Transit Reaction. *Research Quarterly. American Association for Health, Physical Education and Recreation* 31, pp. 217–228. DOI: 10.1080/10671188.1960.10613098. eprint: https://doi.org/10.1080/10671188.1960.10613098.

Smith, S. M. and Brady, J. M. (1997). SUSAN—A New Approach to Low Level Image Processing. *International Journal of Computer Vision 1997 23:1* 23, pp. 45–78. DOI: 10.1023/A:1007963824710.

Sodickson, D. K. and Manning, W. J. (1997). Simultaneous acquisition of spatial harmonics (SMASH): Fast imaging with radiofrequency coil arrays. *Magnetic Resonance in Medicine*. DOI: 10.1002/mrm.1910380414.

Song, J., Lin, H., and Liu, S. (2023). Basal ganglia network dynamics and function: Role of direct, indirect and hyper-direct pathways in action selection. *Network: Computation in Neural Systems*, pp. 1–38.

Song, S., Zilverstand, A., Song, H., D'Oleire Uquillas, F., Wang, Y., Xie, C., Cheng, L., and Zou, Z. (2017). The influence of emotional interference on cognitive control: A meta-analysis of neuroimaging studies using the emotional Stroop task. *Scientific Reports*. DOI: 10.1038/s41598-017-02266-2.

Springer, E., Dymerska, B., Cardoso, P. L., Robinson, S. D., Weisstanner, C., Wiest, R., Schmitt, B., and Trattnig, S. (2016). Comparison of Routine Brain Imaging at 3 T and 7 T. *Investigative Radiology*. DOI: 10.1097/RLI.0000000000000256.

Stafford, J. L., Albert, M. S., Naeser, M. A., Sandor, T., and Garvey, A. J. (1988). Age-Related Differences in Computed Tomographic Scan Measurements. *Archives of Neurology* 45, pp. 409–415. DOI: 10.1001/archneur.1988.00520280055016.

Steen, R. G., Reddick, W. E., and Ogg, R. J. (2000). More than meets the eye: Significant regional heterogeneity in human cortical T1. *Magnetic Resonance Imaging* 18, pp. 361–368. DOI: 10.1016/S0730-725X(00)00123-5.

Stevenson, N. R., Innes, R. J., Boag, R. J., Miletić, S., Isherwood, S. J. S., Trutti, A. C., Heathcote, A., and Forstmann, B. U. (2023). Joint modelling of latent cognitive mechanisms shared across decision-making domains. *submitted*.

Strike, L. T., Hansell, N. K., Couvy-Duchesne, B., Thompson, P. M., De Zubicaray, G. I., McMahon, K. L., and Wright, M. J. (2019). Genetic complexity of cortical structure: Differences in genetic and environmental factors influencing cortical surface area and thickness. *Cerebral Cortex*. DOI: 10.1093/cercor/bhy002.

Stroop, J. R. (1935). Studies of interference in serial verbal reactions. *Journal of Experimental Psychology*. DOI: 10.1037/h0054651.

Stüber, C., Morawski, M., Schäfer, A., Labadie, C., Wähnert, M., Leuze, C., Streicher, M., Barapatre, N., Reimann, K., Geyer, S., Spemann, D., and Turner, R. (2014). Myelin and iron concentration in the human brain: A quantitative study of MRI contrast. *NeuroImage* 93, pp. 95–106. DOI: 10.1016/j.neuroimage.2014.02.026.

Stucht, D., Danishad, K. A., Schulze, P., Godenschweger, F., Zaitsev, M., and Speck, O. (2015). Highest resolution in vivo human brain MRI using prospective motion correction. *PLoS ONE*. DOI: 10.1371/journal.pone.0133921.

Sudlow, C., Gallacher, J., Allen, N., Beral, V., Burton, P., Danesh, J., Downey, P., Elliott, P., Green, J., Landray, M., Liu, B., Matthews, P., Ong, G., Pell, J., Silman, A., Young, A., Sprosen, T., Peakman, T., and Collins, R. (2015). UK Biobank: An Open Access Resource for Identifying the Causes of a Wide Range of Complex Diseases of Middle and Old Age. *PLoS Medicine*. DOI: 10.1371/journal.pmed.1001779.

Sul, J. H., Kim, H., Huh, N., Lee, D., and Jung, M. W. (2010). Distinct roles of rodent orbitofrontal and medial prefrontal cortex in decision making. *Neuron* 66, pp. 449–460. DOI: 10.1016/J.NEURON.2010.03.033.

Sullivan, E. V., Rosenbloom, M., Serventi, K. L., and Pfefferbaum, A. (2004). Effects of age and sex on volumes of the thalamus, pons, and cortex. *Neurobiology of Aging* 25, pp. 185–192. DOI: 10.1016/S0197-4580(03)00044-7.

Sutton, R. S., Barto, A. G., et al. (1998). *Introduction to reinforcement learning*. Vol. 135. MIT press Cambridge.

Swann, N., Tandon, N., Canolty, R., Ellmore, T. M., McEvoy, L. K., Dreyer, S., DiSano, M., and Aron, A. R. (2009). Intracranial EEG reveals a time- and frequency-specific role for the right inferior frontal gyrus and primary motor cortex in stopping initiated responses. *The Journal of neuroscience : the official journal of the Society for Neuroscience* 29, pp. 12675–12685. DOI: 10.1523/JNEUROSCI.3359-09.2009.

Swick, D., Ashley, V., and Turken, U. (2011). Are the neural correlates of stopping and not going identical? Quantitative meta-analysis of two response inhibition tasks. *NeuroImage*. DOI: 10.1016/j.neuroimage.2011.02.070.

Tallantyre, E. C., Morgan, P. S., Dixon, J. E., Al-Radaideh, A. M. I., Brookes, M. J., Evangelou, N., and Morris, P. G. (2009). A comparison of 3T and 7T in the detection of small parenchymal veins within MS lesions. *Investigative radiology*. DOI: 10.1097/RLI.0b013e3181b4c144.

Tannock, R., Schachar, R. J., Carr, R. P., Chajczyk, D., and Logan, G. D. (1989). Effects of methylphenidate on inhibitory control in hyperactive children. *Journal of Abnormal Child Psychology* 17, pp. 473–491. DOI: 10.1007/BF00913735.

Tardif, C. L., Steele, C. J., Lampe, L., Bazin, P. L., Ragert, P., Villringer, A., and Gauthier, C. J. (2017). Investigation of the confounding effects of vasculature and metabolism on computational anatomy studies. *NeuroImage* 149, pp. 233–243. DOI: 10.1016/j.neuroimage.2017.01.025.

Tardif, C. L., Schäfer, A., Trampel, R., Villringer, A., Turner, R., and Bazin, P. L. (2016). Open Science CBS Neuroimaging Repository: Sharing ultra-high-field MR images of the brain. *NeuroImage*. DOI: 10.1016/j.neuroimage.2015.08.042.

Tatu, L., Moulin, T., Bogousslavsky, J., and Duvernoy, H. (1998). Arterial territories of the human brain: Cerebral hemispheres. *Neurology* 50, pp. 1699–1708.

Taylor, A. J., Kim, J.-H., and Ress, D. (2018). Characterization of the hemodynamic response function across the majority of human cerebral cortex. *Neuroimage* 173, pp. 322–331.

Taylor, J. R., Williams, N., Cusack, R., Auer, T., Shafto, M. A., Dixon, M., Tyler, L. K., Cam-CAN, and Henson, R. N. (2017). The Cambridge Centre for Ageing and Neuroscience (Cam-CAN) data repository: Structural and functional MRI, MEG, and cognitive data from a cross-sectional adult lifespan sample. *NeuroImage*. DOI: 10.1016/j.neuroimage.2015.09.018.

Team R. Core. (2019). R: A language and environment for statistical computing. *Industrial and Commercial Training*. DOI: 10.1108/eb003648.

Tennyson, S. S., Brockett, A. T., Hricz, N. W., Bryden, D. W., and Roesch, M. R. (2018). Firing of putative dopamine neurons in ventral tegmental area is modulated by probability of success during performance of a stop-change task. en. *eNeuro* 5.

Tian, Y., Margulies, D. S., Breakspear, M., and Zalesky, A. (2020). Topographic organization of the human subcortex unveiled with functional connectivity gradients. *Nature Neuroscience* 23, pp. 1421–1432. DOI: 10.1038/s41593-020-00711-6.

Tinaz, S., Courtney, M. G., and Stern, C. E. (2011). Focal cortical and subcortical atrophy in early Parkinson's disease. *Movement Disorders* 26, pp. 436–441.

Tobia, M. J., Guo, R., Gläscher, J., Schwarze, U., Brassen, S., Büchel, C., Obermayer, K., and Sommer, T. (2016). Altered behavioral and neural responsiveness to counterfactual gains in the elderly. *Cognitive, Affective and Behavioral Neuroscience* 16, pp. 457–472. DOI: 10.3758/s13415-016-0406-7.

Torrisi, S., Chen, G., Glen, D., Bandettini, P. A., Baker, C. I., Reynolds, R., Yen-Ting Liu, J., Leshin, J., Balderston, N., Grillon, C., and Ernst, M. (2018). Statistical power comparisons at 3T and 7T with a GO / NOGO task. *NeuroImage*. DOI: 10.1016/j.neuroimage.2018.03.071.

Tovi, M. and Ericsson, A. (1992). Measurements of T1 and T2 over time in formalin-fixed human whole-brain specimens. *Acta Radiologica* 33, pp. 400–404. DOI: 10.1080/02841859209172021.

Treiber, J. M., White, N. S., Steed, T. C., Bartsch, H., Holland, D., Farid, N., McDonald, C. R., Carter, B. S., Dale, A. M., and Chen, C. C. (2016). Characterization and Correction of Geometric Distortions in 814 Diffusion Weighted Images. *PLOS ONE* 11. Ed. by J. Najbauer, e0152472. DOI: 10.1371/journal.pone.0152472.

Trutti, A. C., Fontanesi, L., Mulder, M. J., Bazin, P.-L., Hommel, B., and Forstmann, B. U. (2021). A probabilistic atlas of the human ventral tegmental area (VTA) based on 7 Tesla MRI data. *Brain Structure and Function*. DOI: 10.1007/s00429-021-02231-w.

Trutti, A. C., Mulder, M. J., Hommel, B., and Forstmann, B. U. (2019). Functional neuroanatomical review of the ventral tegmental area. *NeuroImage*. DOI: 10.1016/j.neuroimage.2019.01.062.

Tullo, S., Patel, R., Devenyi, G. A., Salaciak, A., Bedford, S. A., Farzin, S., Wlodarski, N., Tardif, C. L., Breitner, J. C., and Chakravarty, M. M. (2019). MR-based age-related effects on the striatum, globus pallidus, and thalamus in healthy individuals across the adult lifespan. *Human Brain Mapping* 40, pp. 5269–5288. DOI: 10.1002/hbm.24771.

Turkeltaub, P. E., Eden, G. F., Jones, K. M., and Zeffiro, T. A. (2002). Meta-analysis of the functional neuroanatomy of single-word reading: Method and validation. *NeuroImage*. DOI: 10.1006/nimg.2002.1131.

Turkeltaub, P. E., Eickhoff, S. B., Laird, A. R., Fox, M., Wiener, M., and Fox, P. (2012). Minimizing within-experiment and within-group effects in activation likelihood estimation meta-analyses. *Human Brain Mapping*. DOI: 10.1002/hbm.21186.

Turner, B. M. (2019). Toward a Common Representational Framework for Adaptation. *Psychological Review*. DOI: 10.1037/rev0000148.

Turner, B. M., Wang, T., and Merkle, E. C. (2017a). Factor analysis linking functions for simultaneously modeling neural and behavioral data. *NeuroImage* 153, pp. 28–48. DOI: 10.1016/j.neuroimage.2017.03.020.

Turner, B. M., Wang, T., and Merkle, E. C. (2017b). Factor analysis linking functions for simultaneously modeling neural and behavioral data. *NeuroImage* 153, pp. 28–48. DOI: 10.1016/j.neuroimage.2017.03.044.

Tustison, N. J., Avants, B. B., Cook, P. A., Zheng, Y., Egan, A., Yushkevich, P. A., and Gee, J. C. (2010). N4ITK: improved N3 bias correction. *IEEE transactions on medical imaging* 29, pp. 1310–1320. DOI: 10.1109/TMI.2010.2046908.

Uddin, L. Q. (2015). Salience processing and insular cortical function and dysfunction. *Nature Reviews Neuroscience* 16, pp. 55–61. DOI: 10.1038/nrn3857.

Uddin, M. N., Figley, T. D., Marrie, R. A., and Figley, C. R. (2018). Can T1w/T2w ratio be used as a myelin-specific measure in subcortical structures? Comparisons between FSE-based T1w/T2w ratios, GRASE-based T1w/T2w ratios and multi-echo GRASE-based myelin water fractions. *NMR in Biomedicine* 31, pp. 1–11. DOI: 10.1002/nbm.3868.

Uddin, M. N., Figley, T. D., Solar, K. G., Shatil, A. S., and Figley, C. R. (2019). Comparisons between multi-component myelin water fraction, T1w/T2w ratio, and diffusion tensor imaging measures in healthy human brain structures. *Scientific Reports* 9, pp. 1–17. DOI: 10.1038/s41598-019-39199-x.

Uğurbil, K., Xu, J., Auerbach, E. J., Moeller, S., Vu, A. T., Duarte-Carvajalino, J. M., Lenglet, C., Wu, X., Schmitter, S., Van de Moortele, P. F., et al. (2013). Pushing spatial and temporal resolution for functional and diffusion MRI in the Human Connectome Project. *Neuroimage* 80, pp. 80–104.

Utter, A. A. and Basso, M. A. (2008). *The basal ganglia: An overview of circuits and function*. DOI: 10.1016/j.neubiorev.2006.11.003.

Van de Moortele, P.-F., Akgun, C., Adriany, G., Moeller, S., Ritter, J., Collins, C. M., Smith, M. B., Vaughan, J. T., and Ugurbil, K. (2005). B1 destructive interferences and spatial phase patterns at 7 T with a head transceiver array coil. *Magnetic Resonance in Medicine* 54, pp. 1503–1518. DOI: 10.1002/mrm.20667.

van der Zwaag, W., Francis, S., Head, K., Peters, A., Gowland, P., Morris, P., and Bowtell, R. (2009). fMRI at 1.5, 3 and 7 T: Characterising BOLD signal changes. *NeuroImage*. DOI: 10.1016/j.neuroimage.2009.05.015.

van der Zwaag, W., Schaefer, A., Marques, J. P., Turner, R., and Trampel, R. (2016). Recent applications of UHF-MRI in the study of human brain function and structure: a review. *NMR in Biomedicine* 29, pp. 1274–1288.

Van Erp, T. G., Hibar, D. P., Rasmussen, J. M., Glahn, D. C., Pearlson, G. D., Andreassen, O. A., Agartz, I., Westlye, L. T., Haukvik, U. K., Dale, A. M., et al. (2016). Subcortical brain volume abnormalities in 2028 individuals with schizophrenia and 2540 healthy controls via the ENIGMA consortium. *Molecular psychiatry* 21, pp. 547–553.

Van Essen, D. C., Smith, S. M., Barch, D. M., Behrens, T. E., Yacoub, E., and Ugurbil, K. (2013). The WU-Minn Human Connectome Project: An overview. *NeuroImage* 80, pp. 62–79. DOI: 10.1016/j.neuroimage.2013.05.041.

Van Veen, V. and Carter, C. S. (2005). Separating semantic conflict and response conflict in the Stroop task: a functional MRI study. *NeuroImage* 27, pp. 497–504. DOI: 10.1016/J.NEUROIMAGE.2005.04.042.

Vanderhasselt, M. A., Raedt, R. de, and Baeken, C. (2009). Dorsolateral prefrontal cortex and Stroop performance: Tackling the lateralization. *Psychonomic Bulletin and Review*. DOI: 10.3758/PBR.16.3.609.

Vaughan, J. T., Garwood, M., Collins, C. M., Liu, W., Delabarre, L., Adriany, G., Andersen, P., Merkle, H., Goebel, R., Smith, M. B., and Ugurbil, K. (2001). 7T vs. 4T: RF power, homogeneity, and signal-to-noise comparison in head images. *Magnetic Resonance in Medicine*. DOI: 10.1002/mrm.1156.

Verbruggen, F., Aron, A. R., Band, G. P., Beste, C., Bissett, P. G., Brockett, A. T., Brown, J. W., Chamberlain, S. R., Chambers, C. D., Colonius, H., Colzato, L. S., Corneil, B. D., Coxon, J. P., Dupuis, A., Eagle, D. M., Garavan, H., Greenhouse, I., Heathcote, A., Huster, R. J., Jahfari, S., Kenemans, J. L., Leunissen, I., Li, C. S. R., Logan, G. D., Matzke, D., Morein-Zamir, S., Murthy, A., Paré, M., Poldrack, R. A., Ridderinkhof, K. R., Robbins, T. W., Roesch, M., Rubia, K., Schachar, R. J., Schall, J. D., Stock, A. K., Swann, N. C., Thakkar, K. N., Van Der Molen, M. W., Vermeylen, L., Vink, M., Wessel, J. R., Whelan, R., Zandbelt, B. B., and Boehler, C. N. (2019). A consensus guide to capturing the ability to inhibit actions and impulsive behaviors in the stop-signal task. *eLife*. DOI: 10.7554/eLife.46323.

Verbruggen, F., Chambers, C. D., and Logan, G. D. (2013). Fictitious inhibitory differences: how skewness and slowing distort the estimation of stopping latencies. *Psychological Science* 24, pp. 352–362. DOI: 10.1177/0956797612457390.

Verheij, R. A., Curcin, V., Delaney, B. C., and McGilchrist, M. M. (2018). Possible Sources of Bias in Primary Care Electronic Health Record Data Use and Reuse. *Journal of medical Internet research*. DOI: 10.2196/jmir.9134.

Vermunt, M. W., Tan, S. C., Castelijns, B., Geeven, G., Reinink, P., De Bruijn, E., Kondova, I., Persengiev, S., Bank, N. B., and Bontrop, R. (2016). Epigenomic annotation of gene regulatory alterations during evolution of the primate brain. *Nature neuroscience* 19, pp. 494–503.

Veroude, K., Jolles, J., Croiset, G., and Krabbendam, L. (2013). Changes in neural mechanisms of cognitive control during the transition from late adolescence to young adulthood. *Developmental Cognitive Neuroscience*. DOI: 10.1016/j.dcn.2012.12.002.

Visser, E., Keuken, M. C., Forstmann, B. U., and Jenkinson, M. (2016). Automated segmentation of the substantia nigra, subthalamic nucleus and red nucleus in 7 T data at young and old age. *Neuroimage* 139, pp. 324–336.

Wade, A. R. (2002). The negative BOLD signal unmasked. *Neuron* 36, pp. 993–995.

Wagenmakers, E.-J. and Farrell, S. (2004). AIC model selection using Akaike weights. *Psychonomic Bulletin Review* 11, pp. 192–196. DOI: 10.3758/bf03206482.

Walhovd, K. B., Fjell, A. M., Giedd, J., Dale, A. M., and Brown, T. T. (2016). Through Thick and Thin: A Need to Reconcile Contradictory Results on Trajectories in Human Cortical Development. *Cerebral Cortex* 27, pp. 1–10. DOI: 10.1093/cercor/bhv301.

Walhovd, K. B., Fjell, A. M., Reinvang, I., Lundervold, A., Dale, A. M., Eilertsen, D. E., Quinn, B. T., Salat, D., Makris, N., and Fischl, B. (2005). Effects of age on volumes of cortex, white matter and subcortical structures. *Neurobiology of Aging* 26, pp. 1261–1270. DOI: 10.1016/j.neurobiolaging.2005.05.020.

Walhovd, K. B., Westlye, L. T., Amlien, I., Espeseth, T., Reinvang, I., Raz, N., Agartz, I., Salat, D. H., Greve, D. N., Fischl, B., Dale, A. M., and Fjell, A. M. (2011). Consistent neuroanatomical age-related volume differences across multiple samples. *Neurobiology of Aging* 32, pp. 916–932. DOI: 10.1016/j.neurobiolaging.2009.05.013.

Wall, M. B., Walker, R., and Smith, A. T. (2009). Functional imaging of the human superior colliculus: An optimised approach. *Neuroimage* 47, pp. 1620–1627. DOI: 10.1016/j.neuroimage.2009.05.094.

Wang, J., Yang, Y., Fan, L., Xu, J., Li, C., Liu, Y., Fox, P. T., Eickhoff, S. B., Yu, C., and Jiang, T. (2015). Convergent functional architecture of the superior parietal lobule unraveled with multimodal neuroimaging approaches. *Human Brain Mapping*. DOI: 10.1002/hbm.22626.

Wang, L., Alpert, K. I., Calhoun, V. D., Cobia, D. J., Keator, D. B., King, M. D., Kogan, A., Landis, D., Tallis, M., Turner, M. D., Potkin, S. G., Turner, J. A., and Ambite, J. L. (2016). SchizConnect: Mediating neuroimaging databases on schizophrenia and related disorders for large-scale integration. *NeuroImage*. DOI: 10.1016/j.neuroimage.2015.06.065.

Wang, Q., Xu, X., and Zhang, M. (2010). Normal aging in the basal ganglia evaluated by eigenvalues of diffusion tensor imaging. *American Journal of Neuroradiology* 31, pp. 516–520. DOI: 10.3174/ajnr.A1862.

Wang, S., Peterson, D. J., Gatenby, J. C., Li, W., Grabowski, T. J., and Madhyastha, T. M. (2017). Evaluation of Field Map and Nonlinear Registration Methods for Correction of Susceptibility Artifacts in Diffusion MRI. *Frontiers in Neuroinformatics* 11. DOI: 10.3389/fninf.2017.00017.

Wang, Y., Xu, Q., Luo, J., Hu, M., and Zuo, C. (2019). Effects of age and sex on subcortical volumes. *Frontiers in Aging Neuroscience* 11, pp. 1–12. DOI: 10.3389/fnagi.2019.00259.

Ward, R. J., Zucca, F. A., Duyn, J. H., Crichton, R. R., and Zecca, L. (2014). The role of iron in brain ageing and neurodegenerative disorders. *The Lancet Neurology* 13, pp. 1045–1060. DOI: 10.1016/S1474-4422(14)70117-6.

Wei, D., Zhuang, K., Ai, L., Chen, Q., Yang, W., Liu, W., Wang, K., Sun, J., and Qiu, J. (2018). Data Descriptor: Structural and functional brain scans from the cross-sectional Southwest University adult lifespan dataset. *Scientific Data*. DOI: 10.1038/sdata.2018.134.

Weiner, M. W., Veitch, D. P., Aisen, P. S., Beckett, L. A., Cairns, N. J., Cedarbaum, J., Donohue, M. C., Green, R. C., Harvey, D., Jack, C. R., Jagust, W., Morris, J. C., Petersen, R. C., Saykin, A. J., Shaw, L., Thompson, P. M., Toga, A. W., and Trojanowski, J. Q. (2015). *Impact of the Alzheimer's Disease Neuroimaging Initiative, 2004 to 2014*. DOI: 10.1016/j.jalz.2015.04.005.

Weiskopf, N., Mohammadi, S., Lutti, A., and Callaghan, M. F. (2015). Advances in MRI-based computational neuroanatomy: From morphometry to in-vivo histology. *Current Opinion in Neurology* 28, pp. 313–322. DOI: 10.1097/WCO.0000000000000222.

Wendelken, C., Ditterich, J., Bunge, S. A., and Carter, C. S. (2009). Stimulus and response conflict processing during perceptual decision making. *Cognitive, Affective and Behavioral Neuroscience*. DOI: 10.3758/CABN.9.4.434.

Wessel, J. R., Ghahremani, A., Udupa, K., Saha, U., Kalia, S. K., Hodaie, M., Lozano, A. M., Aron, A. R., and Chen, R. (2016a). Stop-related subthalamic beta activity indexes global motor suppression in Parkinson's disease. *Movement Disorders* 31, pp. 1846–1853.

Wessel, J. R., Jenkinson, N., Brittain, J.-S., Voets, S. H., Aziz, T. Z., and Aron, A. R. (2016b). Surprise disrupts cognition via a fronto-basal ganglia suppressive mechanism. *Nature communications* 7, pp. 1–10.

Wessel, J. R. (2018). Prepotent motor activity and inhibitory control demands in different variants of the go/no-go paradigm. *Psychophysiology* 55, e12871. DOI: https://doi.org/10.1111/psyp.12871. eprint: https://onlinelibrary.wiley.com/doi/pdf/10.1111/psyp.12871.

Wessel, J. R. and Aron, A. R. (2013). Unexpected events induce motor slowing via a brain mechanism for action-stopping with global suppressive effects. *The Journal of neuroscience : the official journal of the Society for Neuroscience* 33, pp. 18481–18491. DOI: 10.1523/JNEUROSCI.3456-13.2013.

– (2017). On the globality of motor suppression: unexpected events and their influence on behavior and cognition. *Neuron* 93, p. 259. DOI: 10.1016/J.NEURON.2016.12.013.

Wessel, J. R., Jenkinson, N., Brittain, J. S., Voets, S. H., Aziz, T. Z., and Aron, A. R. (2016c). Surprise disrupts cognition via a fronto-basal ganglia suppressive mechanism. *Nature Communications* 7. DOI: 10.1038/ncomms11195.

Wessel, J. R., Waller, D. A., and Greenlee, J. D. (2019). Non-selective inhibition of inappropriate motor-tendencies during response-conflict by a fronto-subthalamic mechanism. *eLife*. DOI: 10.7554/eLife.42959.

West, K. L., Zuppichini, M. D., Turner, M. P., Sivakolundu, D. K., Zhao, Y., Abdelkarim, D., Spence, J. S., and Rypma, B. (2019). BOLD hemodynamic response function changes significantly with healthy aging. *NeuroImage*. DOI: 10.1016/j.neuroimage.2018.12.012.

Whelan, R., Conrod, P. J., Poline, J. B., Lourdusamy, A., Banaschewski, T., Barker, G. J., Bellgrove, M. A., Büchel, C., Byrne, M., Cummins, T. D., Fauth-Bühler, M., Flor, H., Gallinat, J., Heinz, A., Ittermann, B., Mann, K., Martinot, J. L., Lalor, E. C., Lathrop, M., Loth, E., Nees, F., Paus, T., Rietschel, M., Smolka, M. N., Spanagel, R., Stephens, D. N., Struve, M., Thyreau, B., Vollstaedt-Klein, S., Robbins, T. W., Schumann, G., and Garavan, H. (2012). Adolescent impulsivity phenotypes characterized by distinct brain networks. *Nature Neuroscience*. DOI: 10.1038/nn.3092.

Wiecki, T. V. and Frank, M. J. (2013). A computational model of inhibitory control in frontal cortex and basal ganglia. *Psychological Review*. DOI: 10.1037/a0031542. arXiv: 1112.0778.

Wiggins, G. C., Zhang, B., Lattanzi, R., Chen, G., and Sodickson, D. (2012). The electric dipole array: an attempt to match the ideal current pattern for central SNR at 7 Tesla. *Proceedings of the International Society for Magnetic Resonance in Medicine* 20, p. 541.

Wildenberg, W. P. M. van den, Boxtel, G. J. M. van, Molen, M. W. van der, Bosch, D. A., Speelman, J. D., and Brunia, C. H. M. (2006). Stimulation of the subthalamic region facilitates the selection and inhibition of motor responses in Parkinson's disease. *Journal of Cognitive Neuroscience* 18, pp. 626–636. DOI: 10.1162/jocn.2006.18.4.626.

Wildenberg, W. P. M. van den, Burle, B., Vidal, F., Molen, M. W. van der, Ridderinkhof, K. R., and Hasbroucq, T. (2010). Mechanisms and dynamics of cortical motor inhibition in the stop-signal paradigm: a TMS study. *Journal of Cognitive Neuroscience* 22, pp. 225–239. DOI: 10.1162/jocn.2009.21118.

Wilson, S. (1912). PROGRESSIVE LENTICULAR DEGENERATION: A FAMILIAL NERVOUS DISEASE ASSOCIATED WITH CIRRHOSIS OF THE LIVER. *Brain* 34.

Wimmer, R. D., Schmitt, L. I., Davidson, T. J., Nakajima, M., Deisseroth, K., and Halassa, M. M. (2015). Thalamic control of sensory selection in divided attention. *Nature*. DOI: 10.1038/nature15398.

Wise, R. G., Ide, K., Poulin, M. J., and Tracey, I. (2004). Resting fluctuations in arterial carbon dioxide induce significant low frequency variations in BOLD signal. *NeuroImage* 21, pp. 1652–1664. DOI: 10.1016/j.neuroimage.2003.11.025.

Wolpe, N., Hezemans, F. H., Rae, C. L., Zhang, J., and Rowe, J. B. (2022). The pre-supplementary motor area achieves inhibitory control by modulating response thresholds. *cortex* 152, pp. 98–108.

Woo, C. W., Krishnan, A., and Wager, T. D. (2014). Cluster-extent based thresholding in fMRI analyses: Pitfalls and recommendations. *NeuroImage*. DOI: 10.1016/j.neuroimage.2013.12.058.

Woolrich, M. W., Ripley, B. D., Brady, M., and Smith, S. M. (2001). Temporal autocorrelation in univariate linear modeling of FMRI data. *NeuroImage* 14, pp. 1370–1386. DOI: 10.1006/NIMG.2001.0931.

Wouwe, N. C. van, Pallavaram, S. S., Phibbs, F. T., Martinez-Ramirez, D., Neimat, J. S., Dawant, B. M., et al. (2017). Focused stimulation of dorsal subthalamic nucleus improves reactive inhibitory control of action impulses. *Neuropsychologia* 99, pp. 37–47. DOI: 10.1016/j.neuropsychologia.2017.02.016.

Xu, B., Levy, S., Butman, J., Pham, D., Cohen, L. G., and Sandrini, M. (2015). Effect of foreknowledge on neural activity of primary go responses relates to response stopping and switching. *Frontiers in Human Neuroscience* 9.

Xu, J., Moeller, S., Strupp, J., Auerbach, E. J., Chen, L., Feinberg, D. A., and Ugurbil, K. (2012). Highly Accelerated Whole Brain Imaging Using Aligned-Blipped-Controlled-aliasing Multiband EPI. *ISMRM proceedings* 5, p. 2306.

Xu, M., Xu, G., and Yang, Y. (2016). Neural systems underlying emotional and non-emotional interference processing: An ALE meta-analysis of functional neuroimaging studies. *Frontiers in Behavioral Neuroscience*. DOI: 10.3389/fnbeh.2016.00220.

Ye, H., Deyle, E. R., Gilarranz, L. J., and Sugihara, G. (2015). Distinguishing time-delayed causal interactions using convergent cross mapping. *Scientific Reports* 5, pp. 1–9. DOI: 10.1038/srep14750.

Ye, R., Rua, C., O'Callaghan, C., Jones, P. S., Hezemans, F. H., Kaalund, S. S., Tsvetanov, K. A., Rodgers, C. T., Williams, G., Passamonti, L., and Rowe, J. B. (2021). An in vivo probabilistic atlas of the human locus coeruleus at ultra-high field. *NeuroImage* 225, p. 117487. DOI: 10.1016/j.neuroimage.2020.117487.

Yekutieli, D. and Benjamini, Y. (1999). Resampling-based false discovery rate controlling multiple test procedures for correlated test statistics. *Journal of Statistical Planning and Inference* 82, pp. 171–196. DOI: 10.1016/S0378-3758(99)00041-5.

Yoon, J. H., Cui, E. D. B., Minzenberg, M. J., and Carter, C. S. (2019). Subthalamic nucleus activation occurs early during stopping and is associated with trait impulsivity. en. *J. Cogn. Neurosci.* 31, pp. 510–521.

Yousaf, M., Kumar, M., Ramakrishnaiah, R., Vanhemert, R., and Angtuaco, E. (2009). Atypical MRI features involving the brain in Wilson's disease. *Radiology case reports* 4, p. 312.

Yu, B., Li, L., Guan, X., Xu, X., Liu, X., Yang, Q., Wei, H., Zuo, C., and Zhang, Y. (2021). HybraPD atlas: Towards precise subcortical nuclei segmentation using multimodality medical images in patients with Parkinson disease. *Human brain mapping* 42, pp. 4399–4421.

Yu, F., Huang, Y., Chen, T., Wang, X., Guo, Y., Fang, Y., and Zhang, L. (2022). Repetitive transcranial magnetic stimulation promotes response inhibition in patients with major depression during the

stop-signal task. *Journal of Psychiatric Research* 151, pp. 427–438. DOI: 10.1016/j.jpsychires.2021.11.058.

Zaitsev, M., Akin, B., LeVan, P., and Knowles, B. R. (2017). Prospective motion correction in functional MRI. *NeuroImage* 154, pp. 33–42. DOI: 10.1016/j.neuroimage.2016.11.014.

Zandbelt, B. B. and Vink, M. (2010). On the role of the striatum in response inhibition. *PLoS ONE*. DOI: 10.1371/journal.pone.0013848.

Zavala, B., Brittain, J.-S., Jenkinson, N., Ashkan, K., Foltynie, T., Limousin, P., Zrinzo, L., Green, A. L., Aziz, T., Zaghloul, K., and Brown, P. (2013). Subthalamic Nucleus Local Field Potential Activity during the Eriksen Flanker Task Reveals a Novel Role for Theta Phase during Conflict Monitoring. *Journal of Neuroscience* 33, pp. 14758–14766. DOI: 10.1523/JNEUROSCI.1036-13.2013. eprint: https://www.jneurosci.org/content/33/37/14758.full.pdf.

Zavala, B. A., Tan, H., Little, S., Ashkan, K., Hariz, M., Foltynie, T., Zrinzo, L., Zaghloul, K. A., and Brown, P. (2014). Midline Frontal Cortex Low-Frequency Activity Drives Subthalamic Nucleus Oscillations during Conflict. *Journal of Neuroscience* 34, pp. 7322–7333. DOI: 10.1523/JNEUROSCI.1169-14.2014. eprint: https://www.jneurosci.org/content/34/21/7322.full.pdf.

Zecca, L., Youdim, M. B., Riederer, P., Connor, J. R., and Crichton, R. R. (2004). *Iron, brain ageing and neurodegenerative disorders*. DOI: 10.1038/nrn1537.

Zhang, F. and Iwaki, S. (2020). Correspondence between effective connections in the stop-signal task and microstructural correlations. en. *Front. Hum. Neurosci.* 14, p. 279.

Zhang, H., Eppes, A., Beatty-Martínez, A., Navarro-Torres, C., and Diaz, M. T. (2018). Task difficulty modulates brain-behavior correlations in language production and cognitive control: Behavioral and fMRI evidence from a phonological go/no-go picture-naming paradigm. *Cognitive, Affective and Behavioral Neuroscience*. DOI: 10.3758/s13415-018-0616-2.

Zhang, L., Sun, J., Sun, B., Luo, Q., and Gong, H. (2014). Studying hemispheric lateralization during a Stroop task through near-infrared spectroscopy-based connectivity. *Journal of Biomedical Optics*. DOI: 10.1117/1.jbo.19.5.057012.

Zhang, R., Geng, X., and Lee, T. M. (2017). Large-scale functional neural network correlates of response inhibition: an fMRI meta-analysis. *Brain Structure and Function*. DOI: 10.1007/s00429-017-1443-x.

Zhang, Y., Brady, M., and Smith, S. (2001). Segmentation of brain MR images through a hidden Markov random field model and the expectation-maximization algorithm. *IEEE Transactions on Medical Imaging* 20, pp. 45–57. DOI: 10.1109/42.906424.

Zhang, Z., Cheng, H., Lin, Z., and Yang, T. (2019). A Sequence Learning Model for Decision Making in the Brain. *bioRxiv*, p. 555862. DOI: 10.1101/555862.

Zuo, X. N., Anderson, J. S., Bellec, P., Birn, R. M., Biswal, B. B., Blautzik, J., Breitner, J. C., Buckner, R. L., Calhoun, V. D., Castellanos, F. X., Chen, A., Chen, B., Chen, J., Chen, X., Colcombe, S. J., Courtney, W., Craddock, R. C., Di Martino, A., Dong, H. M., Fu, X., Gong, Q., Gorgolewski, K. J., Han, Y., He, Y., He, Y., Ho, E., Holmes, A., Hou, X. H., Huckins, J., Jiang, T., Jiang, Y., Kelley, W., Kelly, C., King, M., LaConte, S. M., Lainhart, J. E., Lei, X., Li, H. J., Li, K., Li, K., Lin, Q., Liu, D., Liu, J., Liu, X., Liu, Y., Lu, G., Lu, J., Luna, B., Luo, J., Lurie, D., Mao, Y., Margulies, D. S., Mayer, A. R., Meindl, T., Meyerand, M. E., Nan, W., Nielsen, J. A., O'Connor, D., Paulsen, D., Prabhakaran, V., Qi, Z., Qiu, J., Shao, C., Shehzad, Z., Tang, W., Villringer, A., Wang, H., Wang, K., Wei, D., Wei, G. X., Weng, X. C., Wu, X., Xu, T., Yang, N., Yang, Z., Zang, Y. F., Zhang, L., Zhang, Q., Zhang, Z., Zhang, Z., Zhao, K., Zhen, Z., Zhou, Y., Zhu, X. T., and Milham, M. P. (2014). An open science resource for establishing reliability and reproducibility in functional connectomics. *Scientific Data*. DOI: 10.1038/sdata.2014.49.

Author contributions per chapter

Contributions per chapter are described below following the Contributor Roles Taxonomy (CRediT; https://www.casrai.org/credit.html; Brand et al., 2015).

Chapter 2

This chapter is published as:
S. J. S. Isherwood, P.-L. Bazin, A. Alkemade, and B. U. Forstmann (2021a). Quantity and quality: Normative open-access neuroimaging databases. *PLOS ONE* 16.3, pp. 1–30. DOI: 10.1371/journal.pone.0248341.

Author contributions

Scott J. S. Isherwood: Conceptualisation, Methodology, Software, Validation, Formal analysis, Investigation, Data curation, Writing – Original draft, Writing – Review & Editing, Visualisation, **Pierre-Louis Bazin**: Conceptualisation, Methodology, Software, Formal analysis, Data curation, Writing – Original draft, Writing – Review & Editing, Supervision, **Anneke Alkemade**: Writing – Review & Editing, Supervision, **Birte U. Forstmann**: Conceptualisation, Methodology, Resources, Data curation, Writing – Review & Editing, Supervision, Project administration, Funding acquisition.

Acknowledgements

Data were provided [in part] by the Brain Genomics Superstruct Project of Harvard University and the Massachusetts General Hospital, (Principal Investigators: Randy Buckner, Joshua Roffman, and Jordan Smoller), with support from the Center for Brain Science Neuroinformatics Research Group, the Athinoula A. Martinos Center for Biomedical Imaging, and the Center for Human Genetic Research. 20 individual investigators at Harvard and MGH generously contributed data to the overall project. Data used in the preparation of this work were obtained from the CamCAN repository (available at http://www.mrc-cbu.cam.ac.uk/datasets/camcan/) [64, 65]. Data collection and sharing for this project was provided by the Cambridge Centre for Ageing and Neuroscience (CamCAN). Data were provided [in part] by the Human Connectome Project, WU-Minn Consortium (Principal Investigators: David Van Essen and Kamil Ugurbil;

1U54MH091657). The Midnight Scan Club data was obtained from the OpenfMRI database. Its accession number is ds000224. The data from Leipzig Mind Brain Body was obtained from the OpenfMRI database. Its accession number is ds000221. This study was supported by a NWO Vici (BUF).

Chapter 3

This chapter is published as:
S. Miletić, P.-L. Bazin, S. J. S. Isherwood, M. C. Keuken, A. Alkemade, and B. U. Forstmann (2022). Charting human subcortical maturation across the adult lifespan with in vivo 7 T MRI. *NeuroImage* 249.July 2021, p. 118872. DOI: 10.1016/j.neuroimage.2022.118872.

Author contributions

Steven Miletić: Conceptualisation, Methodology, Software, Validation, Formal analysis, Investigation, Data curation, Writing – Original draft, Writing – Review & Editing, Visualisation, **Pierre-Louis Bazin**: Conceptualisation, Methodology, Software, Formal analysis, Investigation, Data curation, Writing – Original draft, Writing – Review & Editing, Supervision, **Scott J. S. Isherwood**: Writing – Review & Editing, **Max C. Keuken**: Writing – Review & Editing, **Anneke Alkemade**: Conceptualisation, Methodology, Validation, Investigation, Resources, Data curation, Writing – Original draft, Writing – Review & Editing, Supervision, Project administration, Funding acquisition, **Birte U. Forstmann**: Conceptualisation, Methodology, Validation, Investigation, Resources, Data curation, Writing – Review & Editing, Supervision, Project administration, Funding acquisition.

Acknowledgements

This research was financially supported by STW/NWO (#14017; BUF and AA), ERC PoC (BUF), NWO Vici (016.Vici.185.052; BUF), and Stichting Ammodo (2019; BUF).

Chapter 4

This chapter is published as:
S. J. S. Isherwood, M. C. Keuken, P.-L. Bazin, and B. U. Forstmann (2021b). Cortical and subcortical contributions to interference resolution and inhibition - An fMRI ALE meta-analysis. *Neuroscience and biobehavioral reviews* 129, pp. 245–260. DOI: 10.1016/J.NEUBIOREV.2021.07.021.

Author contributions

Scott J. S. Isherwood: Conceptualisation, Methodology, Software, Validation, Formal analysis, Investigation, Data curation, Writing – Original draft, Writing – Review & Editing, Visualisation, **Max C. Keuken**: Methodology, Software, Validation, Formal analysis, Investigation, Data curation, Writing – Original draft, Writing – Review & Editing, Visualisation, **Pierre-Louis Bazin**: Methodology, Investigation, Writing – Review & Editing, Visualisation, Supervision, **Birte U. Forstmann**: Conceptualisation, Methodology, Validation, Investigation, Resources, Data curation, Writing – Review & Editing, Supervision, Project administration, Funding acquisition.

Acknowledgements

We would like to thank all contacted authors who kindly responded to our requests for additional information on the MRI acquisition and analysis parameters as well as providing the results of contrast not explicitly reported in the original publication. In addition, we thank T. Salo for his helpful suggestions regarding the use of NiMARE. This study was supported by a NWO Vici (BUF) and ERC Consolidator Grant (BUF).

Chapter 5

This chapter is published as:
S. J. S. Isherwood, P.-L. Bazin, S. Miletić, N. R. Stevenson, A. C. Trutti, D. H. Y. Tse, A. Heathcote, D. Matzke, R. J. Innes, S. Habli, D. R. Sokolowski, A. Alkemade, A. K. Håberg, and B. U. Forstmann (2023a). Investigating Intra-Individual Networks of Response Inhibition and Interference Resolution using 7T MRI. *NeuroImage*, p. 119988.

Author contributions

Scott J. S. Isherwood: Conceptualisation, Methodology, Software, Validation, Formal analysis, Investigation, Data curation, Writing – Original draft, Writing – Review & Editing, Visualisation, **Pierre-Louis Bazin**: Conceptualisation, Methodology, Software, Formal analysis, Investigation, Data curation, Writing – Original draft, Writing – Review & Editing, Supervision, **Steven Miletić**: Methodology, Software, Formal analysis, Investigation, Data curation, Writing – Review & Editing, **Niek R. Stevenson**: Methodology, Software, Formal analysis, Writing – Review & Editing, **Anne C. Trutti**: Methodology, Software, Formal analysis, Writing – Review & Editing, **Desmond H.Y. Tse**: Methodology, Software, Data

curation, **Andrew Heathcote**: Methodology, Writing – Review & Editing, **Dora Matzke**: Methodology, Writing – Review & Editing, Project administration, **Reilly J. Innes**: Software, Formal analysis, Writing – Review & Editing, **Sarah Habli**: Investigation, Data curation, Writing – Review & Editing, **Daniel R. Sokołowski**: Data curation, **Anneke Alkemade**: Methodology, Writing – Review & Editing, **Asta K. Håberg**: Resources, Writing – Review & Editing, Supervision, Project administration, **Birte U. Forstmann**: Conceptualisation, Methodology, Validation, Investigation, Resources, Data curation, Writing – Review & Editing, Supervision, Project administration, Funding acquisition.

Acknowledgements

We would like to thank PE. Goa for his help with the ongoing collaboration between the University of Amsterdam and the Norwegian University of Science and Technology. This study was supported by a NWO Vici (BUF) and ERC Consolidator Grant (BUF).

Chapter 6

This chapter is submitted as:
S. J. S. Isherwood, S. Kemp, S. Miletić, N. R. Stevenson, P.-L. Bazin, and B. U. Forstmann (2023b). The canonical stopping network: Revisiting the role of the subcortex in response inhibition. *submitted*.

Author contributions

Scott J. S. Isherwood: Conceptualisation, Methodology, Software, Validation, Formal analysis, Investigation, Data curation, Writing – Original draft, Writing – Review & Editing, Visualisation, **Sarah Kemp**: Conceptualisation, Validation, Investigation, Writing – Original draft, Writing – Review & Editing, Visualisation, **Steven Miletić**: Methodology, Software, Investigation, Data curation, Writing – Review & Editing, **Niek R. Stevenson**: Methodology, Software, Formal analysis, Writing – Review & Editing, **Pierre-Louis Bazin**: Conceptualisation, Methodology, Software, Formal analysis, Data curation, Writing – Original draft, Writing – Review & Editing, Supervision, **Birte U. Forstmann**: Conceptualisation, Methodology, Validation, Investigation, Resources, Data curation, Writing – Review & Editing, Supervision, Project administration, Funding acquisition.

Acknowledgements

This study was supported by a NWO Vici (BUF) and ERC Consolidator Grant (BUF).

Data and code availability

The code used for the chapter within this thesis was always made publicly available. Whenever possible, the accompanying data was also uploaded to a public repository.

Chapter 2

The code used in the analysis phase of this chapter can be found at https://github.com/scottyish/Quantity-and-Quality-Code. Links to download the data used in this chapter can be found in Table A.1.

Chapter 3

A prior version of the individual qMRI maps has been released as AHEAD (Alkemade et al., 2020a) can be found at https://doi.org/10.21942/uva.10007840.v1. All derived participant-wise and region-wise measures can be downloaded from our app at https://subcortex.eu/app. All code used to estimate the models and produce the figures can be found at https://osf.io/mvdbe/.

Chapter 4

The code used in the methods and analysis phases of this chapter can be found at https://github.com/scottyish/interference-resolution-and-inhibition-A
n-fMRI-ALE-meta-analysis.

Chapter 5

The code used in this chapter can be found at https://github.com/scottyish/Investigating-Intra-Individual-Networks. The data collected and analysed in this chapter can be found at https://uvaauas.figshare.com/articles/dataset/Investigating_Intra-

Individual_Networks_of_Response_Inhibition_and_In
terference_Resolution_using_7T_MRI_data/22240393.

Chapter 6

The code used in this chapter can be found at https://github.com/scottyish/The-canonical-stopping-network.

Full publication list

* indicates equal contributions

Groot, J., Miletić, S., **Isherwood**, **S. J. S.**, Tse, D. H. Y., Habli, S., Haberg, A. K., Forstmann, B. U., *Bazin, P.-L., and *Mittner, M. (2023). Echoes from intrinsic connectivity networks in the subcortex. *The Journal of Neuroscience*. DOI: https://doi.org/10.1523/JNEUROSCI.1020-23.2023.

Isherwood, **S. J. S.**, Bazin, P.-L., Miletić, S., Stevenson, N. R., Trutti, A. C., Tse, D. H. Y., Heathcote, A., Matzke, D., Innes, R. J., Habli, S., Sokolowski, D. R., Alkemade, A., Håberg, A. K., and Forstmann, B. U. (2023a). Investigating Intra-Individual Networks of Response Inhibition and Interference Resolution using 7T MRI. *NeuroImage*, p. 119988.

Isherwood, **S. J. S.**, Kemp, S., Miletić, S., Stevenson, N. R., Bazin, P.-L., and Forstmann, B. U. (2023b). The canonical stopping network: Revisiting the role of the subcortex in response inhibition. *submitted*.

Stevenson, N. R., Innes, R. J., Boag, R. J., Miletić, S., **Isherwood**, **S. J. S.**, Trutti, A. C., Heathcote, A., and Forstmann, B. U. (2023). Joint modelling of latent cognitive mechanisms shared across decision-making domains. *submitted*.

Keuken, M. C., Liebrand, L. C., Bazin, P.-L., Alkemade, A., van Berendonk, N., Groot, J. M., **Isherwood**, **S. J. S.**, Kemp, S., Lute, N., Mulder, M. J., Trutti, A. C., Caan, M. W., and Forstmann, B. U. (2022). A high-resolution multi-shell 3T diffusion magnetic resonance imaging dataset as part of the Amsterdam Ultra-high field adult lifespan database (AHEAD). *Data in Brief* 42, p. 108086. DOI: https://doi.org/10.1016/j.dib.2022.108086.

Miletić, S., Bazin, P.-L., **Isherwood**, **S. J. S.**, Keuken, M. C., Alkemade, A., and Forstmann, B. U. (2022). Charting human subcortical maturation across the adult lifespan with in vivo 7 T MRI. *NeuroImage* 249, p. 118872. DOI: https://doi.org/10.1016/j.neuroimage.2022.118872.

Isherwood, **S. J. S.**, Bazin, P.-L., Alkemade, A., and Forstmann, B. U. (2021a). Quantity and quality: Normative open-access neuroimaging databases. *PLOS ONE* 16, pp. 1–30. DOI: 10.1371/journal.pone.0248341.

Isherwood, **S. J. S.**, Keuken, M. C., Bazin, P.-L., and Forstmann, B. (2021b). Cortical and subcortical contributions to interference resolution and inhibition – An

fMRI ALE meta-analysis. *Neuroscience and Biobehavioral Reviews* 129, pp. 245–260. DOI: https://doi.org/10.1016/j.neubiorev.2021.07.021.

Alkemade, A., Mulder, M. J., Groot, J. M., Isaacs, B. R., van Berendonk, N., Lute, N., **Isherwood**, **S. J. S.**, Bazin, P.-L., and Forstmann, B. U. (2020). The Amsterdam Ultra-high field adult lifespan database (AHEAD): A freely available multimodal 7 Tesla submillimeter magnetic resonance imaging database. *NeuroImage* 221, p. 117200. DOI: https://doi.org/10.1016/j.neuroimage.2020.117200.

English summary

The field of cognitive neuroscience has predominantly focused on studying the cerebral cortex, often neglecting the subcortex, which accounts for about 25% of the brain. This underrepresentation can be attributed to two main reasons. Firstly, the subcortex was considered less important compared to the cortex, with the belief that the cortex is responsible for all higher-level cognition. However, emerging evidence indicates that the subcortex plays a crucial role in various aspects of human cognition and behavior. Secondly, the subcortex has been challenging to study due to its deep location, small size, and close proximity to other structures. Traditional neuroimaging techniques have struggled to provide high-resolution images of the subcortex. However, recent advancements in neuroimaging and neurophysiological methods have enabled us to explore the subcortex more precisely. As a result, there is growing recognition of the significance of the subcortex in understanding the complexities of the human brain.

One specific area where the subcortex has garnered attention is its role in the implementation of inhibition-related functions, namely response inhibition and interference resolution. Response inhibition describes the ability to stop an already initiated action, while interference resolution describes the ability to ignore or suppress task-irrelevant information. Both processes are paramount for successful functioning in day-to-day life. Subcortical diseases such as Parkinson's, OCD and dystonia often come hand in hand with deficiencies in one or both subtypes of inhibition. The core objectives of the work within thesis are therefore twofold: the first is to expand our knowledge on the structure and function of the human subcortex, and the second is to investigate the neural and computational dynamics of response inhibition and interference resolution. To achieve these objectives, an interdisciplinary approach combining meta-analyses, structural and functional ultra-high field magnetic resonance imaging (UHF MRI), and cognitive modelling is employed. By combining these modalities, we can gain novel insights into how these subtypes of inhibition are implemented in the brain and to what extent they overlap on both behavioral and computational scales.

The thesis consists of several chapters that cover different aspects of the research. In Chapter 2, the investigation begins by creating an up-to-date catalogue of MRI

databases focused on the neurotypical population. The purpose is to extract quantitative measures of image quality across these databases to gain a comprehensive understanding of the current state of the field. This chapter highlights the advantages of using UHF MRI for brain imaging, particularly when examining the subcortex. It also discusses the trade-offs involved in parameters such as acquisition time, spatial resolution, and SNR (Signal-to-Noise Ratio). Furthermore, the chapter emphasizes the benefits of open-access data sharing and the choices researchers face when balancing data quantity and quality.

Chapter 3 expands the structural investigation into the deep brain, specifically focusing on age-related changes throughout adulthood and the composition of 17 subcortical structures. The chapter defines these regions in terms of their iron and myelin contents, as well as their morphometry. By doing so, novel insights are gained into the heterogeneity of these complex regions, including changes in their location, which have significant implications for constructing accurate atlases of the human subcortex. This chapter underscores the importance of precisely mapping subcortical structures for both structural and functional inference, and it outlines the wealth of information that can be obtained from tailored MR sequences.

Moving on to Chapter 4, I delve into the existing literature on response inhibition and interference resolution. This comprehensive review serves as a foundation for the subsequent research conducted in the thesis. While the previous chapters focused on the structural understanding of the subcortex, Chapter 4 shifts the perspective towards investigating their functional counterparts. To achieve this, I employed activation likelihood estimation to aggregate previous functional studies related to inhibition. The results reveal a relatively incongruous functional map, with significant differences observed in regions between different meta-analyses and various subtypes of inhibition. While some questions regarding inter-individual similarities and differences are addressed, many questions remain unanswered.

Chapter 5 complements the inter-individual results of the meta-analysis by investigating response inhibition and interference resolution at the intra-individual level. Leveraging the insights gained from the previous chapters, we designed and optimized a functional study that provides state-of-the-art structural, functional, and behavioral data for both response inhibition and interference resolution tasks. This methodology enables the comparison of different subtypes of inhibition while minimizing individual differences through intra-individual comparisons. The findings indicate that response inhibition and interference resolution tasks have

relatively little behavioral overlap and are rooted in distinct networks within the brain. Moreover, employing a model-based technique reveals differences in the computational aspects of these two inhibition-related functions.

Chapter 6 represents the culmination of the exploration into response inhibition. The outcomes of the functional and behavioral investigations are merged, and four additional datasets related to stop signal task (SST) are reprocessed and reanalyzed to shed light on the inconsistencies present within the field. Utilizing open-access data, the research combines data points from multiple datasets, enabling a comprehensive analysis beyond summary measures alone. Contrary to historical models of response inhibition, the findings suggest that successful inhibition does not solely rely on the canonical cortico-basal-ganglia pathways. Instead, it is discovered that failures of response inhibition activate multiple subcortical nodes that were previously theorized to underpin successful inhibition. These findings, combined with other relevant literature, indicate the need for further investigation into the networks that underlie successful response inhibition in the human subcortex.

Finally, in Chapter 7, a comprehensive summary of the key findings presented throughout the thesis is provided. The implications of these findings for future research are elucidated, and a contextual discussion is presented in relation to recent publications. This chapter serves as a conclusion, highlighting the significant contributions of the research to the field of subcortical functioning and providing directions for future studies.

Nederlandse samenvatting

Het gebied van de cognitieve neurowetenschappen heeft zich voornamelijk gericht op het bestuderen van de hersenschors, waarbij de subcorticale gebieden, die tezamen ongeveer 25% van het volume van de hersenen beslaan, onderbelicht zijn gebleven. Er zijn twee belangrijke reden waarom de subcortex historisch gezien op de achtergrond is gebleven. Ten eerste werd de subcortex als minder belangrijk beschouwd in vergelijking met de cortex, met de overtuiging dat de cortex verantwoordelijk is voor alle hogere cognitieve functies. Er is echter steeds meer bewijs dat de subcortex een cruciale rol speelt in verschillende aspecten van menselijke cognitie en gedrag. Ten tweede was de subcortex moeilijk te bestuderen vanwege de diepe ligging in de hersenen en de beperkte omvang van afzonderlijke gebieden. Met traditionele beeldvormingstechnieken is het moeilijk om gedetailleerde en hoogwaardige beelden van de subcortex te verkrijgen. Recente ontwikkelingen in beeldvormingstechniek en neurofysiologische methoden maken het nu echter mogelijk de subcortex nauwkeuriger te onderzoeken. Hierdoor wordt het belang van de subcortex voor het begrijpen van de complexiteit van het menselijk brein steeds meer erkend.

De subcortex heeft eerder aandacht gekregen vanwege zijn rol in de uitvoering van functies met betrekking tot inhibitie, met name responsinhibitie en interferentieresolutie. Responsinhibitie verwijst naar het vermogen om een reeds gestarte handeling te stoppen, terwijl interferentieresolutie het vermogen beschrijft om taakirrelevante informatie te negeren of te onderdrukken. Beide processen zijn van cruciaal belang voor succesvol functioneren in het dagelijks leven. Ziekten die verband houden met de subcortex, zoals de ziekte van Parkinson, OCD en dystonie, vertonen vaak tekortkomingen in een of beide subtypes van inhibitie. De hoofddoelen van dit proefschrift zijn tweeledig: ten eerste het verdiepen van onze kennis over de structuur en functie van de menselijke subcortex, en ten tweede het onderzoeken van de neurale en computationele processen onderliggend aan responsinhibitie en interferentieresolutie. Om deze doelen te verwezenlijken wordt een interdisciplinaire aanpak gehanteerd die meta-analyses, structurele en functionele ultra-high field magnetische resonantiebeeldvorming (UHF MRI), en cognitief modelleren combineert. Het combineren van deze methoden stelt

ons in staat nieuwe inzichten te verkrijgen in hoe deze subtypes van inhibitie worden geïmplementeerd in de hersenen en in welke mate ze overlappen, op zowel gedrags- als computationeel niveau.

Het proefschrift bestaat uit verschillende hoofdstukken die verschillende facetten van het onderzoek behandelen. In hoofdstuk 2 begint het onderzoek met het samenstellen van een actueel overzicht van bestaande MRI-databases gericht op de neurotypische populatie. Het doel hierbij is het verkrijgen van kwantitatieve metingen van de beeldkwaliteit in deze databases, om inzicht te verkrijgen in de huidige stand van zaken in dit onderzoeksgebied. Dit hoofdstuk belicht de voordelen van het gebruik van UHF MRI voor beeldvorming van de hersenen, met name bij het onderzoeken van de subcortex. Bovendien bespreekt het de afwegingen die gemaakt moeten worden met betrekking tot parameters als acquisitietijd, spatiele resolutie en SNR (signaal-ruisverhouding). Verder benadrukt het hoofdstuk het belang van het openbaar beschikbaar stellen van data, en wijst het op de keuzes die onderzoekers moeten maken bij het maken van de afweging tussen kwaliteit en kwantiteit van data.

Hoofdstuk 3 breidt het structurele onderzoek naar de subcortex uit en richt zich specifiek op de samenstelling van 17 subcorticale structuren en leeftijdsgerelateerde veranderingen daarin. In het hoofdstuk worden de gehaltes ijzer en myeline van deze regio's vastgesteld, alsmede enkele morfometrische kenmerken. Het onderzoek belicht de heterogeniteit en complexiteit van deze regio's. Het laat ook zien dat zelfs de locatie van gebieden kan veranderen met de leeftijd, wat belangrijke implicaties heeft voor het creëren van nauwkeurige atlassen van de subcortex. Dit hoofdstuk benadrukt het belang van het nauwkeurig in kaart brengen van subcorticale structuren voor het begrip van zowel structurele als functionele eigenschappen, en het toont de rijkdom aan informatie die kan worden verkregen uit op maat gemaakte MRI-sequenties.

In hoofdstuk 4 duik ik in de bestaande literatuur over responsinhibitie en interferentieresolutie. Dit uitgebreide overzicht dient als basis voor het verdere onderzoek in dit proefschrift. Terwijl de vorige hoofdstukken zich richtten op het structurele begrip van de subcortex, verlegt hoofdstuk 4 het perspectief naar het onderzoeken van hun functies. Om dit te bereiken gebruikte ik een methode genaamd activation likelihood estimation om de resultaten van eerdere functionele studies met betrekking tot inhibitie te integreren. De resultaten laten een relatief onvoorspelbare functionele kaart zien, waarbij aanzienlijke variaties in de betrokken hersengebieden naar voren komen tussen verschillende meta-analyses en verschillende subtypes van inhibitie. Hoewel sommige vragen met betrekking

tot inter-individuele gelijkenissen en verschillen worden behandeld, laat het veel vragen onbeantwoord.

Hoofdstuk 5 vult de inter-individuele resultaten van de meta-analyse uit hoofdstuk 4 aan door responsinhibitie en interferentieresolutie op intra-individueel niveau te onderzoeken. Gebaseerd op de inzichten uit de voorgaande hoofdstukken hebben we een functionele studie ontworpen en geoptimaliseerd, waarin state-of-the-art structurele, functionele en gedragsdata worden verzameld over zowel responsinhibitie als interferentieresolutie. Deze methodologie maakt het mogelijk om subtypes van inhibitie te vergelijken op intra-individueel niveau. De resultaten tonen aan dat responsinhibitie en interferentieresolutie zowel op het gebied van gedrag, als op het gebied van de onderliggende hersennetwerken, relatief weinig overlap vertonen. Bovendien werpt het gebruik van een modelgebaseerde benadering licht op de verschillen in computationele aspecten van deze twee inhibitie-gerelateerde functies.

Hoofdstuk 6 vormt het hoogtepunt van het onderzoek naar responsinhibitie. De resultaten van de functionele en gedragsmatige studies worden samengevoegd, en vier aanvullende, reeds bestaande datasets met betrekking tot de stopsignaaltaak (SST) worden opnieuw geanalyseerd om licht te werpen op bestaande inconsistenties binnen het veld. Door gebruik te maken van publiek toegankelijke data worden meerdere datasets gecombineerd, wat het mogelijk maakt een diepgaande analyse te maken. In tegenstelling tot traditionele modellen van responsinhibitie, suggereren de bevindingen dat succesvolle inhibitie niet alleen berust op de gebruikelijke cortico-basale-ganglia verbindingen. In plaats daarvan toont het onderzoek aan meerdere subcorticale knooppunten actief worden als responsinhibitie faalt, terwijl eerder werd gedacht dat die gebieden juist actief worden tijdens succesvolle responsinhibitie. Deze bevindingen, in combinatie met andere relevante literatuur, benadrukken de noodzaak van verder onderzoek naar de netwerken die ten grondslag liggen aan succesvolle responsinhibitie in de menselijke subcortex.

Tot slot wordt in hoofdstuk 7 een uitgebreide samenvatting gegeven van de belangrijkste bevindingen van dit proefschrift. Tevens worden de bevindingen geplaatst in de context van de bredere wetenschappelijke literatuur rond inhibitie. Dit hoofdstuk dient als conclusie en afsluiting, waarin de belangrijke bijdragen van dit werk aan het domein van subcorticale functies worden benadrukt en richtingen voor verder onderzoek worden aangegeven.

Acknowledgements

Dear colleagues, family, and friends,

First of all, thank you for taking the time to read this thesis. It has been many years in the making, and would not have been possible without the support of a number of people. So, without further ado, I would like to extend my gratitude to the people who made this work possible:

My warmest thanks of course goes to my inspiring supervisors Prof. Dr. Birte U. Forstmann and Dr. Pierre-Louis E. A. Bazin. Without their unwavering support and invaluable insights, I would not have been able to achieve the current standard of this work. Birte, I have been lucky to have you as a supervisor during this emotional roller coaster of a PhD. I have learnt a tremendous amount from you, and I hold deep admiration for the passion and dedication you bring to the group. Pilou, thank you for the positivity and for always having a solution to my many many problems. Without your day-to-day guidance I would have barely got through the first chapter.

Andrew, I will miss the intense academic discourse over Friday drinks. Thank you for all the help and I hope the La Chouffe's never stop flowing. Anne, though Wednesday hangouts ended a long time ago, your moral support has been continuous. The lab would not have been the same without you. Anneke, thank you for always being the most critical of my manuscripts, I never knew how bad my English was until you gave me feedback. Bernadette, I hope you are enjoying your new home at the VU, thanks for making the lab fun while you were here. Beth, though our overlap was short, the impression you made was long lasting. I hope you are doing well on your new path. Dora, thank you for all your guidance on my many modelling needs and for the car storage program you extended to me. Ettore, thanks for showing the dutch people that cheese sandwiches are not the only lunch available in the world. Ivar, we made it. Thanks for putting up with me as a flatmate and for all the lengthy late night venting and deliberation. Jos, though we preferred you in Amsterdam, I'm glad you have had such a good time in Trømso. Leendert, thanks for setting me up well in my first internship in the lab, you made the heavy learning curve fun and inspired me to nerd out over cognitive modelling. Max, I appreciate your help and experience on the project we worked

on together and I hope your new path outside of academia means that you never have to do a meta-analysis again. 19,598 abstracts is enough for a lifetime. Niek, without your modelling insight I would still be on chapter four right now. It was fun working and drinking together. Reilly, Monday mules has forever scarred me. I hope your dad jokes are as appreciated at your new place of work as they were here in the lab. Russ, the stories you shared are not ones I can ever repeat but they will stay with me forever. Sarah, it was a pleasure. Thank you for taking over lab meeting duties with such enthusiasm, I am sad to not see you in your element. Steven, thank you for being a great supervisor, colleague, and friend. I hope we continue to enjoy our fine dining, fine wining, and general tech jibber jabber.

To our collaborators at NTNU; Asta, Pål Erik, Desmond, Daniel and Sarah, thank you for all the hard work it took to get the projects up and running. My thesis would not have been the same without your help. I would also like to thank the doctorate committee for agreeing to assess and in the end, approving this thesis.

To my family and friends, I thank you all for the unconditional support and encouragement over the entirety of this PhD. I especially thank my parents for always standing by my pursuits. I would have never have made it to where I am if it weren't for you. Yasmin, thank you for finally moving back to this side of the world! It's so nice to have you back and I'm sorry I up'd and left just as you got here. Maybe next time we'll have more luck! Mica, I am immensely thankful that you came into my life when you did. As with most PhD's, my work has been my life all day everyday for the last four years. I am grateful that you have made the rest of my life so meaningful. My last shoutout is to Piri and Lucifer, for their attempts at emotional support. I hope to be there for you all in the future as you have been there for me.